MICROSTRUCTURAL, THERMAL AND MECHANICAL PROPERTIES ON THE TIN-BISMUTH EUTECTIC SOLDER ALLOY UPON ADDITIONS OF ZIRCONIA AND MOLYBDENUM NANOPARTICLES

AMARES SINGH GILL

DOCTOR OF PHILOSOPHY (ENGINEERING)

LEE KONG CHIAN FACULTY OF ENGINEERING AND SCIENCE,
UNIVERSITI TUNKU ABDUL RAHMAN

APRIL 2021

MICROSTRUCTURAL, THERMAL AND MECHANICAL PROPERTIES ON THE TIN-BISMUTH EUTECTIC SOLDER ALLOY UPON ADDITIONS OF ZIRCONIA AND MOLYBDENUM NANOPARTICLES

By

AMARES SINGH GILL

A dissertation submitted to the Department of Mechanical and Material Engineering,
Lee Kong Chian Faculty of Engineering and Science,
Universiti Tunku Abdul Rahman,
in partial fulfillment of the requirements for the degree of
Doctor of Philosophy (Engineering)
April 2021

ABSTRACT

MICROSTRUCTURAL, THERMAL AND MECHANICAL PROPERTIES ON THE TIN-BISMUTH EUTECTIC SOLDER ALLOY UPON ADDITIONS OF ZIRCONIA AND MOLYBDENUM NANOPARTICLES.

Amares Singh Gill

This research investigates the effects on the microstructural, thermal and mechanical properties of the low temperature lead free tin (Sn)-bismuth (Bi) solder alloy upon mechanically mixing 1 %, 2 % and 3 % molybdenum (Mo) and zirconia (ZrO_2) nanoparticles separately. The solder alloy is chosen to replace the hazardous lead solder and to accommodate low temperature soldering. Nanoparticles of molybdenum (Mo) and zirconia (ZrO_2) with high melting point and low density will not react with the elements in the solder alloy and exerts its influence as discrete particles. The melting temperatures with the lowest temperature were recorded for the 2 % Mo additions (139.73 °C) and the 2 % ZrO_2 additions (140.89 °C). Low melting point solders serves as platform for low temperature soldering to preserve other components from high temperature thermal shock. The microstructures of the solder alloy reinforced with molybdenum (Mo) and zirconia (ZrO_2) nanoparticles solder alloys consist of the typical lamellar structure of

bismuth (Bi) and tin (β-Sn) with presences of nanoparticles as well. Compared with the bare solder alloy, the bismuth (Bi) area in all the percentages of nanoparticles addition were smaller except for the 2 % Mo additions because of improper segregation of the nanoparticles. The reinforced nanoparticles appeared as discrete particles on the microstructure and acted as heterogenous site for nucleation process and at the same time restricted the grain growth of the bismuth (Bi) area. The intermetallic (IMC) layer thickness for the 3 % ZrO_2 added SB/Cu joint measures the thinnest (0.4804 µm) as the ZrO_2 existed as discrete particles at the solder joint to prevent vast diffusion process. Whereas, in all molybdenum added solder joint, reaction between molybdenum and tin produced Mo_2Sn IMC leaving no molybdenum as discrete particles. Thin IMC layer, discrete nanoparticles and other strengthening IMC's will boost the solder joint's strength. Hardness measurement based on microhardness values were calculated. The microhardness values of 1 % ZrO_2 and 3 % Mo nanoparticles additions increases 12 % and 1.4 % each compared to the SB solder. The 3 % Mo and 3 % ZrO_2 added solder joints produced the highest shear stress of 137.72 MPa and 174.26 MPa respectively, compatible with the thin IMC layer. Improvement to the contact angle, spreading area and ratio upon additions of both nanoparticles for all percentages of addition were observed with the smaller sized ZrO_2 additions emerging with better results. The reinforcement of ZrO_2 nanoparticles, specifically with the 3 % additions appeared to produce better improvement to the properties.

ACKNOWLEDGEMENT

Firstly, I would want to thank the almighty God for giving me a good health throughout this research. I would like to take this opportunity to show my appreciation to my wife and my parents for giving me full moral support throughout my progress to succeed this project.

My gratitude goes to my supervisor Ir. Professor. Dr. Rajkumar Durairaj, who had guided me throughout this research in all circumstance. His expertise on the subject area and his guidance lead to a smooth success in the research. The success of the objectives for this project relied on his expertise. On the other half, I am thankful to my co-supervisor, Assistant Professor Dr. Kuan Seng How, who not in any less manner had helped me in the completion of this research. Credits also goes to all staff and technicians from Lee Kong Chian Faculty of Engineering and Science (LKCFES), Universiti Tunku Abdul Rahman (UTAR) who have assisted me in conducting experiments as well.

Finally, I would thank to all those who helped me in competing this project. All the assistance by any personnel or group is kindly appreciated.

APPROVAL SHEET

This dissertation/thesis entitled "**MICROSTRUCTURAL, THERMAL AND MECHANICAL PROPERTIES ON THE TIN-BISMUTH EUTECTIC SOLDER ALLOY UPON ADDITIONS OF ZIRCONIA AND MOLYBDENUM NANOPARTICLES.**" was prepared by AMARES SINGH GILL and submitted as partial fulfillment of the requirements for the degree of Doctor of Philosophy (Engineering) at Universiti Tunku Abdul Rahman.

Approved by:

(Ir. Dr. Rajkumar Durairaj) 2nd APRIL 2021

Professor/Supervisor
Department of Mechanical and Material Engineering
Lee Kong Chian Faculty of Engineering and Science
Universiti Tunku Abdul Rahman

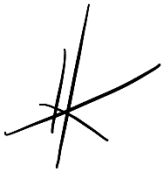

(Dr. Kuan Seng How) 5th APRIL 2021

Assistant Professor/Co-supervisor
Department of Mechanical and Material Engineering
Lee Kong Chian Faculty of Engineering and Science
Universiti Tunku Abdul Rahman

LEE KONG CHIAN FACULTY OF ENGINEERING AND SCIENCE

UNIVERSITI TUNKU ABDUL RAHMAN

Date: 5th APRIL 2021

SUBMISSION OF THESIS

It is hereby certified that *Amares Singh Gill* (ID No: 16UED07161) has completed this thesis entitled "*MICROSTRUCTURAL, THERMAL AND MECHANICAL PROPERTIES ON THE TIN-BISMUTH EUTECTIC SOLDER ALLOY UPON ADDITIONS OF ZIRCONIA AND MOLYBDENUM NANOPARTICLES.*" under the supervision of Professor Ir. Dr. Rajkumar Durairaj (Supervisor) from the Department of Mechanical and Material Engineering, Lee Kong Chian Faculty of Engineering and Science, and Assistant Professor Dr. Kuan Seng How (Co-Supervisor) from the Department of Mechanical and Material Engineering, Lee Kong Chian Faculty of Engineering and Science.

I understand that University will upload softcopy of my thesis in pdf format into UTAR Institutional Repository, which may be made accessible to UTAR community and public.

Yours truly,

(*AMARES SINGH*)

DECLARATION

I hereby declare that the dissertation is based on my original work except for quotations and citations which have been duly acknowledged. I also declare that it has not been previously or concurrently submitted for any other degree at UTAR or other institutions.

AMARES SINGH GILL

5th APRIL 2021

TABLE OF CONTENTS

LIST OF TABLES

LIST OF FIGURES

LIST OF ABBREVIATIONS

Sn	Tin
Bi	Bismuth
Mo	Molybdenum
ZrO2	Zirconia
SB	Tin-bismuth solder alloy
SB/Cu	Tin-bismuth/copper solder joint
SB + Mo/Cu	Tin-bismuth added with molybdenum /copper solder joint
SB + ZrO_2/Cu	Tin-bismuth added with zirconia /copper solder joint
SAC	Tin-argentum-copper solder alloy
SA	Tin-argentum solder alloy
Ag	Argentum
Ni	Nickel
Cu	Copper
Co	Cobalt
Al_2O_3	Alumina
TiO_2	Titanium dioxide
Ca	Calcium
Pb	Lead
O	Oxygen

C	Carbon
Pd	Palladium
Pt	Platinum
Fe	Iron
Ti	Titanium
Er	Erbium
Au	Gold
S	Sulphur
Cr	Chromium
Zn	Zinc
Sb	Antimony
Zr	Zirconium
In	Indium
La	Lanthanum
Ce	Cerium
Ge	Germanium
Yb	Ytterbium
Eu	Europium
Pr	Praseodymium
NiO	Nickel oxide
$SrTiO_3$	Strontium titanate

Fe_2NiO_4	Iron nickel oxide
Fe_2O_3	Ferric oxide
Bi_2Te_3	Bismuth telluride
ZnO	Zinc oxide
FeCl	Ferric chloride
TiC	Titanium carbide
SiC	Silicon carbide
SiO_2	Silica
ITO	Indum tin oxide
GNS	Graphene nanosheets
CNT	Carbon nanotube
SWCNT	Single wall carbon nanotube
POSS	Polyhedral oligomeric silsesquioxane
$SnSO_4$	Stannous sulfate
SnS	Tin(II) sulfide
SnO	Tin(II) oxide
$AgNO_3$	Silver nitrate
$Cu(NO_3)_2$	Cupric nitrate
γ_{sv}	Surface tension between solid and vapor
γ_{lv}	Surface tension between liquid and vapor
CTE	Coefficient of thermal expansion

SMT	Surface mount technology
PCB	Printed circuit board
IMC	Intermetallic compound
SEM	Scanning electron microscope
EDX	Energy dispersive X-ray
XRD	X-ray diffraction
DSC	Differential scanning calorimetry
UTS	Ultimate tensile strength

CHAPTER 1

INTRODUCTION

The fundamental on the field of study related to the nanoparticles additions in solder alloy will be looked upon in this chapter. This chapter provides the outline of the knowledge and the purposes of the research. The soldering process, solder alloys and its application together with its current development are explained.

1.1 Area of Interest

In the research, the area of interest will be focusing on nanoparticles addition on a specific low temperature solder alloy for soldering purpose in the electronic packaging technology. In pursuit of that, several important properties such as the thermal, microstructural and mechanical properties will be investigated to produce better substantiation of the new solder alloy's efficiency.

1.2 Background of Research

Soldering is a renowned metallurgical joining method that takes place below 425 °C. (Efzan, et al., 2013). Soldering uses a molten filler metal as a medium that connects the electronic component with the PCB board. This process will steer the formation of metallurgical bonds between the filler metal and the electronic components. The soldering process is separated into three stages, spreading, base metal dissolution and formation of an intermetallic compound layer

(J.Shen & Y.C Chan, 2009). Solders alloys are used to connect chips to the packaging substrates in the surface mounting technology (SMT) (Cheng, et al., 2017). As a joining material, solders must provide electrical, thermal and mechanical continuity in electronics assemblies and serve as a course for dissipation of the heat generated by the semiconductor.

The tin-lead (SnPb) solders have been used in the electronic industry for quite some time. The Pb composition in the solder allows melting at a low temperature, while the Sn gives more strength (Gao, et al., 2009). Common applications of solder alloys are done in the packaging of electronic devices in the PCB, where the eutectic and near-eutectic SnPb solders are frequently used. However, concerns arise over the usage of lead in products and the health safety of people who work with it. In 2006, the European Union (EU) banned lead consumption in products sold in Europe. In recent years, environmental concerns have been raised regarding the usage of lead containing solder in electronic products. Increased health concerns over the toxicity of lead in eutectic SnPb solder have triggered the development of lead-free solders. A study shows only up to 40 % to 70 % from the wasted electrical components (e.g. television, computers, PCB, mobile phones, etc.) can be recovered (R. Khanna, et al., 2014). In the same study, taking an example of one ton of waste mobile phones excluding the batteries, the materials inside the mobile phone contains up to 130 kg of Cu, 3.5 kg of Ag, 340 g of Au and 140 g of Pd that can be recycled and reused. In a separate gathered data for mobile phone usage, the presences of Sn and Pb are 31.6 ± 13.5 g/kg and 12.0 ± 8.7 g/kg respectively (M. Sahan, et al., 2019). This indicates that the amount of

the out of date electronic devices that enter the waste stream worldwide is more than 43 million tons annually. Together with electronic waste, the numbers are predicted to be increasing by 3-5 % per year.

The lead free solder alloys are immensely being developed in electronic applications as a potential replacement to the SnPb solder (Y. Tang, et al., 2019). The sustained trend towards miniaturization and functional density enhancement also necessitates smaller solder joints and fine-pitch interconnections in the microelectronic packaging (e.g.: portable electronic devices, such as portable computers and mobile phones) (Abdelhadi, 2013). This is because these devices have become thinner and smaller with more complicated functions. Corresponding to that, to provide the resemblance in the miniaturization of electronic industry, nanoparticles reinforcements are made to provide the mechanical integrity needed on a lead-free solder, as well as keeping the solder hazard-free (A. Fawzy, et al., 2013). Solder alloys are reinforced with nanoparticles to produce a nanocomposite or nanoparticles reinforced solder alloy to be applicable in the electronic field (Haseeb, et al., 2017). Nanoparticles reinforcements will act as discrete particles and does not alloy to the elements in the solder alloy. This is important to preserve the melting temperature of the solder alloy and provide enhancement to other properties such as mechanical strength by being discrete particles. Nanocomposite solders are solders that are intentionally reinforced with nano-scaled ($\times 10^{-9}$) reinforcements (L. C. Tsao, et al., 2010). The dimensions are studied particularly in nano scale, parallel to the miniaturization of the electronic devices in this era as well as for future needs. The influence of different weight percentages and types of

nanoparticles reinforcement are important in influencing the properties of the solder. Several materials that have been used as the nanoparticle reinforcement are such as Ag (Koscielski, et al., 2010), ZrO_2 (Gain, et al., 2011), Co (Bashir, et al., 2016), Mo (A.S.M.A. Haseeb, et al., 2012), Al_2O_3 (T. H. Cheng, et al., 2011) and TiO_2 (Nasir, et al., 2014).

In this research, the Mo and ZrO_2 nanoparticles are chosen due to the low density and the high melting point of each nanoparticles. Adding to that, these nanoparticles provides two distinguished type element, Mo which is a transition metal and ZrO_2 being an oxide metal. This provides distinctive comparison data. The weight percentage of additions of 1 %, 2 % and 3 % are chosen for this study. It was found out that there is no optimal amount for the percentage of additions, yet most literature provided a range of 1 % in between two percentages of additions. Gathered literature review have shown result that additions more than 3 % provided negative impact to the properties. This was taken as the guideline in this study to choose the percentage of additions as mentioned.

One of the important properties in benchmarking the efficiency of a solder alloy is the thermal properties. Melting temperatures obliges as an important parameter in describing the thermal properties (Lee & Jeong, 2014). The melting temperature should be lower than the traditional lead solder alloy (Koppes , et al., 2012). In microelectronic packaging, the microstructure properties intensely affect the reliability of the solder joints (L.S.Silva, et al., 2019). In the solder-substrate joint reliability, a thin IMC layer is desirable as it enhances the mechanical strength

by having a strong bonding at the interface (Laurila, et al., 2005). The rationale behind the nanoparticle's addition is that these nanoparticles should lead to dispersion strengthening and are expected to stabilize the microstructure by restricting the growth of different phases in the solder. Spreading properties is another property that links to the nanoparticle reinforcement in the solder alloy. Spreading properties can be categorized to spreading area, contact angle and spreading ratio that investigates the ability of the solder to wet and melt on the Cu substrate (Wang, et al., 2017). Hardness property is one more aspect that is significant towards studying the solder's mechanical properties. The microstructure and the presence of IMC in the solder contributes to the hardness of a solder (Spinelli, et al., 2014). Existence of nanoparticles in the solder affects the hardness property. The shear strength meanwhile is directly related to the solder joint and depends on the thickness of the IMC layer. The nanoparticles as active elements will influence the growth velocity of the plane and the diffusion process (S.L. Tay, et al., 2013). In this study, the ZrO_2 and Mo have their own physical properties by being in the nanoparticles form.

1.3 Problem Statements

Among the problem in this field of study is the low mechanical properties of shear stress and hardness of a low melting temperature solder system such as the SnBi solder. Moreover, research focusing on the addition of nanoparticles into the low melting solders system such as in the SnBi solder are still limited. Numerous studies are conducted on nanoparticles additions to the high melting temperature

solders, such as SAC and SA solder system. Nanoparticles, for instance, GNS, Al_2O_3, CNT, TiO_2, Mo, ZrO_2, $SrTiO_3$, NiO, C, $F_{e2}NiO_4$, Fe_2O_3, ITO and many more are added to the SAC solder system and the properties were improved. Frequently, the additions of nanoparticles to the high melting point solders are found to enhance the mechanical capability of the solder.

Research gap occurs here as most studies have focused on high melting temperature solder alloy, with minimal focus given to the nanoparticle's additions into low melting temperature solder alloys. Knowing that the low melting temperature solders can protect other electronic components from thermal damage, further investigation in improving the mechanical properties should be considered. Again, unfortunately, not many works been conducted towards these solders. The closest study involves additions of Mo nanoparticles in the SnBi solder (Yang, et al., 2019) but with different percentage of additions. Even in that study, not all properties were investigated. At the same time, less comparison was made with other types of nanoparticles reinforcements such as the oxide metal. This leaves vagueness to the effect of Mo to the SnBi solder. Being a transition metal, the Mo nanoparticles in a separate study involving the SnAgCu system increases the hardness of the reinforced solder (M.M. Arafat, et al., 2011). This stimulates to one of the objectives in this research in analyzing the effect of Mo to the hardness and the shear strength of the SnBi solder. Compared to other metal particles such as Ni, Cu and Ag, the Mo nanoparticles act as discrete particles and does not react with Sn to produce IMC compounds at the solder. The probability of the Mo nanoparticles effectively influencing the SnBi was forecasted in this study as the

melting point of the SnBi is much lower to endure any diffusion process among elements.

This research also involves the additions of ZrO_2 nanoparticles which is a ceramic material. Incorporation of ZrO_2 provides another variation in studying the properties. The results could be unique as not much literature studied ZrO_2 additions in the low melting solder alloys. However, the SAC solder was among the solder system that utilized the additions of ZrO_2 (Gain, et al., 2011). The ZrO_2 acts as the second phase dispersion strengthening mechanism to increase the shear strength almost 19 % compared to the pristine solder. Another explanation pointed out the oxide metal particles can have better segregation at the IMC layer. The involvement of ZrO_2 in the low melting temperature solder alloy is rarely found. So, knowing that the ZrO_2 boosts the mechanical properties of the SAC solder, it is chosen in this project and predicted to provide better mechanical aspect to the SnBi solder alloy as well.

Adding these ZrO_2 and Mo are predicted to produce enhancement especially in the mechanical properties, with these two types of nanoparticles serving as comparison data. This leads to other investigations on properties like the thermal, microstructural and mechanical properties in this research.

1.4 Objectives

As this research involves nanoparticles reinforcement into the Sn58Bi lead free solder alloy, several objectives are targeted to be accomplished. The objectives of this research are:

a) To characterize the thermal properties of Sn-Bi solder alloy reinforced with different weight percentages of ZrO_2 & Mo nanoparticles.
b) To investigate the relationship of microstructural in terms of Bi grain size area and element presence to the hardness and IMC thickness with different weight percentage of ZrO_2 & Mo nanoparticles added in Sn-Bi solder alloy.
c) To determine the effect to mechanical properties of shear strength and hardness with different weight percentage of ZrO_2 & Mo nanoparticles added in Sn-Bi solder alloy.
d) To analyse the effect of interfacial reaction on Cu substrate by spreading test using different weight percentage of ZrO_2 & Mo nanoparticles on Sn-Bi solder.

Further, all the measures that conjoins with the main objectives above will also be discussed and imported as part of the result analyses. This research will be providing results that will be analysed to deliver the influence of the nanoparticles to the properties of the Sn-Bi solder alloy. The analyses will be used as data to interpret and conclude this research.

1.5 Outcomes

The period of completion of this research is planned within 4 years. For the first year, the research will be based on development of the nanoparticles reinforced solder alloy. The second and third year focuses on the testing and results analyses. The last year will be utilised for the thesis write up and work completion before the viva session. The goals of this research are to satisfy the objectives mentioned and at the same time recommend the suitable nanoparticles reinforced solder alloy based on the result analyses. During this period, a manuscript has been accepted for publication in a Scopus indexed international journal.

CHAPTER 2

LITERATURE REVIEW

Literatures on the solder alloy's properties will be discussed in this chapter. The developments and existing literature from this field of study is referred to perform this research. All results and findings were tabulated and reviewed in this part which are used as references to this research. Reviews of solder alloy development from bulk alloy to nanoparticles solder alloy reinforcements are crucial to make this research successful as proposed in the objectives.

2.1 Solder Alloys

Generally, the solder alloys are processed from combination of raw materials that will be merged to produce the required solder alloy. The solder alloy acts as the medium of connection between the components and substrates. Essentially, the solder alloy should provide electrical (Jing, et al., 2013), thermal (Duan, et al., 2004), physical (Zhang, et al., 2010) and mechanical continuity (El-Daly, et al., 2014) in electronic assemblies. These solder alloys must be able to hold the components together and allow the components to contract and expand and at the same time exchange signals (Anderson & Harringa, 2004). The electrical properties of a solder alloy are secured as most of the solder alloys conducts electric and is not a major concern. As for the thermal properties of the solder alloy, melting temperature of the solder alloy should be within a certain range to protect other component from high temperature damage (Tan, et al., 2015). At the same, this

property influences in providing the structure integrity of the solder alloy. Now, that shifts the focus to the microstructural property of the solder alloy and is one of the factors that contributes in enhancing the mechanical strength. Adding to that, the physical properties such as the spreading properties also points to a better mechanical property of the solder alloy (Efzan, et al., 2010). Thus, from the earlier statement, the importance of each properties are closely interrelated. All these properties are reviewed in this section.

A solders life cycle is presented in Figure 2.1 and in the electronic packaging industry; common practice of implementation solder alloy is through the surface mount technology (SMT) method in the PCB board. An advantage of this solder alloy is the consumption of solder alloy can be recycled at the early stage, yet, once the soldering process is completed, the recovery is impossible which leads dumping of the component causing landfilling. Usually solders are in the form of alloys whereas in some application, it might be sole metals depending on the application (M.R. Harrison, et al., 2001). Alloying element must closely relate to the phase diagrams of any solder alloy (Baker, 1999; Kattner, 2002). The phase diagrams are widely available in many research and standards which alloys the industry to pick the suitable alloy for the application.

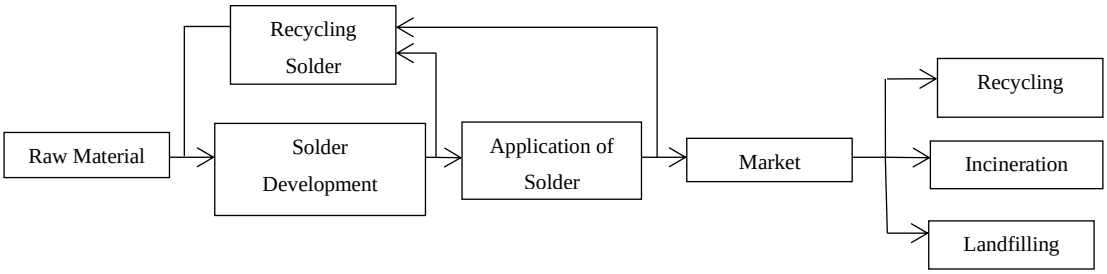

Figure 2. 1: Life cycle of a solder.

2.2 Phase Diagrams

Solder alloys are developed based on its phase diagram, which provides information on the composition and phases in a solder alloy (Askeland & Phule, 2006). Phase diagram distinguishes the microstructures and phases presented in the solder alloy at different composition and temperature. It is an important source that assists in choosing the solder alloy comparable with the lead solder alloy. This then provides information of the necessary temperature in order to control and predict the phases (Kattner, 2002). There are few categories of solder alloys based on phase diagrams such as unary, binary and ternary, depending on the total element used. The phases present in the phase diagram can be homogenous, materially dissimilar and be mechanically distinguished by a given composition commonly by weight percentage (wt. %) and structure which consist of liquid, L, solid solution, β and α and gases (Shim, 2008). Common terms such as eutectic phases are used in representing the lowest melting point of a solder alloy which appear as the two solid phases formed from a liquid phase (Callister & Rethwisch, 2011; Li & Kuribayashi, 2006). This eutectic point is ideally used as the lowest possible temperature of the solder alloy and knowing the phases presented at that point, it would assist in studying the mechanical properties. The subtopic 2.3 to 2.4 onwards will be

discussing on the phase diagram of the traditional lead and common lead free solder alloys.

2.3 Tin-Lead (SnPb) Solder Alloy

Applications of solder alloys in electronic industry are commonly linked to the lead solder alloy (Sn-Pb) (Suganuma , 2001; Kar, et al., 2007; Gao, et al., 2010). Due to its advantageous properties, the solder alloy established itself as the model solder alloy in the electronic packaging industry (D.C. Lin, et al., 2003; Zeng, et al., 2012). Looking in to the elements shown in Figure 2.2, Sn acts as the base material with Pb additions usually as 63 wt.% Sn and 37 wt.% Pb (M.R. Harrison, et al., 2001) which is the eutectic point (Boettinger, et al., 2006). The volume calculation of this compositions can be calculated by using the lever rule. The eutectic temperature of SnPb is 183 °C and this happens after the addition of Sn in the Pb, which lowers the pure melting temperature of the Pb (Duan, et al., 2004). Eutectic temperature allows the phases to solidify at a single point of temperature rather than varying temperature. At the eutectic temperature, the liquid will solidify in to two different compositions, the ($\alpha + \beta$) shown in Figure 2.2. This is an important aspect that allows choosing and configuring an alloy because at this point, all the liquids will solidify to two phases of solids at a lower point of temperature contributing to better microstructure.

The needs of low melting point solder in electronic industries is basically to avoid thermal damages to other components such as polymers during soldering.

SnPb solder very much obeys this requirement (Mayappan & Ahmad, 2010). As the desirable reflow (soldering) temperature is within 210-250 °C (Mei, et al., 1996; Suganuma , 2001), the SnPb satisfies this requirement making it as the reference for other solder alloys. Another plus point of SnPb is the availability of Pb throughout the globe, which helps in ensuring the rapid production of the solder alloy. Adding to that, the mechanical properties prevailed by this solder alloy are advantageous as shown in Table 2.1. (Ghosh, et al., 2009; Yu-peng, et al., 2010).

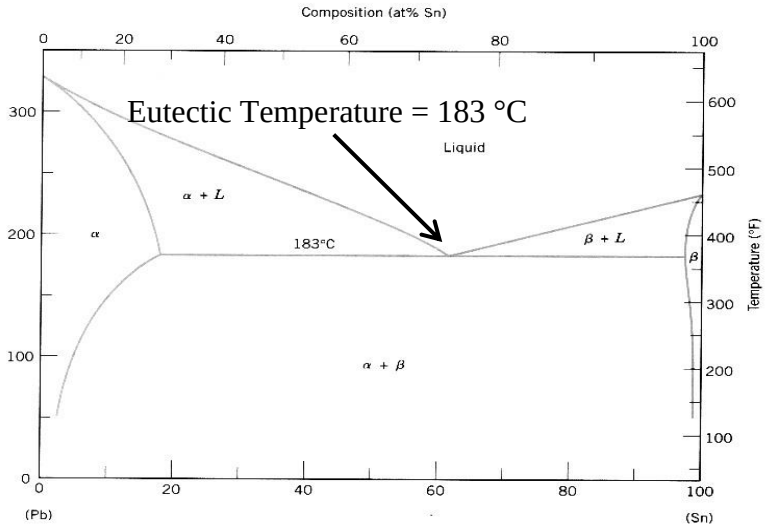

Figure 2.2: Phase diagram of SnPb solder alloy (Callister & Rethwisch, 2011).

Table 2. 1: SnPb solders alloy properties.

Material Properties	**100 % Sn**	**100 % Pb**	**63 % Sn - 37 % Pb**
Melting temperature, °C	232	327.5	183
Surface Tension, N/m	0.545	0.435	0.490
Shear Strength, MPa	27.57	13.79	23.79
Tensile Strength, MPa	21.5	17.3	27.5

Despite the SnPb solder alloy's beneficial properties, toxicity of Pb have been a major issue that it is a potential risk the environmental and human. The Environmental Protection Agency (EPA) listed the Pb as among the top 17 chemicals (Suraski & Karl , 2001). Concerns over the toxicity of Pb in eutectic SnPb solder have stimulated development towards new lead-free solders (Wu, et al., 2016). Yet, as this lead solder sustained its efficiently in the industry for a long time, its properties are set as a benchmark for the other alternative lead free solder alloy.

2.4 Lead Free Solder Alloys

Consequently, the elimination of the lead solder alloy prompts to the study and application of lead free solder alloys (Whalley, 2004). Lead free solder alloys are defined as solder alloys that does not use the Pb as one of its alloying elements, while the base materials can vary to any elements. But the Sn is usually chosen as base metal. Sadly, the lead free solder alloys are not renowned for significant application in manufacturing in the electronic industry as the lead solder (Amagai, 2008).

Therefore, new lead free solder alloys should be able to compete and be compatible as the lead solder. Binary lead free solder alloys such as SnCu (Liu, et al., 2009), SnAg, SnZn (Mayappan, et al., 2006) and SnBi (H.F. Zou, et al., 2012; Miao & Duh, 2001) are commonly investigated. In some studies, combinations of

three metals are used to produce a ternary solder alloy system, such as the SnAgCu (Kanlayasiri, et al., 2009), SnAgZn (El-Daly & Hammad, 2010), and Sn-Zn-Bi (El-Daly, et al., 2009). The phase diagrams still are the recipe to detect and analyse the phases presented for these solder alloys.

2.4.1 SnBi Solder Alloy

The eutectic SnBi alloy has an eutectic composition of 42 wt. % Sn and 58 wt. % Bi with a eutectic melting temperature as of 139 °C (P. Lobry, et al., 2011). A lower melting point is observed here as both elements melt earlier. Accompanied with the melting point of Bi being 271 °C, it contributes in lowering the overall melting point of the solder alloy. The mentioned weight percentage is actually the eutectic composition; however, the quantity can vary according to the application (i.e. mass used). Evidently, this solder alloy is categorized among the low melting temperature solder alloys and is essential for low melting temperature soldering applications in the electronic assembly (Singh, et al., 2017). This characteristic protects other components from high temperature failure. As the Sn has a low solid solubility in Bi as per noted from phase diagram, Figure 2.3 at the eutectic temperature, the Bi element tends to exist as pure element on the Sn matrix. These two elements do not react nor diffuse at low temperature (Miao & Duh, 2001). This is again confirmed with the presence of the two solid phases in the phase diagram in Figure 2.3.

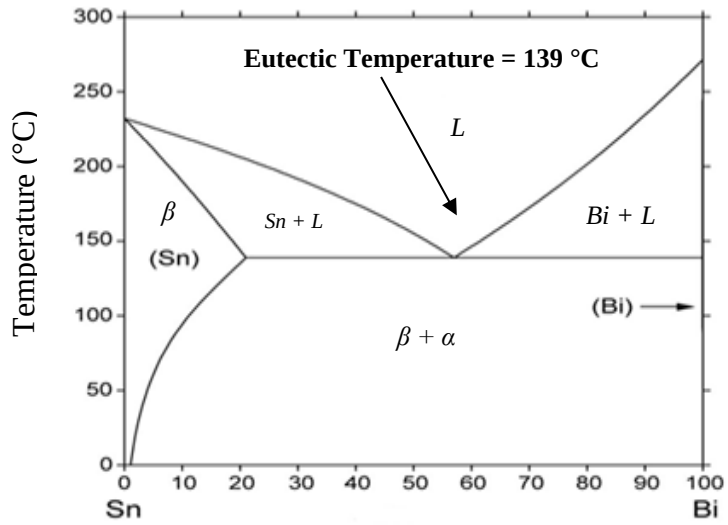

Figure 2. 3: Phase diagram of SnBi solder alloy (Okamoto, 2010).

2.4.2 SnAg Solder Alloy

Among other lead free solder is the SnAg solder alloy, which is a mixtures of the base metal Sn with the Ag. The eutectic composition of this solder alloy is at 96.5 wt. % Sn and 3.5 wt. % Ag giving a eutectic temperature of 221 °C, as shown in the Figure 2.4. Adding the Ag to the base Sn increases the temperature of the solder alloy due to the reactivity of Sn and Ag by diffusion process. The increases the melting temperature happens since the melting point of Ag (962 °C).

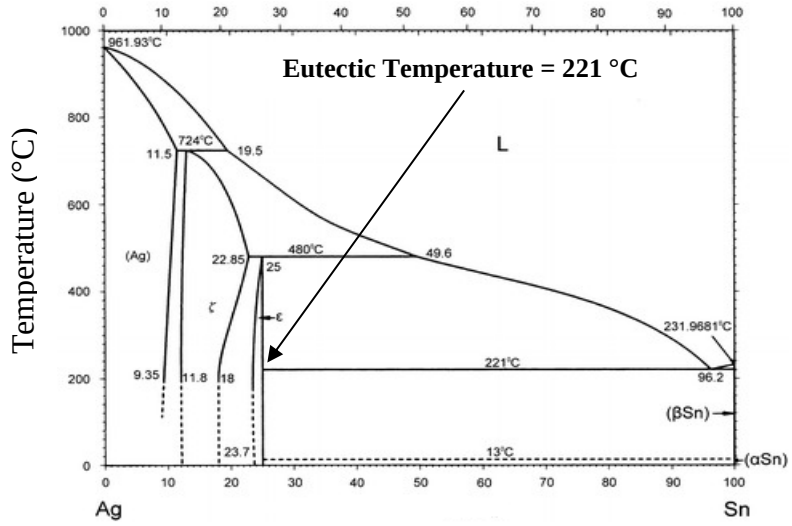

Figure 2. 4: Phase diagram of SnAg solder (Okamoto, 2010).

2.4.3 SnCu Solder Alloy

The SnCu lead free solder alloy is another alternative for the lead solder alloy. The phase diagram of the SnCu solder alloy is shown in Figure 2.5. The eutectic temperature of this solder alloy is at 227 °C with the composition of 93 wt. %Sn and 7 wt. %Cu (Huizhen, et al., 2017). Similar like the SnAg system, the increase in the temperature is due to the reactivity of Sn and Cu that will be affecting the heat needed to diffuse the atoms. In addition, the high temperature of Cu at 1085 °C contributes to the high melting temperature.

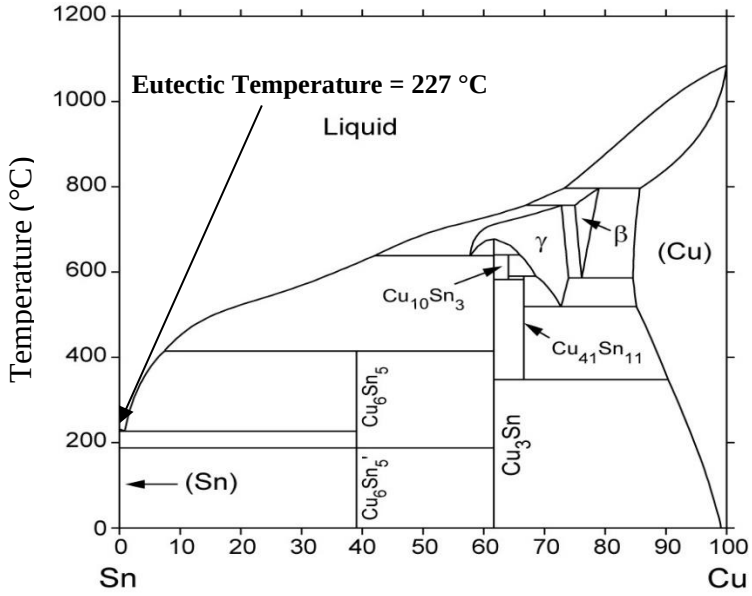

Figure 2. 5: Phase diagram of SnCu solder (Okamoto, 2010).

2.4.4 SnAgCu Solder Alloy

Sometimes, third elements maybe added to improve the property of a binary solder alloy. The SnAgCu solder alloy is one of them. The element Cu is added to the SnAg solder alloy to produce the ternary SnAgCu solder alloy. This solder alloy is among the most researched ternary solder alloy and been proposed as the suitable candidate to replace the SnPb solder alloy (J.Keller, et al., 2011). The eutectic composition of this solder varies according to few nations; Japan (96.5Sn3.0AgCu), Europe (95.5 Sn3.8AgCu) and the United States (95.5SnAg-0.6Cu) (Zhang, et al., 2012). Nevertheless, the eutectic melting temperature does not differ much as it is agreed to be 217 °C from those three compositions (Gao, et al., 2010). A typical phase diagram of the SAC solder alloys is shown in Figure 2.6. The addition of Cu as the third element contributes to providing the strengthening effect where both Ag_3Sn and Cu_6Sn_5 IMC's were visible in the study of (C.L. Chuang , et al., 2012).

Apart from the SAC ternary solder alloy, other ternary solder alloys such as the SnZnBi (Ren & N.Collins, 2019) and SnZnAg (Zhang & K.N Tu, 2014) are also studied; nonetheless, the literatures are scarce. The SAC solder alloy has its own drawbacks as shown in Table 2.2. The list of the advantages and disadvantages of other studied solder alloys are also listed in Table 2.2. The temperature exceeds 200 °C, which is having higher melting point that the lead solder.

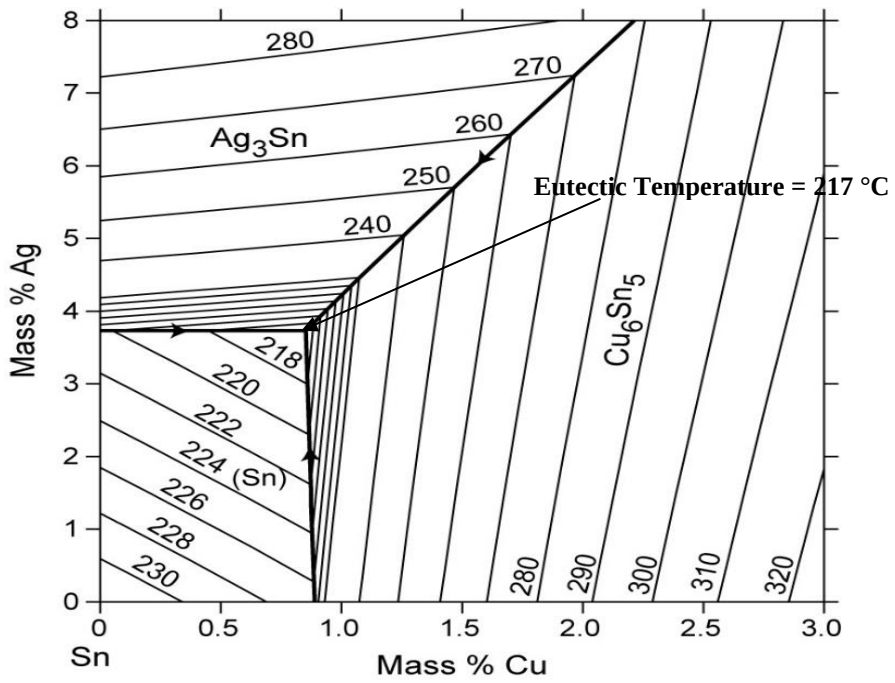

Figure 2. 6: Phase diagram of SnAgCu solder (Okamoto, 2010).

Looking at the lead and lead free solders, the present era highlights the importance in reduction and focused density improvement. As highlighted, it demands much smaller sized solder joints and delicate interconnections (J.Shen & Y.C Chan, 2009). In a simple word, it requires better solder-joint reliability with a solder with low density and mass that at the same time holds high strength. Unfortunately, many researches are conducted based on bulk solder alloy only

(Zou, et al., 2010). Agreeing to solve this issue, nanoparticles reinforcement are contested to provide better mechanical integrity to a lead free solder and these area of study is the recent problem statement (L.C. Tsao & S.Y. Chang, 2010). Nanoparticles can act as separate/discrete particles (oxide and high temperature nanoparticles) or even involve in diffusion and effect the properties by an alloying manner (metals elements) (F.Khodabakhshi, et al., 2017; Y.Tang, et al., 2017). Plenty studies have incorporated nanoparticles in to solder alloys to enhance the properties but not many has argued on the reinforcements of the nanoparticles in the low melting solder alloy.

Table 2. 2: Characteristics (aces and concerns) of common solder alloys.

Solder Alloys	Characteristics		References
	Aces	Concerns	
Sn-37Pb	- Low meting temperature (183 °C) - High shear/tensile strength - Good spreading properties - Good interfacial property	- High toxicity (Pb)	(Efzan M.N & Marini A, 2012; Liu, et al., 2009)
Sn-3.0Ag-0.5Cu	- High hardness and shear/tensile strength - Good spreading properties - Good interfacial property (at low soldering/reflow temperature and short time usage) - Availability	- High melting temperature (217 °C) - Excessive growth of Cu_6Sn_5 layer upon aging and high temperature - Grains coarsening - High CTE	(Wang, et al., 2016; Wang, et al., 2017)
Sn-3.5Ag	- High hardness and shear/tensile strength - Availability	- High melting temperature (221 °C) - Low ductility	(Guo, et al., 2019)
Sn-0.7Cu	- High hardness and shear/tensile strength - Availability	- High melting temperature (227 °C) - Excessive growth of Cu_6Sn_5 IMC layer - CTE	(Huizhen, et al., 2017; L.C. Tsao, et al., 2012)
Sn-50In	- Low melting temperature (125 °C) - High hardness - Good microstructural properties, smaller grains	- Expensive - Rare element (Indium) - Decrease in properties at high concentration of indium	(R. Kotadia, et al., 2014; Kanlayasiri & Sukpimai, 2016; Cheng, et al., 2017)
Sn-9Zn	- High performance in mechanical strength, especially in tensile strength - Availability	- High melting temperature (198 °C) - Prone to corrosion (oxidation)	(Gancarz, 2016; Ichitsubo, et al., 2005)
Sn-58Bi	- Low melting temperature (139 °C) - Large spreading area - Good spreading properties - Low CTE - Availability - Excellent microstructure and IMC properties	- Low mechanical properties	(Ma & Wu, 2015)

2.5 Nanoparticles additions in Solder Alloys

Usually, in solder alloy reinforcements, the reinforcements can take up various sizes from large particles, micro ($\times 10^6$) to nano ($\times 10^9$) sized particles. Even though the sizes differ in a minor range, the effects are quite distinguished compared to each other (Efzan, et al., 2013). Adding the nano-scale reinforcement comes in various distinguished amongst which are mechanical mixing method and chemical reduction methods (C.Y Lin, et al., 2010). In another research, (C.Y Lin, et al., 2009) the SnAgZn solder alloy was synthesized to a nano-scale by chemical reduction method producing the SnAgZn nano solder alloy. This method was likewise applied by (Wang, et al., 2017) by synthesizing the SnAgCu solder alloy. The mechanical mixing method is defined as solder alloys that are intentionally reinforced with nanoparticle by a mode of stirring. Most research focused on the mechanical mixing method because of its efficient cost and also having the same effect compared to the expensive chemical reduction method. At the same time, the latter method is hazardous during preparation (Cheng, et al., 2017). Table 2.3 summarised to provide a clear description of these methods used to add nanoparticles into a solder alloy. These nanoparticles can influence the initial properties of a solder alloy by affecting the solubility or the energy of the solder alloy taking part in the diffusion process. Contrast to that, nanoparticles can be discrete particles and influence in increasing the mechanical strength. The influences of the nanoparticles should be related with the important properties such as melting temperature (C. Morando, et al., 2012), wettability (spreading

properties) (Efzan, et al., 2010), microstructural and intermetallic (El-Daly, et al., 2013) and mechanical properties (R.Garcia, et al., 2010). These aspects are crucial to give solid proofs as a solder alloy's performances. The next sections will focus on the properties that been the concern relating to the solder alloy and the influence made by the nanoparticles on the properties.

Table 2. 3: Mechanical mixing and chemical reduction method.

Mixing Method		Condition	Description	Advantage (s)	Disadvantage (s)
Mechanical Mixing	Milling (ball milling)	Dry and wet powder	Usage of grinding process and incorporating particles to the solder alloy	- Can be used for large batches.	- Slow process - Cleanliness issue - Chances to break the nanoparticles
	Stirring (magnetic stirrer or overhead stirrer)	Liquid or solid powder	Usage of magnetic stirrer or overhead stirrer with speed to rotate and mix the particles and the molten solder alloy.	- Does not break the nanoparticles - Cheap - Fast.	- Improper additions can lead to agglomeration
	High Speed Homogenise	Liquid	Usage of rotor stator generator probe where the rotor acts as the centrifugal pump to circulate the nanoparticles and subjected to shear and collision to the solder alloy.	- Large liquid batches.	- Restricted to liquid type nanoparticles - No literature for dispersion.

Table 2. 3 continued: Mechanical mixing and chemical reduction method.

Mixing Method	Condition	Description	Advantage (s)	Disadvantage (s)
Chemical Reduction	Liquid or solid	Usage of precursors to reduce the size of the solder alloy.	- Ability to obtain the desired nanoparticles material without any impurities. - Avoids agglomeratio n(with usage of surfactants)	- Expensive. - Hazardous. - Obtaining correct formula as reducing agent. - Less literature. - Used to reduce solder alloy to nanoparticles size rather than producing a nanoparticles element.

2.6 Influences of Elements and Nanoparticles Additions on Solder Properties

2.6.1 Thermal Properties

Thermal properties mainly concern on the melting temperature, which has been always the priority given to all solder alloys to ensure that the PCB as well as other components are protected. A melting point of a material is a natural physical property, mainly determined by the inter-atomic distance and the atomic mean-square displacements (Khrapak, 2020). It is pointed out that an increase in 10 °C temperature can reduce the life span of electronic products by 50 % (Halbo & Ohlckers, 1995). The usual soldering temperature used in the electronic industries is 250 °C. The Sn is mostly used as the base material for the solder alloy. Prior to addition of nanoparticles to Sn based solder alloys, elements are added to the Sn

base solder alloy to reduce the melting point. Addition of third element can supress the melting point by diffusing together with other elements by a solid state process (Luo, et al., 2012). The mixture of elements may or may not produce different phases and IMCs on the new solder alloy and this could be determined with the aid of phase diagram. Melting point of a base solder will decrease due to the presences of the elements that possesses lower melting point than the eutectic matrix of the based solder. This followed by the drop in the crystalline size (Efzan Mhd Noor & Singh, 2014).

The melting point is an important characteristic because this temperature will be used to select the soldering temperature of a solder alloy. Nevertheless, the soldering temperature would not be changed, as it has been the common temperature (230-250 °C) used in electronic industries, thus the attention is made to the melting temperature of the solder alloys. Table 2.4 lists the common bulk solder alloy's melting temperature that serves as literature. As observed, the melting temperatures are determined by the liquidus temperature (T_L), which should occur below 225 °C (Hu, et al., 2010). Liquidus temperature is defined as the point where solder exists in molten form and is an important aspect to avoid thermal damage to the device during soldering process (Zhou, et al., 2005). The solidus temperature (T_s) meanwhile, is the maximum temperature at which a solder stays as solid. This stage is crucial to provide enhanced integrity between the solder and substrate (Lee & Chen, 2002; Kanlayasiri, et al., 2009). The difference between the T_S and T_L is termed the pasty range or known as the temperature range (T_R) (P. Lobry, et al.,

2011; El-Daly & Hammad, 2010). Pasty range is when the solder is in the form of both liquid and solid phases that subsequently happens after liquidus temperature and before the solidus temperature. This part is where the microstructure possessions takes place (R.M Shalaby, 2010). Quicker solidification and better grain refinements are produced as a results of small pasty range, while a wider pasty range has a high probability of porosity and hot tearing (Kanlayasiri, et al., 2009). At this stage of time, the pasty range allows the grain to grow larger as a reason of high heat energy being provided (T.L. Yang, et al., 2015). The additions of elements in the solder alloy shows a mixed variation of slight increase and decrease in the melting temperature (Table 2.4). As observed in the study of (Ma & Wu, 2015), adding Zn to Sn58Bi decreases the melting temperature about 3 °C and the reason behind this reduction is due to upsurge in the instability together with the increase in surface energy caused by the addition of Zn. At this time, the interfacial and surface energy of the molten solder alloy are not fully consumed, and inhibition of the energy needed by Zn presumably reduces the solidus temperature. Similar result and justification was made in the study of (Liu, et al., 2015) in adding In to the Sn3Bi8Zn solder alloy. Contradict to that study; even with using the same mother solder Sn3Bi8Zn, addition of antimony (Sb) increases the melting temperature by 1 °C (Ren & N. Collins, 2017). This was also the case in the investigation by (Huizhen, et al., 2017) with addition of sulphur (S) in the Sn0.7Cu and (Bang, et al., 2018) with additions of chromium (Cr) in Sn3.0Ag0.5Cu. The increase in the melting temperature here could be due to the increase in the melt undercooling

endured upon the addition of the elements (Tu, et al., 2017). In another explanation given by (Chen, et al., 2016), the additions of elements can have a different thermal conductivity compared to the mother solder. Thus, a lower thermal conductivity of reinforcement or element additions might reduce the total thermal conductivity of composite solder and cause the increase in its melting range.

Advanced researches on nanoparticle's influence in the melting temperature vastly explored in current solder alloy studies. Since the additions of element in a solder alloy seems to affect the melting temperature with much impact to the mother solder alloy's initial melting point, the nanoparticles should prevail somewhat different affect to avoid thermal discontinuity of the mother solder and the substrate. Table 2.5 shows variation of nanoparticles additions in the solder alloy and its influence towards the melting temperature. The additions of nanoparticles here are in the range of weight percentage of 0.05 % to 3 % and the materials used are mainly ceramic (oxide) nanoparticles. (Shen & Chan, 2009) pointed out that large particle size would lead to an elevated melting and was supported by the study of (Zhu, et al., 2018) upon addition of different sizes of CNT in Sn0.3Ag0.7Cu. In that research, even with the same 0.05 wt. % of CNT additions (10-20 nm, 40-60 nm and 60-100 nm), the melting temperature increases about ± 2 °C with the increase in diameter size and the reason is due to the dissolution of the CNT that has higher melting point. Several results were accompanied with this increase of melting temperature. To explain in further, certain nanoparticles inserted in the solder will produce conflicting fluctuating trends in the melting temperatures,

indicating that the peripheral (size) structure of nanoparticles plays an important role its melting behaviour (Gao, et al., 2010).

Large surfaced nanoparticles (small in diameter size) will normally lose their instability at a lower temperature than their bulk precursors and contributes in lowering the temperature. Yet, an opposing effect will be achieved if the surface area is small (large diameter size) (Gong, et al., 2009). Another research showed the additions TiO_2 nanoparticles in the Sn3.5Ag0.7Cu had higher melting temperature than the bare solder alloy (Chang, et al., 2011). Equally, (L. C. Tsao, et al., 2010) found that the addition of Al_2O_3 nanoparticles to the Sn3.0Ag0.5Cu increases the melting temperature about 0.5 °C. Similar results were obtained by adding ZrO_2 (Gain, et al., 2011) and TiO_2 (Chang, et al., 2011) into SnAgCu solder alloys respectively.

Table 2. 4: Melting temperature of bulk solder alloys and solder alloys added with elements.

Solder alloy	T_S (°C)	T_M (°C)	T_L(°C)	References
Sn37Pb	-	183	187	(Cheng, et al., 2017), (Efzan Mhd Noor & Singh, 2014)
Sn3.5Ag	221	223	221	(J. Sundelin, et al., 2006), (Chang, et al., 2011)
Sn0.7Cu	-	228	-	(Bang, et al., 2018)
Sn0.7Cu		230.09		(N.A. Saleh, et al., 2017)
Sn0.7Cu		227.1		(Huang, et al., 2016)
Sn0.7Cu + 0.2 S	-	227.7	-	
Sn0.7Cu + 0.1 S	-	227.6	-	
Sn0.7Cu + 0.05 S	-	226.6	-	
Sn0.7Cu + 0.02 S	-	226.8	-	
Sn0.7Cu + 0.5 Zn		230.93		(N.A. Saleh, et al., 2017)
Sn0.7Cu + 1.0 Zn	-	228.22	-	
Sn0.7Cu + 1.5 Zn	-	227.63	-	
Sn8Zn3Bi + 1.5 Sb	194.2	197.4	200.3	
Sn2Ag3Bi	182	-	204	(Jeon, et al., 2013)
Sn2Ag3Bi + 2 % In	177	-	202	
Sn2Ag3Bi + 4 % In	177	-	197	
Sn2Ag3Bi + 6 % In	171	-	192	

Table 2. 4 continued: Melting temperature of bulk solder alloys and solder alloys added with elements.

Solder alloy	T_S (°C)	(°C)	T_L(°C)	References
Sn5Sb	245	245	245	(Zeng, et al., 2012)
Sn9Zn	-	198.5	202.1	(Ren & N. Collins, 2017)
Sn58Bi	139.03	142.25	144.62	(Ma & Wu, 2015)
Sn58Bi + 0.7 Zn	136.30	140.89	142.43	
Sn3.0Ag0.5Cu	-	219	-	(Bang, et al., 2018)
Sn3Ag0.5Cu + 0.2 Cr	-	231	-	
Sn3.0Ag0.5Cu	211.93	222.76	-	(Jung, et al., 2018)
Sn3.0Ag0.5Cu	217.5	218.9	218.9	(Chellvarajoo & M.Z. Abdullah, 2016)
Sn-3.0Ag-0.5Cu	217.0	221.33	-	(Gain, et al., 2011), (Fouzder, et al., 2011)
Sn3.5Ag0.7Cu	-	219.0	.	(K. Mehrabi, et al., 2016)
Sn3.5Ag0.7Cu	214.49	219.22	226.7	(F.Khodabakhshi, et al., 2017)
Sn0.3Ag0.7Cu	216.6	-	231.2	(Kanlayasiri & Meesathien, 2018)
Sn0.3Ag0.7Cu	218.37	226.45	-	(Zhu, et al., 2018)
Sn3Bi8Zn	191.5	203.12	-	(Zhao, et al., 2017)
Sn8Zn3Bi	193.0	196.3	199.0	(Ren & N. Collins, 2017)
Sn8Zn3Bi + 0.5 Sb	193.4	197.0	199.3	
Sn8Zn3Bi + 1.0 Sb	194.0	197.5	199.8	

In another research, outcome of reinforcing strontium titanate ($SrTiO_3$) in Sn3.0Ag0.5Cu gives an increment from 217 °C to 217.7 °C (Fouzder, et al., 2011). The explanation of all these increase in melting temperature are identical stating that the nanoparticles addition produces a dissolution of the nanoparticles in the solder (Gain & Y.C. Chan, 2012). However, these slight increments did not appear to deteriorate and affect the performance of the solder as the range is minimal. Research by (Kanlayasiri & Meesathien, 2018) illustrated that there was not much increase or even decrease in the melting point of the parent solder upon addition of ZnO in the Sn0.3Ag0.7Cu solder alloy. This was noted to be agreement with the Lindemann's melting theory stating that the temperature of a sole material is an inherent asset that is influenced by the interatomic distance and the root mean vibration amplitude. This shows that the presence of nanoparticles will not alter the melting point. (Chen, et al., 2016) upon addition of titanium carbide (TiC) nanoparticles to Sn3.0Ag0.5Cu gave similar explanations.

Meanwhile, some studies prevail reduction in the melting point of the parent solder after additions of nanoparticles. There was a reduction in the melting temperature of the TiO_2 nanoparticles added Sn-0.7Cu solder alloy because of the rise in the surface instability with the greater surface free energy extracted by TiO_2 nanoparticles (L.C Tsao, 2011). This was in agreement with the study of (Gao, et al., 2010) where a reduction in melting temperature was found in the SnAgCu nanoparticles solder. Apart from additions or nanoparticles to a solder alloy, few literatures report on the reduction of the solder alloy itself to a nanoscale by

chemical reduction method. Study done by (Wang, et al., 2017) synthesized Sn3.0Ag0.5Cu solder alloy using $SnSO_4$, $AgNO_3$ and $Cu(NO_3)_2$ and surfactant to produce a nanosized Sn3.0Ag0.5Cu which reduces the melting temperature to lowest point of 211.4 °C with highest amount of surfactant of 5 g. The reduction in the melting point compared to the typical SnAgCu (217 °C) solder alloy is because of the reduction in the particle size that enables more surface area to be exposed and endure surface instability as explained earlier. Reduction of the size of bulk SnAg and SnAgCu to nanoparticles by (S. Delsante, et al., 2018) records a reduction of 7-10 °C with similar justification. Though such reduction could be possible with presence of surfactants to retard agglomeration that could produce undesirable results. Table 2.5 gathers the literature of melting properties for some nanoparticles added solder alloys of.

As a conclusion for the melting literature, the additions of nanoparticles did not alter the melting point significantly neither with increase or decrease in temperature. This characteristic is important as there is no need to adjust the soldering temperature or tweak any thermal properties to accommodate nanoparticles additions (E.H. Amalu, et al., 2011).

Table 2. 5: Melting temperature of bulk solder alloys and solder alloys added with nanoparticles.

Solder alloy (Initial T_M °C)	**Nanoparticles Additions**	**T_S °C**	**T_M °C**	**T_L °C**	**References**
Sn3.5Ag0.7 Cu (219.22)	0.05 % GNS	-	222.69	-	(F.Khodabakhshi , et al., 2017)
	0.1 % GNS	-	223.75	-	
	0.2 % GNS	214.97	226.95	236.08	
Sn9Zn	0.25 % Al_2O_3	197.5	-	201	(Ding, et al., 2018)
	0.5 % Al_2O_3	197.9	-	200.8	
	0.75 % Al_2O_3	197.1	-	200.4	
	1 % Al_2O_3	197.8	-	201.2	
Sn9Zn (198.5)	0.5 % Al_2O_3	-	198.4	201.7	(Xing, et al., 2017)
	1 % Al_2O_3	-	197.8	201.2	
Sn0.3Ag0.7 Cu (216.6)	0.25 % ZnO	216.6	-	231	(Kanlayasiri & Meesathien, 2018)
	0. 5% ZnO	216.9	-	232.2	
	0.75 % ZnO	216.8	-	231.6	
	1.0 % ZnO	216.9	-	231.9	
Sn0.3Ag0.7 Cu (218.37)	0.05 % CNT	218.40	-	226.57	(Zhu, et al., 2018)
Sn3.0Ag0.5 Cu (218.9)	0.5 % Diamond	217.2	218.3	218.3	(Chellvarajoo, et al., 2015)
	1.5 % Diamond	217.2	218.3	218.3	
	2.5 % Diamond	217.1	218.2	218.2	

Table 2. 5 continued: Melting temperature of bulk solder alloys and solder alloys added with nanoparticles.

Solder alloy (Initial T_M °C)	**Nanoparticles Additions**	**T_S (°C)**	**T_M (°C)**	**T_L(°C)**	**References**
Sn3.0Ag0.5Cu (222.76)	0.21 % TiO_2	213.09	223.90	-	(Jung, et al., 2018)
	0.03 % TiO_2 + Graphene	212.69	222.88	-	
	0.12 % TiO_2 + Graphene	217.77	223.42	-	
	0.21 % TiO_2 + Graphene	213.01	223.9	-	
	0.60 % TiO_2 + Graphene	213.22	224.60	-	
Sn-3.0Ag-0.5Cu (217)	0.5 % ZrO_2	217.08	-	221.63	(Gain, et al., 2011)
	1 % ZrO_2	217.12	-	221.65	
	3 % ZrO_2	217.25	-	221.95	
Sn-3.0Ag-0.5Cu (217)	0.5 % $SrTiO_3$	217.7	-	221.53	Fouzder et al. (2011)
Sn3.0Ag0.5Cu (218.9)	0.5 % NiO	217.8	219.0	219.0	(Chellvarajoo & M.Z. Abdullah, 2016)
	1.5 % NiO	217.9	219.3	219.3	
	2.5 % NiO	218.1	219.7	219.7	
Sn3.5Ag0.7Cu (219.0)	0.1 % Al_2O_3	-	222.5	-	(K. Mehrabi, et al., 2016)
	Ni coated with Al_2O_3	-	221.5	-	
Sn3.0Ag0.5Cu (217.54)	0.5 % Fe_2NiO_4	-	218.18	218.18	(Chellvarajoo & M.Z. Abdullah, 2018)
	1.5 % Fe_2NiO_4	-	218.3	218.3	
	2.5 % Fe_2NiO_4	-	218.37	218.37	
	0.5 % Fe_2O_3	-	217.8	217.8	
	1.5 % Fe_2O_3	-	218.3	218.3	
	2.5 % Fe_2O_3	-	218.3	218.3	
	0.5 % ITO	-	217.51	217.51	
	1.5 % ITO	-	217.52	217.52	
	2.5 % ITO	-	217.54	217.54	

2.6.2 Spreading Properties

Another important parameter to be studied is the spreading properties that is defined as the ability of a solder to melt on the substrate. The spreading properties of a solder alloy is influenced by surface tension (S. M. L. Nai, et al., 2006), wetting time (Chang , et al., 2003), contact angle (H. Lee, et al., 2013) and spreading area (Yeo & Han, 2009). These parameters are important to evaluate the efficiency of a solder joint forming between the solder alloy and substrate (Satyanarayan & K.N Prabhu, 2011). The intermolecular contact of the elements in the solder and the substrate (Cu) during the soldering process creates a spreading area and a contact angle between the solder and substrate (Murad, et al., 2017). Spreading area and contact angles are influence by the surface tension of the molten solder alloy. Consequent to that, the production of IMC layer relies on the reaction of solder and substrate, which will be discussed in Section 2.6.4. A lower surface tension and viscosity of the molten solder are the preferred (S.L. Tay, et al., 2013). The surface tension of a liquid is defined as the amount of energy required to isothermally expand the liquid surface area (Callister & Rethwisch, 2011). According to (Efzan, et al., 2010) and (S. M. L. Nai, et al., 2006), the Young's equation is used to determine the surface tension of an interconnection.

The contact angles on the other hand could be directly measured with an incorporated measurement software in microscopes or by applying the sessile drop or dipping method (Daniel , et al., 2010). A smaller contact angle with larger spreading area is worthwhile to produce a good joint as these features are seen to produce thin IMC layer (Kanlayasiri, et al., 2009). Contact angle is the tangent line drawn at the triple point between the three phases (solid, liquid and vapor) and the substrate surface (Figure 2.7). There is no baseline for an ideal contact angle to be achieved, but according to (Ervina & S.Y, 2013), contact angles lower than 50 ° are described to provide better joint.

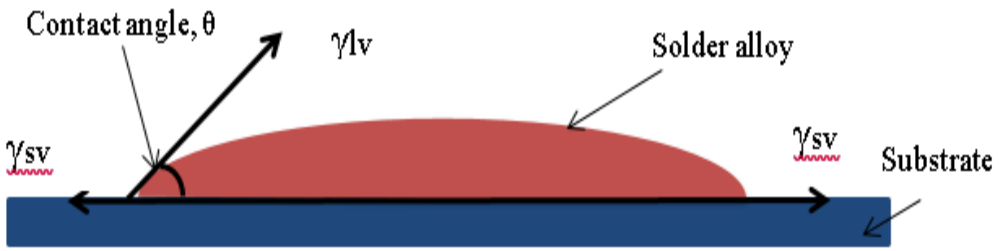

Figure 2. 7: Contact angle schematic diagram.

During the soldering process, wetting force builds up between the solder and substrate and with an increase in this force, the surface tension of the joint decreases and enables the solder to spread widely and with a low contact angle (S.L. Tay, et al., 2013). Research done by (Satyanarayan & K.N Prabhu, 2011) justified that the temperature for the soldering process is within (250 °C-300 °C) because the solder alloys usually displays low surface tension which this temperature range would be adequate and there is no need for increase in the soldering temperature.

Not many researches are available in obtaining the contact angle of solder alloys, but some results were managed to be gathered and shown in Figure 2.8 to illustrate the trend of the contact angle of some common solder alloys (Abtew & Selvaduray, 2000; Fouzder, et al., 2011; T. Laurila, et al., 2011; Efzan, et al., 2013; L.C Tsao, 2011; J. Sundelin, et al., 2006).

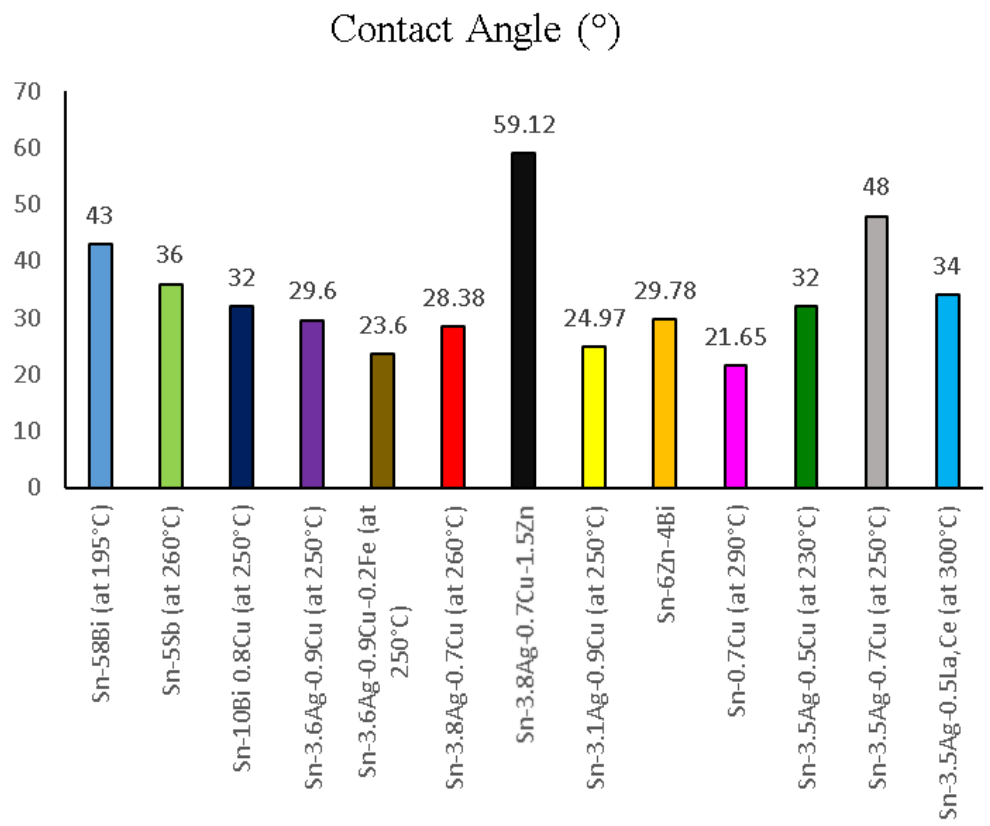

Figure 2. 8: Contact angles of solder alloy and solder alloy added with elements.

Reduction in the surface tension can be achieved by addition of elements to the solder alloy, for example additions of Bi decreased the surface tension of the SnZn solder alloy and lowers the contact angle (R. Kotadia, et al., 2014). (Bo-In

Noh, et al., 2011) added rare earth element of Ce up to 0.3 % in the Sn1.0Ag solder alloy and found a decrease in the surface tension consequent to an increase in the wetting force. The contact angle was reduced and the spreading area was increased by adding 0.1-0.5 % Ni to the Sn2.5Ag0.7Cu, as the Ni accumulates at the solder and flux region which reduces the surface tension of the solder (Wang, et al., 2017). Adding to that, the soldering temperature was maintained at 300 °C and observing the Ni-Cu phase diagram; there would be no diffusion of Ni and Cu that could increase the surface tension at that particular temperature. The soldering temperature also emphasizes to another aspect in the spreading properties by constraining the energy for the formation of additional IMC layer (e.g Cu_3Sn) that would increase the contact angle. However, excessive additions of element can degrade the spreading properties by the means of oxidation due to temperature exposure as pointed out by (Ren & N. Collins, 2017). The increase of Zn content in the SnZn solder causes oxidation in the that study. Thus, it is practical to keep the temperature as below 300 °C to allow good spreading of molten solder on substrate. Adding 1 wt. % Bi to the Sn3.0Ag0.5Cu improves the contact angle of the solder alloy. The research conducted by (Erer, et al., 2018) by varying the soldering temperature of 250 °C, 280 °C and 310 °C, with the highest temperature contributing to lower contact angle of 35.6 °. The research concluded that the thin IMC layer is the reason of the low contact angle. Viscosity of a solder alloy was reduced to allow high or larger spreading area of the solder on the substrate. The viscosity parameter is related to the fluidity of a solder alloy and the fluidity is

influenced by the melting temperature (Huizhen, et al., 2017). This statement was proved by the study done by (Liu, et al., 2015) that records a better spreading area (34 % larger) and contact angle of the SnZnBi added with 1 wt.% In. The obtained solidus temperature is lower with the In addition and the solder experiences increase of fluidity at the same soldering temperature. This phenomenon accelerates the spreading of the solder on the substrate and improve the spreading properties. Figure 2.9 obtained from the research show clear difference of the contact angle and the spreading area with In additions. The surface tension of the molten SnCu solder alloy reduces with the additions of S that consequently lowers the contact angle and increases the wetting force. This was reported in the research of (Huizhen, et al., 2017). Another contribution of S to the spreading properties is to avoid oxidation caused by the SnO. It allows better spreading of the solder alloy, but with high amount of S, there was no beneficial effect in the spreading properties as the production SnS and $SnSO_4$ could be immense and avoid proper flow of during the molten stage. This clarification was agreeable in the research of (H. Lee, et al., 2013) explaining the high content of Zn in the CuZn system promotes oxide layer that inhibit proper flow of the molten solder. However, in the research, the high melting temperature parameter looked to provide higher wetting force to enhance the spreading properties.

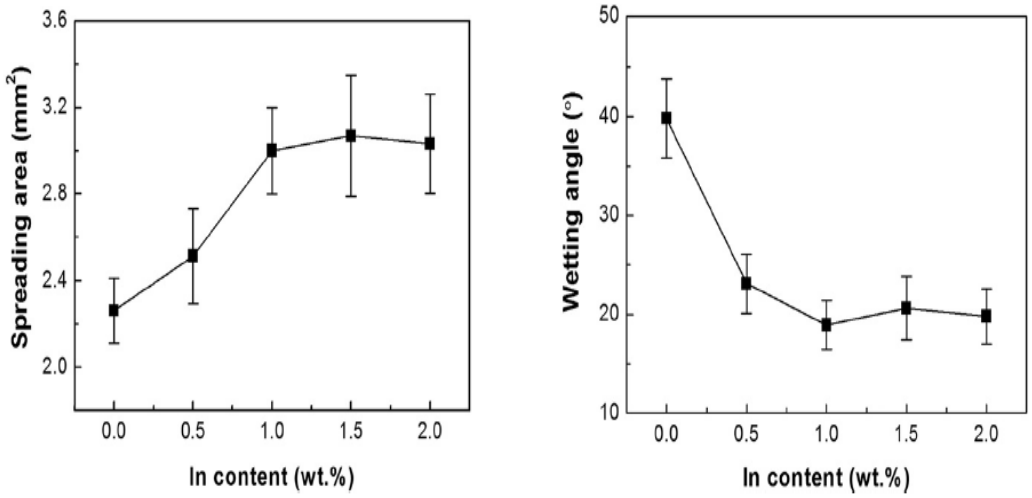

Figure 2. 9: Spreading area and contact angle result with In additions in SnZnBi solder (Liu, et al., 2015).

Recognizably the contact angles are affected with presence of new elements in solder alloys, and presently, additions of nanoparticles are made to influence the spreading properties of solder alloy. As discussed earlier in section 2.6.1, most nanoparticles do not take part in any diffusion process and such behaviour distinctively influences the spreading properties. With the gathered literature of the nanoparticles additions, there are several influence made by the nanoparticles to the parent solder alloy. The nanoparticles that been added to the solder alloy can be entrapped to the solder alloy either by reacting or not reacting with the solder alloy (Bo-In Noh, et al., 2011). If the nanoparticles is a ceramic material, it is obvious that the nanoparticles would not react with the solder alloy and appears as a discrete particle, and in contrast, some metal nanoparticles will diffuse with the elements in the solder alloy and produce IMCs (S.L. Tay, et al., 2013). Nonetheless, the former condition is usually observed.

In some circumstances, too much presence of nanoparticles irrelevant of metal or ceramic, the nanoparticles would be pushed away by the molten solder alloy during soldering. This statement was proved by an earlier research done by (An & Wu, 2007) with additions of 1-5 wt.% Ag and Cu particles to the Sn3.0Ag0.5Cu solder alloy. The findings showed these particles were leached out to the flux residues, indicating the particles were pushed out by the molten solder alloy. This occasion is dependent on the amount of nanoparticles added to the solder alloy and its influence to the surface tension and viscosity of the solder alloy. Conclusive result was provided by (Jung, et al., 2018) with the TiO_2 and graphene nanoparticles additions. In that study, the 0.21 % of additions increases the wetting force to 6.90 mN and the wetting force dropped to 5.99 mN with 0.60 % additions. Moreover, the surface tension of the former percentage was 19 % less than compared to the later and afterwards contributes to a better spreading and lower contact angle. Relating to the statement, additions of ZnO nanoparticles to the Sn3.0Ag0.7Cu solder revealed similar reduction in the surface tension and lead to lower contact angle (Kanlayasiri & Meesathien, 2018). The liquid-solid and liquid-vapor surface tensions decreased with 0.25 wt.% ZnO nanoparticles additions but then the viscosity increased with further additions up to 1.0 wt.% ZnO which increased the contact angle again. The justification behind this is that the optimal amount of nanoparticles will reduce the surface energy and increase the wetting force of the molten solder alloy by the cause of the nanoparticles being the surface-active elements. This observation was supported by (L. C. Tsao, et al., 2010) with

additions of Al_2O_3 nanoparticles. Crosswise, an increase in the surface energy and a decrease in the wetting force because of the weak Van der Waals force between the vast amount of nanoparticles and agglomeration between them that causes de-wetting of the solder and substrate. Research by (Y. Tang, et al., 2014) agreed to this inference. In sync with this, vast amount of nanoparticles will not have a well dispersion and held the leading edge of the molten solder to spread and increase the contact angle that leads to an improper wetting (Rui, et al., 2012). In another research by (Gu, et al., 2015), the wetting force showed a higher force of 3.35 mN for the 0.4 wt.% Fe_2O_3 nanoparticles and then decreases to 3.17 mN for 1 wt.% additions. These results further approved with the study of the surface tension of the molten Sn1.0Ag0.7Cu with 0.4 % and 1.0 % additions and those results in the less percentage resulting in a less surface tension. It is known that even the size of the nanoparticles will influence the wetting force of the molten solder as found out by (Zhao, et al., 2016) when the 20 nm Fe_2O_3 nanoparticles had higher wetting force than the 50 nm and 100 nm size. Independently, the TiO_2 nanoparticles was believed to be the agent to reduce surface tension on the molten Sn0.7Cu0.05Ni that help decrease the contact angle and improve the wetting character (Ramli, et al., 2016). Nanoparticles with less weight percentage had more even distribution in the molten solder alloy and these follows to a reason of the exposure of higher surface area and higher surface energy displayed by the nanoparticles (Koscielski, et al., 2010). As known, at the interface between the solder and substrate, the bonding force is higher. This condition is a plus point for the nanoparticles with

higher surface energy to slot itself at this interface and locate itself at the substrate (solid). Intermixing Al_2O_3 nanoparticles in Sn3.5Ag0.5Cu found to be beneficial as the contact angle of the solder joint is reduced due to the additions (L. C. Tsao, et al., 2010). In the same study, too much additions of Al_2O_3 (>0.5 wt. %) nanoparticles increase the contact angle and deteriorate the spreading properties. The reason for the increase in contact angle is as the additions are made, the nanoparticles tends to pin at the leading edge of the molten solder alloy that increases the viscosity and causing harder spreading of the liquid solder. Vice versa, conferring to (L Wang, et al., 2002), small weight percentage of nanoparticles additions helps the solder alloys to lose its surface instability easier and reduces the contact angle. In analysing the spreading properties of graphene reinforced Sn2.5Ag0.7Cu solder, the property was enhanced (Wang, et al., 2019). Upon soldering, the GNS's tend to float on the melted solder/flux interface and drift away with flux. This happens due to the density difference between Cu and GNSs and melted solder (An & Wu, 2007). However, interfacial of GNSs endure disequilibrium in the solid–liquid interface resulting in the reduced surface tension, and the melted solder further spreads. Presence of the nanoparticles then lowers the total surface tension of the molten solder alloy and deduced to a lower contact angle. Research by (Salleh, et al., 2017) mentions that the production of thin IMC layer happens due to the lower contact angles. A comprehensive discussion of the IMC layers will be discussed in section 2.6.4. Gathered information and results of

the spreading properties of the nanoparticles added solder alloys are shown in Table 2.6.

Table 2. 6: spreading properties of solder alloys with element and nanoparticles additions.

Solder Alloy	Element Additions	Nanoparticles additions	Contact angle (°)	Spreading Area (mm^2)	Wetting Force (mN)	References
Sn0.7Cu			24.5			(Fathian, et al., 2017)
		0.5 % SiO_2	24.00			
		1 % SiO_2	23.00			
		1.5 % SiO_2	17.50			
		2 % SiO_2	16.00			
Sn0.3Ag0.5Cu	1 % Bi		34.70	1.955		(Chen, et al., 2016)
		0.05 % TiC	32.10	2.005		
		0.10 % TiC	30.30	2.168		
		0.20 % TiC	33.80	1.995		
			54.97			(Erer, et al., 2018)
Sn.3.5Ag 0.7Cu			37.31			(F.Khodabakhshi, et al., 2017)
		0.05 % GNS	36.14			
		0.1 % GNS	34.90			
		0.2 % GNS	32.19			
		0.2 % Ni-GNS	33.43			
Sn0.3Ag0.7Cu			22.10			(Kanlayasiri & Meesathien, 2018)
		0.25 % ZnO	9.90			
		0.5 0% ZnO	11.80			
		0.75 % ZnO	14.60			
		1.0 % ZnO	17.00			
Sn9Zn		1.5 % Al_2O_3		58		(Lu, et al., 2018)
		0.5 % Al_2O_3	53.00			(Xing, et al., 2017)
		1 % Al_2O_3	76.00			

Table 2. 6 continued: Spreading properties of solder alloys with element and nanoparticles additions.

Solder Alloy	Element Additions	Nanoparticles additions	Contact angle (°)	Spreading Area (mm^2)	Wetting Force (mN)	References
Sn			59			(Shang, et al., 2019)
		0.2 % Cu	57			
		0.5 % Cu	48			
		1 % Cu	32			
		2 % Cu	27			
Sn5Sb			32.8			(T.T.Dele-Afolabi, et al., 2015)
		0.01 % CNT	30.7			
		0.05 % CNT	28.4			
		0.1 % CNT	29.2			
Sn3.5Ag					0.59	(Md Hasnine , 2018)
	1.0 % In and 1.4 % Sb				0.581	
	1.5 % In and 2.1 % Sb				0.588	
	1.5 % In and 1.0 % Sb				0.609	
Sn0.7Cu0.05Ni			23.61			(N.A. Saleh, et al., 2017)
	0.5 % Zn		17.32			
	1.0 % Zn		26.78			
	1.5 % Zn		28.48			
	0.024 % Eu				2.70	(Zhang & K.N Tu, 2014)
	0.039 % Eu				3.00	
	0.061 % Eu				2.80	
	0.105 % Eu				2.85	
Sn58Bi			12.2			(Liu , et al., 2016)

2.6.3 Microstructural Properties

Solder alloys as explain earlier is a mixture of typically two or sometimes three elements at higher temperature. This mixture generates a certain morphology of the solder alloy due to different temperatures and rate of undercooling during solidification (Gao, et al., 2010). Based on these parameters, the microstructure of a solder alloy forms and it is crucial to provide better mechanical strength of the solder alloy. The nucleation process of a microstructure is not yet clear in this field of study but based on many literatures, melting point of the primary phase and interfacial energy measurements are the factors contributing to the formation and initiation of a microstructure in a solder alloy (Hu, et al., 2013). The SnAgCu solder alloy system is used as a reference to actually explain a microstructure formation in a solder alloy. Primary Sn grains, eutectic and IMC particles are the main component of microstructure in the SnAgCu. (J.Keller, et al., 2011). Nucleation of Sn takes place after the enough driving force gathered. Kinetic energy of the Sn atom increased after the hike in the temperature initial temperature. This followed by the development of Sn dendrites in the remaining molten solder (Gong, et al., 2009). The common undercooling temperature of the SnAgCu solder alloy is between 15-30 °C prior to the solidification of the Sn phase (R. Kotadia, et al., 2014). Since the Sn acts as the base material with massive composition (> 90 wt.%), the Sn becomes the domain phases. Availability of the Ag and Cu influences dendrite structure developments (R.M Shalaby, 2010). Two phases of Sn formation happen at this point, firstly the Sn dendrites develops prior to Sn matrix and this happens in the eutectic phase. Secondly, a

large dendritic structure is developed in the Sn matrix. The diffusion rate of the Ag is high in the liquid state that it can make way for the formation of Sn crystals. In fact, this formation is not affected by the depletion of the adjacent Sn atoms in a eutectic composition (C. Morando, et al., 2012). Moreover, (F.X. Che, et al., 2010) found that with higher amount of Ag, the Sn dendrite grows in finer manner. Here, the size of Sn grains is primarily controlled by the formation activities of the Sn dendrites. This produces different phases at different temperature and can be determined using the phase diagram of solder alloys. This also depicts that the presence of phases in the microstructure are dependent on the temperature. A typical microstructure of the SnAgCu solder alloy it consists of eutectic regions and the β-Sn grains as comparable by two different studies (C.M.T. Law, et al., 2006) and (J. Sundelin, et al., 2006). The eutectic regions consist of the Cu_6Sn_5 and Ag_3Sn intermetallic compound as visible in Figure 2.10 and these IMC's are important source for enhancing the mechanical strength of the solder which discussed in section 2.6.5 (F.Khodabakhshi, et al., 2017). The formation of the IMC compounds are due to the high reactivity of the Cu towards Sn and the Ag towards Sn in the solder alloy. The solubility of Cu in Sn is high compared to the solubility of Ag in Sn, and this is the reason of presence of high numbers of Cu_6Sn_5 IMC in the solder matrix (pebble shaped) in the SnAgCu solder alloy compared to the Ag_3Sn (Back, et al., 2017). This finding was similarly confirmed in the research of (Lin, et al., 2016) as where it was clearly states the Cu_6Sn_5 as there was very less of Ag atoms diffusing in to the Sn atoms (less than 0.5 %). In the same study, the Ag flux was even neglected for the calculation of the activation energy for the other IMC. Yet, the presence of the Ag_3Sn must be clarified

further to understand the microstructure of the SnAgCu solder alloy. The microstructure formation starts with primary β-Sn forming around 210 °C, Cu_6Sn_5 binary eutectic structure forming around 220 °C, and finally eutectic Ag_3Sn nucleating around 216 °C. This again clarifies the vast diffusivity of Cu towards Sn. As explained, the Cu_6Sn_5 forms after β-Sn and at this instant the Ag is rejected. The formation is proceeded during the growth of Cu_6Sn_5 binary eutectic structure because of the poor or no solubility of Ag in β-Sn and Cu_6Sn_5 (Lin, et al., 2016). Observing the interface, the liquid fraction at the commencement of ternary solidification was small, making the mixing in the liquid phase to deprive. So, the rejected Ag was likely to accumulate at the interface of Cu_6Sn_5 binary eutectic phase. As the temperature decreased to the ternary eutectic point, the eutectic Ag_3Sn nucleated upon solidification at the nearby Ag concentrated zone. Then, the Ag_3Sn binary eutectic structure formed in this zone as there were less Cu. The formation of the Ag_3Sn as discussed above was the exact research statement found in the work of (Takamatsu, et al., 2012). The study derived the flow of phases present was as from liquid → primary β-Sn → Cu_6Sn_5 eutectic → ternary eutectic reaction, which was same as shown by (Gong, et al., 2009). The SnAgCu solder alloy is represented in this discussion of the microstructure formation as this solder alloy is the most commonly studied and lack of in-depth study of other solder alloys for the microstructure formation. A typical microstructure of the SnAgCu solder alloy is shown in Figure 2.10. However, the formation of the microstructure could be identified with the aid of phase diagram upon checking the phases at the temperature ranges, especially using the lever rule. With the in-depth explanation of the SnAgCu system earlier, this literature would provide an

executive information for understanding the other solder alloy's microstructure evolution.

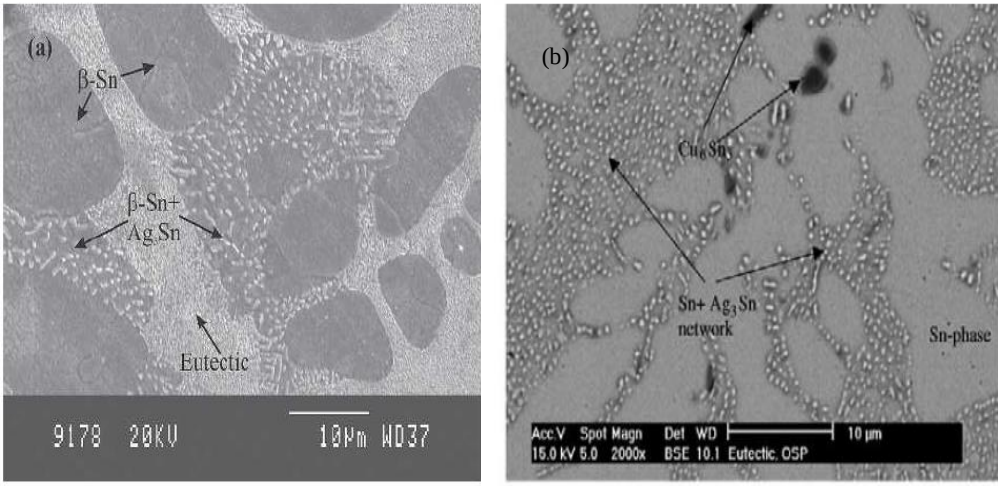

Figure 2. 10: a) Sn-3.5Ag-0.7Cu (C.M.T. Law, et al., 2006) and b) Sn-3.0Ag-0.5Cu (J. Sundelin, et al., 2006).

Since this research involves the application of the SnBi solder alloy, it is a necessity to discuss the microstructure effect of this solder system. This particular solder alloy have a very distinctive lamellar type microstructure with two main phases upon solidification, the β-Sn phase (dark phase) and the Bi precipitation (light phase) (S.Amares, et al., 2014). It was found out that the SnBi solder alloy is a mixture of fine crystals structure of Bi-rich solid solution and contains a little amount of Sn and Sn-rich solid solution with primary crystals as in Figure 2.11. Since the solubility of the Bi in Sn is very low (21 %) according to (Chriastelova & Ozvold, 2008), the Bi presents as discrete solid precipitation out from the supersaturated Sn phase (Y. Miyazawa & T.Ariga, 1999; Shen, et al., 2017). The solid solubility of the Bi in the Sn-rich solid solution decreases greatly until the equilibrium composition of Sn-rich solid solution is reached as the temperature decreases. This makes the SnBi solder

alloy to exist in a metastable condition consisting of the supersaturated Sn-rich solid solution crystals in a eutectic matrix (Miao & Duh, 2001). Likewise, the Sn52Bi alloy showed that the solder had two eutectic characteristic; a finer eutectic appeared as sequestered 'island' between the eutectic mixture and the Sn-rich dendrites and another type as the commonly observed fishbone (lamellar) eutectic morphology located nearby to the Bi-rich lamellar phases (Silva, et al., 2014).

a) b)

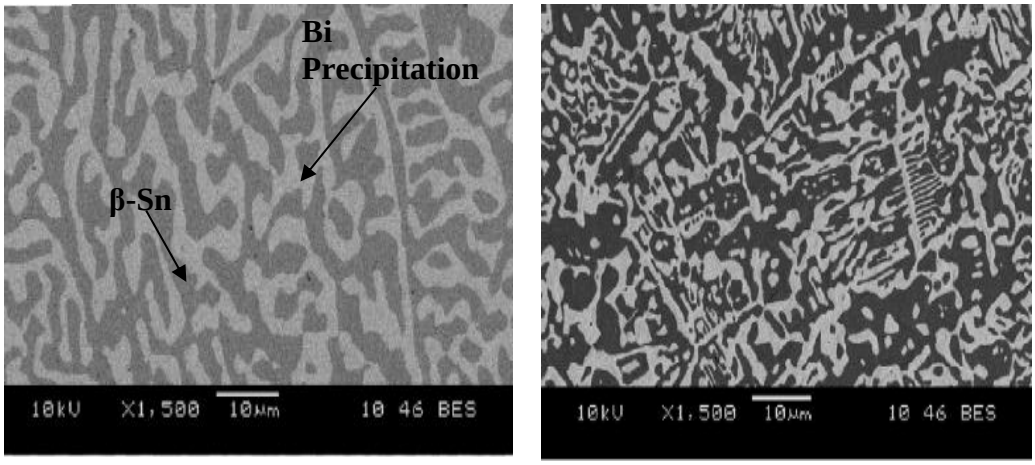

Figure 2. 11: a) and b) Sn-58Bi (Shen, et al., 2017).

The microstructure of the SnBi and even other solder alloys do change as some additional element are added to the base solder, usually to enhance the reliability of the solder alloy. Some influence of element additions on the SnBi will be discussed to provide even better literature on the microstructural aspect of the SnBi solder alloy. One of the study conducted by the additions of Sb provides a slight change in the proportion of quasi-peritectic structure as the area increases with more Bi phases than the Sn matrix due to the presence of Sb that stops nucleation of Sn (Zhang, et al., 2014). Meanwhile, the additions of 1, 3 and 5 % In in the of 42SnBi shows an opposing trend with decrease of the Bi

phases and increase in the Sn matrix (Chen, et al., 2015) due to the formation of BiIn IMC in the solder alloy. As known, the Bi have low solubility in Sn, thus promotes the Bi to react with In to produce these IMCs that are seen as isolated particles distributed in the Sn matrix. The BiIn IMC particles formed by reacting with the Bi phase, while the balance In are segregated in the Sn matrix. The Zn element were also added in the SnBi solder alloys in few studies (Q.S. Zhu, et al., 2005; Ma & Wu, 2015) and the observation of the microstructure evidently changed with the Bi area reduced upon addition of Zn from 1336 to 480 μm^2. The happens because at the stage of the grain growth, difference in the decrease of volume free energy is much slower than the increase of surface energy that inhibits larger grain growth. Among other common elements added to the SnBi solder alloy is the Cu which seems to alter the microstructure properties of the parent solder. As notified in the study by (L. Silva, et al., 2017), the additions of Cu and Ag introduces a new phase in the microstructure by the means of IMC's such as Cu_6Sn_5 and Ag_3Sn. These IMC productions occur because of the high reactivity of Sn towards Cu and Ag compared to Bi. Figure 2.12 shows the solidification of the Cu_6Sn_5 and Ag_3Sn according to temperature and noticed here, the solidification happens within the 216-222 °C. It is noted that the distribution of the Bi particles was not proper as the precipitation area increases. In one of the study conducted by (Ma & Wu, 2015), it was clarified that the addition of Zn in the SnBi solder alloy modifies the microstructure by suppressing the growth and coarsening of Bi in accordance to the surface energy theory.

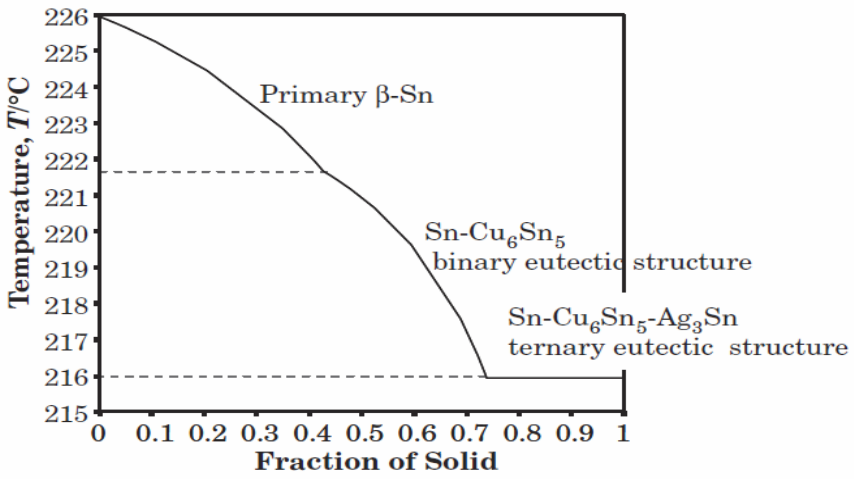

Figure 2. 12: Solidification of the Cu_6Sn_5 and Ag_3Sn according to temperature (Takamatsu, et al., 2012).

Elements additions to the SnBi certainly provides a drastic influence of the microstructure of a solder alloy. In a research by (K.Kannachai & Kongchayasukawat, 2018), the research used the base solder of SnCuNiGe, which was added with different elements of 0.1Ag. 0.1Bi, 0.1In and 0.1Sb. The base solder's β-Sn dendrite area (78.9 μm) was compared with the new area upon additions of the elements. Table 2.7 shows the change of the β-Sn area based on the additions.

Table 2. 7: Influence of element additions in the β-Sn area.

	Element Added	**β-Sn Area (μm)**
Sn-0.6Cu-0.05Ni-Ge (78.9 μm)	0.05Ag	118.34
	0.1Ag	124.2
	0.05Bi	44.9
	0.1Bi	59.0
	0.05In	77.7
	0.1In	56.1
	0.05Sb	67.1
	0.1Sb	62.3

The addition of Ag causes an increase in the β-Sn area and this was pointed out to be due to the solidification at 9 °C later compared to the base solder alloy, and this allows a larger growth of the dendrite. Rapid solidification inhibits rapid growth of the grains but at larger temperatures and longer time, the growth kinetics increases and produces larger dendrite (Murad, et al., 2017). However, opposing to that, the additions of the Bi, In and Sb show a reverse trend of decrease in the dendrite area due to fast cooling of the additions of the elements, also agreed by (K.N. Prabhu, et al., 2012). Together with this, it was clear that these elements do not take part in any diffusion process with SnCuNiGe due to low percentage of additions (0.05 and 0.1 %) and of the nature of element itself of having low solubility in the Sn matrix and acts as heterogeneous nucleation site, which reduces the grain size. The Sb (0.5, 1.0 and 1.5 %) elements was added in the SnZnBi solder alloy in another study and the microstructures (Figure 2.13) was noted to have a larger eutectic area, longer Zn needle shape with smaller size of β-Sn and α-Zn as a result of enhanced solidification because of the narrower pasty range (Ren & N. Collins, 2017).

Some rare earth elements were also added to improve the microstructure of the solder alloys and among the element was the Ytterbium (Yb) element additions of 0.05 wt. % and 0.1 wt. % to the SnAgCu solder alloy by (Zhang & K.N Tu, 2014). In the study, the microstructures were refined by reduction in the Sn area with increase in the eutectic area and with the presence of $YbSn_3$ IMC in the microstructure. All these beneficial attributions are again caused by the high surface energy consumed upon absorption of the Yb during solidification.

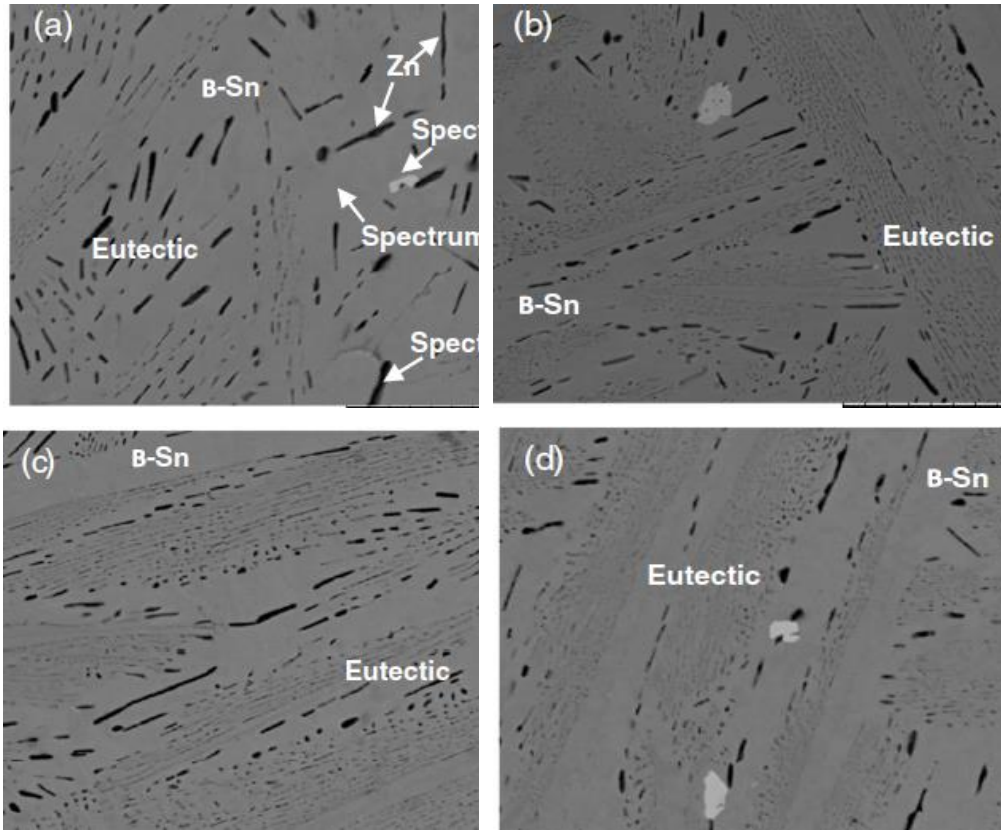

Figure 2. 13: Microstructure of a) Sn8Zn-3Bi, b) Sn8Zn-3Bi + %0.5Sb, c) Sn8Zn-3Bi + %1.0 Sb and d) Sn8Zn-3Bi + 1.5% Sb (Ren & N. Collins, 2017).

(Efzan Mhd Noor & Singh, 2014) also similarly stated the surface energy implication in a review study. (C.L. Chuang , et al., 2012) added the Ti elements in the Sn3.5Ag0.5Cu to study the microstructure of the base solder and noticed that the grain size of the β-Sn reduces about 80% compared to the base solder area. The reduction was explained according to the heterogeneous nucleation theory based on the model proposed by Volmer and Weber in the of (Bai & Li, 2006). Together, IMC of Ti_2Sn_3 was found in the microstructure in accordance to the Ti-Sn-Cu phase diagram and it is clarified that the Gibbs energy for TiSn IMC was lower compared to other IMC (e.g. AgSn, CuSn) funding the formation of the Ti_2Sn_3 IMC.

It was quite evident that the additions of the elements change the microstructure of SnAgCu solder alloy especially the β-Sn grain size and this was not different in additions of rare earth element of Ce and Zn in the SnAgCu where the dendrite structures of β-Sn changes to granular type which results in smaller grain size (Lin & Chuang, 2010). The Ce elements in another study by (Xiao-yan, et al., 2007) replenished a uniform the microstructure of the SnAgCu by providing non-homogeneous site of nucleation, and then changes the growth velocities of crystal along with various crystalline directions. (Koo, et al., 2014) clarified similar explanation in the microstructure refinement of Sn0.7Cu with the additions of Pd, Cr and Ca. A different element of 0.3-0.5 % Cr was incorporated into the SnZnBi solder alloy that shows an improved microstructure because of reduced pasty range. So, the solidification rate escalates (Luo, et al., 2009). This was concurrent to the statement by (Mayappan, et al., 2007). It was also predicted that the primary Zn phase, Sn-Zn eutectic phase and Sn phase in the SnZnBi solder alloy might be a heterogeneous nucleation at the IMC surface, thus increasing the nucleation rate. Recently, Ce additions into Sn1.0Ag also provided improvement in the microstructure and was attributed to the dispersion of Ce at the grain boundary. Consequently, this decreases the boundary movement, providing a homogeneous distribution, a finer α-Sn grains with more density and refinement of the precipitates at the grain boundaries (B.X.Vuong, et al., 2018).

The SnBi solder alloys also been subjected with elements additions that alter the microstructure properties of the base solder alloy. Little amount literature been made for this particular solder alloy but those available literatures

will be discussed to provide the in-depth observation of the effect of elements in the SnBi solder system. (Q.S. Zhu, et al., 2005) added the Zn to SnBi solder alloy and the microstructure of the parent solder was noticed to be refined as the microstructure with more oriented lamellar structure with reduced mean intercept length of Bi-rich phase in SnBiZn alloy. On the other hand, incorporation of In to the Sn58Bi showed the intensity of Bi decreases as the In content increase as a result of formation of isolated BiIn IMC. This IMC that connects with the Bi strengthens the microstructure (Chen, et al., 2015). Using the same composition of Sn58Bi, Ni was added to the base solder alloy and the study prevails that comparing with the SnBi solder, the cell volume, and crystal size of Ce added solders for β-Sn, β-SnBi, and Bi phases decrease with the increasing Ni content. Adding to that, the Bi and β-Sn phase remains rhombohedral and body centered tetragonal even though the Ni reacts with Sn, which suggests that the cells are either expanded or contracted uniformly, where the diffraction lines merely shift their positions. At the same time, the Ni_3Sn_4 IMC were formed with increasing size and with this, the bond between adjacent phases become stronger and contributing to enhancement of equilibrium stability of phases and refinement of crystal structures. (Yang, et al., 2015) reported all these statement in their research.

The additions of nanoparticles to the solder alloys also produces distinctive observation in the microstructure too. The additions of the nanoparticles have more profound effect in the microstructure, which also increases the mechanical properties. Additions of nanoparticles in the solder alloy can influence the molten solder alloy by three main types of reaction as

drawn in shown in Figure 2.14. Additions of Al_2O_3 nanoparticles into Sn3.5Ag0.5Cu refines the dendrite Sn grains, the Ag_3Sn grains and reduces the average spacing of Ag_3Sn phase (D.C. Lin, et al., 2003; L. C. Tsao, et al., 2010). It was also reported that the eutectic part was further enlarged to a network area after the addition of Al_2O_3 nanoparticles. An increase in the adsorption of the Al_2O_3 nanoparticles, which acts as the surface-active element at the Ag_3Sn grain borders decreases its surface energy and therefore decreases the growth rate of this phase. This process is termed as the Gibbs adsorption theory that was in correlation to the study of (Wu, et al., 2016).

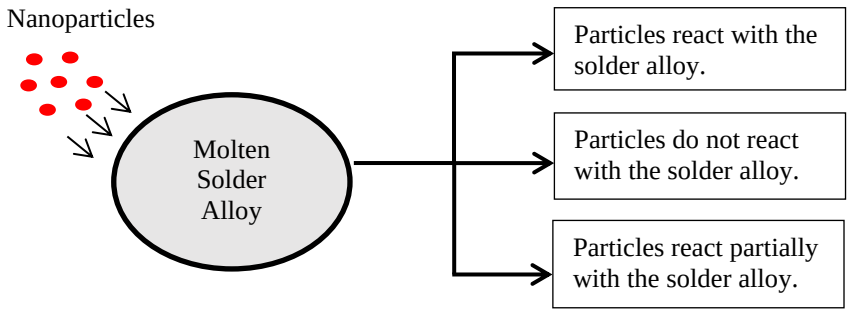

Figure 2. 14: Influence of nanoparticles in the molten solder alloy.

In another research, TiO_2 was added into Sn0.7Cu solder and notes that the TiO_2 nanoparticles reinforced solder alloy had a refined microstructure than the non-added solder alloy (L.C. Tsao, et al., 2012) The Sn-rich phases became smaller, and more Cu_6Sn_5 IMC particles were isolated in the microstructure in the nanoparticles reinforced solder. The addition of TiO_2 nanoparticles show the eutectic area Sn3.5Ag and Sn3.5Ag0.5Cu had an obvious increment in the eutectic area. This observation was compatible to the study of (Ahmed, et al., 2010) as the Ag micro particles were added to the Sn9Zn solder alloy. Besides

that, (Chang, et al., 2011) remarked similar opinion. The combination of the improved nano-sized second phases and IMC's will enhance the mechanical properties of the solder alloy. Recent study by (Ma, et al., 2017) added GNS of 0.03, 0.05 and 0.1 wt.% to the SnBi solder alloy where the crystal size, cell volume of Bi and β-Sn was reduced due to the cell volume contraction. The grain size reduced from 1.63 µm to 0.75 µm with the presence of 0.03 wt.% GNS. The effect of refinement was not that evident for 0.1 wt.% of GNS. The Sn3.0Ag0.7Cu was incorporated with CeO_2 nanoparticles and the grain size was reduced with presence of 0.5 wt. % CeO_2 nanoparticles. It was explained that the refining effect was attributed to the heterogeneous nucleation theory. The CeO_2 acts as the nucleation site for the Sn and eutectic phases that will induce higher nucleation rate and hence reduces the grain size as shown in Figure 2.15 (a) and (b). Nevertheless, with higher content as seen in Figure 2.15 (d), the grain size had not much of refinement (Z.H. Li, et al., 2019). (Yang, et al., 2019) reported similar heterogeneous nucleation theory explanation upon the addition of Mo nanoparticles in the Sn58Bi solder alloy.

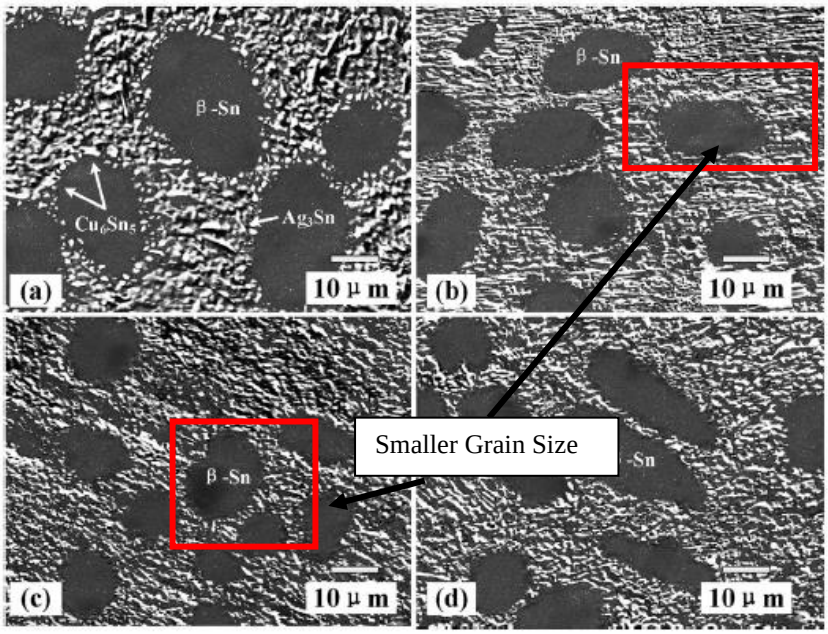

Figure 2. 15: Microstructure and grain size of a) Sn3.0Ag0.7Cu added with b) 0.1 wt.% CeO_2, c) 0.5 wt.% CeO_2 and d) 1 wt.% CeO_2 (Z.H. Li, et al., 2019).

(Xing, et al., 2017) found out that the Al_2O_3 nanoparticles were located at the surrounding area of eutectic the SnZn solder and it is related to the nucleation theory as this research. The presence of Al_2O_3 nanoparticles proves that it serves as barrier for the growth of larger acicular SnZn eutectic region. Likewise, the whisker formation of SnBi was inhibited by Polyhedral Oligomeric Silsesquioxane (POSS) nanoparticles in a research conducted by (Hu, et al., 2016).

Another theory termed Zener pinning theory was used by (Chellvarajoo, et al., 2015) to explain the grain refinement of Sn3.0Ag0.5Cu solder alloy with the additions of diamond nanoparticles. In that research, the presence of diamond nanoparticles prohibits the dynamic grain sliding together with reduction of the grain kinetic of the solder which contributes to grain refinement. (A.E Hammad & A.A. Ibrahiem, 2017) explained that the ZnO

particles had the capability of limiting the grain growth and decreasing the size of the Ag_3Sn needle like particles in the Sn3.0Ag0.5Cu solder alloy by pinning reaction of the ZnO on the grain boundaries. Adding to that, the presences of ZnO as surface-active element decreases the surface energy of the Ag_3Sn and thus limits the growth. The ZnO nanoparticles added to the Sn5Sb solder alloy showed the decrease in the average size of the SnZn IMC from 17.95 µm to 12.94 µm and 19.23 µm to 14.05 µm at 100 °C and 125 °C annealing temperature respectively (E.A. Eid, et al., 2016).

Apart from that, the undercooling temperature is another key factor for the refinement of the grains (A. Nabihah & M.S Nurulakmal, 2019). Undercooling is the indicator of the level of difficulty of a nucleation process during solidification, ($T_{onset\ heating} - T_{onset\ cooling}$). The additions of Al_2O_3 nanoparticles in the Sn3.0Ag0.7Cu solder reduces the degree of undercooling almost 65 % compared to the bare solder, and thence the average size of the β-Sn was reduced (Wu, et al., 2019). Apart from the undercooling effect on the microstructure, the surface area per unit volume of the adhesion nanoparticles contributes to refinement of the microstructure. According to (G.K. Sujan, et al., 2017), Co nanoparticles in the Sn3.0Ag0.5Cu contributes to rapid solidification that forms much more uniform microstructure. Micro alumina particles addition to Sn9Zn provides uniform microstructure (Figure 2.16) with similar explanation (Ding, et al., 2018). However, some studies provided information of degradation due to overweight percentage additions of nanoparticles in the solder alloy. For example, (Ani, et al., 2018) found out that over additions of TiO_2 promotes agglomeration among the nanoparticles, which

resulted in the formation of micro pores in the solder matrix. The micro pores reduced the suppression of the IMC growth. Research by (Wu, et al., 2019) noted same issue with over additions of Al_2O_3 nanoparticles (>0.06 wt.%) causes agglomeration to the Sn0.3Ag0.7Cu solder. This disables less amount of Al_2O_3 nanoparticles to be absorbed because of the reduced surface energy. This was the case for the Pr nanoparticles as well.

As a whole, the additions of nanoparticles provides improvement to the microstructure of the solder alloy. These nanoparticles clearly act as heterogeneous nucleation site and at the same time reduces the activation energy to limit excessive grain growth. In another side of the study, over additions of nanoparticles could reverse the improvement to deterioration as the agglomerations of nanoparticles occurs and disables the refining process.

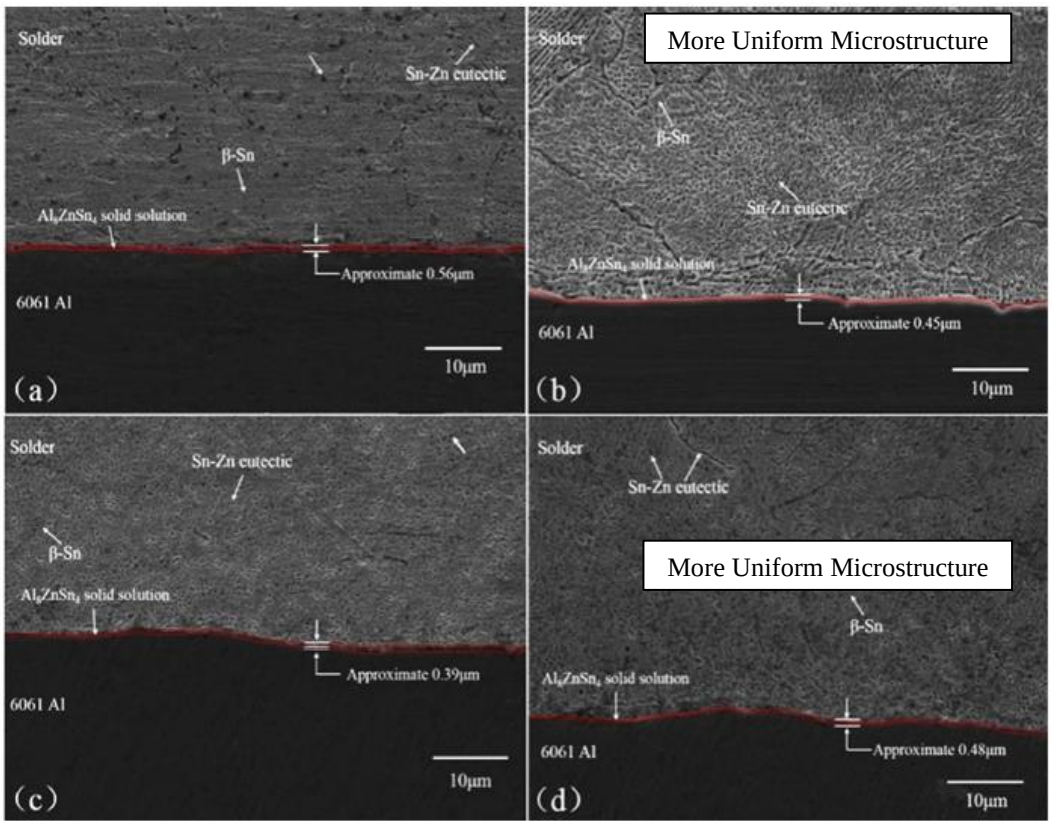

Figure 2. 16: Microstructure and grain size Sn9Zn added with a) 0.25 wt.% Al_2O_3 b) 0.5 wt.% Al_2O_3, c) 0.75 wt.% Al_2O_3 and d) 1 wt.% Al_2O_3. (Ding, et al., 2018).

2.6.4 Interfacial (Intermetallic Layer) Properties

Interfacial properties here concern on the intermetallic compound layer that is produced in between the solder and substrate. Since the base solder here is Sn, the reaction of Sn towards Cu in the PCB board will be discussed. When a liquefied solder alloy reacts with a substrate, there exists a reaction at the interface. Outcome of this reaction is a product is named an intermetallic compound (IMC) layer (Mayappan & Ahmad, 2010). This IMC layer forms an interfacial continuity between the solder and substrate and is a diffusion controlled process (Efzan, et al., 2013). The process of IMC layer formation takes place during the soldering process when some of the elements in solder

alloy where the solder joint formed are dissolved into the molten solder. In some cases, the IMC layers may consist of one or more IMC compounds (E.Hare, 2013). The composition of the IMC compound depends on the combination of the elements in the substrate and solder used in the application (Tegehall, 2006). Thin continuous and uniform IMC layer is desired while a thick IMC is prone to cracking and stimulates failure to the solder joint (Yang, et al., 2013).

Taking in to the Sn reaction with the Cu substrate, upon contact with the substrate at a certain temperature (phase diagram), the Sn from the solder will react with the Cu from the substrate, and vice versa. This activity happens in between the solder alloy and the substrate and after some time, the layer of Cu_6Sn_5 will be first produced, and normally in the form of scallop irregular shape. With further ageing time or increasing temperature, there would be further increment in the thickness of the IMC layer. The reaction of Cu_6Sn_5 and Cu will form Cu_3Sn IMC in between the Cu_6Sn_5 and the Cu, while the reaction of Sn from solder side toward the Cu_6Sn_5 will produce thicker Cu_6Sn_5 layer. In studying the Sn58Bi, similar IMC layer of Cu_6Sn_5 was noted when the Sn58Bi soldered to the Cu at 200 °C (Liu , et al., 2016). This was also the case in the research by (Yoon, et al., 2002). Figure 2.17 shows some extracted image on the presence of this Cu_6Sn_5 layer. The activation energy needed to form the Cu_6Sn_5 is less compared to activation energy for the Cu_3Sn layer, that could be only produced with higher temperature or ageing time (Ma, et al., 2003; Yang, et al., 2013). Aforementioned, the Cu_3Sn will be produced with further ageing and high temperature exposure (M. Abdelhadi & Ladani, 2012). This production of IMC layer will thicken the IMC layer together with the presence

of the Cu_6Sn_5 that will increase the chances of tear at the joint (Hu, et al., 2017). The soldering time also takes part in determining the formation of IMC layer, as longer soldering time allow more Cu and Sn to react and form the Cu_6Sn_5 IMC layer (Wang, et al., 2016). An investigation by (N Mookam, et al., 2018) manipulated the reflow time as seen in Figure 2.18 with an obvious trend of thick IMC layer observed with the increase in time. At the soldering time of 240 s, the growth of Cu_6Sn_5 tends to decompose, which happened as the Sn react with Cu by passing through the Cu_6Sn_5 layer to form the Cu_3Sn layer. At the same time, the Sn from the Cu_6Sn_5 was subtracted at longer time resulting in the formation of the Cu_3Sn layer. This finding explains the reason behind the presence of Cu_3Sn IMC layer in a Cu-Sn interacting system. Another review study made a point that the formation of IMC at first is controlled by reaction diffusion and by a high growth rate. Then, the thickness of the IMC will be influenced by the grain boundary diffusion mechanism (Lee & Mohamad, 2013).

a) b)

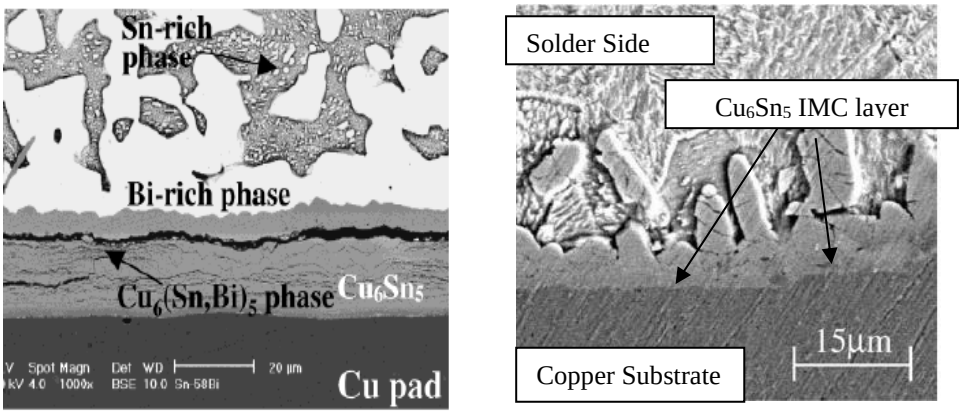

Figure 2. 17: Cu_6Sn_5 IMC layer for a) SnBi solder joint (Yoon, et al., 2002) and b) Sn3.8Ag0.7Cu solder joint (Ma, et al., 2003).

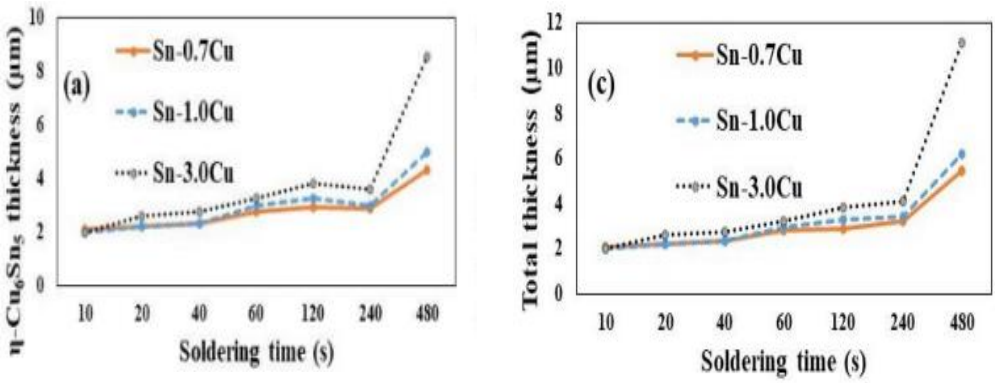

Figure 2. 18: IMC layer thickness at different soldering time (N Mookam, et al., 2018).

The formation of the Cu_3Sn layer is in between the Cu_6Sn_5 and Cu pad, and the chemical reaction is as such, $Cu_6Sn_5 + Cu \rightarrow Cu_3Sn$ where the Cu atoms from the Cu pad reacts rapidly with the Cu_6Sn_5 layer to produce Cu_3Sn layer. This action retards the growth of the Cu_6Sn_5 layer due to absence Cu that mainly contribute to the growth of Cu_3Sn layer (Zhang, et al., 2012). Figure 2.19 shows the presence of the Cu_3Sn layer adopted from few researches. As these interfacial properties serves as among the important aspect to characterize a reliable joint, research focuses on producing thin IMC layer mainly concerning the CuSn layer (Guo, et al., 2019; Sun & Zhang, 2015). Among the approach is addition of element to the base solder alloy. The Sb content up to 1 wt.% added to the Sn3.5Ag0.7Cu reduces the diffusion coefficient of the Cu_6Sn_5 IMC layer and limits the thickness (G.Y Li et al 2010). Not only that, the presence of Sb atoms tends to replace some of the Sn atoms in Sn based compounds and dissolve in the β-Sn matrix or in the Cu_6Sn_5, or even form Ag_3Sb that precipitates with Ag_3Sn. This action by the Sb known as the grain boundary pinning mechanism. Presence of these Ag_3Sb in between the Cu_6Sn_5 and Cu pad blocks the Sn from solder side to react with the Cu_6Sn_5 and produce thicker

Cu_3Sn layer. The activation energy of Cu_6Sn_5 was increase from 30.26 kJ/mol to 33.18 kJ/mol (for 0.2 wt.%) and there was much difference in the activation energy of the Cu_3Sn.

a) b)

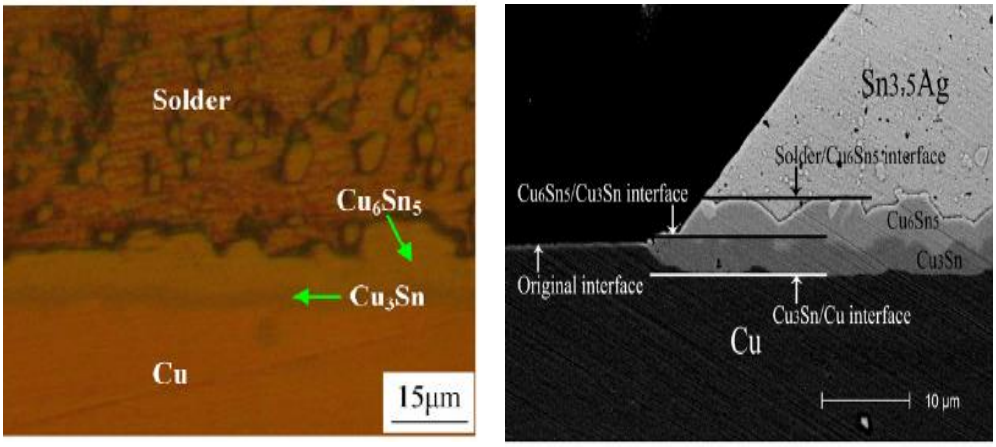

Figure 2. 19: Cu_3Sn IMC layer for a) SnAgCu solder joint (Zhang, et al., 2012) and b) Sn3.5Ag solder joint (Yang, et al., 2013).

In a different research, Sn3.0Ag0.5Cu was added with element of Ce and Zn and the Sn diffusion was restricted, inhibiting thick Cu_6Sn_5 IMC layer (Lin & Chuang, 2010). (Chen, et al., 2015) recorded similar explanation with additions of In to the Sn58Bi solder. The element Ni meanwhile contributes to the formation of $(Cu,Ni)_6Sn_5$ layer that has higher phase stability than the less stable Cu_6Sn_5 in the Sn0.6Cu0.05NiGe solder, subsequently produces thin IMC layer (Kanlayasiri & Meesathien, 2018). The Ni element was added to the Sn58Bi solder and the Cu_3Sn IMC was not detected due to the formation of $(Cu,Ni)_6Sn_5$. However, the effect was not beneficial as the IMC layer seem to induce crack due to low soldering temperature used since this temperature is not suited for the hexagonal $(Cu,Ni)_6Sn_5$ to be formed. In a different study, (Kanlayasiri & Sukpimai, 2016) explained a similar explanation that the Cu_3Sn

and Cu_6Sn_5 decreased in thickness for a lower content of In in the Sn0.3Ag0.7Cu solder, but later thickens as the In content increases. (Mayappan & Jasli, 2018) studied the Sn8Zn3Bi added with Ag and clarified that the additions of Ag produced $(Cu,Ag)_6Sn_5$ layer and this allows Bi to retard higher diffusion process. Quite different from all these suppression effect to the IMC layer, in a certain study of (T.Y Kang, et al., 2011), the growth of Cu_6Sn_5 IMC layer was not retarded but enhanced due to the presence of Bi. This was claimed due to the reason of Bi acting as catalyst that breaks the Cu and Sn bond. Thus, acceleration of these atoms increases and diffusion occured rapidly and produce a thicker Cu_6Sn_5 IMC layer. However, the result unlikely to occur in the eutectic Sn58Bi since the prior study uses Sn10Bi.

Additions of elements could depress the IMC thickness to produce better joint, but then the element additions would increase the mass of the solder that is not suitable for current trend of miniaturized electronic components. Therefore, concurrent to the trend, many new studies have used nanoparticles as additions to the solder alloy and its interfacial properties were investigated. Referring to the experiment by (Haseeb & Leng, 2011), the study notified that the additions of Co nanoparticles to Sn3.8Ag0.7Cu (SAC) contributes to flatter IMC layer. Moreover, the thickness of the Cu_3Sn IMC layer is thicker in the bare SAC compared with the Co nanoparticles reinforced SAC solder under all conditions. The inter-diffusion coefficient in the Cu_3Sn contributes to the shrinkage of the Cu_3Sn IMC layer, as a result of the reduction in the growth rate of the IMC layer by Co nanoparticles. (Chang, et al., 2011) also reported this explanation for the TiO_2 additions, while (Hu, et al., 2010) mentioned this for

the Cr reinforcements. In meantime, the addition of Mo nanoparticles contributes to a reduction in overall IMC layer thickness of Sn3.8Ag0.7Cu (Haseeb, et al., 2012). The Mo nanoparticles serving as a discrete particle engages at the grain borders of interfacial IMC scallops due to the higher energy state at the interfacial (Gain & Y.C. Chan, 2012; Callister & Rethwisch, 2011). Hence, the Mo nanoparticles blocks the channels of diffusion and hinders the movement of Cu atoms from the substrate to solder and vice versa (L.C. Tsao, et al., 2012). The reduction in the flux ripening also occurs due to the Mo additions and at the instance the Mo acts as a barrier to the combination of neighbouring scallops and causes a decrease in the scalloping diameter of the IMC layer. (Fouzder, et al., 2011) studied the reinforcement of $SrTiO_3$ nanoparticles in Sn3.0Ag0.5Cu solder system and discussed this statement too. Subsequently, (Gain, et al., 2011) specifies that the presence of ZrO_2 nanoparticles appeared to inhibit the IMC layer in the Sn3.0Ag0.5Cu and Sn9Zn solder alloy. Presence of TiO_2 nanoparticles delays and impedes the development of the IMC layer from further elongation. The nanoparticles of Fe_2NiO_4 at the solder joint in the Sn3.0Ag0.5Cu prevents the movement of the Cu atoms from the Cu pads and preserves thin IMC layer. This shows that the Fe_2NiO_4 did not involve in any diffusion process and only present itself as discrete particles, and was the similar contribution done by the Co nanoparticles (Haseeb & Leng, 2011). The Mo nanoparticles in a separate study was added to the Sn3.0Ag0.5Cu with ageing effect and the Mo nanoparticles was seen to not involve in any diffusion activity as well at the interfacial site and disperses itself in the solder side only. In view of that, these Mo nanoparticles acts as barriers along the atomic diffusion paths to control the Cu_6Sn_5 layer from growing

drastically (Yang, et al., 2019). The TiO_2 nanoparticles was mechanically mixed to the Sn0.7Cu0.05Ni solder which shows an observation in a flatter and thinner IMC layer of $(Cu,Ni)_6Sn_5$ compared to the bare Sn0.7Cu0.05Ni. This was evident too even with an increasing annealing time; the Sn0.7Cu with the TiO_2 content had thinner total and Cu_3Sn IMC layer as shown in Figure 2.20. Likewise, (Salleh, et al., 2017) provided all the information in their research. This justification of suppression of the IMC layer consistently gathered in studies by (Xing, et al., 2017; Fouzder, et al., 2011). As a result, the activation energy of diffusion is enhanced with reduction of the growth rate of the Cu_6Sn_5 layer. The TiC nanoparticles was mixed to the Sn3.0Ag0.5Cu and was left to age to attain the effect of the nanoparticles on the IMC layer (Chen, et al., 2016). The common Cu_6Sn_5 and Cu_3Sn IMC layer was found in the interface, yet an interesting observation was noted with the growth rate of the IMC layer in the TiC added solder was lower compared to the non-added solder. The reason for such slow growth rate is the existence of the TiC nanoparticles at the surface of the IMC layer due to rejection of the nanoparticles by the flux. In the same way, other researches (e.g. (Zhang & Gao, 2015) (La_2Lo_3 nanoparticles in SnAgCu), (Kanlayasiri & Meesathien, 2018) (ZnO nanoparticles in Sn0.3Ag0.7Cu), (Gu, et al., 2015) (Fe_2O_3 nanoparticles in Sn1.0Ag0.7Cu), (Li & Y.C Chan, 2015) (Ag nanoparticles in Sn58Bi) have also explained this rejection trend of nanoparticles that influences in obstruction of thicker IMC layer. (Efzan Mhd Noor & Singh, 2014) and (Zhang, et al., 2019) also provided literature review on these as well. Schematic diagram in Figure 2.21 shows the presence of nanoparticles on the IMC layer surface. Coupled with that, (Yang, et al., 2018) linked the Kirkendall voids relationship to explain the influence of the 0.25

wt.% Mo nanoparticle in the Sn58Bi solder joint. It is common in a solder joint to possesses Kirkendall void as these voids appears as the vacancies when the Cu atom leaves or moves further up to react with Sn (Hsu, et al., 2019) . The Mo reinforced solder had no such occurrence of the Kirkendall voids because of the suppression effect of the nanoparticles in the solder alloy. The presence of the void was only found after 1200 thermal cycles.

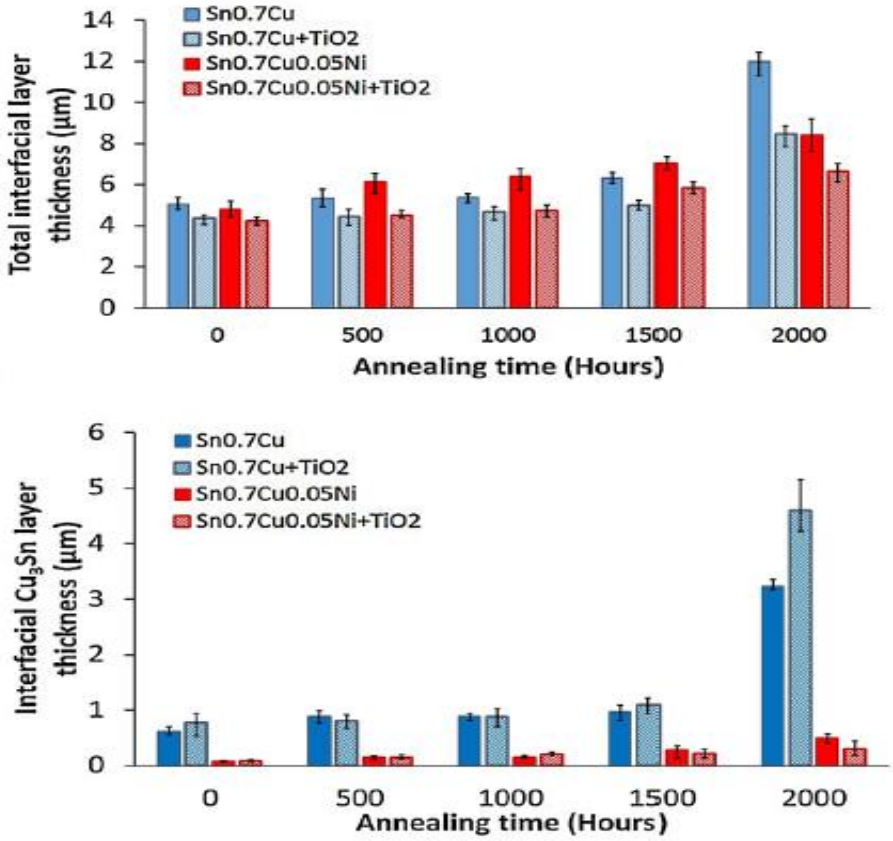

Figure 2. 20: a) Total IMC thickness and b) Cu_3Sn IMC thickness of Sn0.7Cu added with TiO_2 and Ni nanoparticles (Salleh, et al., 2017).

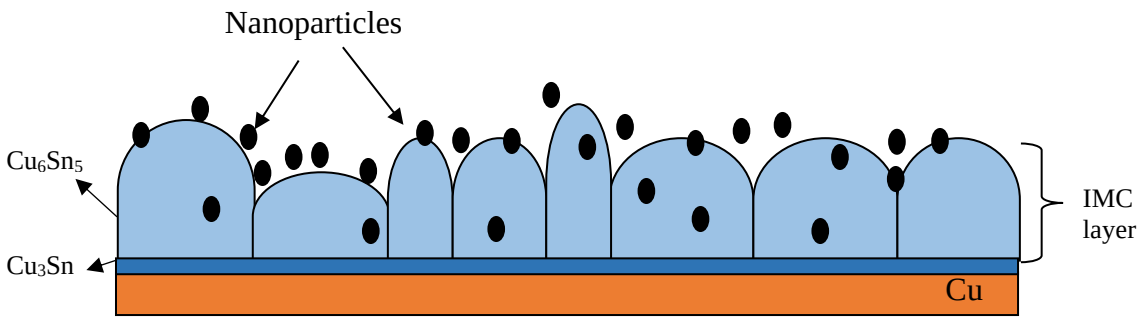

Figure 2. 21: Schematic diagram of existence of nanoparticles on the surface of IMC layer.

A factor that contributes to the presence of the nanoparticles at the surface of the IMC is the buoyancy of the molten solder. This buoyancy induces an acted upward force on the nanoparticles and thus pushes the nanoparticles upwards to the surface. Secondly, the less dense nanoparticles will also urge themselves to being pushed upwards to the IMC surface. These was the findings claimed by (Ani, et al., 2018) with TiO_2 nanoparticles. Nonetheless, not all researches has pronounced that the additions of nanoparticles are beneficial to the interfacial property. Although there is no specific weight percentage additions standard to follow, some research for example by (Shang, et al., 2019) mentioned that over addition (> 3 wt. %) of nanoparticles will have no effect on the reduction in IMC layer and in some cases even produce thicker IMC layer. In that research, Cu nanoparticles was added to the SnCu solder and the 2 wt.% of Cu nanoparticles had thicker IMC than the 1 wt.% Cu nanoparticles, shown in Figure 2.22. This was parallel to the report by (Ding, et al., 2018) with Al_2O_3 nanoparticles additions.

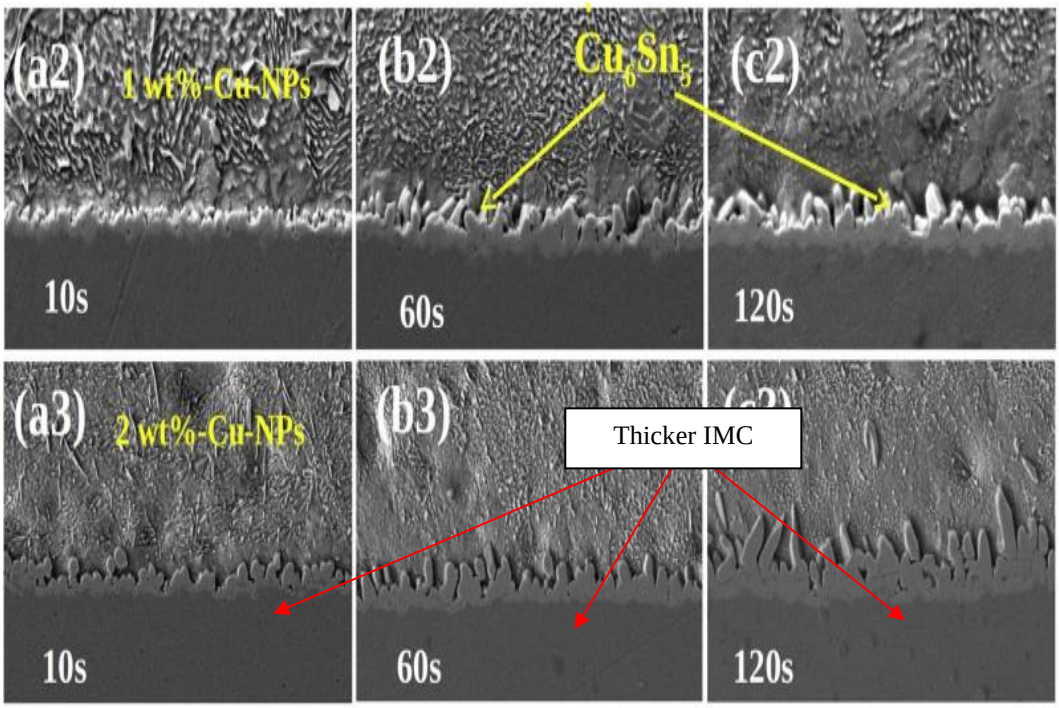

Figure 2. 22: IMC layer of 1 wt.% Cu and 2 wt.% Cu nanoparticles in SnCu joint (S. Shang et al. 2019).

2.6.5 Mechanical Properties

In a solder alloy, strength is likely to be the most important factor for a solder alloy and maintaining a good integrity (Hongtao & Suhling, 2009; Wang, et al., 2016). In accomplishing that, stability of the presence of nanoparticles in accordance to the size and inter-particle spacing will be a key aspect (Duan, et al., 2004). Among the factors that attribute to the hardness (Y. Tang, et al., 2014) and shear strength (H. Tsukamoto, et al., 2010; Roubaud, et al., 2001; Gain, et al., 2011) of the nanoparticles reinforced to the solder alloy are such as Hall–Petch effect, Orowan strengthening, production of geometrically required and load-bearing effects owing to the nano sized reinforcements. The nanoparticles as active elements will reduce the growth velocity of the plane and reduces the size of the IMC's and grains as explained earlier. Furthermore, these finer

IMC's and nanoparticles inputs as second phase dispersion strengthening elements. In terms of joint integrity, the nanoparticles as discrete particles will block the diffusion process between the solder and substrate to preserve thinner IMC layer for better bonding (S.L. Tay, et al., 2013).

2.6.5.1 Hardness

Hardness is the ability of a material to resist deformation upon load and this concept applies to the solder alloy too. The microstructures and the presence of IMC in the solder contributes to the hardness of a solder (L. Silva, et al., 2017). Since the microstructure production is based on the element used in solder alloy, the element that been added will directly contribute to the hardness aspect (R. Kotadia, et al., 2014). The Vickers microhardness value could be calculated basically by this equation:

$$HV = 1.854F/d^2 \qquad \text{Equation 2.1}$$

F = Indentation force, d = mean diagonal of the indentation

The In addition in the Sn9Zn solder increases the hardness of the composite solder alloy as the high concentration of In refines the needle shaped Zn phases (Y.T. Wang et al. 2013). The solid solution hardening was explained by (Ali, et al., 2016) when the hardness of the Sn1.0Ag0.5CuFe solder alloy was put to test. The hardness value increased from 10.5 HV to 22.2 HV with the 2 wt.% Bi additions. According to that research, the increase in hardness is caused by the solid solution of the Bi in the solder alloy, or in other words, it means the Bi just present itself as solid discrete particles to enhance the

hardness. (Shen, et al., 2017) agreed to this increase in hardness is due to the solid solution effect. In contrast, some other studies argue that the high hardness value is contributed by the microstructure phases and formation, which in fact is true (Sunderraj, et al., 2018). One of the research that agrees with this explanation is (Giuranno, et al., 2016), whom successfully showed that the additions of 2.1 wt.% Sb increases the hardness of the bulk Sn1.9Ag0.4Cu as finer microstructure was produced. The Ni additions to the Sn58Bi solder increases the hardness value too due to the more elongated and thinner lamellar structure (Liu , et al., 2016). The presence of added elements could be seen influencing the solder matrix either by being solid solution strengthening mechanism or by influencing a production of uniform microstructure.

Looking in to the review study done by (Efzan, et al., 2013), a smaller surface area per unit volume of a solder alloy increases the hardness property. Relating to that, grain size refinement decreases the surface area of the grain under a certain volume of the solder matrix (N.K. Liyana, et al., 2019; Sun & Zhang, 2015). Confirming with that, (N.A. Saleh, et al., 2017) incorporated Zn elements to the Sn0.7Cu solder and attained increment in hardness compared to the bare Sn0.7Cu. Though, with higher content of Zn (1.5 wt.%), the hardness value dropped compared to the 0.5 wt.% additions. The grain refinement due to the presence of Zn was justified as the reason for the increase. In a separate research, alloying Sb refined the Sn8Zn3Bi solder by displaying a finer α-Zn phase uniformly distributed in the β-Sn. That phase noted to impede dislocation movement, and by impeding the motion, the hardness of the solder was enhanced (Ren & N.Collins, 2019). The eutectic microstructure and the

presence of IMCs of Cu_6Sn_5 and Ag_3Sn in the Sn3.8Ag0.7Cu solder matrix (Figure 2.23) increases the microhardness as the IMCs and the eutectic region contributes to strengthening effect (Amares & Ervina , 2015). According to that study, a wider eutectic area has grain boundaries with smaller surface area. It is more difficult to disorder the grain boundaries, resulting in enhanced resistance. This is actually known as the theory of dislocation strengthening (B.S.S.Chandra Rao, et al., 2010; C.L. Chuang , et al., 2012).

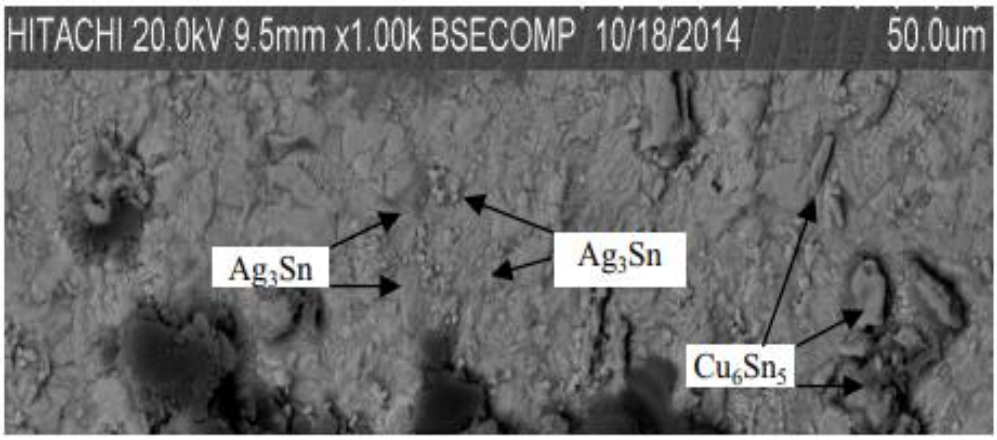

Figure 2. 23: Presence of IMC in the Sn3.8Ag0.7Cu solder matrix (Amares & Ervina , 2015).

Element of Ti added to the Sn3.5Ag0.5Cu reported similar grain refinement and also finer β-Sn with smaller width of the eutectic area that contributes to the increase in the hardness of the solder alloy (C.L. Chuang , et al., 2012). The initial measurement of the eutectic area for the bare Sn3.5Ag0.5Cu was 6.87 µm, which reduced to 1.2 µm after the Ti addition. Similarly, the β-Sn had reduced in the size as well. Additionally, the IMC of Ag_3Sn was identified in the microstructure and suspected to increase the hardness of the solder alloy. The graph in Figure 2.24 from the study of (C.L. Chuang , et al., 2012) shows the increment in hardness after Ti additions.

Separately, alloying of Cu and Zn promoted precipitation hardening through forming IMC particles (Cu_6S_{n5}) and transforming the Bi-rich phase from massive dendritic crystal into globular shape in the SnBi solder (Shen, et al., 2014). Both these effects decreased the diameter of the grain and hinders the dislocation motion contributing to higher hardness value.

Reinforcements of nano scale particles into the bare solder alloy effects the hardness property of the solder as well. The reinforcement of TiO_2 nanoparticles in the Sn3.5Ag0.5Cu solder alloy increases the microhardness from 14.1 HV to 19.3 HV after 0.1 wt.% TiO_2 additions. The reason behind it is the suppression of grain size of Ag_3Sn due to the presence of the nanoparticles (Y. Tang, et al., 2014). Moreover, the pinning of the dislocations due to the stress acting on the surface of the nanoparticles is rectified as the other reason of hardness increase. Equally, (Chang, et al., 2011) in their study added TiO_2 in the Sn3.5Ag and Sn3.5Ag0.7Cu and reported similar increase in the reinforced solder alloy with similar reason due to the grain refinement of Ag_3Sn by the TiO_2 nanoparticles. The TiO_2 nanoparticles was also used by (Nasir, et al., 2019) in the study of the Sn3.0Ag0.5Cu solder and in that research, 1.0 wt.% of TiO_2 nanoparticles creates finer Ag_3Sn and Cu_6Sn_5 IMC in the solder matrix. Therefore, these IMC's resisted deeper penetration upon indentation resulting in higher hardness (increase in 27 %). Identically, smaller depth of penetration was shown by (Y.D. Han, et al., 2019) after adding Ag-GNS nanoparticles to the Sn3.5Ag solder shown in Figure 2.24. Despite the increase in the hardness, additions of 0.2 wt.% Ag-GNS nanoparticles produced lower hardness compared to lower weight percentage additions. This is because the excessive

amount of Ag-GNSs causes a diffusion barrier, which leads to vacancy transition and this vacancy acts as the site for easy penetration. Correlating to that, (Sharma, et al., 2015) found similar decrease in hardness for higher concentration of La_2O_3 nanoparticles but the reasoning behind this is the agglomeration of the high content of these nanoparticles that tend to form clusters among them. By this agglomeration, the grain refining effect is disabled and no production of finer grain to increase hardness and, the agglomerated particles becomes the weakening side and easily penetrated upon load (Salleh, et al., 2012; Mahdavifard, et al., 2015). In some cases, the high amount of nanoparticle tends to evaporated after being pushed away by the molten solder and have no contribution in the hardness value, e.g. diamond nanoparticles in Sn3.0Ag0.5Cu (Chellvarajoo, et al., 2015). (Yahaya, et al., 2016) proves the refinement of the IMC (Ag_3Sn and Cu_6Sn_5) found in the solder Sn3.0Ag0.5Cu is the mechanism that contributes to higher hardness. The study clarified in certain that the presence of TiO_2 nanoparticles is the reason behind the finer IMC, and the indentation depth decreases with higher amount of TiO_2 additions. The IMC's also hinders further force distribution in the solder matrix and acts as a barrier mainly by pinning dislocation movement as pointed out by other researchers too.

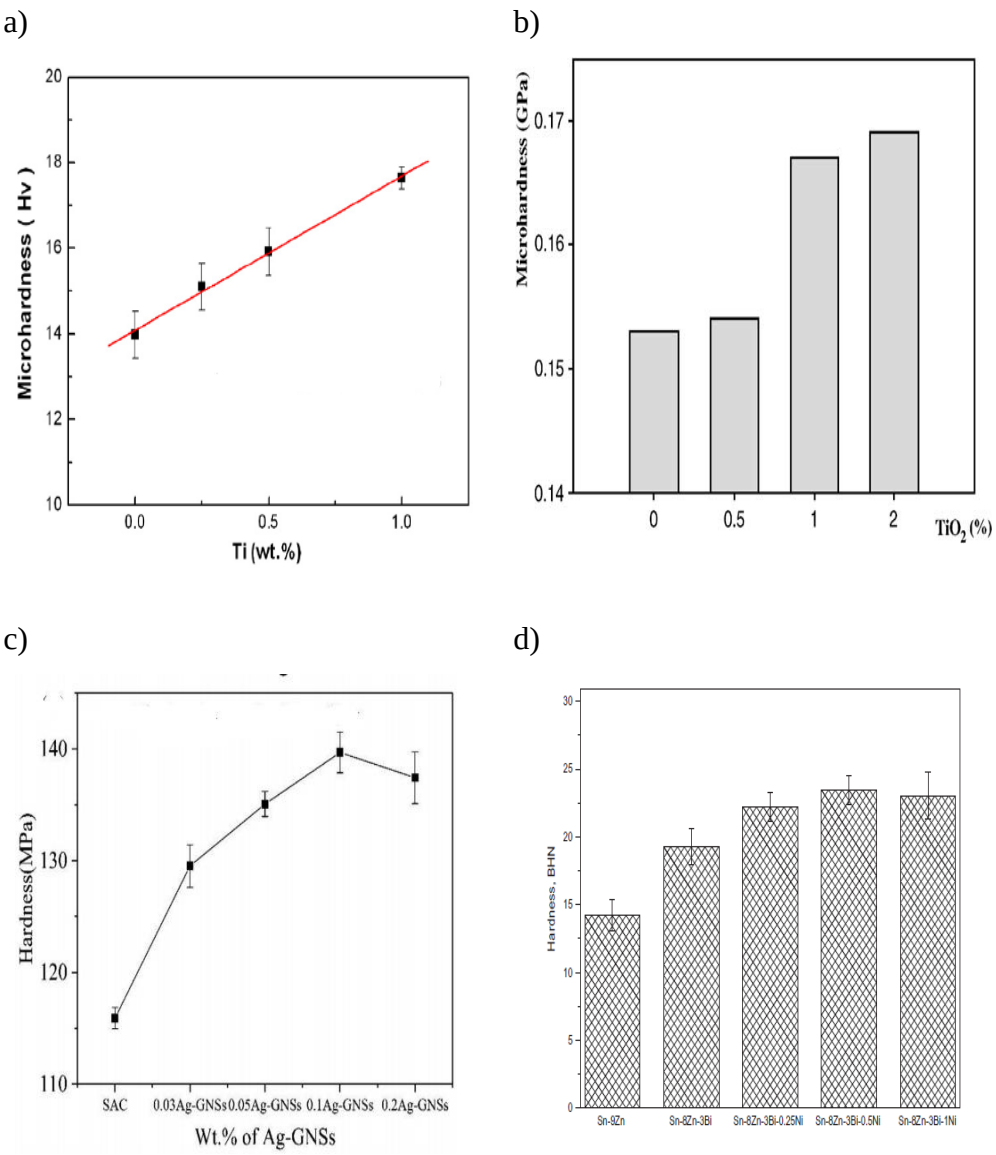

Figure 2. 24: Effect of a) Ti additions in the microhardness of Sn3.5Ag0.5Cu (C.L. Chuang , et al., 2012) b) TiO_2 additions in the Sn37Pb (D.C. Lin, et al., 2003), c) Ag-GNS nanoparticles in Sn3.5Ag0.5Cu (Y.D. Han, et al., 2019) and d) Ni micro-sized additions in Sn8Zn (Billah, et al., 2014).

Quite some time ago, as the SnPb was the most used solder alloy in the electronic packaging industry, this solder in a particular research was added with TiO_2 micro powders to investigate the hardness (D.C. Lin, et al., 2003), and with 2 wt.% nanoparticles, the hardness value was 0.169 GPa compared to the bare SnPb's value of 0.153 GPa. These second phase particles (TiO_2) nanoparticles increase the hardness together with the primary dispersion

strengthening. The addition of Cu micro and nano scale particles in the Sn3.5Ag solder denotes that the smaller sized nano scaled particles contributes to a higher Knoop hardness (14.6 kg/mm^2) than the micro particles (13.2 kg/mm^2) (D.C. Lin, et al., 2007). It was discovered that the nano particles promoted more Cu_6Sn_5 IMC and the Ag_3Sn formation in the solder. Higher hardness of the nano scale Cu additions seen compared to the micro scale. Instead, the production of finer Ag_3Sn IMC because of the single wall carbon nanotube (SWCNT) nanoparticles was clarified as the reason for the hardness increase in the Sn3.8Ag0.7Cu solder (Kumar, et al., 2008). Nonetheless, the agreement is based on the same theory of IMC grain refinement. The investigation also points out another factor for the increase in the hardness which is the load bearing effect. (Ma, et al., 2017) agreed to this statement as the GNS nanoparticles were used as the reinforced particles to the Sn58Bi solder. The increase of hardness was quite obvious with the presence of nanoparticle added solder with a jump in of the hardness value from 309 MPa to 380 MPa. Literally, the increase in hardness is due to the presence of finer grains, pinning of grain boundaries and also the increase in the dislocation density as was discussed in most researches (L.C Tsao, et al., 2013; Gain & Y.C. Chan, 2012; Billah, et al., 2014; Zhu, et al., 2018).

2.6.5.2 Shear Strength

The shear strength is related directly to the solder alloy's joint. Usually the shearing strength of the solder alloy depends on the thickness of the IMC layer produced. The nanoparticles as active elements will reduce the growth velocity of the plane and reduces the size of the IMC's and grains as explained

earlier. Additionally, in terms of joint integrity, the nanoparticles as discrete particles will block the diffusion process between the solder and substrate to preserve thinner IMC layer (S.L. Tay, et al., 2013).

The SnPb solder alloy was brought to test with the shear test by testing different aging times at different temperature of the solder joint (Jeon, et al., 2012). Obvious drop in the shear strength was obtained with increasing strain rate as the aging time increased. The nanoparticles as discrete particles are also known to block the diffusion process between the solder and substrate. The as-reflowed sample of the Sn37Pb and Sn3.0Ag0.5Cu produced a thin Cu_6Sn_5 IMC layer. The layer grew thicker in the samples at the 170 °C aged with the thin layer of Cu_3Sn produced between the Cu and the Cu_6Sn_5 layer. The explanation of the Cu_3Sn was explained earlier and this thick IMC layer reduces the joint strength. (Kim, et al., 2008) testified similar drop in the shear strength (Figure 2.25) due to the thick IMC layer even after using the Ni–P to block the diffusion barrier to Cu substrate for both Sn37Pb and Sn3.0Ag0.5Cu solder. In that research, an observation on the type of failure shows the aged samples seems to have more of a sudden failure. This was noted as the fractured surface is flat and sharp with the crack path running slightly above the boundary of the solder and IMC layer (Jeon et al. 2012). As the aging increased, the failure is more of a brittle manner and the crack propagates along the IMC layer. Noteworthy here, the failure mode is a key factor in the study of the solder alloy's strength, as studied by (Affendy & Mohamad, 2015) in conducting an experiment using the Sn9Zn solder. The reflow process causes the change in the shear strength and it was evident that with the increase in the number of reflow, the IMC layer

thickens and degrades the shear strength of the Sn37Pb solder joint (Hu, et al., 2014). (Kar, et al., 2008) provided very clear result on the shear strength obtained for the SnPb (55.6 MPa) and SnAgCu (67.9 MPa) which been referred as the model for other researches. In that research, the width of the brittle IMC layer of Cu_6Sn_5 plays a dominant role in increasing the shear strength whereby a thinner width of the reaction layer in the joint SnAgCu/Cu joint contributes higher shear strength than SnPb/Cu joint.

The strain rates were also studied to analyse the shear strength of a solder joint (Choudhury & Ladani, 2016; Jeon, et al., 2012). The fracture of Sn58Bi solder joint occurred inside the IMC layer with increasing strain rate (3.33×10^{-1} s^{-1}, 1.66 s^{-1} and 3.33 s^{-1}), which was inverse to the fracture observed in the solder for the lower strain rate (3.33×10^{-4} s^{-1}) (Wan, et al., 2018). Thus, the strain rate literally can control the type of fracture to the solder joint, Figure 2.26.

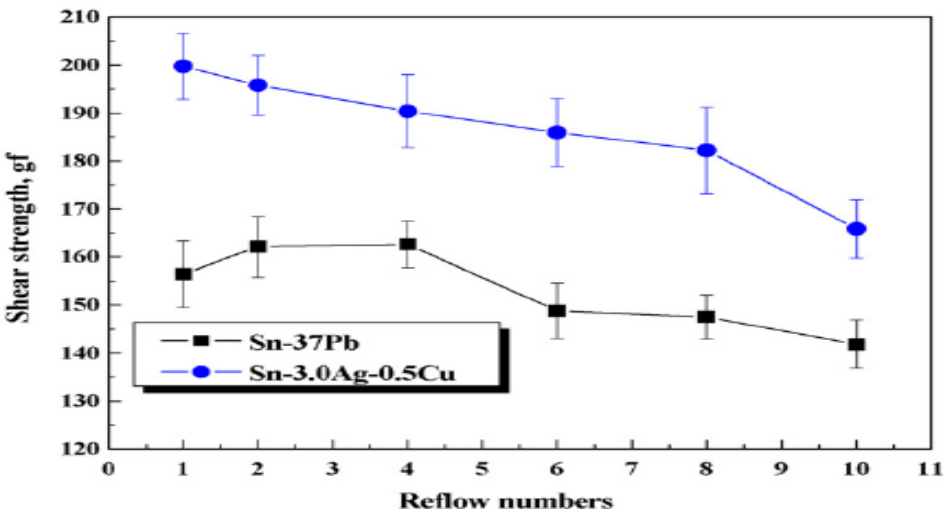

Figure 2. 25: Shear strength of Sn37Pb and Sn3.0Ag0.5Cu solder with different numbers reflow (Kar, et al., 2008).

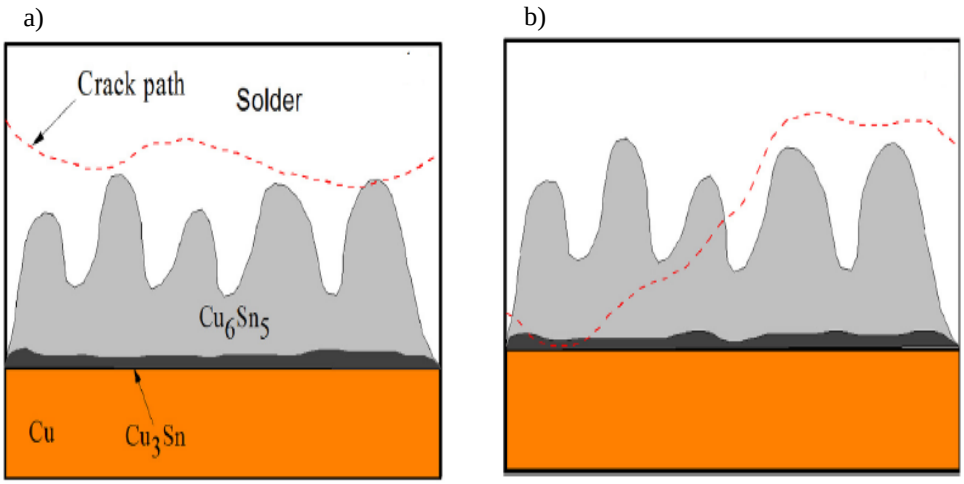

Figure 2. 26: Fracture at a) low strain rate b) high strain rate.

The ball shear test was conducted to the Sn37Pb and Sn3.8Ag0.7Cu solder alloy with difference surface finishing of Ni/Au and OSP (Liu, et al., 2009). The shear strength of the SnPb recorded 11.7 kg (for Cu coated) and 11.5 kg (for Ni/Au coated), while the Sn3.8Ag0.7Cu recorded 13.7 kg (for Cu coated) and 12.7 kg (for Ni/Au coated). The shear strength values were different between these two solder alloys because of the Ni in the Ni/Au solder alloy that blocks the vast diffusion of Cu and Sn to react and produce thick Cu_6Sn_5 IMC layer. The common Cu_6Sn_5 IMC layer was indeed present in the Cu and Ni/Au pad, yet the later surface finish had the Ni_3Sn_4 IMC layer that consumes the Sn to avoid thick Cu_6Sn_5 layer. (Lee & Lee, 2007) provided similar recognition of shear increase. In both earlier studies, the shear strength dropped with ageing time.

Most of the study involving the SnBi solder alloy concluded this solder to have low strength due its low melting point. (Wang, et al., 2016) did the interfacial study to the shear strength of the Sn58Bi solder and the interfacial

joint prevailed ductile to brittle fracture mode that occurred at the solder side resulting in higher shear strength. The research found out the IMC layer contained Bi precipitates that hold the integrity of the joint by preserving a thin IMC layer. As a matter of fact, the study was done with difference percentage of Bi and the result is as shown in Figure 2.27. The increase in the Bi content had mixed result to the shear strength, whereby the 3 wt.% Bi gave a rise in shear strength of about 20 MPa (Zhou, et al., 2005).

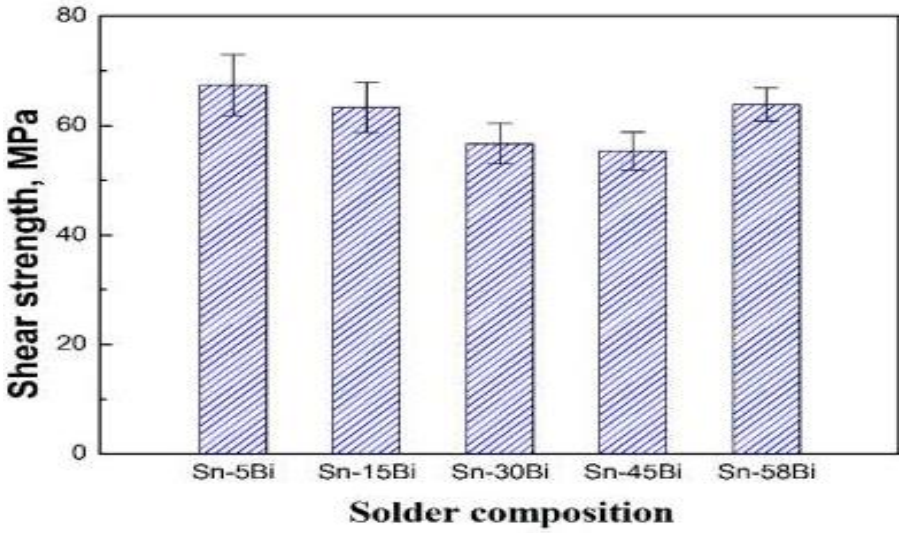

Figure 2. 27: Shear strength of different weight of Bi in SnBi solder (Zhou, et al., 2005).

Just like the earlier report, the tensile strength increased for the SnBi solder alloy with added Zn element. The involvement of Zn was visible as the IMC layers of CuZn and $Cu_6(Sn,Zn)_5$ were produced between the Cu substrate and solder. The CuZn layer is believed to retard the diffusion of both Cu and Sn, leading to a decreased consumption rate of the Cu in contact with the molten Sn58Bi. This phenomenon increases the tensile strength from 63.96 MPa to 67.8 MPa, as the study of (Ma & Wu, 2015) discuses on this. However, as the content

of Zn exceeded 0.5 wt.%, the tensile strength dropped because of the production of ZnO IMC that permits easy crack propagation. The Sn1.0Ag0.5Cu solder alloy's shear strength was tested with the additions of Fe, and the production of flat and thin IMC layer of $FeSn_2$ together with the Cu_6Sn_5 increased the shear strength value of the solder joint (Zhang, et al., 2014). The ultimate tensile strength and shear strength increased immensely upon addition of Sb to the Sn8Zn3Bi as the Sb promotes finer α-Zn particles that acts as hampers the dislocation movement (Ren & N. Collins, 2017).

One of the research argued that the crosshead speed contributes to different shear strength of a solder joint (Affendy & Mohamad, 2015). In that study, the higher crosshead speed (3 mm/min) resulted in 130.41 MPa while the lower crosshead speed (0.5 mm/min) resulted in 106.11 MPa for the Sn9Zn/Cu solder. The reason is because the stress will not have any time for relaxation and thus, the highest UTS is obtained. The type of fracture surface analysis was conducted to relate the strength with the findings stating at the higher speed, the failure occurs at the joint rather than the solder region, shown Figure 2.28. Mentioning the shear strength reliability that analysed based on the fracture surface, the presences of voids also taken as an important guidance to relate the shear strength. The different thicknesses of Ag layer in an investigation focusing on the Au/Ni substrate produced high shear strength that said to be attributed to a fracture path through Ni_3Sn_4 and Ag_3Sn and not through the voids. The 50 nm thick layer possessed better shear strength than the 100 nm with the Ag_3Sn IMC produced better thickness. These are the findings reported by (Chu, et al., 2015)

that reassured that the fracture mechanism are definitely related to the high shear strength.

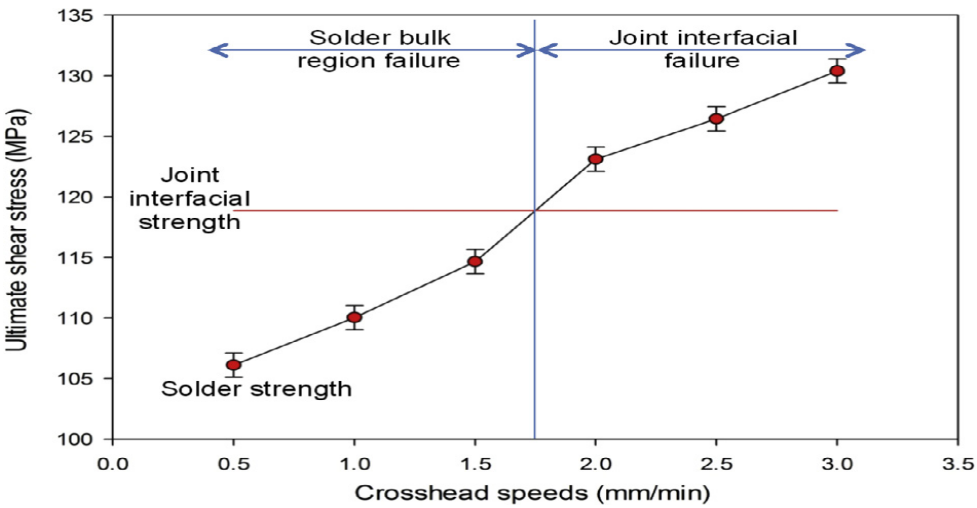

Figure 2. 28: Types of failures at different crosshead speed (M.G. Affendy and A.A. Mohamad 2015).

Shear strength of solders are documented to increase with presence of element added to the solder that effects the IMC layer at the joint. The Ni elements are added in the solder to increase the shear strength. The shear strength of the Sn3.0Ag0.5Cu/Cu doped with 0.1 wt.% Ni was higher than the bare solder because of the production of $(Cu,Ni)_6Sn_5$ IMC layer with reduction in the energy of the Cu_6Sn_5 IMC formation (Chou, et al., 2019). The research has also used the Ni substrate and found even higher shear strength, as there were not much of Cu to react with the Sn because of the presence of Ni that has more chance to react with the Cu. A ductile fracture manner was seen in the Ni doped Sn0.7Cu that resembles the rise in the shear strength as discussed by (Salleh, et al., 2017). In that study too, the TiO_2 nanoparticles was reportedly added to the mother solder to provide even higher shear strength than the Ni

nanoparticles added solder. This is simply due to the Cu barrier effect at the interfacial layer by the enforced by the TiO_2 nanoparticles. Among other researches that provided the improvement of shear strength of the Ni additions are (Q.B.Tao, et al., 2016) (additions to Sn0.8Ag0.7Cu3Bi), (A.E.Hammad, 2018) (additions to Sn1Ag0.5Cu) and (Wang & Shen, 2010) (additions to Sn0.7Cu). The Sn58Bi also benefited in increase in tensile strength with 0.5 wt.% and 1 wt.% Ni additions since the Ni_3Sn_4 IMC act as crack interrupter during loading (Yang, et al., 2015). Apart from that, (Q.V Bui & S.B Jung, 2013) added Ce in the Sn1Ag and found the improved shear strength at high temperature aging but had no effect in the low speed test. The study claimed that the decrease in the lengths and concentrations of $(Ni,Pd)_3Sn_4$ IMC layer between the ENEPIG substrate due to the presence of Ce is the reason behind the increase in the shear strength. Looking up to this point, the IMC layer change due to the presence of the elements are the clear reason behind the increase in the shear or tensile strength. Correlating to that, Co additions improved the shear strength with the formation of the $(Cu,Co)_3Sn_2$ IMC layers together with more faceted type Cu_6Sn_5 layer (J.S Lee et al. 2008). Figure 2.29 shows the shear strength of the Co added solder. The formation of the earlier IMC layer is due to the reactivity of the Co towards Sn while the refining of the faceted Cu_6Sn_5 is similar to the explanation done by other researches of (Ali, et al., 2016; Maeshima, et al., 2016). Nonetheless, the shear strength dropped with 2 wt.% additions because of the thicker $(Cu,Co)_3Sn_2$ IMC layers gathering together and forming a star-like structure owing to the drastic increase in number of the $(Cu,Co)_3Sn_2$ IMC. In a different study, the CuSn IMC particles were finer and more evenly distributed that effects the pinning movement of dislocations of the

Sn0.7Cu with the additions of In which consequently rises the shear strength (A. Nabihah & M.S Nurulakmal, 2019). The interfacial free energy of the Cu_6Sn_5 layer decreased and the presence of $CeSn_3$ IMC in the Sn3.0Ag0.5Cu increases the ultimate tensile strength. This $CeSn_3$ accompanied by the Ag_3Sn IMC together blocks the higher diffusion rate. This action increases the UTS as well (Tu, et al., 2017). A study done by (Bang, et al., 2018) mentioned that unlike most element additions (e.g. Ni, Cu, Ce), the Cr element did not take part in any diffusion process at the interfacial side, but seem to suppress the Cu diffusion. The inhibition of IMC layer by the CNT in the Sn5Sb solder joint after thermal ageing produces higher shear strength than the bare Sn5Sb (T.T.Dele-Afolabi, et al., 2015). At this point, the CNT's role of being surface active element endures to such situation. Since the IMC compound and the IMC layer thickness clearly deeds to the increase in the shear strength of a solder joint, the additions of Zr in the Sn3.0Ag0.5Cu solder joint was put in to test to testify this case (Lu, et al., 2019). The results showed conformance with the hypothesis whereby the Zr elements not only helps to produce thinner IMC layer of Cu_6Sn_5, but also reacts with the Sn to develop a new IMC of $ZrSn_2$ that becomes an additional strength to the solder joint. The fracture mode was noted to have more dimples that relates to the ductile type failure. The fracture of the Sn3.0Ag0.5Cu in a another research also provides a ductile fracture as the slow transition from ductile to brittle mode was noted and this was because of the presence of Pt element (Yee, et al., 2019). The fracture of the SnBi added with Ag solder alloy shows a thin layer of cracked IMC layer with some IMC grains (Cu_6Sn_5) observed. Hence, the fracture is predicated to occur in the solder close to the Cu_6Sn_5/solder interface that resulted in higher tensile strength (F.Q. Hu

et al., 2018). The bare SnBi's solder joint was seen to have the Cu_3Sn layer appeared between the Cu substrate and Cu_6Sn_5 layer and the crack was accompanied with many micro voids.

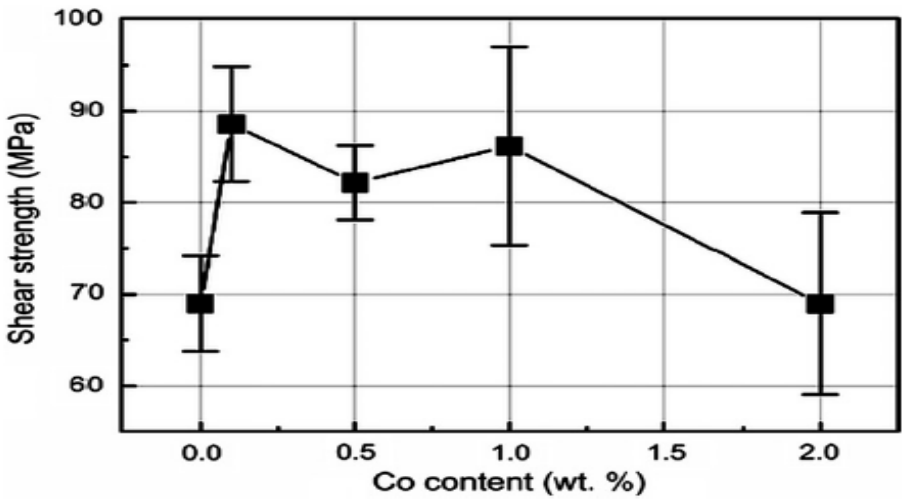

Figure 2. 29: Shear strength with different Co content in Sn1Ag.

As discussed earlier, the joint strength of a solder joint is usually high if the IMC layer absorbs the stress to break. In some cases, two elements may be added to enhance the shear strength of the solder alloy which was experimented in a study that investigates the Ti and Cu element in the 25SnZn solder system (Lin, et al., 2019). As commonly resulted in the research of (Ichitsubo, et al., 2005), the CuZn IMC layer was produced in the solder joint. However, the interesting part was in one of the samples, the Ti content was kept constant and the Cu element was added at a different weight percentage to the 25SnZn solder. The influence of Ti was clarified as being the site for heterogeneous nucleation for the primary during the solidification process. So, the IMC layer was finer resulting in high shear strength. Even rare earth element such as Erbium (Er) creates finer CuZn IMC by reducing the growth velocity that produces higher

tensile strength to the Sn9Zn solder alloy (Zhang, et al., 2012). A separate investigation used another rare earth element of Yb to check on the tensile strength of the SnAgCu solder joint. The result was convincing because the small Yb and the Sn particles contributes to dispersion strengthening mechanism. Later this mechanism was linked with the creep theory as the number of dislocations increases remarkably due to the hard and brittle nature of Sn and Yb particles (Zhang & Tu, 2014). Not all researches have resulted in a beneficial outcome in the shear strength. As encountered by (Peng, et al., 2019) with the Sn20In2.8Ag solder alloy, the result of the shear strength was not convincing. The segregation of In in the solder produced three-phase eutectic Ag_2In, β-Sn and α-Sn distributed at the grain corner of Ag_2In. This offered high probabilities of failure to take place.

Further advances in the solder technology sees the reinforcements of nanoparticles to the solder alloy. The shear strength of the Sn3.5g0.5Cu solder joints containing ZrO_2 nanoparticles produces a higher strength than unreinforced solder joints as shown in Figure 2.30. This situation is attributed to the second phase dispersion strengthening mechanism of ZrO_2 nanoparticles explained by (Gain, et al., 2011). The improvement in the shear strength was credited to the presence and distribution of fine dispersed particles that obliged to the influence of the deformation characteristics by inhibiting grain boundary sliding and at the same time retarding dislocation movement as notified by (D.C. Lin, et al., 2003). In comparison, the thick Cu_3Sn IMC layer significantly known as the destruction cause in a solder joint, was suppressed with the presence of the TiC nanoparticles in the Sn3.0Ag0.5Cu and produced higher shear strength

(Chen, et al., 2016). Adding to that, the dispersion strengthening mechanism was noted to be another cause of high shear strength of the solder joint. Meanwhile, (Shen & Chan, 2009) have proved that ZrO_2 nanoparticles in of Sn9Zn improved the interfacial area per unit volume as increased shear strength of the solder joints was observed. This is because of the ZrO_2 nanoparticles that limits the possibility of fracture passing through the interface between the solder and IMC layer. This was parallel to the study of (Haseeb, et al., 2012).

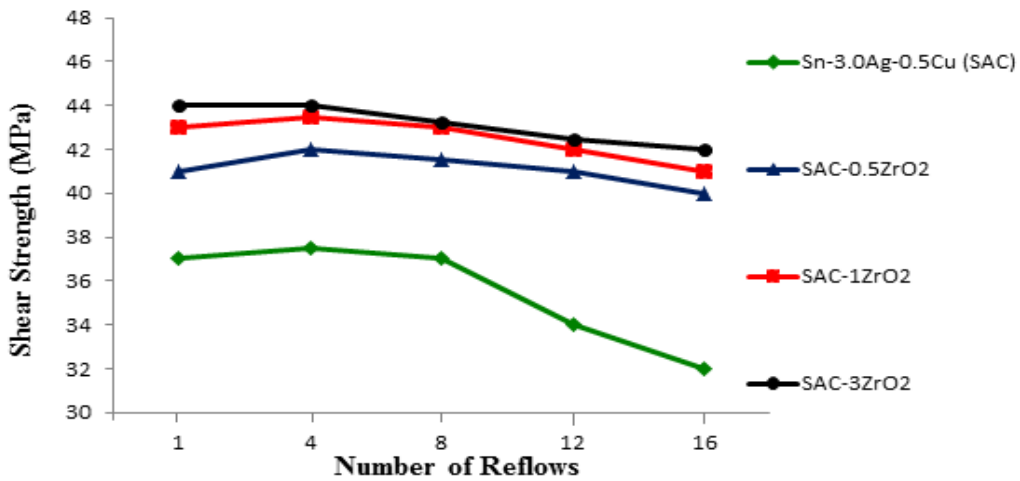

Figure 2. 30: Shear strength of ZrO_2 nanoparticles added Sn3.0Ag0.5Cu (Efzan, et al., 2013).

Another important reason for the increase in shear strength is the pinning of grain boundary by the nanoparticles which then increases the dislocation density at the boundary and the stress needed to move the dislocation (Billah, et al., 2014). This was exhibited by the $SrTiO_3$ nanoparticles upon additions to the Sn9Zn solder alloy (Fouzder, et al., 2011). The CeO_2 nanoparticles acts as the strengthening mechanism and together with the fine IMC particles, the shear properties of the Sn3.0Ag0.7Cu solder alloy increased as these finer particles that serve as obstacles which inhibit the mobility of dislocations (Z.H. Li, et al.,

2019). (Y.Tang, et al., 2017) denoted the same effect in increase in the tensile strength with Mn additions in the Sn3.0Ag0.7Cu solder. The fracture character does make up its influence to the shear strength as well. The unreinforced Sn58Bi solder alloy subjected to ball shear strength endured the fracture at the Cu_6Sn_5/solder interface indicating the place as the weakest area at the joint. Inverse to that, the fracture path of the Sn58Bi solder alloy added with Ag nanoparticles was noticed at the solder region indication that the IMC layer had stronger joint with ductile failure and the weak path was transferred to the solder side. The recorded solder strength was 4.47 N compared to 3.68 N for the pristine solder. The discussion concluded by (Li & Y.C Chan, 2015) explains the refining strengthening (Hall-Petch) and dispersion strengthening (Orowan strengthening) by the Ag_3Sn IMC nanoparticles influences the hike in the shear strength. Research by (Ding, et al., 2018) further elaborated this strengthening mechanism when they discovered the effect of the addition of Al_2O_3 nanoparticles in the Sn9Zn solder alloy. The study unveiled the importance of the particle's size, which contributes to almost 21 % of the total tensile strength. Besides the mentioned strengthening mechanism, in this study the load transfer effect adds as being another source of the strengthening mechanism that these particles can hinder crack propagation. This load transfer effect is a combination of mechanical interlocking effects and van der Waals forces between the Al_2O_3 particles and the solder. Similar response identified with Ni-coated CNT additions in the Sn58Bi solder, as the load transfer occurs to the CNT rather than the Ni_3Sn_4 IMC (Yang, et al., 2015). Accompanied by many research's explanation, in an experiment conducted by (Ramli, et al., 2016), the TiO_2 nanoparticles locks the grain boundaries, preventing grain dislocation and

retarding grain growth. Therefore, the shear strength of the joint increased. The pinning effect of the Zn nanoparticles was also found in the Sn58Bi solder joint to increase the tensile strength (Zhou, et al., 2018). In a separate study by (Wu, et al., 2019), the unreacted rare earth Pr (0.06 wt.%) was added to the Sn0.3Ag0.7Cu solder and exerted the pinning effect to the IMC and increases the strength of the joint. Yet, a noteworthy observation was seen when a minor Al_2O_3 nanoparticles content was added to the solder alloy with the presence of Pr. The pinning effect was more efficient upon the additions as the Pr and the Al_2O_3 nanoparticles had a synergistic effect and enhances the shear force at the joint even further (Figure 2.31). Nevertheless, over additions did not impose positive outcomes as the agglomeration of the Al_2O_3 nanoparticles becomes site for crack initiation. (Liu , et al., 2016) and (Fathian, et al., 2017) agreed to this validation. The Mo nanoparticles was incorporated in the Sn58Bi solder alloy and the tensile strength was improved (Yang, et al., 2019). The Mo nanoparticles seems to be bypassed by the dislocation due to the characteristics of the hard Mo particles that could not be penetrated causing the dislocation to pile up and improving the mechanical strength. The simple schematic drawing in Figure 2.32 shows the pile up of dislocation phenomenon.

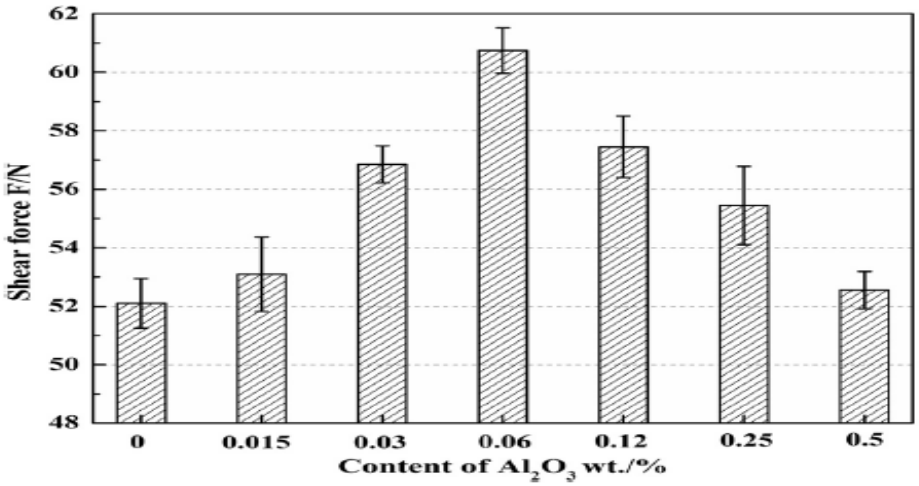

Figure 2. 31: Shear force of coupling Pr and Al_2O_3 nanoparticles in Sn0.3Ag0.7Cu (Wu, et al., 2019).

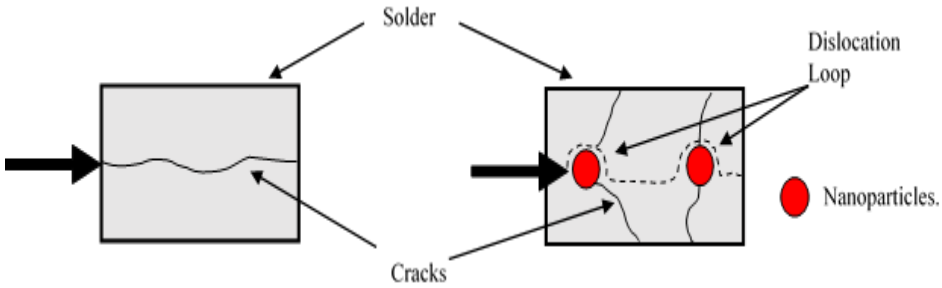

Figure 2. 32: Schematic diagram of stress/load penetration a) bare solder and b) nanoparticles added solder.

The refinement of the β-Sn and Cu_6Sn_5 IMC grains upon the Cu nanoparticles addition in Sn3.0Ag0.5Cu was considered as the central factor for the enhancement of the shear behavior by (Liu, et al., 2016). Another study (E.A. Eid, et al., 2016) confirms the finer grain with nanoparticles as hardening mechanics can increase the mechanical properties of a solder. The ZnO nanoparticles are found within the eutectic regions and the nanoparticles act as pinning centers which inhibits the mobility of dislocations that concentrated around grain boundaries. So the increment in the tensile strength was clear. The Orowan strengthening mechanism was clarified as well to have a certain

influence in the mechanical strength in that research. The pinning effects of the 0.5 wt.% La_2O_3 nanoparticles boosts the mechanical properties of the Sn3.0Ag0.5Cu (Sharma, et al., 2015). The dislocation reinforcement shearing was transferred to the dislocation reinforcement bypassing in that research as to enhance the strength. One more study by (Chen, et al., 2015) reported similar explanation of the impeding motion that improves the shear strength. In that research, the Bi_2Te_3 nanoparticles in the Sn3.0Ag0.5Cu solder matrix impedes the motion of dislocations during the shear test, and in addition, the refined Sn dendrites plays a part in improving the shear strength (Figure 2.33).

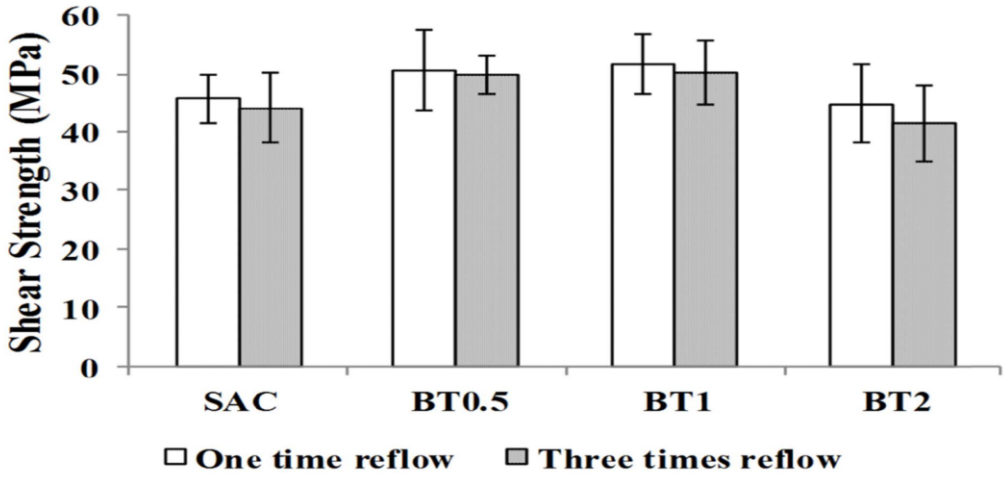

Figure 2. 33:Shear strength of Sn3.0Ag0.5Cu upon Bi_2Te_3 nanoparticles additions.

Relationship between the grain size and the mechanical strength is very evident when the GNS was added to the Sn58Bi solder (Ma, et al., 2017). Despite the similar observation of the grain refinement and the task of impeding the dislocation motion in the grain boundary, the lower CTE of the GNS (-8×10^{-9}/K) compared to the Sn58Bi (-15×10^{-6}/K) restricts the growth of the SnBi matrix, thus ensures smaller grains in the microstructure. (Shen, et al., 2017)

used the activation energy concept to produce comparable explanation on the grain refinement with Al_2O_3 nanoparticles in the Sn58Bi. The graph in Figure 2.34 displays the clear production of high shear strength of the Ni coated with Al_2O_3 nanoparticles in the Sn3.5Ag0.7Cu solder joint even after ageing time (K. Mehrabi, et al., 2016). This is because of the reduction of the growth kinetic of the IMC layer caused by the presence of the nanoparticles. The thinner IMC layer allows better durability of the solder joint. Using same context of the activation energy explanation, the mechanical properties (tensile creep) of the ZnO nanoparticles reinforced Sn3.0Ag0.5Cu was enhanced compared to the bare solder alloy. The activation energy in the ZnO reinforced solder was higher (53.1 kJ/mol) than the bare solder (50.5 kJ/mol). This proves that the production of finer grains to contributes to better mechanical strength. This was the investigation and discussion testified by (A.E Hammad & A.A. Ibrahiem, 2017). The 1.5 wt.% SiO_2 nanoparticles resisted the plastic deformation of the Sn0.7Cu solder and increases the UTS to 46.5 MPa, which was 38 % higher than the pure Sn0.7Cu, solder. (Fathian, et al., 2017) conducted this study and also mentioned that the high CTE differences were another key aspect in the increase in the strength.

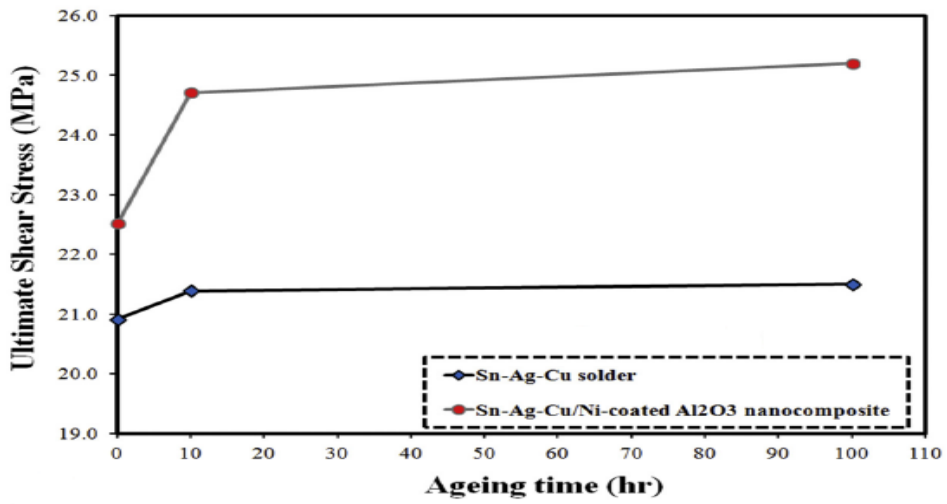

Figure 2. 34: Shear strength of Ni coated with Al_2O_3 nanoparticles in the Sn3.5Ag0.7Cu solder joint with ageing time.

Talking on the aspect of nanoparticles additions and its effect to the solder strength, the question on the sizes of the nanoparticle arises among few researches. The research completed by (Zhu, et al., 2018) solves this problem statement as one of the objectives differ the sizes of the CNT (10-20 nm, 40-60 nm and 60-100 nm) and investigate its influence on the mechanical strength of the Sn0.3Ag0.7Cu solder. The strength of the CNT doped solder was higher compared to the bare Sn0.3Ag0.7Cu. The difference here was that the CNT with the 40-60 nm sizes had higher strength compared to the other two sizes. The Zener relationship theory explains this with the smaller β-Sn produced as reason of the presence of the CNT (20-60 nm). In like manner, the 6 nm and 20 nm TiO_2 nanoparticles was added to the Sn1.0Ag0.5Cu solder alloy and the shear strength of the larger sized particles was lower (Wen, et al., 2017). Even after thermal cycles, the prior sized additions had higher strength compared to the 20 nm additions, shown in Figure 2.35. As explained earlier, higher surface tension with lesser solder/Cu interfacial tension is endured by the smaller sized particles than the larger nanoparticles (Gu, et al., 2015). For this reason, the 6 nm TiO_2

nanoparticles were seen easier to be absorbed on the solid surface to minimize the molten solder alloy's surface energy. By the same means, the smaller size Fe_2O_3 nanoparticles additions in the Sn1.0Ag0.5Cu solder alloy produced the high shear strength (Zhao, et al., 2016). The explanation replicates to the previous study stating that the smaller size particles had better effect to refine the grains which increases the grain boundary area and effectively impede the dislocation motion. The 20 nm sized Fe_2O_3 nanoparticles succeeded to produce the highest shear strength. (Li & Y.C Chan, 2015) tallied their discussion in the experiment involving different Ag nanoparticles size addition to the Sn58Bi solder.

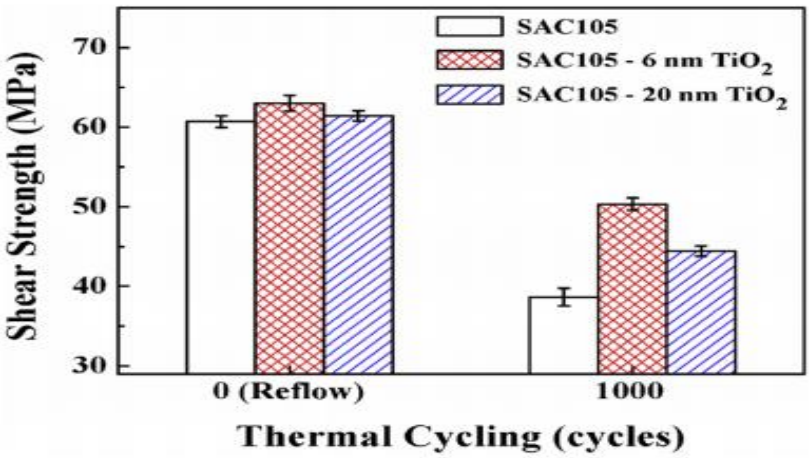

Figure 2. 35: Shear strength with different size TiO_2 additions in the Sn1.0Ag0.5Cu solder alloy upon reflow and 1000 cycles (Wen, et al., 2017).

2.7 Summary

The literature review provided discussion on the current studies that conducted with reinforcements of nanoparticles. Nevertheless, there are few research gaps that occurs observed. Firstly, most studies reinforced

nanoparticles to the high melting temperature SnAgCu and other solder alloy with melting temperature above 200 °C. Not many have made such studies on the low melting temperature solder alloys. Secondly, studies on the properties of the nanoparticles added to low temperature solder alloys are limited, for example, the GNS nanoparticles were added to the Sn58Bi solder to investigate the shear properties but no other properties like IMC layer thickness (Ma, et al., 2017). These two concerns are obviously seen to be a research gap in the nanoparticle's reinforcement study towards solder alloys.

This research opts to close these research gaps by studying the effect to the properties of the Sn58Bi solder alloy reinforced with Mo and ZrO_2 nanoparticles with different percentages of additions. These two nanoparticles were chosen because of their high melting point. The analyzation of the properties will provide sufficient fundamental knowledge on the low temperature solder alloy. Nanoparticles reinforcement will provide lesser mass and density to the solder alloy and at the same time will tweak the properties without effecting the low temperature of Sn58Bi solder.

CHAPTER 3

METHODOLOGY

In the research, lead free solder alloy of Sn58Bi (SB) will be reinforced with Mo nanoparticles (Sigma Aldrich 99.9 % purity) and ZrO_2 (Sigma Aldrich 99.9 % purity) nanoparticles separately. The SB solder alloys are reinforced with the nanoparticles of Mo and ZrO_2 distinctively by a mechanical mixing method. The SB solder alloy will be added with 1, 2 and 3 weight % of Mo and ZrO_2 nanoparticles separately. These solder alloys will be investigated based on the thermal, microstructural and mechanical properties as part of the objectives. Flow chart of the research is shown in Figure 3.1.

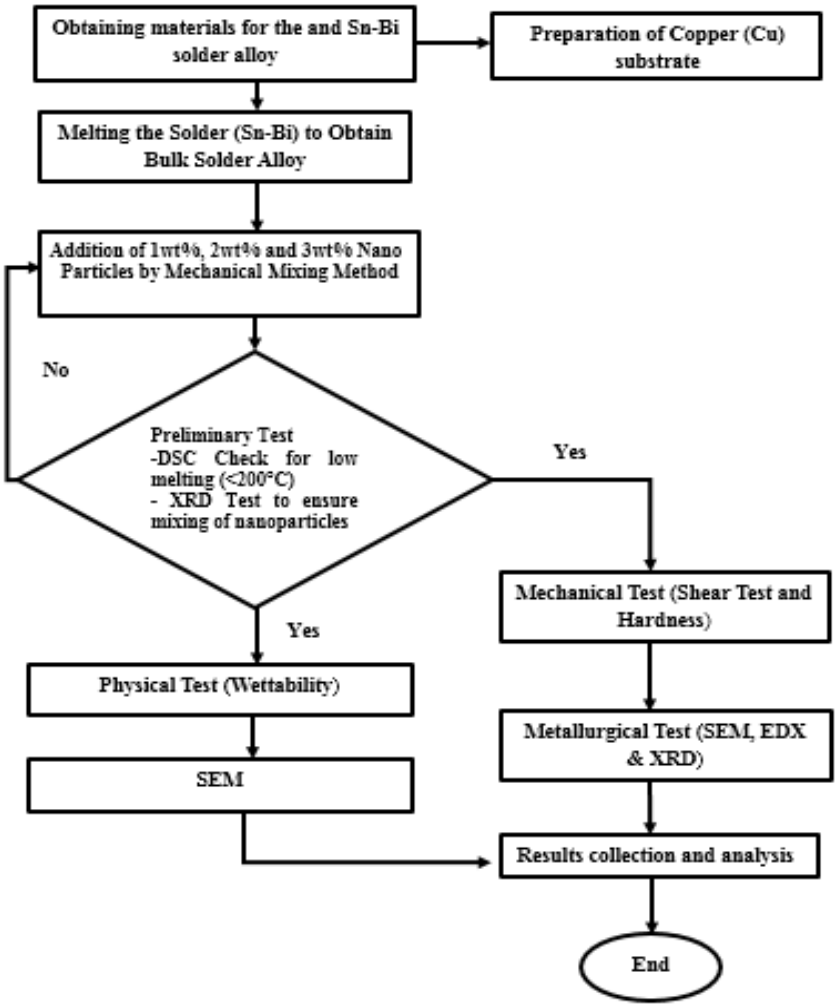

Figure 3. 1: Flow chart of the project.

3.1 Solder Alloy Preparation

Initial step involves the development of the bare solder alloy. The Sn and Bi were weighed according to the eutectic composition of 42 % Sn and 58 % Bi with a 20 g overall composition. After weighing, the Sn and Bi were put in an alumina crucible separately to be melted. The melting of the elements was conducted using a heat treatment furnace with constant temperature of 600 °C during the melting of these elements. The holding time was maintained for one and half-hour to ensure proper melting and a homogenous mixing of the

elements. Then, another six sets of SB added with (1, 2 and 3 % nanoparticles of Mo and ZrO_2) separately are melted with the same procedure. The mass composition of these percentages of additions was done by using Equation 3.1. Based on thorough research, there are no optimal amount for choosing the percentage of additions. Though, most literature provided range of 1 % in between two percentages of additions. This range of percentage difference (1 %) is predicted to give distinct effect to the properties. Collected literature have shown negative result with percentages of additions more than 3 % provided. This was taken as the guideline in this study to choose the percentage of additions as mentioned. Figure 3.2 and Table 3.1 shows the total samples and composition of the elements and nanoparticles in the solder alloys prepared in this project.

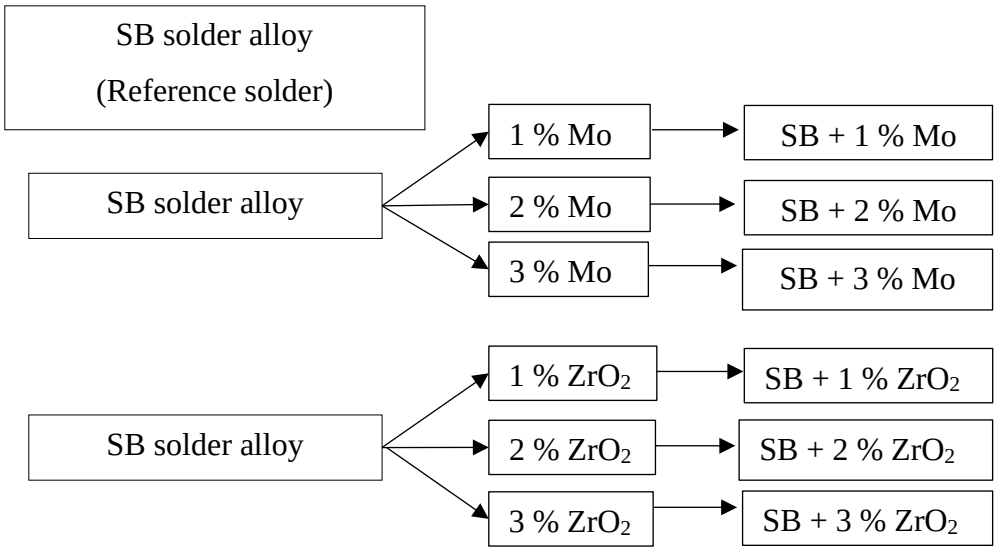

Figure 3. 2: SB solder alloy (base solder) and nanoparticles added SB solder alloy.

A simple weight calculation as in Equation 3.1 (G. Rethwisch, 2007) was used to find the weight of the nanoparticle's additions.

$$C = \frac{m_1}{M} \times 100 \qquad \text{(Equation 3.1),}$$

C = weight concentrations of nanoparticles, m_1 = weight of nanoparticles, M = total weight of solder alloy (20 g)

Table 3. 1: Weight composition of the tin, bismuth, Mo and ZrO_2 nanoparticles.

Solder Alloy (20 g) / Elements/ Nanoparticles	**Sn**	**Bi**	**1% Mo**	**2% Mo**	**3% Mo**	**1% ZrO_2**	**2% ZrO_2**	**3% ZrO_2**
SB								
SB + Mo	8.4 g	11.6 g	0.2 g	0.4 g	0.6 g			
SB + ZrO_2						0.2 g	0.4 g	0.6 g

3.2 Particles Size Measurement

The particles size of the Mo and ZrO_2 measured with the aid of the measuring tools from the SEM image. The measurement was done by taking the two different images of × 50000 and × 60000 magnifications for both nanoparticles. The image is shown in Chapter 4 captioned Figure 4.1 for the Mo and Figure 4.2 for the ZrO_2 nanoparticles to link the result and discussion part.

3.3 Re-melting and Stirring of Solder Alloys

Once all the SB, SB + Mo and SB + ZrO_2 had been mixed in the furnace, these solder alloys are re-melted on hotplate at 350 °C as illustrated in Figure 3.3 (a). The re-melting was done to ensure the nanoparticles are again mixed well in the molten solder alloy. Stirring at 100 rpm was done for 15 minutes to further ensure the mixing of the nanoparticles to the molten solder alloy. During the re-melting process, the crucible was covered with a custom-made alumina foil enclosure shown in Figure 3.2 (a) to avoid oxidation. The molten solder alloys were then poured on to ceramic plate and let to solidify in the room temperature, to imitate the real-life cooling temperature. The solidified solder alloys shown in Figure 3.2 (b) were hot pressed to obtain a 1 mm thickness as shown in Figure 3.2 (c). This 1 mm thick solder alloys were then punched to form billets with 5 mm diameter as shown in Figure 3.2 (d). This small size preparation allows less consumption of solder alloy and avoid wastage of materials. At the same time, the less composition will replicate the less volume of solder used in the microelectronic packaging industry.

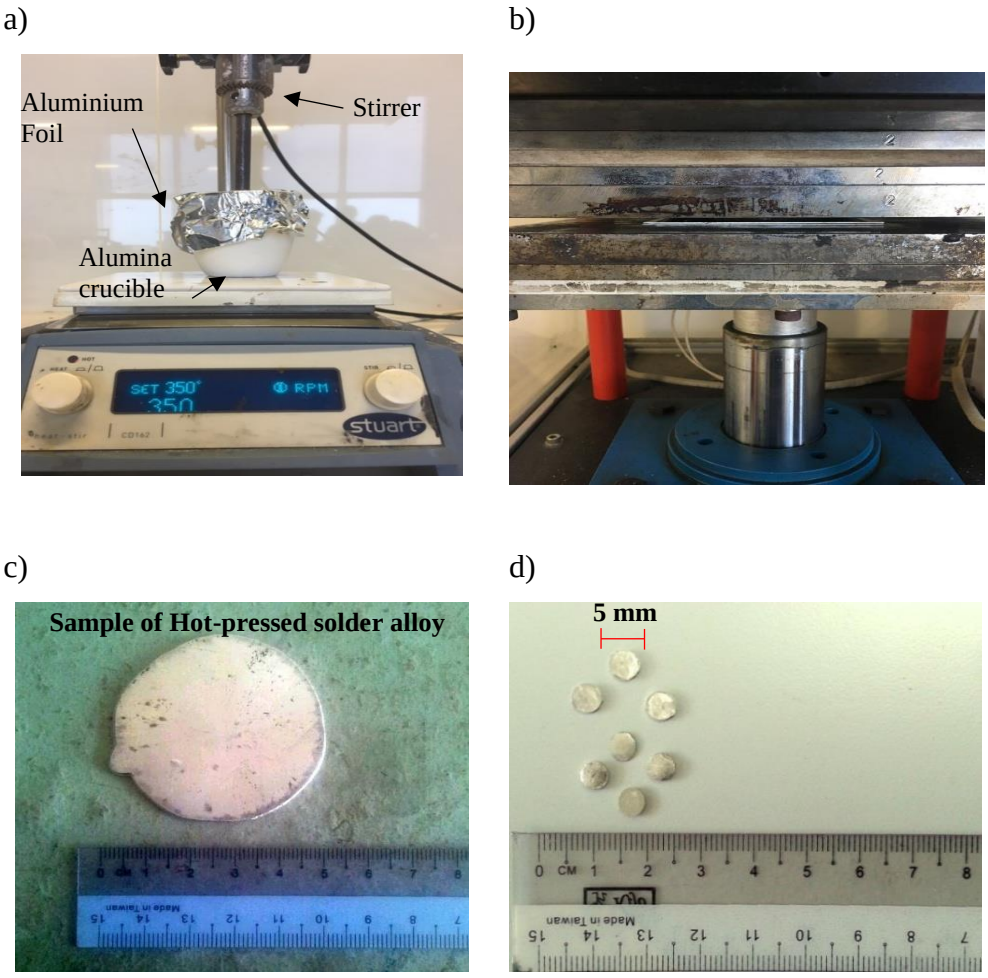

Figure 3. 3: a) Re-melting process, b) hot press machine, c) sample after hot pressed and d) billet preparation.

3.4 Polishing and Etching Process of Solder Alloys

The billets of the reference SB solder and the SB reinforced with nanoparticles solder alloys are polished using the polishing/grinding machine (Metkon Forcipol 2V). The solder alloy billets are polished using the finest polishing pad. The nanopolish of alumina with the diamond polycrystalline solutions were applied during the polishing process onto the polishing pad to create a better polished surface. Then, etching was done by dipping the samples in the FeCl for 10 seconds and then flushed with distilled water immediately. The reason for this is to extract the microstructure of the solder alloy for SEM

imaging. The equipment for the polishing and etching procedure are shown in Figure 3.4.

a)

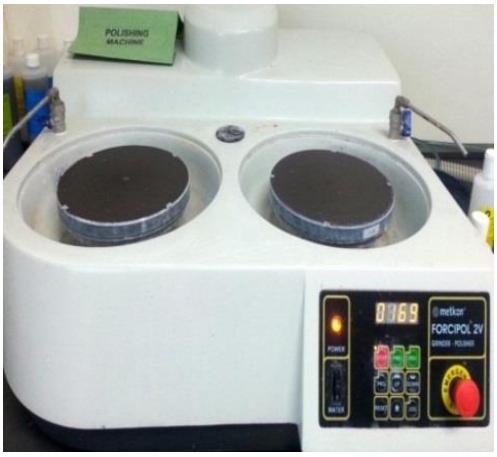

The polishing machine used to polish the billets. The slow speed of rotation is kept constant to produce an even polishing surface. Grinding was not conducted to avoid removal of the nanoparticles on the surface of the billet.

b)

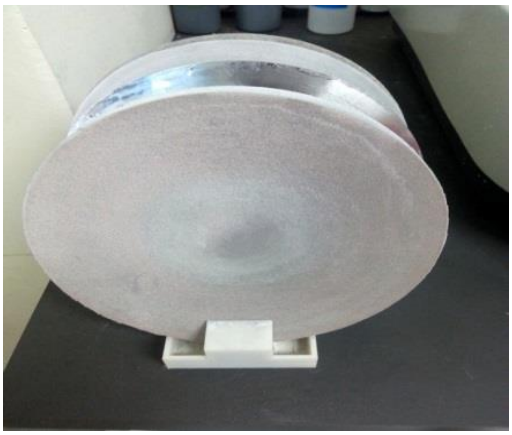

Polishing pad of 0.05 µm to the solder billets. It is also to give much finer surface for the better microstructure analyses.

c)

Alumina nanopolish and the diamond polycrystalline solution applied to the polishing pad to create a better shiny surface of the billets.

Figure 3. 4: Equipment used for polishing and etching process.

3.5 Thermal Properties Test of Solder Alloys

The DSC test was conducted to study the thermal properties of the reference SB and SB solder alloy reinforced with nanoparticles. The DSC curve provides the quantity of heat required to either absorb (endothermic) or release (exothermic) by the solder alloy undergoing the enthalpy changes at a constant pressure. Nitrogen gas was used as the atmospheric medium for all the DSC tests to make sure no contamination and external activity to the solder alloy during the process. The DSC curve is represented by the heat flow (y-axis) and temperature (x-axis) that relates to the energy released/absorbed at a certain temperature. The heat flow for all solder alloys was kept at 20.00 °C/min with temperature range from 100 °C to 300 °C. Both the heating and cooling curve (Figure 3.5) was analysed to provide proper discussion on the thermal properties. The DSC machine and sample preparation are shown in Figure 3.6. The mass for the sample of solder are shown in Table 3.2.

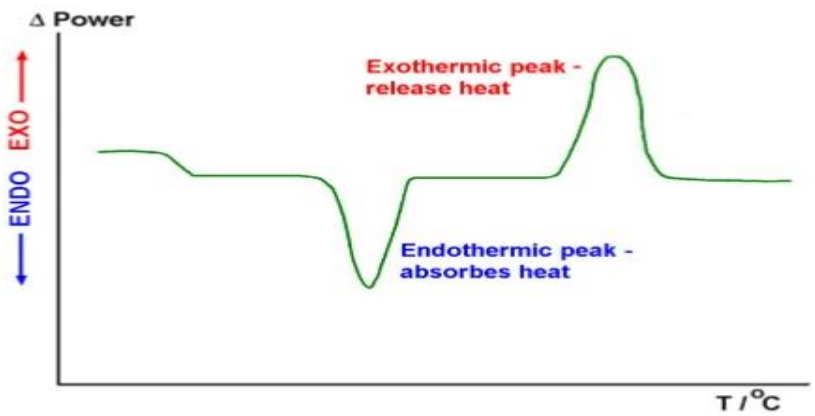

Figure 3. 5: Typical heating and cooling curve of a substance.

a) b)

Figure 3. 6: a) Sample preparation/aluminium holder to place the solder and b) DSC machine

Table 3. 2: Mass of samples for DSC testing.

Samples	Mass (mg)
SB	25.45
SB + 1 % Mo	23.39
SB + 2 % Mo	14.71
SB + 3 % Mo	14.18
SB + 1 % ZrO_2	25.09
SB + 2 % ZrO_2	4.23
SB + 3 % ZrO_2	36.53

Table 3. 3: T-Test for two samples variance using the onset and endset temperatures for a) SB + 3%Mo and b) SB solder alloys.

a)

t-Test: Two-Sample Assuming Unequal Variances	SB + 3%Mo	
	Onset Temperature	**Endset Temperature**
Mean	141.79	150.844
Variance	0.5101	6.93883
Observations	5	5
Hypothesized Mean Difference	0	
df	5	
t Stat	-7.417858519	
P(T<=t) one-tail	0.000350613	
t Critical one-tail	2.015048373	
P(T<=t) two-tail	0.000701226	
t Critical two-tail	2.570581836	

b)

t-Test: Two-Sample Assuming Unequal Variances	SB	
	Onset Temperature	**Endset Temperature**
Mean	141.782	148.138
Variance	1.61272	19.69027
Observations	5	5
Hypothesized Mean Difference	0	
df	5	
t Stat	-3.079275942	
P(T<=t) one-tail	0.013746124	
t Critical one-tail	2.015048373	
P(T<=t) two-tail	0.027492247	
t Critical two-tail	2.570581836	

The T-Test based on the melting temperature was conducted on the SB and the SB + 3 % Mo nanoparticles solder to confirm the statistical difference of the solder alloys. The statistics were shown in Table 3.3 (a) and (b). The values of P = 0.000701226 (SB + 3% Mo) and P = 0.027492247 (SB) are less than 0.05, stating the rejection of null hypothesis and conclude that both samples and the other samples to be statically different. This statistic result also acts as the preliminary test to ensure that the nanoparticles are producing different result in the testing.

3.6 Microstructural and Intermetallic Compound Layer Characterization of Solder Alloys

The SEM, EDX and XRD tests was conducted to analyse the microstructure and the interfacial property of the solder alloys. The microstructure property focuses on the solder sides' property of the SB, SB added with Mo and ZrO_2 nanoparticles. Magnifications up to × 5000 is used to study the microstructure of the solder alloy. Together, the EDX test was conducted to study the element presented in the solder alloy. The XRD test was

added as part of the testing parameter to confirm the phases and element presented in the solder alloy. These tests were also set as the preliminary test to ensure the mixing of the nanoparticles in the SB solder alloy. The Bi size area was measured using the Digimizer software to analyse the effect of nanoparticles towards the solder's microstructural aspect.

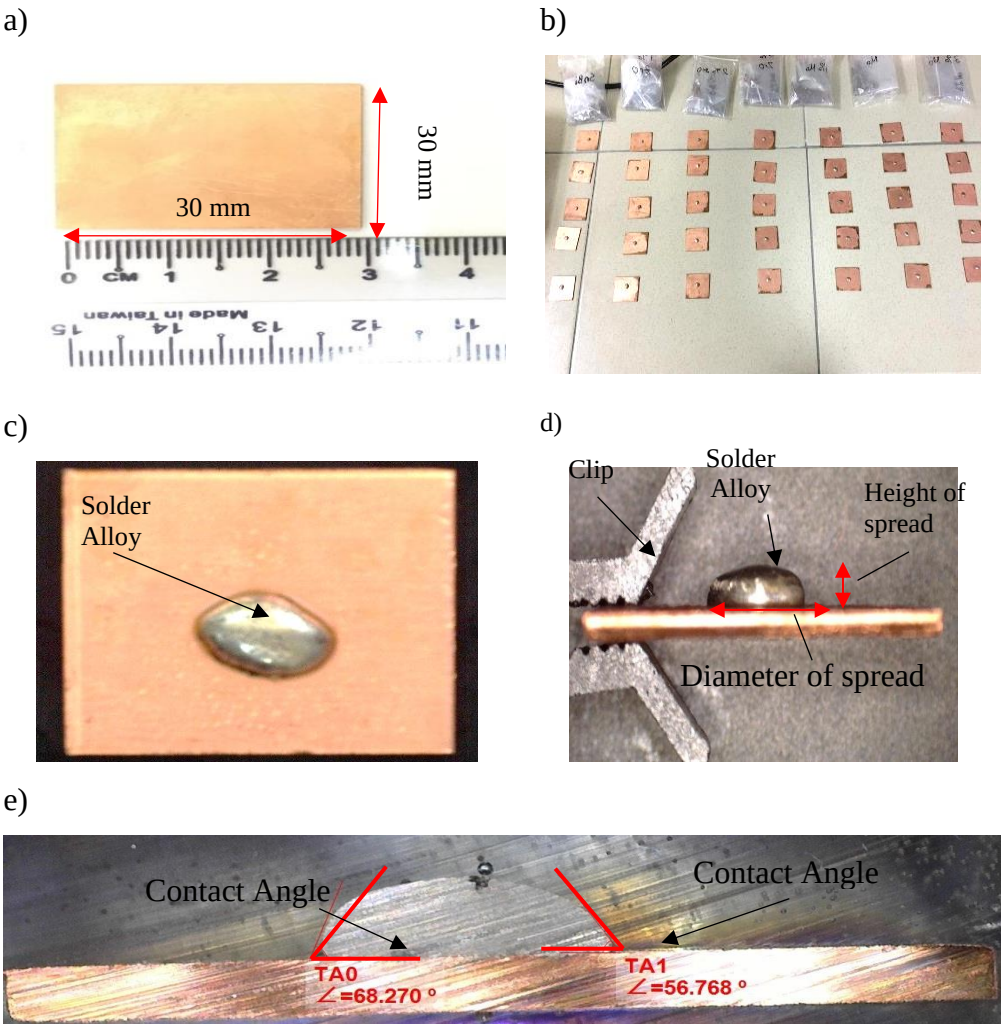

Figure 3. 7: a) Copper Substrate specimen, b) soldered samples, c) solder on the copper substrate (top view), d) side view and e) cross section of solder joint.

The SEM, EDX and XRD test was used to analyse the interfacial property at the solder joint as well. The interfacial property provides the information on the IMC's at the IMC layer. At the same time, the IMC layer thicknesses were measured using the measurement tools from the SEM. The XRD test for all the solders investigates the phase formation with the CuKα radiation at an angle of diffraction of 20 - 80 ° and a scan range of 2 min/°. The epoxy mounted cross section samples in Figure 3.7 was used as the sample for the interfacial analyses. The pure nanoparticles powder of Mo and ZrO_2 was also analysed using the XRD to obtain the peak and diffraction angle to be compared with the reinforced solder alloy. The SEM and XRD machine shown in Figure 3.8.

a) b)

Figure 3. 8: a) SEM machine (S3400N HITACHI)) and b) XRD machine (XRD 6000 SHIMADZU).

3.7 Vickers Microhardness Test of Solder Alloys

The hardness test is conducted to study the strength of the solder alloy using the Vickers microhardness tester (Figure 3.9). The Vickers microhardness test was performed on the solder billets with indentation at five different points, Figure 3.9 (a). Equation 3.1 was used to calculate the Vickers microhardness value. The load applied is low that it replicates a slow deformation process, typically taking place in the microelectronic devices. A load of 1 kgf was applied to all solder billets with a dwelling time of 15 seconds. The Fisher Statistical-Test is conducted to statistically confirm the difference of the SB, SB + Mo and SB + ZrO_2 solder alloy. The hardness sample of SB and SB + 3 % Mo was used to conduct the analyses. To clarify the statistical difference of these samples, the raw data of D_1 and D_2 representing the diagonal diameters was tested with the Fisher Statistical-Test. The two variances (Variance 1: SB and Variance 2: SB + 3 % Mo) was taken to validate the hypothesis. The calculated F value (F = 0.709652224) was larger than the critical F value ($F_{Critical}$ = 0.314574906) stating that the null hypothesis can be rejected. This statistic results are shown in Table 3.4. This result validates the statistical difference between the SB and SB + 3 % Mo solder alloy, that then confirms that all samples are statistically different.

$$HV = 1.854(F/D^2) \qquad \text{(Equation 3.1)}$$

HV = Vickers Hardness Number, F = Indentation Force (1 kgf : 9.81 N), D = Average diagonal diameter ($\frac{D1+D2}{2}$).

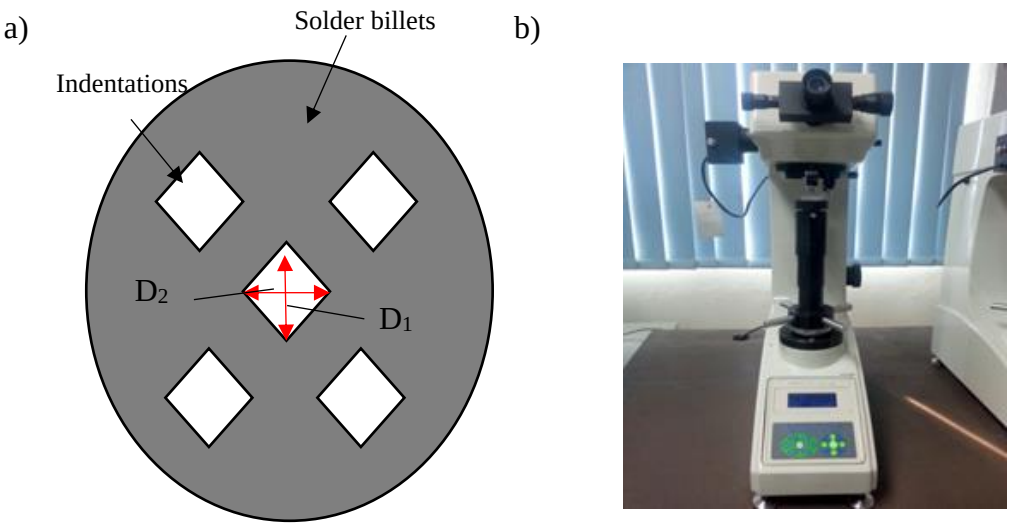

Figure 3. 9: a) Indentation spot on the solder alloy and b) Vickers microhardness machine.

Table 3. 4: F-Test for two samples variance using diameter of indentations.

	D1	**D2**
Mean	80.122	79.505
Variance	5.869395556	8.270805556
Observations	10	10
Df	9	9
F	0.709652224	
P(F<=f) one-tail	0.308811638	
F Critical one-tail	0.314574906	

3.8 Shear Stress Test of Solder Alloy Joints

The solder billets were soldered on Cu substrate at 230 °C for 60 seconds, which follows the recommended specification of the soldering temperature in the electronic industry. A single shear lap test, Figure 3.10 was chosen as the test method based on the ASTMD1002 specification for mechanical testing of alloys. The crosshead speed of 1.3 mm/min was used to duplicate the slow failure that usually occurs in the actual electronic assemblies. This is also the recommended speed stated in the ASTMD1002 standard. The

specimen for the shear stress test, equipment and the process are shown in Figure 3.10. The soldered area was 5 ×10 mm and the Cu substrate's dimension is 40 × 10 × 1 mm. The shear test specimens were prepared as in Figure 3.10 (a). These specimens were inserted in the furnace for the soldering process. This process is to allow soldering without exposing the specimen to the room atmosphere. After the soldering, the samples were cleaned using the ultrasonic (10 minutes) machine with ethanol and water to remove dirt and debris. Five samples from each solder alloy were tested using the Universal Testing Machine (Instron 5582Q4970), Figure 3.10. Maximum shear strength (MPa) and the maximum load (kN) at break was calculated to discuss the shear stress of the solder joint.

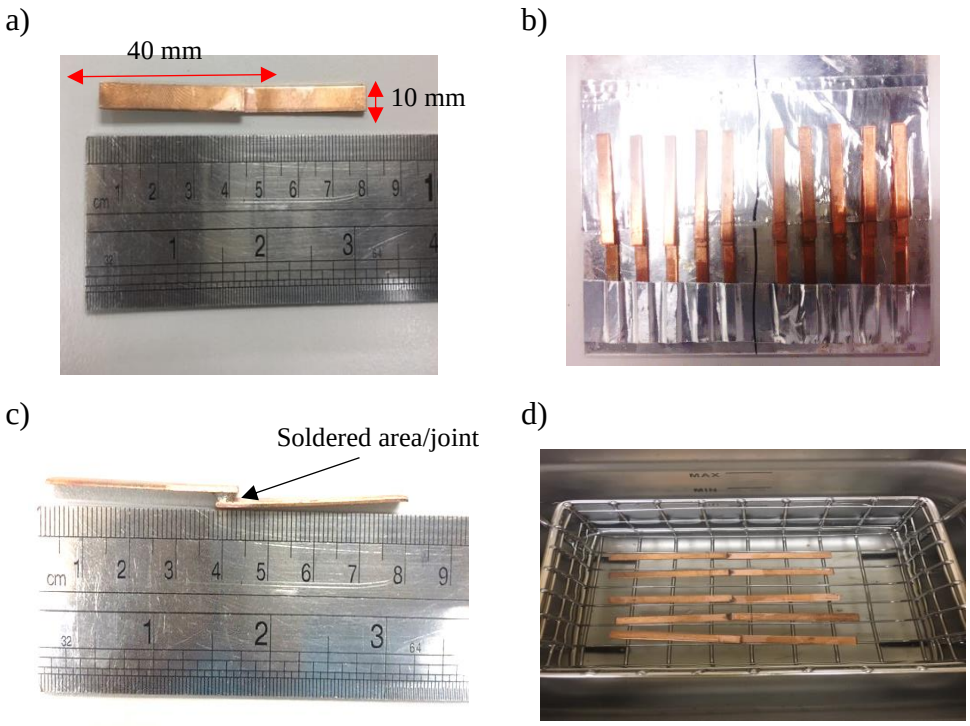

e) f)

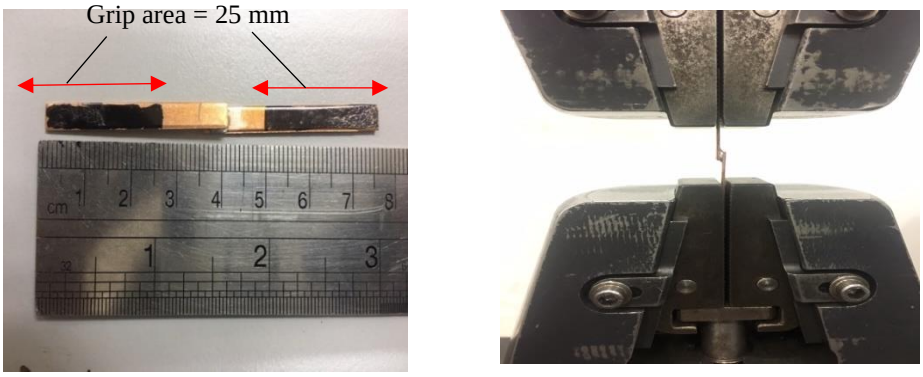

Figure 3. 10: a) Single shear lap specimen before soldering, b) arrangement of samples prior soldering, c) shear lap specimen after soldering d) shear lap specimen cleaning with ultrasonic machine, e) shear lap specimen prior testing and f) shear test using universal tensile machine.

3.9 Spreading Test of Solder Alloys

The spreading test was based on the contact angle, spreading area and spreading ratio between the solder and Cu substrate. All solders were soldered onto the Cu substrate at 230 °C as this temperature serves as the reflow temperature. The reflow temperature was decided to be 230 °C as the usual soldering temperature at the industry is as of 230 °C - 250 °C. The soldering process was done using the furnace and the specimen was let to solidify under room temperature. Prior to the soldering, the zinc chloride (ZnCl) flux was applied on the copper substrate to avoid oxidation and enable better bonding. The copper substrate was cut into 30 mm × 30 mm dimension. After completing the soldering process, the specimens were cleaned to remove excessive flux. All the sample's spreading area and spreading ratio was measured before the samples are mounted using an epoxy resin and hardener. The spreading ratio is calculated using equation 3.2. These mounted samples were cross sectioned and

the contact angle were measured using the VIS Pro software incorporated in the optical microscope. Figure 3.11 (a) and (b) shows the spreading tests samples.

Spreading ratio = $\frac{D-H}{D} \times 100\%$ (Equation 3.2)

D = diameter of spread (mm), Height of spread (mm)

a)

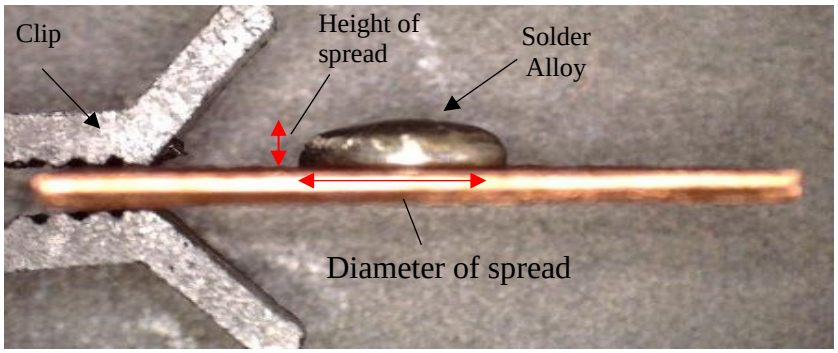

b)

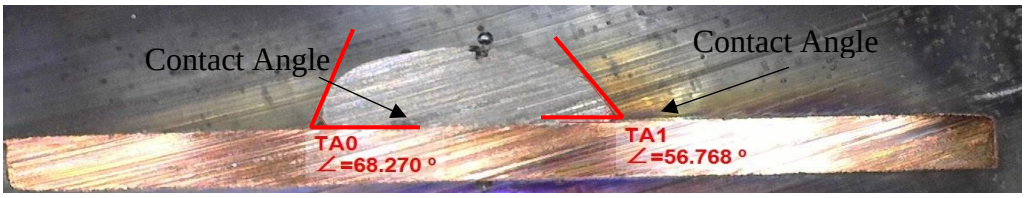

Figure 3.11: Spreading tests specimens.

3.9 Overall List of Test Specimens

SEM/EDX/XRD Analyses
- Particles Size

- Mo Nanoparticles
- ZrO_2 Nanoparticles

DSC Test
- Melting Properties

- SB Solder Alloy
- SB + 1 % Mo Solder Alloy
- SB + 2 % Mo Solder Alloy
- SB + 3 % Mo Solder Alloy
- SB + 1 % ZrO_2 Solder Alloy
- SB + 2 % ZrO_2 Solder Alloy
- SB + 3 % ZrO_2 Solder Alloy

Spreading Test
- Contact Angle
- Spreading Area
- Spreading Ratio

- SB Solder Alloy/Cu joint
- SB + 1 % Mo Solder Alloy/Cu joint
- SB + 2 % Mo Solder Alloy/Cu joint
- SB + 3 % Mo Solder Alloy/Cu joint
- SB + 1 % ZrO_2 Solder Alloy/Cu joint
- SB + 2 % ZrO_2 Solder Alloy/Cu joint
- SB + 3 % ZrO_2 Solder Alloy/Cu joint

SEM/EDX/XRD Analyses
- Microstructure (Elements)
- Bi grain size area

- SB Solder Alloy
- SB + 1 % Mo Solder Alloy
- SB + 2 % Mo Solder Alloy
- SB + 3 % Mo Solder Alloy
- SB + 1 % ZrO_2 Solder Alloy
- SB + 2 % ZrO_2 Solder Alloy
- SB + 3 % ZrO_2 Solder Alloy

SEM/EDX/XRD Analyses
- Interfacial properties (Elements and phases)
- IMC layer thickness

- SB Solder Alloy/Cu joint
- SB + 1 % Mo Solder Alloy/Cu joint
- SB + 2 % Mo Solder Alloy/Cu joint
- SB + 3 % Mo Solder Alloy/Cu joint
- SB + 1 % ZrO_2 Solder Alloy/Cu joint
- SB + 2 % ZrO_2 Solder Alloy/Cu joint
- SB + 3 % ZrO_2 Solder Alloy/Cu joint

Hardness Test

- Microhardness value

- SB Solder Alloy
- SB + 1 % Mo Solder Alloy
- SB + 2 % Mo Solder Alloy
- SB + 3 % Mo Solder Alloy
- SB + 1 % ZrO_2 Solder Alloy
- SB + 2 % ZrO_2 Solder Alloy
- SB + 3 % ZrO_2 Solder Alloy

Shear Test

- Maximum Shear Stress
- Maximum load

- SB Solder Alloy/Cu joint
- SB + 1 % Mo Solder Alloy/Cu joint
- SB + 2 % Mo Solder Alloy/Cu joint
- SB + 3 %Mo Solder Alloy/Cu joint
- SB + 1 % ZrO_2 Solder Alloy/Cu joint
- SB + 2 % ZrO_2 Solder Alloy/Cu joint
- SB + 3 % ZrO_2 Solder Alloy/Cu joint

Figure 3.12: List of test and samples used for the test.

Overall, the list of tests and samples are shown in Figure 3.12. All the results from the tests are collected and analysed without any alteration. The results are based on experimental testing and all the test are carefully conducted to avoid any human error. The results are taken in term of average of many samples in order to provide sound results to be discussed. The shear tests are conducted based on ASTM standard to produce a genuine result. Chapter 4 compiles and discusses all the result from the experimental test.

CHAPTER 4

RESULTS AND DISCUSSIONS

4.1 Nanoparticles Size and Diffraction Angle (2Ɵ) of Molybdenum (Mo) and Zirconia (ZrO_2) Nanoparticles

Image of the dispersed Mo and ZrO_2 nanoparticles are shown in Figure 4.1 and Figure 4.2 respectively. The sizes of the Mo nanoparticles range between 30-60 nm with an average size of 48.5 nm. The ZrO_2 nanoparticle's size ranges between 20-40 nm with the average size of 29 nm. These sizes were measured by observing the high magnification FESEM images and the average size measured from random particles.

a) b)

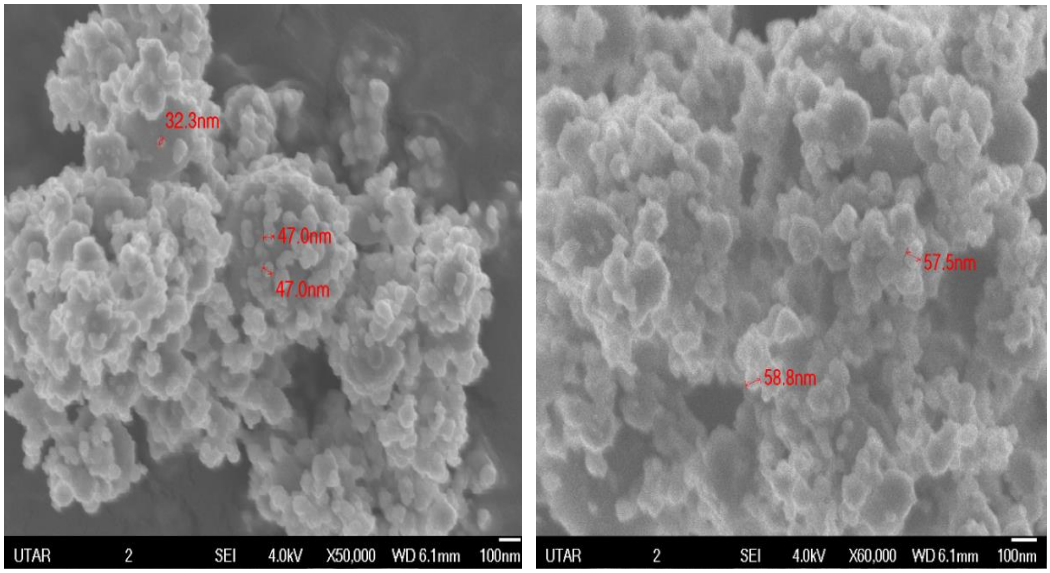

Figure 4. 1: Mo nanoparticles size a) × 50000 and b) × 60000 magnifications.

a) b)

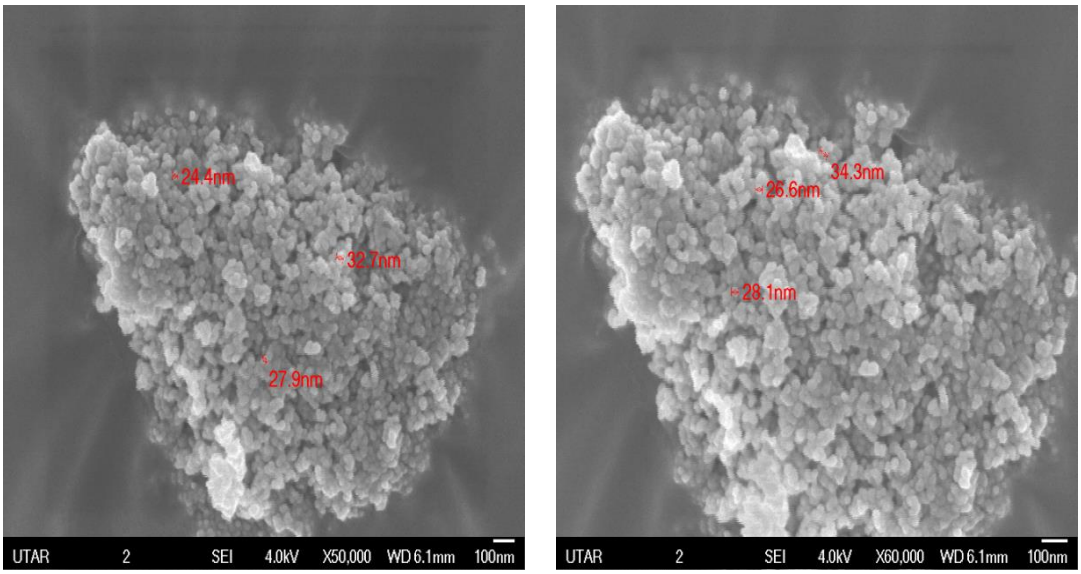

Figure 4.2: ZrO_2 nanoparticles size a) × 50000 and b) × 60000 magnifications.

The strongest peaks in the XRD for Mo nanoparticles were observed at 2Θ = 40.5494 °, 58.668 ° and 73.7225 ° (Figure 4.3). The strongest peaks were noted at 2Θ = 31.5000 °, 45.5200 °, and 62.9200 ° for the ZrO_2 nanoparticles (Figure 4.4). These XRD peaks are taken as a reference to detect the presence of these particles after adding into the SB solder alloy.

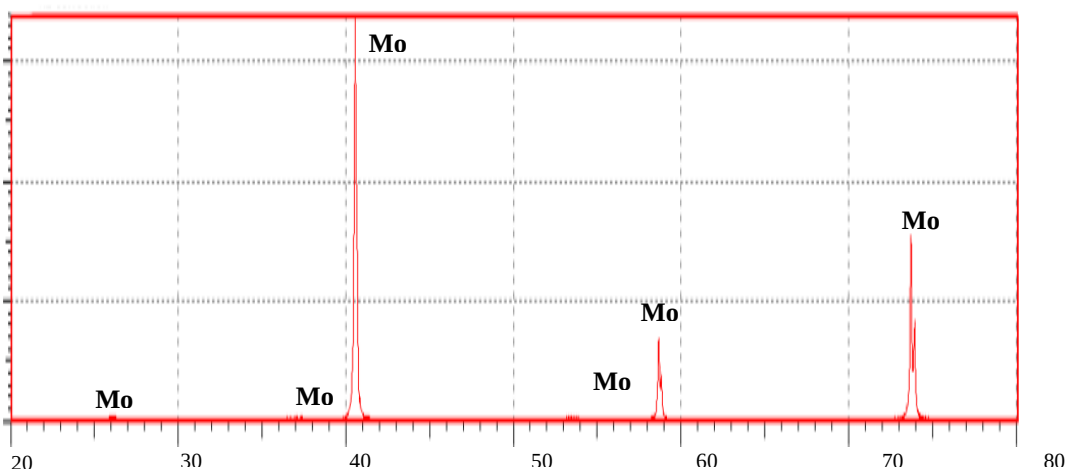

Figure 4. 3: XRD of Mo nanoparticles.

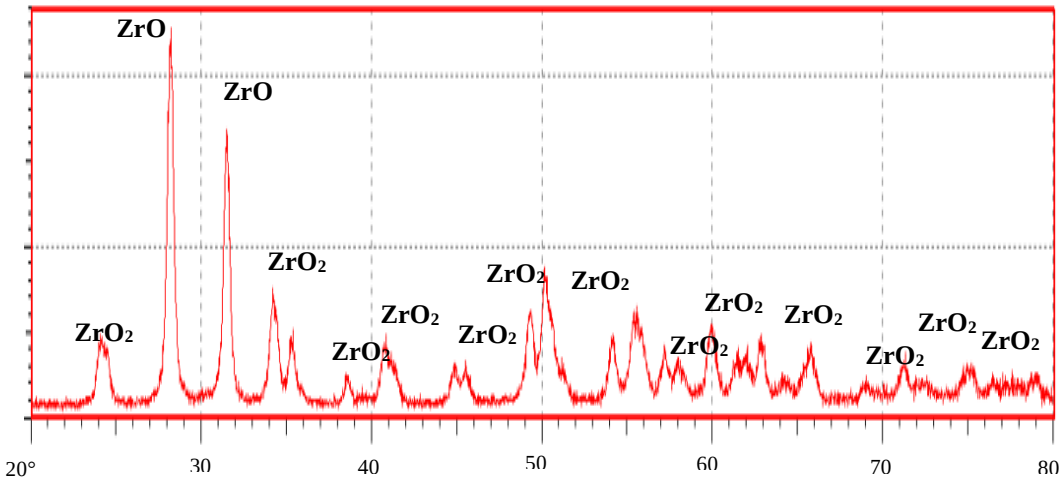

Figure 4. 4: XRD of ZrO_2 nanoparticles.

4.2 Characterization of Thermal Properties of SnBi, SnBi (with Mo Nanoparticles) and SnBi (with ZrO_2 Nanoparticles) Solder.

The thermal properties of the SB, SB + Mo and SB + ZrO_2 nanoparticles solder alloys are listed in Table 4.1. The solder alloy's thermal properties were evaluated based on both endothermic and exothermic curves that provide the peak temperature, solidus temperature (T_S) and liquidus temperature (T_L). The T_S is the melting temperature of the solder alloy.

Table 4. 1: Thermal properties of SB, SB + Mo nanoparticles and SB + ZrO_2 nanoparticles solder alloys.

Solder	Temperature(°C)				
	Solidus	**Peak**	**Liquidus**	**Undercooling**	**Pasty Range**
SB	142.30	144.83	146.35	16.51	4.05
SB + 1 % Mo	145.93	148.50	149.70	14.95	3.77
SB + 2 % Mo	139.73	148.00	149.62	19.27	9.89
SB + 3 % Mo	140.62	148.67	150.35	10.30	8.05
SB + 1 % ZrO_2	145.11	147.33	148.82	19.2	3.71
SB + 2 % ZrO_2	140.89	144.00	145.15	14.97	4.26
SB + 3 % ZrO_2	143.84	146.00	147.44	17.86	3.6

The additions of Mo and ZrO_2 nanoparticles to the SB solder alloys showed mixed trend to the melting temperature. The 2 % Mo added solder alloy produced the lowest melting temperature of 139.73 °C followed by the 3 % Mo additions of 140.62 °C and the 1 Mo % additions of 145.93 °C. The 2 % and 3 % Mo added SB solder alloys had lower melting temperature than the SB solder alloy. The pasty range for the 1 % and 3 % Mo added solder alloy was lower than the 2 % Mo added SB solder. This observation shows that the 1 % and 3 % Mo added solder alloy existed in the molten form for a shorter time compared to the 2 % additions, which will influence the microstructure formation. This is because of the proper segregation of these nanoparticles that makes the solder to melt later but solidify earlier.

Observed upon the ZrO_2 nanoparticles additions, the 2 % additions produced the lowest melting temperature of 140.89 °C compared to the other two percentages of additions and the SB solder alloy. The solder remains in the molten form of liquid and solid longer and only fully melts at 145.15 °C, thus

producing a larger pasty range. Meanwhile, the highest melting temperature of 145.11 °C was produced by the 1 % ZrO_2 added SB solder alloy. The solder fully melts at 148.82 °C but was noticed to melt quicker than the SB solder alloy. The 3 % ZrO_2 added SB solder alloy starts to melt at 143.84 °C and fully melts at 147.44 °C. The smaller sized ZrO_2 produced local dissolutions by increasing the melting temperature but has quicker solidification compared to the Mo additions.

In analysing the thermal properties of any solder alloys, important concerns are given to the melting temperature and the pasty range. Melting temperature of a newly developed solder alloys are usually compared with the traditional SnPb solder. The melting temperature of the SnPb solder is 183 °C. In this study, the ZrO_2 nanoparticles added solder alloy's melting temperatures are much lower, especially for the 2 % additions. Reduction in melting temperature was also seen for the Mo added solder alloys. Together, the pasty ranges for both nanoparticles added solder alloys were within 1-5 °C (except for 2 and 3 % Mo additions), which is considered a short range. This range allows for better microstructure formation. In a study conducted by (Xing, et al., 2015), the SnZnBi/Cu solder produces a pasty range of 6.8 °C that refined the microstructures. Here, the highest pasty range was measured only to be 4.26 °C for the 2 % ZrO_2 additions. So, refinement of microstructures could be inevitable. A narrow pasty range is important in allowing the solder to exist as liquid in a short time of period and promotes for a smaller grain production upon solidification (R. Kotadia, et al., 2014). Adding to that, such characteristic avoids any ripping of the solder at high temperatures (Xing, et al., 2015). The

larger sized Mo nanoparticles depends more on proper segregation to produce low pasty range, while smaller sized ZrO_2 nanoparticles did not endure such dependency to produce smaller pasty range. Proper segregation enables the molten solder to melt later but solidify quicker to enable better microstructure production.

The SB solder alloy's thermal properties serve as the benchmark for these Mo and ZrO_2 nanoparticles added solders. As stated, the 2 % ZrO_2 and 2 % Mo nanoparticles added solder produced the lowest melting temperature. The explanation for the temperature decrease of the 2 % ZrO_2 and 2 % Mo added SB solders are related to the vast presence of these nanoparticles that possess higher surface energy that can achieve up to 2830 mJ/m^2 for Mo (E.N. Hodkin, et al., 1970) and 3058 mJ/m^2 for ZrO_2 (Z. Moser, et al., 2001). High energy will increase the surface instability of the molten SB solder alloy that will decrease the melting temperature. The highest melting temperatures were produced by the 1 % ZrO_2 and 1 % Mo added solder alloys. The 1 % additions for both nanoparticles had the same mass quantity of 0.2 g which is also the reason for this similar trend. Increase in the melting temperature is also related to the physical characteristics of the ZrO_2 nanoparticles as an oxide element. The ZrO_2 nanoparticles could absorb thermal energy during the melting process, hence, slightly increasing the temperature. Research conducted by (S.Chellvarajoo, et al., 2015) stated a similar reason with additions of Fe_2NiO_4 nanoparticles to Sn3Ag0.5Cu solder. Apart from that, the ZrO_2 nanoparticles affect the melt undercooling before the molten solder solidifies and contributed as another factor to the increase in the temperature. Quite clearly, there was a mixed trend

in the melting temperature results upon additions of nanoparticles. This trend is found by other studies too (Jung, et al., 2018; Chellvarajoo, et al., 2015). The additions of Al_2O_3 nanoparticles in the Sn9Zn solder decreased the melting temperature of the Sn9Zn by ~ 1 °C (Xing, et al., 2017). In a different study, Al_2O_3 additions to the Sn58Bi had an increase of ~ 3 °C compared to the bare Sn58Bi solder alloy (Singh, et al., 2017). Many other studies correspondingly contributed to similar findings (Salleh, et al., 2017; Z.L. Li, et al., 2016). Besides, the melting properties of solders are a natural property of a material and is influenced by the interatomic spacing. Additions of any nano-sized materials will not affect the melting properties unless larger-sized alloying element are added (Kanlayasiri & Meesathien, 2018).

It is important to note here with these Mo and ZrO_2 additions to the SB solder alloy, there will be no need for any alteration to the current soldering temperature.

4.3 Characterization of Microstructural Properties of SnBi, SnBi (with Mo Nanoparticles) and SnBi (with ZrO_2 Nanoparticles) Solder

The elements in the SB solder alloy were analysed using the EDX from the SEM image in Figure 4.5. More SEM images and EDX detections of this solder are shown in Appendix B.

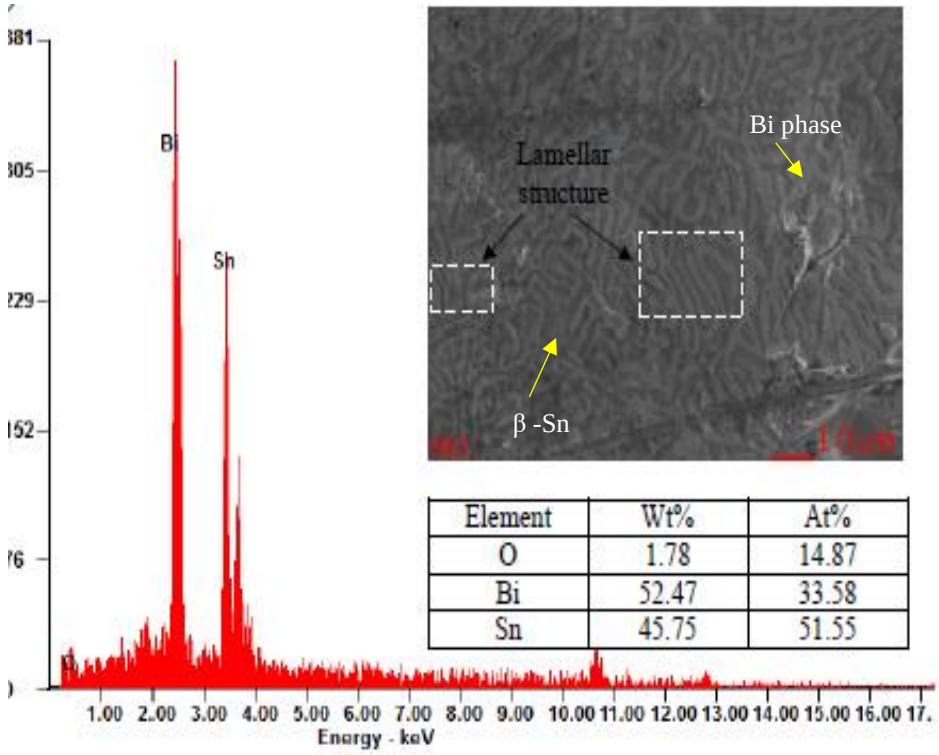

Figure 4. 5: SEM and EDX of SB solder.

The SB solder alloy consists of the lamellar structure of β-Sn (dark phase) and Bi (light phases). This was confirmed by the EDX test. The Bi did not react with Sn to form IMCs in the solder matrix because of its low solubility towards Sn (Silva, et al., 2017). Revisiting the phase diagram, at the temperature of 140 °C, the phases were matched as found in this study. This was consistent with the report by (Wang, et al., 2016). The XRD peaks of the SB solder alloy are shown in Figure 4.6.

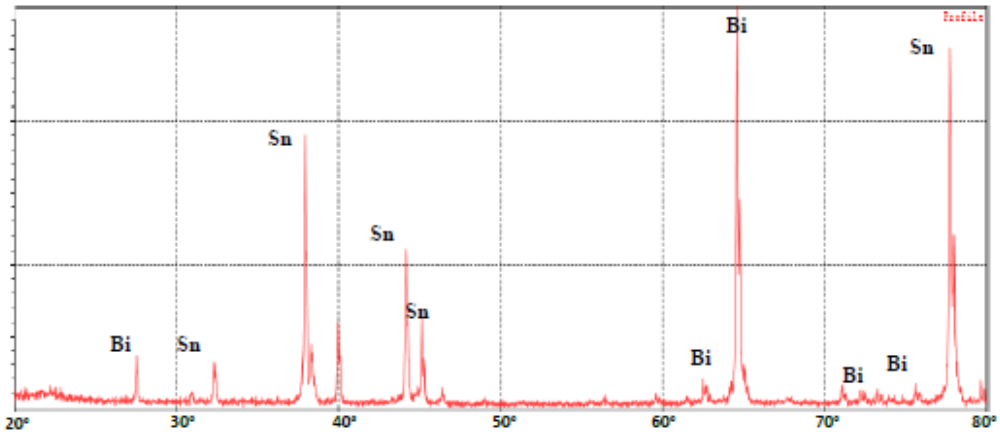

Figure 4. 6: XRD result of SB solder alloy.

Microstructures of Mo added SB solder alloy are shown in Figures 4.7, 4.8 and 4.9. The EDX result confirms the presence of Mo nanoparticles in the 1 %, 2 % and 3 % Mo nanoparticles added SB solder alloy. Clear alteration on the microstructure of the SB added with the Mo nanoparticles were observed. The white particles observed in the SEM images are confirmed as Mo nanoparticles. The 1 % and 2 % additions showed no lumping of Mo particles and had a more uniform type lamellar structure. Meanwhile, 3 % additions had agglomerations of Mo nanoparticles at various places.

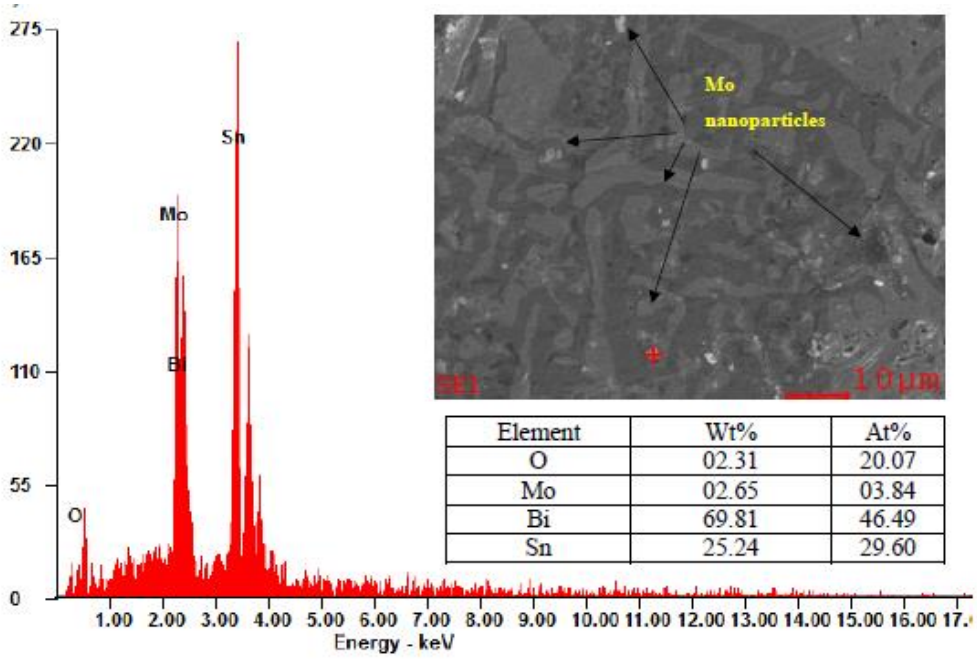

Element	Wt%	At%
O	02.31	20.07
Mo	02.65	03.84
Bi	69.81	46.49
Sn	25.24	29.60

Figure 4. 7: SEM and EDX of SB + 1 % Mo solder.

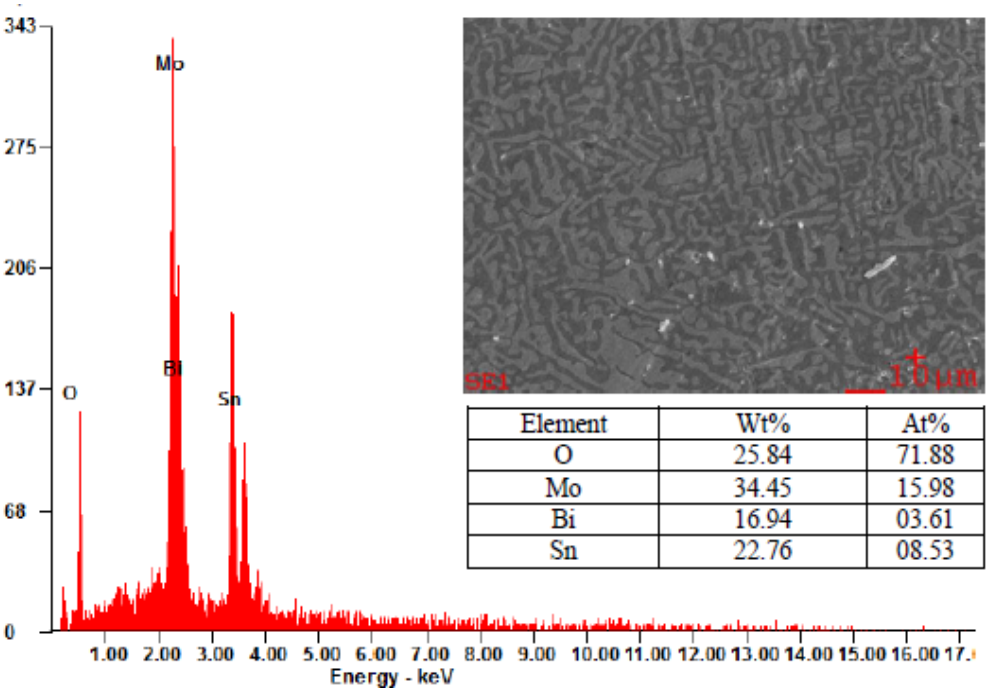

Element	Wt%	At%
O	25.84	71.88
Mo	34.45	15.98
Bi	16.94	03.61
Sn	22.76	08.53

Figure 4. 8: SEM and EDX of SB + 2 % Mo solder.

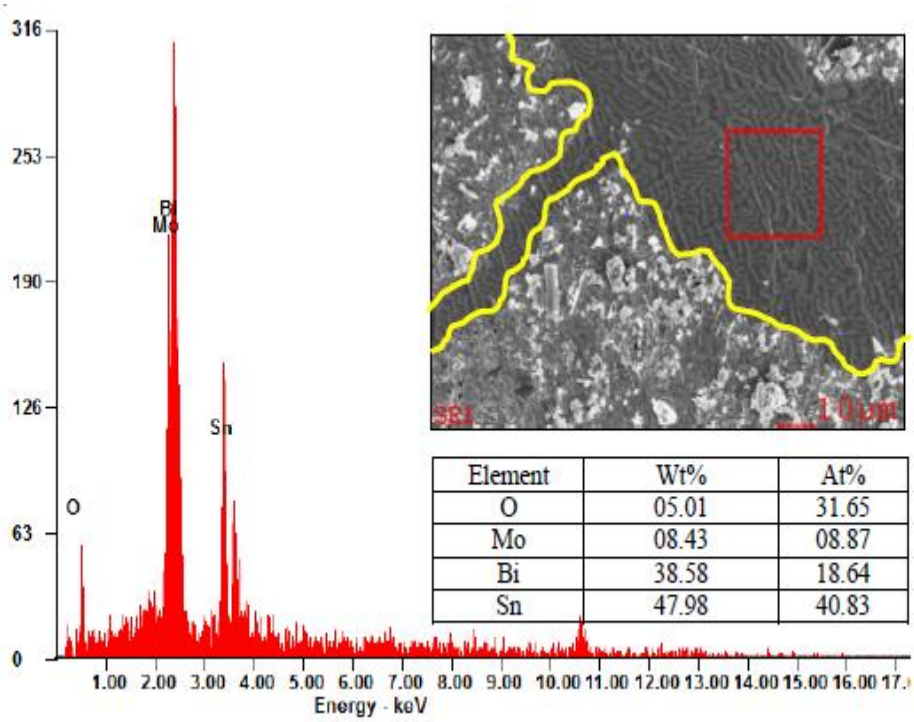

Element	Wt%	At%
O	05.01	31.65
Mo	08.43	08.87
Bi	38.58	18.64
Sn	47.98	40.83

Figure 4. 9: SEM and EDX of SB + 3 % Mo solder.

The addition of Mo nanoparticles visibly provides a distinguished morphology compared to the bare SB solder alloy. The Mo nanoparticles do not react with the β-Sn and Bi elements (Yang, et al., 2018). As can be observed from Figure 4. 9, the 3 % Mo added solder alloy had agglomerated nanoparticles that appeared on the top of the lamellar Sn and Bi phases. Consequently, these Mo nanoparticles would change the growth velocity of the solder alloy as it appears as discrete particles in the molten SB solder alloy. (A.S.M.A. Haseeb, et al., 2012) established similar incidence with the reinforcement of Mo nanoparticles in Sn3.8Ag0.7Cu solder. The yellow borders seen in Figure 4.9 surrounds the lamellar structure of the SB + 3 % Mo. These structures were finer and the Bi phases were narrower with better elongation compared to the SB solder alloy. The EDX analyses confirm that not much of Mo particles existed at this area. This observation explains that Mo affects the solidification

and grain growth of the β-Sn and Bi. The Mo nanoparticles act as separate sites for nucleation during solidification and restricts the surface energy of the molten solder alloy. Hence, the high activation energy of the Sn and Bi would be limited, resulting in a smaller β-Sn matrix and Bi. This was closely linked to the research by (Shin, et al., 2009) explaining a similar reason after adding SiC nanoparticles to the Sn58Bi solder alloy. This statement was also presented by (Gain & Zhang, 2019).

The agglomerations of Mo nanoparticles observed in Figure 4.9 did not have much effect on refining the microstructure since the weight percentage is considered low. This was supported by (Zhang & K.N Tu, 2014) providing a similar clarification. Plus, during the molten state, the molten SB is highly viscous and rejects or pushes the agglomerated Mo nanoparticles to the top of the lamellar structures. The Mo nanoparticles are less dense compared to the molten SB resulting it to be displaced to the surface, as seen in Figure 4.9. (Chellvarajoo & M.Z. Abdullah, 2016) gave a similar proclamation with additions of NiO nanoparticles in the Sn3.0Ag0.5Cu solder alloy. It is a typical characteristic of nanoparticles to not involve in any diffusion process at low temperatures (Zhang & Gao, 2015). However, it is important to control the limit for the weight percentage of nanoparticles additions as higher weight percentage will deteriorate the grain refining process, as found by (Jung, et al., 2018) with an increase of the β-Sn grain size. In the same report, the combined weight percentages of 0.6 % for TiO_2 and graphene resulted in 34 % of increase on the β-Sn area. Further confirmation of the presence of Mo nanoparticles in the SB solder alloy was proved by the peaks in Figure 4.10. The peaks of Mo in the 1

% Mo nanoparticles added SB solder alloys matched the earlier peaks in the XRD for the sole Mo. Similar peak detection was seen for the 2 % and 3 % additions and are provided in Appendix B.

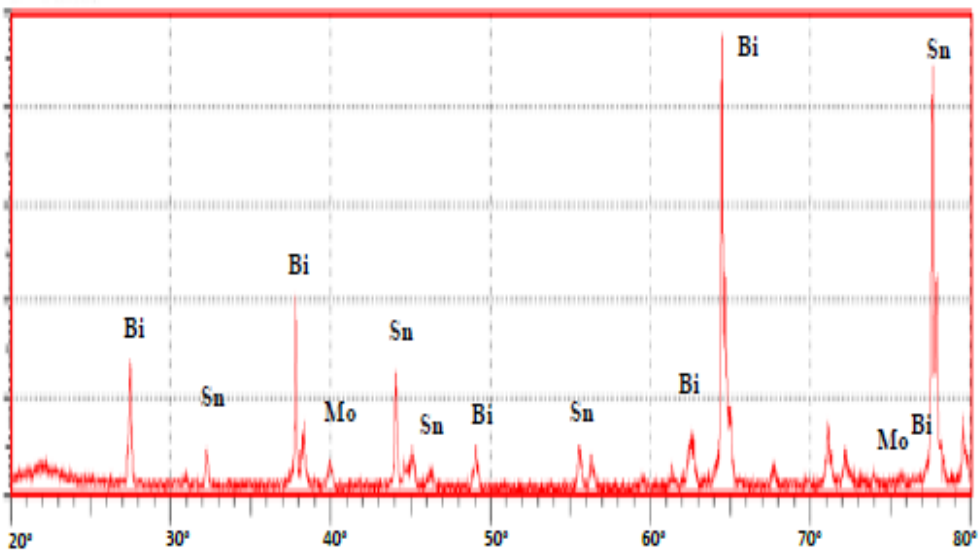

Figure 4. 10 : XRD of SB + 1 % Mo solder alloy.

Presences of the 1 %, 2 % and 3 % ZrO_2 nanoparticles in the solder alloy are shown in Figures 4.11, 4.12 and 4.13. There were also differences noticed to the microstructure of the ZrO_2 nanoparticles added solder. It was apparent that the EDX analyses proved the presence of ZrO_2 nanoparticles in each weight percentages of addition. The white particles were confirmed as the ZrO_2 nanoparticles. Dissimilar to the additions of Mo nanoparticles, the ZrO_2 nanoparticles additions did not show any clear agglomeration. The 1 %, 2 % and 3 % ZrO_2 additions did not lump together but were distributed evenly. Further increase in the weight percentage of ZrO_2 additions alters the primary microstructure of the solder alloy. It was visible that the ZrO_2 nanoparticles did not entrap itself in the solder matrix but appeared as being pushed to the top of the lamellar structure. Alike Mo, ZrO_2 nanoparticles does not react with β-Sn

and Bi. The study by (A.S.M.A. Haseeb, et al., 2012) concluded similarly with the reinforcement of Mo nanoparticles in a higher melting temperature Sn3.8Ag0.7Cu solder. A high melting point of 2715 °C for the ZrO_2 disables any possibility of breaking the ZrO_2 atoms to influence the melting temperature since the nanoparticles were mixed and melted at a temperature of 600 °C. There is no chance for the ZrO_2 to even react with β-Sn or Bi by atom substitution or dissolution. The additions of 1 % ZrO_2 nanoparticles in the SB solder alloy alters the microstructure to a finer and uniform lamellar structure. In the meantime, the lamellar structures of the 2 % ZrO_2 nanoparticles added SB solder alloy were suppressed with nearing alternating gaps between them as seen in the red highlighted region in Figure 4.12. The ZrO_2 nanoparticles accumulated around this region and contributes to the nearer lamellar structure production. Previously, this was seen for the 3 % Mo additions.

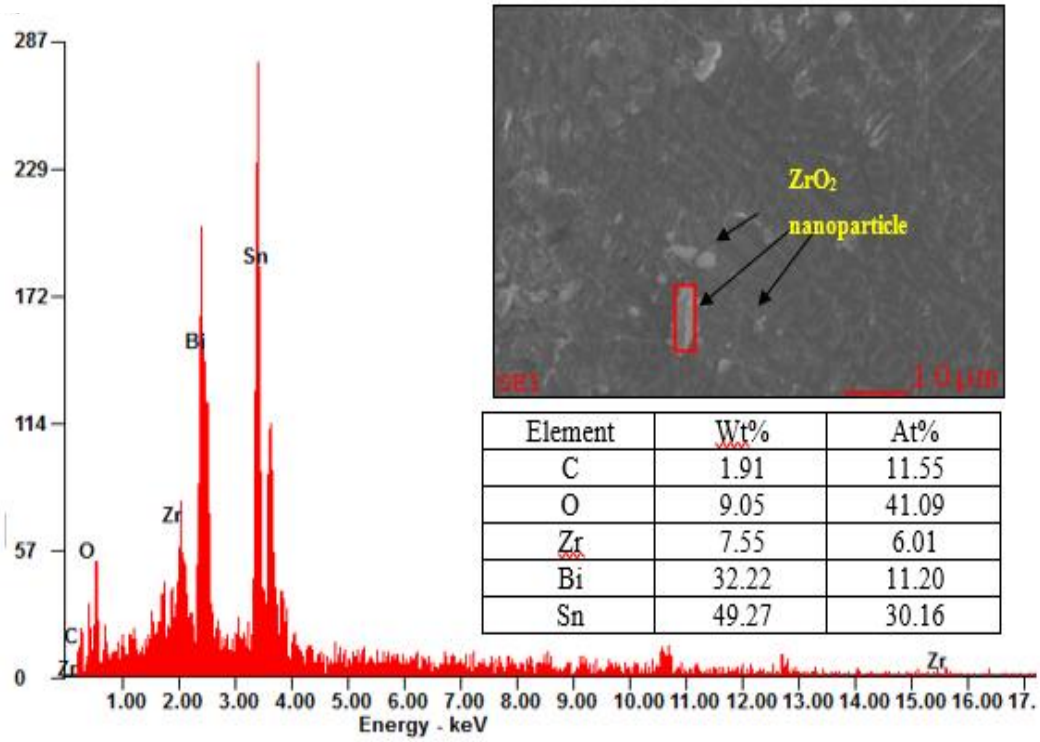

Element	Wt%	At%
C	1.91	11.55
O	9.05	41.09
Zr	7.55	6.01
Bi	32.22	11.20
Sn	49.27	30.16

Figure 4. 11: SEM and EDX of SB + 1 % ZrO_2 solder.

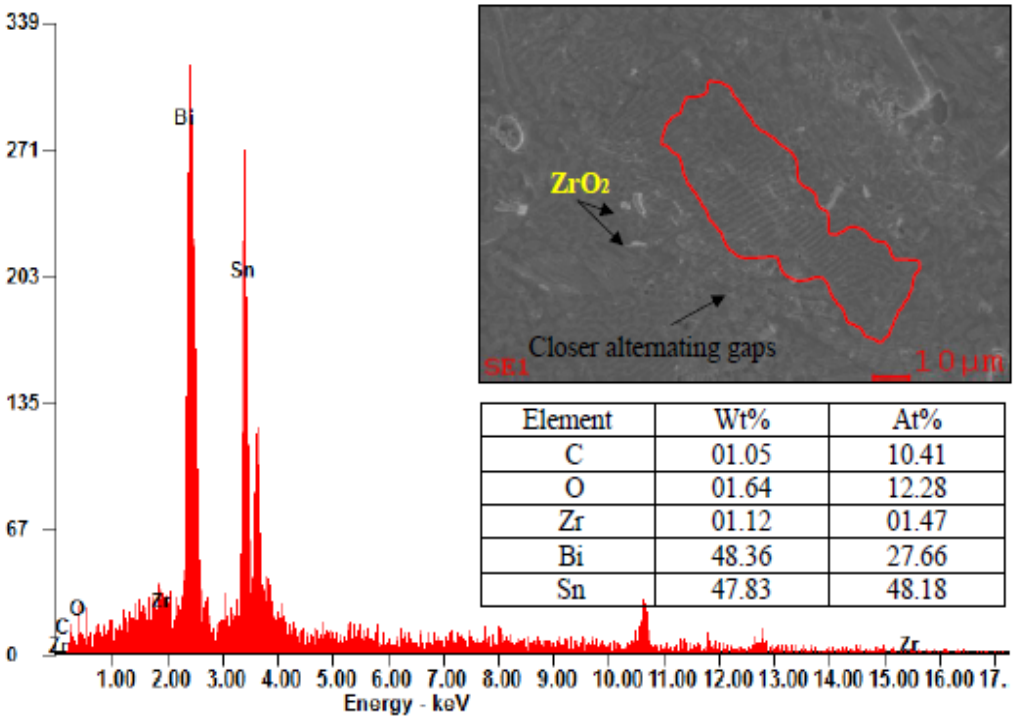

Element	Wt%	At%
C	01.05	10.41
O	01.64	12.28
Zr	01.12	01.47
Bi	48.36	27.66
Sn	47.83	48.18

Figure 4. 12: SEM and EDX of SB + 2 % ZrO_2 solder.

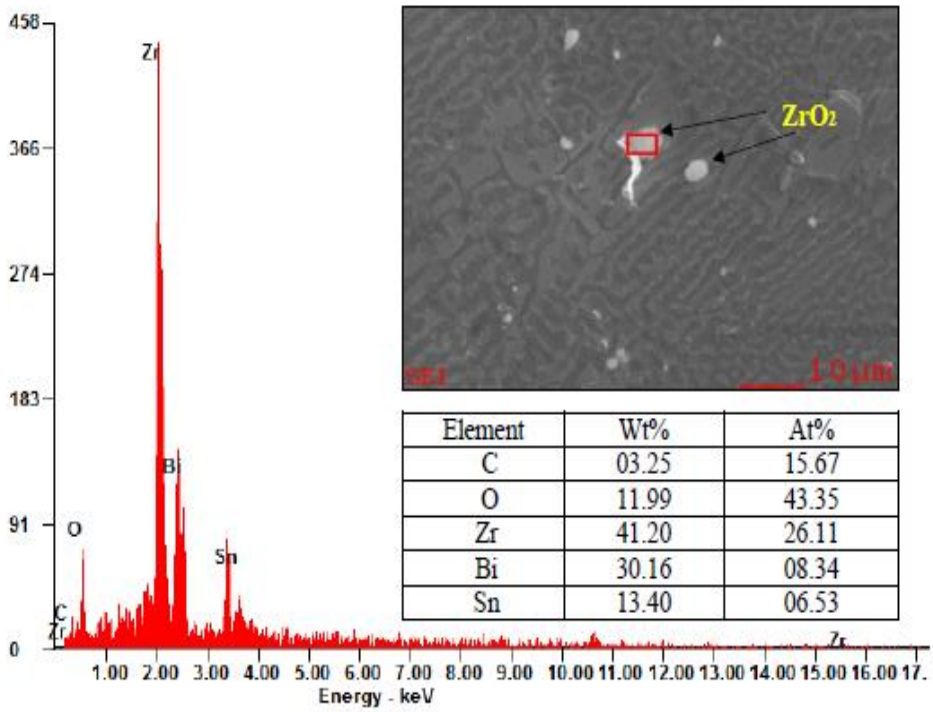

Element	Wt%	At%
C	03.25	15.67
O	11.99	43.35
Zr	41.20	26.11
Bi	30.16	08.34
Sn	13.40	06.53

Figure 4. 13: SEM and EDX of SB + 3 % ZrO_2 solder.

As reported by many studies, nanoparticles accumulates at a high-energy site in a molten solder (Shang, et al., 2019; A.E.Hammad, 2018; B.X.Vuong, et al., 2018). Similarly, ZrO_2 nanoparticles accumulated in the SB solder alloys and serve as heterogeneous nucleation sites for β-Sn phase and eutectic phase (Sn and Bi phase). This will increase the nucleation rate of the grains in the solder and consequently reduce the sizes by suppressing the lamellar structure. The reduction of the Bi area discussed in section 4.3.1 confirms this claim. A different study by (Z.H. Li, et al., 2019) with additions of CeO_2 nanoparticles also reported a similar finding. This occurrence is termed as surface absorption theory, which defines that the plane with the maximum surface tension grows fastest (acting as the nucleation site) with an increasing of an adsorption element (ZrO_2 nanoparticles) and with that increase taking place; the surface energy and the growth velocity of the plane will be reduced. Several type of researches provided a parallel explanation (Wu, et al., 2019; Hu, et al., 2014). There were more presences of ZrO_2 nanoparticles in the 3 % additions with some particles existing in an agglomerated manner. This would have less effect on the refinement of microstructure. (Zhang & K.N Tu, 2014) reported likewise. The XRD peaks of SB added with the 1 % ZrO_2 nanoparticles is shown in Figure 4.14 and matched with the earlier XRD peaks of the sole ZrO_2. Similar detection was noted for the 2 % and 3 % additions and are shown in Appendix B.

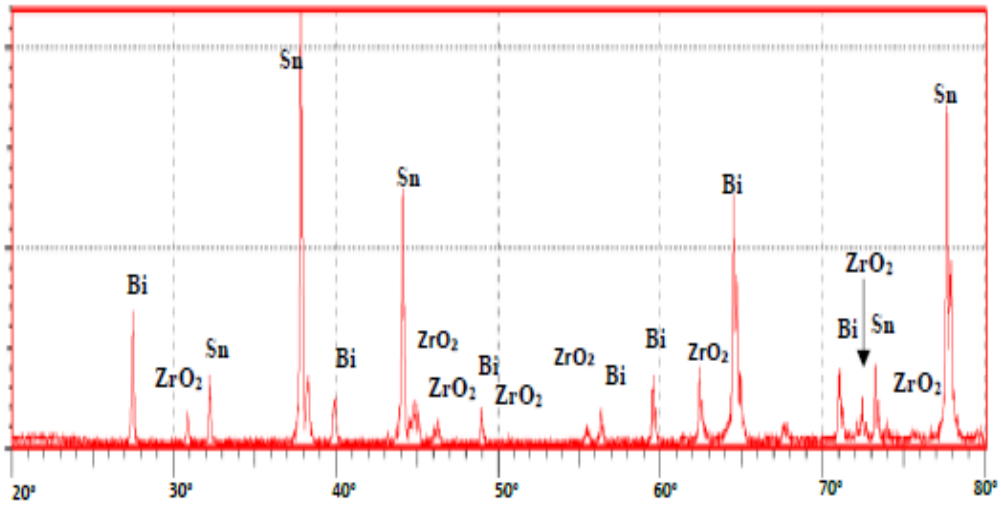

Figure 4. 14: XRD of SB + ZrO_2 solder alloy.

4.3.1 Characterization of Microstructural on Bismuth (Bi) Size Area of SnBi, SnBi (with Mo Nanoparticles) and SnBi (with ZrO_2 Nanoparticles) Solder.

The Bi element in the SB microstructure directly influences the mechanical properties of a SB solder system. Hence, the Bi area was measured as the parameter of investigation to analyse the changes made by the nanoparticles and show its effect towards the mechanical properties. The average Bi area in the SB solder alloy was 431557.8 μm^2. The 1 %, 2 % and 3 % Mo added SB solder produced an average Bi area of 193340.59 μm^2, 564397.3 μm^2 and 331351.19 μm^2 respectively. The 1 % ZrO_2 added SB solder alloy produced an average area of 271166.5 μm^2. The 2 % ZrO_2 added SB solder alloy produced an average area of 253981.67 μm^2 while the 3 % ZrO_2 added SB solder alloy measures an average area of 333094.3 μm^2. Figure 4.15 shows the average Bi area of both Mo and ZrO_2 additions.

Initially, the Bi area for the 2 % Mo additions increased and then decreased for the 3 % additions. The largest Bi area was recorded for the 2 % additions and the smallest area was recorded for the 1 % additions. Opposing to that, a decrease on the Bi area for the 2 % of ZrO_2 additions was observed followed by a minimal increase on the area for the 3 % ZrO_2 additions. Added with that, the different sizes of both these nanoparticles contributes to such variation. This observation clarifies the distinctive influence made by the nanoparticles to the microstructure.

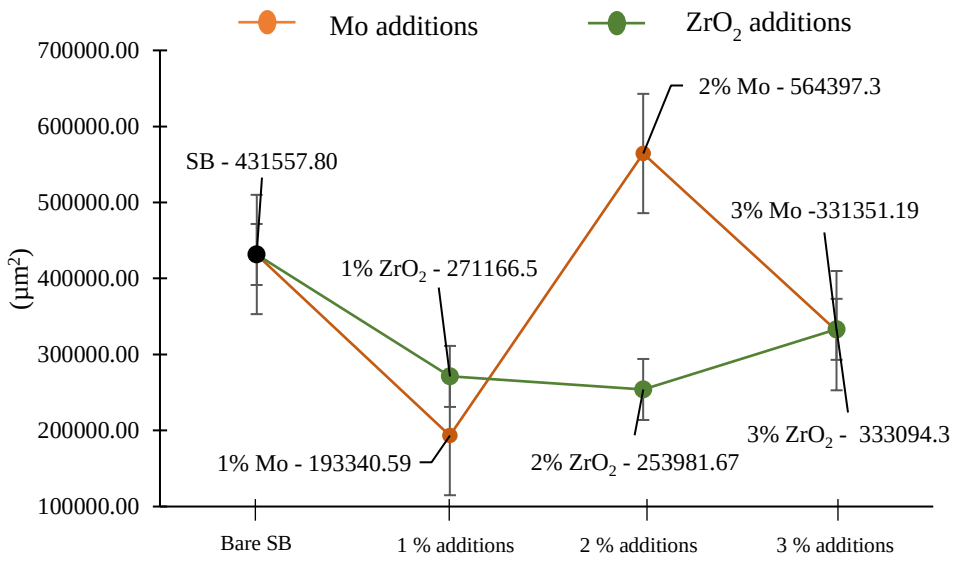

Figure 4. 15: Total average Bi area of SB, SB added with Mo and ZrO_2 nanoparticles solders.

The Bi area for the 2 % and 3 % ZrO_2 additions were smaller compared to the 2 % and 3 % Mo reinforced solder. The differences here are related to the Mo particles size, which is comparably larger than the ZrO_2. So, a minimal weight percentage of Mo is adequate to provide refinement on the Bi area while higher weight percentage of additions would increase the Bi area. The large particles of Mo had lesser refinement effect on the microstructure than the ZrO_2

nanoparticles. In other words, the Mo particles fail to properly segregate on the microstructure and to reduce the surface energy. Too much presence of larger sized nanoparticles will not act as heterogeneous nucleation sites and restrict the growth rate. (Y.M Youssef, et al., 2005) agrees to this statement.

Meanwhile, smaller sized ZrO_2 provided refinement to the microstructure by having smaller Bi areas in all three percentages of addition. The differences among the largest Bi area (3 % ZrO_2) and lowest area (2 % ZrO_2) was 0.02 % only. Smaller sized nanoparticles will have a higher surface area per unit volume to enable itself to be absorbed at the solid-liquid interface. Reduction on the surface energy occurred with these ZrO_2 nanoparticles existing at the interface and will restrict the grain growth in the solder. The scientific term for this phenomenon is defined as Gibbs energy. This statement was also explained by (Yang, et al., 2019) providing resemblance with this study.

Though, both nanoparticle's additions produced smaller Bi area compared to the pristine SB solder alloy, except for the 2 % Mo added SB solder alloy because of improper segregation of the nanoparticles. The microstructure of the solder alloy added with the ZrO_2 nanoparticles showed better improvement. Figure 4.16 is drawn based on EDX analysis to show the distribution of Mo and ZrO_2 nanoparticles on the β-Sn and Bi phases and their influences on the Bi area. Figure 4.16 (a) represents the β-Sn and Bi phases and Figure 4.16 (b) shows the presences of the nanoparticles. Reduction in the Bi area occurs for all three percentages of ZrO_2 additions and for the 1 % and 3 % of Mo additions due to the proper segregation of these particles as demonstrated

in Figure 4.16 (c) and (d). Agglomerations found in the 2 % of Mo addition resulted in non-refinement of the Bi area as revealed in Figure 4.16 (e).

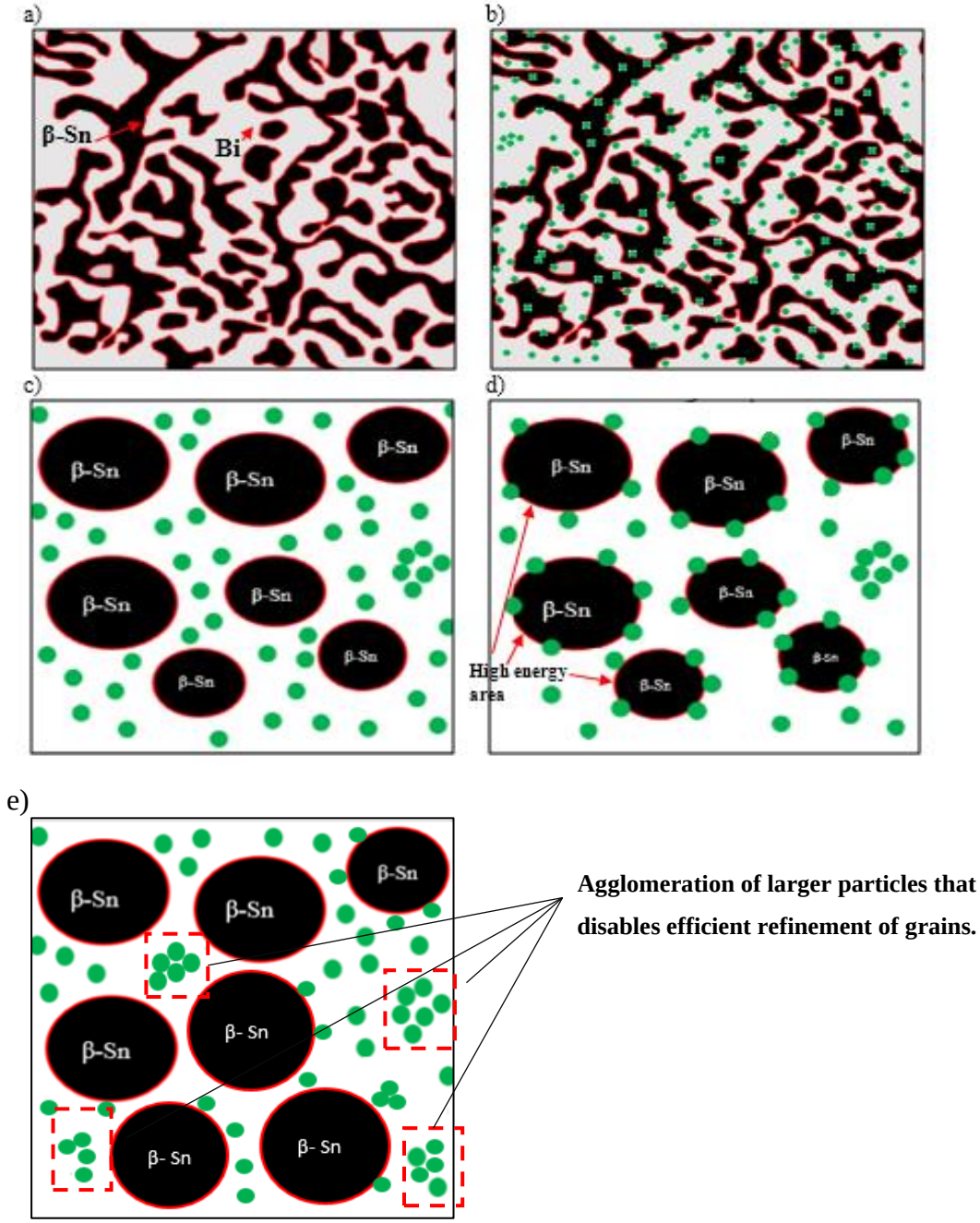

Figure 4. 16: a) β-Sn and Bi matrix, b), c) Presence of 1 %, 2 % and 3 % ZrO_2 and 1 % and 3 % Mo nanoparticles, d) Absorption of 1 %, 2 % and 3 % ZrO_2 and 1 % and 3 % Mo nanoparticles and e) 2 % Mo nanoparticles.

4.4 Analyses of the Element, Phases and Intermetallic (IMC) Layer Thickness of SnBi, SnBi (with Mo Nanoparticles) and SnBi (with ZrO_2 Nanoparticles) Solder Joints.

The SEM and EDX analyses at the IMC layer for the SB/Cu, SB + Mo/Cu and SB + ZrO_2/Cu provides the morphology and presences of the elements. These EDX analyses provides an initial prediction on the presences of element which will be further investigated using the XRD results.

This section will discuss on the IMC layer morphology and the presence of elements at the joint upon additions of nanoparticles. More SEM and EDX analyses are placed in Appendix C. The elemental detection was randomly picked at the centre of the IMC layer as labelled as the red box in each SEM images. High amount of Bi was detected at the intermetallic layer for the bare SB/Cu, proving that the IMC layer production is controlled by the Bi element. A typical lamellar structure on the solder side was noted. This is presented in Figure 4.17.

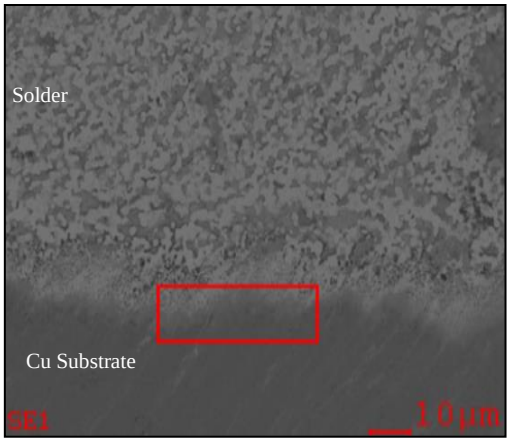

Element	Wt. %	At. %
Cu	23.14	43.53
Bi	48.14	27.54
Sn	28.72	28.93

Figure 4. 17: SEM/EDX analyses of IMC layer of SB/Cu solder joint.

The Mo nanoparticles successfully presented itself at the interface between the solder and substrate. Presences of Mo at the IMC layer for the 1% additions as shown in Figure 4.18 (a) was less compared to the 2 % and 3 % additions as shown respectively in Figure 4.18 (b) and Figure 4.18 (c). Elemental analyses showed that Mo nanoparticles were scattered and not uniformly distributed for all the three percentage of additions. The Mo nanoparticles are larger than ZrO_2 nanoparticles, therefore the detection of Mo was much evident. Nevertheless, the scattering detection found from the EDX in terms of the nominal weight percentage shows that the Mo nanoparticles did not segregate well. These EDX analyses are used as an initial prediction on the presence of Mo at the IMC layer before the XRD analyses were done to obtain further clarification.

a)

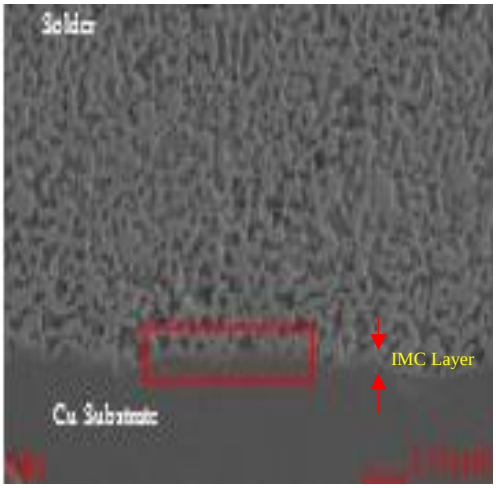

Element	Wt. %	At %
Mo	01.94	01.88
Bi	28.40	12.64
Sn	24.21	18.97
Cu	45.44	66.51

b)

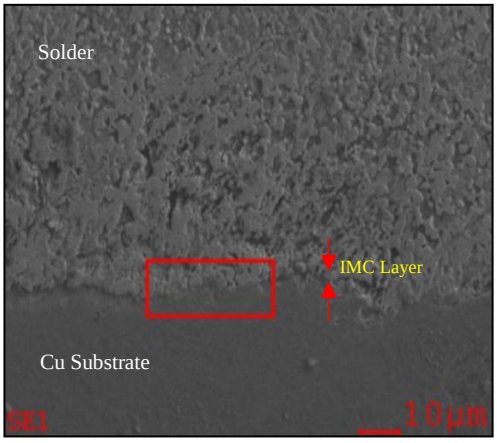

Element	Wt. %	At. %
Mo	04.13	06.01
Bi	51.93	34.68
Sn	36.44	42.85
Cu	07.49	16.45

c)

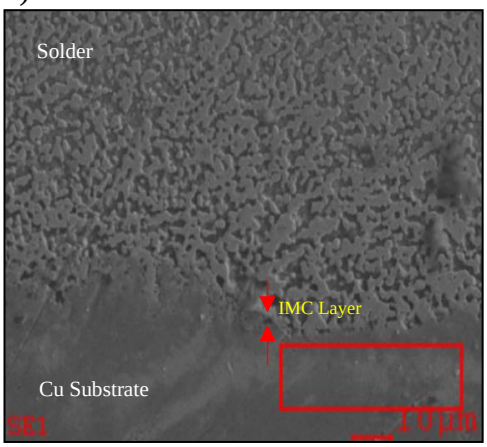

Element	Wt. %	At. %
Mo	04.32	04.93
Bi	40.80	21.39
Sn	26.15	24.14
Cu	28.74	49.55

Figure 4. 18: SEM/EDX of a) SB + 1 % Mo/Cu b) SB + 2 % Mo/Cu and c) SB + 3 % Mo/Cu solder joints.

The IMC layers formed uniformly between the solder and substrate for the ZrO_2 nanoparticles additions as shown in Figures 4.19. The nominal weight percentages of the Zr were more consistent suggesting the segregation of ZrO_2 nanoparticles were more uniform. A high amount of Zr was observed for the 1 % and 2 % additions as shown in Figure 4.19 (a) and (b). Less detection on the Zr's nominal weight percentage was spotted for the 3 % addition as shown in Figure 4. 19 (c). These EDX analyses are used as an initial prediction on the presence of the ZrO_2 at the intermetallic layer.

a)

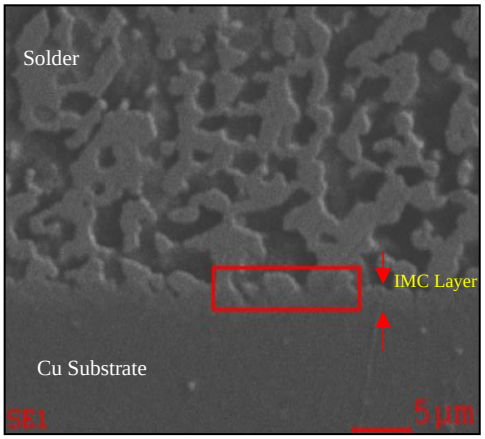

Element	Wt. %	At. %
Zr	03.98	07.11
Bi	74.07	57.81
Sn	17.82	24.49
Cu	04.12	10.59

b)

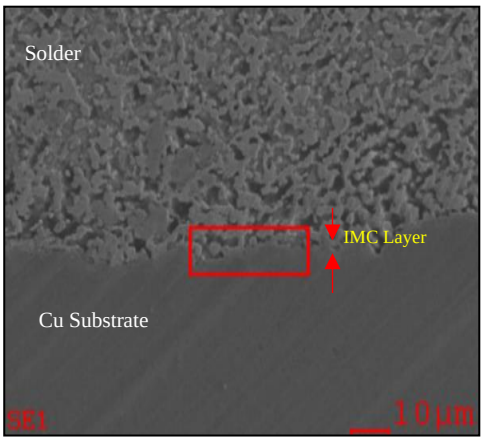

Element	Wt. %	At. %
Zr	03.18	04.26
Bi	52.90	30.89
Sn	21.85	22.47
Cu	22.07	42.39

c)

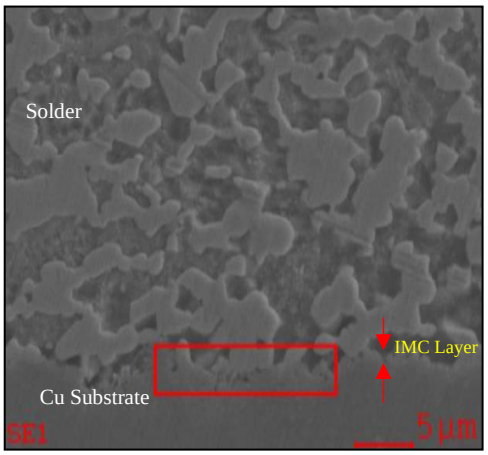

Element	Wt. %	At. %
Zr	01.25	01.64
Bi	45.86	26.25
Sn	31.39	31.63
Cu	21.50	40.48

Figure 4. 19: SEM/EDX of SB + 1 % ZrO_2/Cu, SB + 2 % ZrO_2/Cu and SB + 3 % ZrO_2/Cu solder joints.

Further analyses using the XRD was done for both the nanoparticles additions and explained hereafter. All raw XRD results are shown in Appendix C. The SB/Cu solder joint possessed the common Bi, Sn, Cu elements. The IMCs of CuSn, Cu_6Sn_5, Cu_3Sn were also found with the Cu_6Sn_5 as the dominant IMC. The Bi did not react with the Cu or Sn to form any IMCs. This shows that Bi would be the element to block the diffusion process between Cu and Sn in the absence of nanoparticles.

The introduction of Mo nanoparticles in the solder joint produced different and additional IMCs compared to the SB/Cu. The Bi, Sn, Cu, CuSn, Cu_6Sn_5 and Cu_3Sn were detected in the 1 % and 3 % Mo additions. All these IMCs were also noted for the 2 % additions but with the absence of Cu_3Sn. There were no presence of Cu_3Sn IMCs as well in the 3 % additions. The possibility for the absence of the Cu_3Sn in the 2 % and 3 % additions is due to the formation of $Cu_{10}Sn_3$. Assisted with the availability of Cu and Sn at the joint, the Cu_6Sn_5 can further diffuse with Cu and Sn to form the $Cu_{10}Sn_3$ IMC. Additional IMCs such as $Cu_{10}Sn_3$ and $MoSn_2$ also appeared for all the three percentages of additions with the domination of $Cu_{10}Sn_3$. Not only that, the high intensity of the Bi peaks was observed. This happens because of the reaction of Mo with Sn to produce $MoSn_2$ which allows the Bi to be highly concentrated at the solder joint. The EDX analyses shows the Mo additions had a lesser but more uniform distribution at the top side of the intermetallic layer. Nevertheless, these observations were not apparent as some of the analysed areas had improper distribution and some even with no detection of nanoparticles (e.g. 2 % Mo + SB/Cu solder joint). This statement tallies with the XRD results in

Appendix C. Distributions of some Mo nanoparticles was quite immensely found at one side of the IMC layer leaving the other side with lesser distributions of nanoparticles. The side with the lesser presence of Mo produced thicker IMC layer due to inconsistent distributions of nanoparticles and less effect on blocking the diffusion process. This finding was exposed by the 1 % Mo nanoparticles added solder joint.

Meanwhile, other IMCs apart from the common CuSn, Cu_3Sn and Cu_6Sn_5 were identified for the ZrO_2 nanoparticles added SB solder joint. All three ZrO_2 weight percentages of additions had different IMCs respective to each other. All the IMCs are shown in Appendix C. The common IMCs found in these ZrO_2 nanoparticles additions are the SnO, SnZr, Zr_5Sn_3, ZrCu and $ZrSn_2$. The ZrO_2 nanoparticles itself was detected as discrete element. The additions of ZrO_2 also allows the Zr to react with the Cu and Sn to form SnZr, Zr_5Sn_3, ZrCu and $ZrSn_2$ IMCs. This happens due to the high reactivity of the Zr towards Sn and Cu. The Bi was not detected in the lesser weight percentage of ZrO_2 additions as all the Bi had been consumed to produce the BiO_2 IMCs. The existence of O allows it to react with Sn, Bi and Zr to produce SnO, BiO_2 and Zr_3O_1 IMCs. The 2 % ZrO_2 added solder alloy joint produced Sn_3O_4 IMC. Likewise, with higher content of ZrO_2, the Zr reacts with Cu to develop the Cu_8Zr_3 IMC. These two IMCs (Sn_3O_4 and Cu_8Zr_3) were not noted in the 1 % additions because of lower content of Zr. In the 3 % ZrO_2 additions, the BiO IMC was not observed as the O elements were found to react with Zr to produce Zr_3O_1 IMC. Apart from that, the formation BiZr IMCs in the 3 % additions clarifies that the Bi tends to react with Zr rather than O when the content of the

Zr is high. Not only that, the sole Bi elements were detected in the 3 % additions explaining that the higher Zr concentration hinders the production of the BiO IMC, leaving the Bi to present in its own form. Influence of Zr in reacting with other elements reduced the production of Cu_6Sn_5 and Cu_3Sn IMC layer that contributes to thin IMC layer.

The IMC layer thickness of the as soldered Mo and ZrO_2 added SB solder joint was measured. Analyses from the earlier EDX and XRD results are related to discuss the IMC layer thicknesses to provide in depth discussion. The bare SB/Cu joint recorded the highest IMC layer thickness of 1.26822 µm while the lowest thickness was measured for the 3 % ZrO_2 of 0.4804 µm. The descending order of the IMC layer thickness are as SB > SB +1 % ZrO_2 > SB + 1 % Mo > SB + 3 % Mo, SB + 2 % Mo > SB + 2 % ZrO_2 > SB + 3 % ZrO_2. The values are shown in Figure 4.20. The additions of the nanoparticles noticeably reduce the IMC layer thickness.

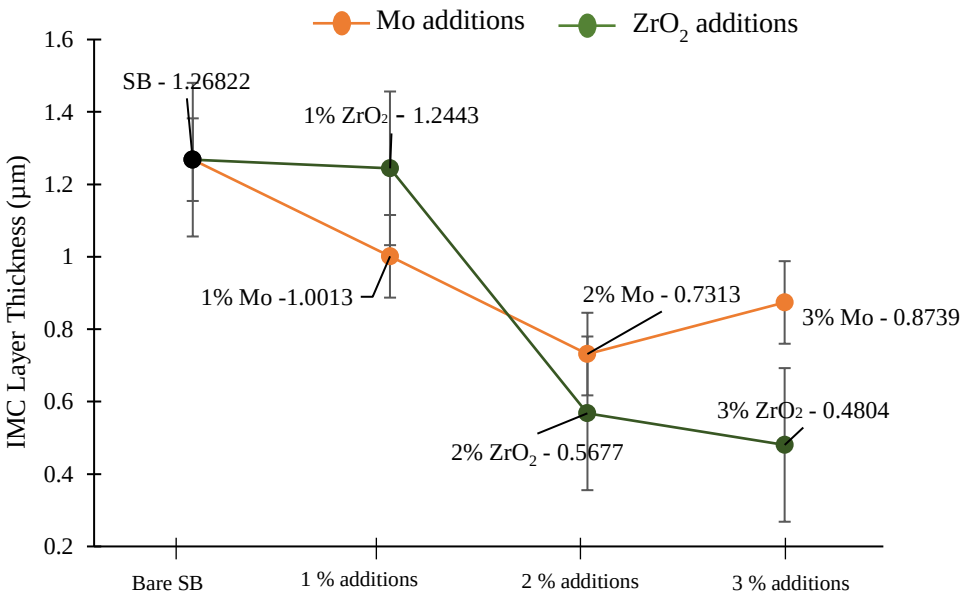

Figure 4. 20: Total average IMC layer thickness of SB/Cu, SB + Mo/Cu, and SB + ZrO_2/Cu solder joints.

Comparing the 2 % and 3 % Mo nanoparticles additions, the 1 % Mo had thicker IMC layer. The thicker IMC layer in the 1 % Mo could be attributed to the failure of Mo in blocking the diffusion between the Cu and Sn. The presences of Cu_6Sn_5 and $Cu_{10}Sn_3$ IMCs were detected from the XRD result and is shown in Appendix C. Typically, the $Cu_{10}Sn_3$ IMC forms from the Cu_3Sn or Cu_6Sn_5 due to the diffusion between these IMCs. This again shows the incapability of Mo in blocking the diffusion process since the Mo did not exist as discrete particles. Based on the initial EDX analyses, the Mo elements were detected and believed to exists as discrete particles. However, with further XRD analyses (Appendix C), the detected Mo was from the $MoSn_2$ IMC as stated earlier. This explains that most of the Mo particles reacted with Sn to form the $MoSn_2$ IMC, leaving no discrete particles of Mo. This causes easier diffusion process and growth of the IMC layer. This was similarly seen for the 2 % and 3 % Mo additions with the presence of the $MoSn_2$ IMCs. It was found that the Mo

nanoparticles only segregated as discrete particles on the solder side and not at the intermetallic layer.

The trend was similar for the ZrO_2 additions. The 2 % and 3 % of ZrO_2 additions had thinner IMC layers than the 1 % additions. The reduction of the IMC layer thickness is attributed to the presences of the ZrO_2 nanoparticles. Moreover, smaller sized ZrO_2 compared to the Cu_6Sn_5 and $Cu_{10}Sn_3$ IMC layers can easily pin on to these layers and reduce the growth velocity of these layers. This contributes to the thinner IMC layers. Besides, the XRD peaks confirm the presence of ZrO_2 as discrete particles. The 1 % ZrO_2 additions did not show much reduction in the IMC layer thickness compared to the 2 % and 3 % additions because of some agglomerations of ZrO_2 nanoparticles found at the joint but with more presence at the solder side that related to the increment of hardness. This was like the observation found for the 2 % and 3 % Mo additions. Though to clarify again, the Mo nanoparticles were found on top of the solder joint rather than at the joint, but the ZrO_2 nanoparticles existed at the joint or at the IMC layer. This was observed from the EDX analyses.

The distribution of the nanoparticles in influencing the IMC layer is shown in Figure 4.21. Figure 4.21 (a) demonstrates the diffusion process between Cu and Sn without the presence of nanoparticles. Figure 4.21 (b) exhibits the influence of nanoparticles at the joint. Both these figures are based from the results of the EDX and XRD analyses shown in Appendix B. Meanwhile, effective blocking of the diffusion process between Cu and Sn to hamper a thick Cu_6Sn_5 IMC layer was observed for 2 % and 3 % ZrO_2 additions, represented by Figure 4.21 (b). Existence of ZrO_2 as discrete particles acts as a

blocking mechanism to the diffusion process. The 3 % ZrO_2 additions produced the thinnest IMC layer because of the existences of other IMCs. This retards the growth of the Cu_6Sn_5 IMC layer as the Cu and Sn reacts with Zr, leaving less availability of these elements to react among them.

Comparing to the Mo added solder, the ZrO_2 added solders show better interfacial result. In all the three percentage of Mo additions, even with the production of $MoSn_2$ IMCs, the availability of Sn still makes it possible to react with Cu to produce a thicker Cu_6Sn_5 layer. This could be avoided with the presence of discrete Mo nanoparticles, but unfortunately, none of Mo presented as discrete particles. Both the XRD analyses of the SB solder alloy added with Mo and ZrO_2 at the intermetallic layer well-matched with the results obtained for the IMC layer thickness. Nevertheless, all IMC layer thicknesses measured in this research was less than 2 µm, considerably thin if compared with other available literature.

a)

b)

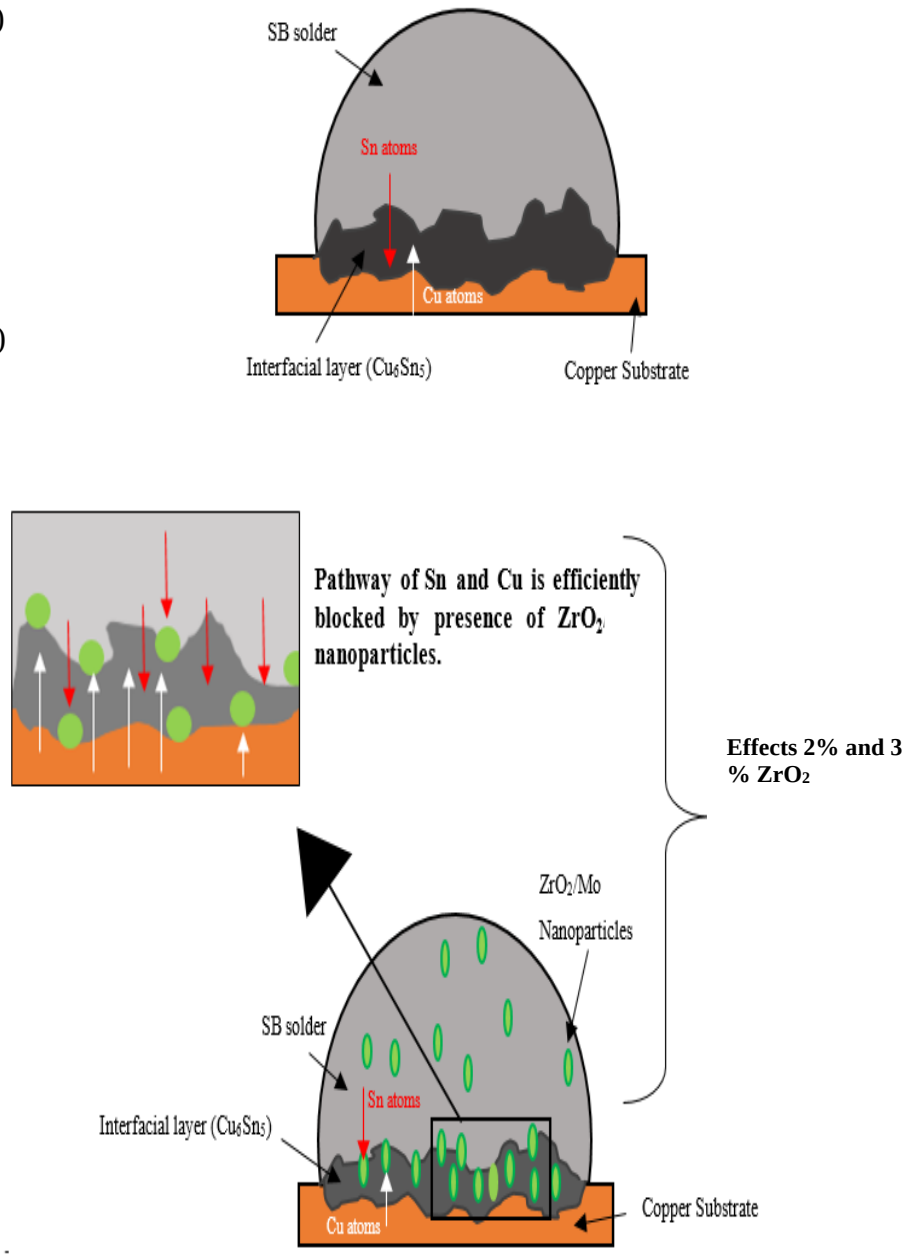

Figure 4. 21: Influence of the nanoparticles at interface of a) without ZrO_2 and Mo nanoparticles, and b) with 2 % and 3 % ZrO_2 nanoparticles added SB solder joint.

4.5 Analyses of Mechanical Properties of SnBi, SnBi (with Mo Nanoparticles) and SnBi (with ZrO_2 Nanoparticles) Solder Joints.

The mechanical properties of microhardness and shear strength were analysed as part of fulfilling the objectives. The following subsections will discuss on these two properties.

4.5.1 Analyses of Microhardness of SnBi, SnBi (with Mo Nanoparticles) and SnBi (with ZrO_2 Nanoparticles) Solder.

The average microhardness values for the SB, SB + Mo and SB + ZrO_2 nanoparticles solder alloy are shown in Figure 4.22. Raw data of the Vickers microhardness can be found in Appendix D. The SB solder alloy recorded an average hardness value of 28.78 HV. The Bi element is responsible to withstand the deformation for the solder alloy. The highest hardness value was calculated for the SB + 1 % ZrO_2 (32.28 HV), while the lowest value was calculated for the SB + 1 % Mo (26.92 HV).

Referring to the SB solder alloy's hardness value, the 1 % Mo additions produced 6 % of lower hardness value. The 2 % and 3 % Mo additions had 0.7 % and 2 % of increment respectively if compared with the SB solder alloy. These observations depict the influence of different percentages of Mo additions to the hardness value. Apart from that, the microstructural property also contributes in the resisting the indentation that relates to the hardness value.

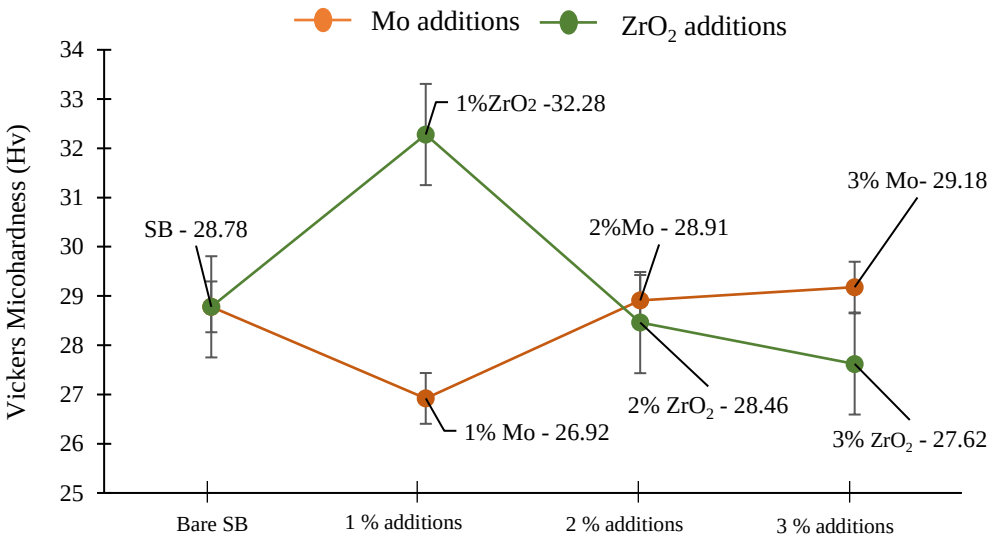

Figure 4. 22: Vickers microhardness of SB, SB added with Mo and ZrO_2 nanoparticles solders.

A different trend was witnessed for the ZrO_2 nanoparticles reinforced SB solder alloy. Compared to the bare SB solder alloy's hardness, the 1 % of ZrO_2 additions produced 12 % higher hardness value. The 2 % and 3 % ZrO_2 additions showed a drop of 1 % and 4 % respectively in the hardness value compared to the SB solder alloy.

Earlier, it was discussed that both Mo and ZrO_2 nanoparticles presented at the solder side. These nanoparticles are known to withstand the load upon indentation. The larger sized Mo nanoparticles had an increment in hardness value upon the increase in weight percentage of additions, but the trend was vice versa for the smaller sized ZrO_2 nanoparticles. Even so, the deviation in the hardness value for both additions of nanoparticles were not huge. This is because of both nanoparticles having a similar effect to the increase in the hardness value.

The load during indentation needs to penetrate through the solder alloy and with the presence of the Mo nanoparticles, the load needs to pass through to the nanoparticles too. The load will be absorbed by the Mo nanoparticles. This was stated alike by (Kumar, et al., 2008) by adding SWCNT into the Sn3.8Ag0.7Cu solder alloy and defined this phenomenon as the load-bearing effect (G.K. Sujan, et al., 2017). Contrariwise, the load penetrates deeper in the bare SB and SB + 1 % Mo solder alloy because of fewer dislocations at the grain boundaries and absence of discrete particles (Mo) to act as second phase strengthening mechanism. This clarification was reported by (Yahaya, et al., 2016) after adding TiO_2 into the Sn3.0Ag0.5Cu and producing an increase in the grain size that reduces the hardness value. A more uniform microstructure with finer Bi area accompanied with narrower lamellar structures increased the hardness of the 3 % Mo reinforced SB solder alloy. Theoretically, a higher surface area of the nanoparticles per unit volume of the total solder alloy can increase the hardness of a material (Kanlayasiri & Meesathien, 2018). According to a very early finding by (Amagai, 2008), the existence of the nanoparticles correspondingly behaves as second phase dispersion strengthening mechanism. The Mo nanoparticles exerts its influence likewise by hindering the movement of the dislocation. Complying with the theory of dispersion, these discrete Mo nanoparticles pin itself at the grain boundaries of the solder matrix. More pinning of these Mo nanoparticles at the grain boundary causes high dense dislocations. This contributes to an increase in the hardness (E.A. Eid, et al., 2016). Additionally, the load needs to loop over the Mo nanoparticles and subsequently creating more piled up dislocations that prompts to an increase in the dislocation density. Consequently, this increases the

resistance of deformation for the solder. Figure 4.23 (a) and (b) shows the penetration of the load without and with nanoparticles. An increase in the hardness values for the additions of 2 % and 3 % Mo are represented as the effect shown in Figure 4.33 (b). (Yang, et al., 2019) pointed out a similar reason for the increase of hardness value.

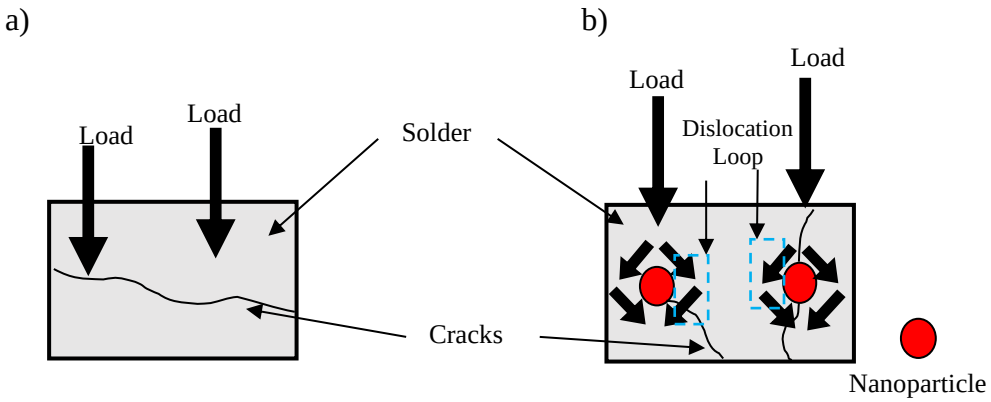

Figure 4. 23: Schematic diagram of stress/load penetration a) Bare SB solder and b) Nanoparticles added solder.

The hardness value decreases with the increase of ZrO_2 additions. Previously, the microstructure of the 1 % ZrO_2 additions provided narrower lamellar structure with the ZrO_2 particles pushed to top of the β-Sn and Bi phases. Together with the microstructural aspect, the ZrO_2 nanoparticles provides another form of strengthening mechanism as discrete particles. This mechanism is demonstrated in Figure 4.23 (b). The study by (Takamatsu, et al., 2012) in inspecting the influence of Ni particles in Sn0.7Cu solder alloy correlated this justification. The increase of the hardness value for the 1 % ZrO_2 additions is also attributed to the microstructure refinement by the production of smaller Bi area supported by the narrow pasty range. Result by (Gain & Zhang, 2019) reported this reason too with the presence of Ni nanoparticles in

the Sn3.0Ag0.5Cu solder alloy. Another role of the ZrO_2 nanoparticles is as a load-bearing particle. In contrast, higher percentages of ZrO_2 additions in the solder alloy reduces the hardness value marginally. It was noted that the pasty range for the 2 % ZrO_2 additions was close to the pasty range of the SB solder alloy, which reckons to the close hardness value recorded for both. Research by (Sharma, et al., 2015) showed the additions of 0.60 % ZrO_2 and graphene nanoparticles in the Sn3.0Ag0.5Cu expands the pasty range and increases the β-Sn size and lowers the hardness value. This supports the earlier statement for this research.

Thus, different trend of the microhardness value for the both nanoparticles additions was observed. However, the presence of discrete nanoparticles is concluded to produce higher hardness value which was observed for both nanoparticles. Refinement on the microstructures influenced the hardness properties more for the ZrO_2 added solder, whereas the larger sized discrete Mo nanoparticles influenced the hardness of the Mo added solders.

4.5.2 Analyses of Shear Strength of SnBi, SnBi (with Mo Nanoparticles) and SnBi (with ZrO_2 Nanoparticles) Solder Joints.

The shear strength was evaluated by using the single shear lap joint in accordance with the ASTMD1002 standard. The average maximum load and average shear stress were taken as the parameter of analyses. Both results are shown in Figure 4.24 and Figure 4.25 The raw data of each solder's average maximum load and average shear stress are presented in Appendix D.

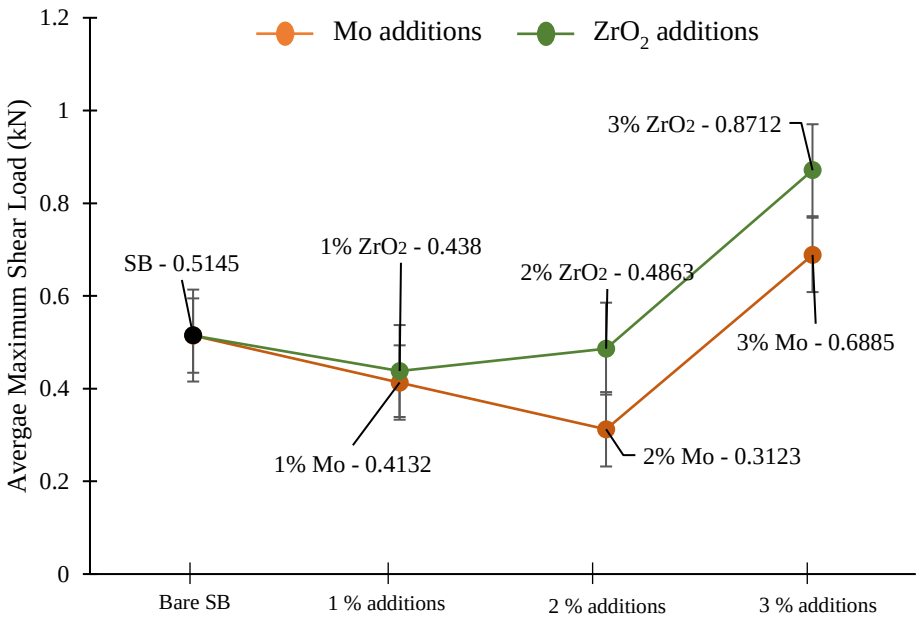

Figure 4. 24: Average maximum load of SB/Cu, SB + Mo/Cu and SB + ZrO_2/Cu nanoparticles solder alloy joints.

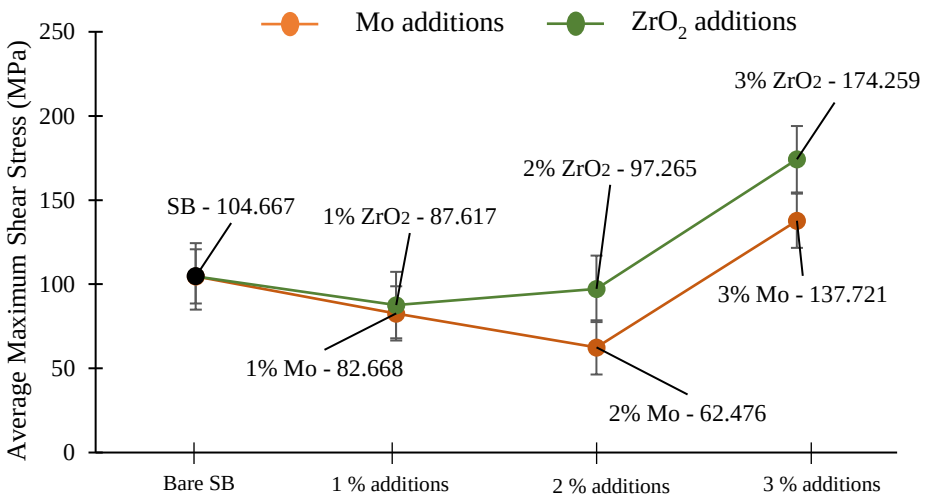

Figure 4. 25: Average maximum shear stress of SB/Cu, SB + Mo/Cu and SB + ZrO_2/Cu nanoparticles solder alloy joints.

The SB/Cu solder joint recorded an average maximum load of 0.5145 kN and the average shear stress of 104.667 MPa. The presence of Bi at the IMC layer region influences the shear stress. The influence of the shear load penetration in the SB/Cu IMC layer is shown in Figure 4.26 (a).

Comparing the 1 % and 2 % additions of Mo nanoparticles with the SB/Cu solder joint, the SB/Cu solder joint had higher average maximum shear stress and load by a percentage of 21 % and 40 % correspondingly. The 3 % Mo additions produced the average maximum shear stress and load of 137.721 MPa and 0.6885 kN respectively. These results are 32 % higher than the bare SB/Cu solder joint. Initially, the average maximum shear stress and load decreases for the 1 % and 2 % Mo additions and then increased for the 3 % Mo additions. The 3 % Mo added solder joint had 40 % and 54 % higher average maximum shear stress compared to the 1 % and 2 % Mo added solder joints.

The SB/Cu solder joint had higher average maximum shear stress and load by 16 % compared to 1 % ZrO_2 additions and by 7 % compared to 2 % ZrO_2 additions. The average maximum shear stress and load of 174.259 MPa and 0.8712 kN was recorded for the 3 % ZrO_2 additions. There was a hike of 66 % compared to the SB/Cu solder joint and 20 % compared to the 3 % Mo added solder joint. The trend for the average maximum shear stress and the load of the ZrO_2 added solder joint was clearer. Increase in the load and stress were documented with an increase in weight percentage of additions. Comparing the 1 % and 2 % ZrO_2 additions, the 3 % ZrO_2 added solder joint had an increment of 50 % and 44 % respectively for the stress and load. Figure 4.26 (b) demonstrates the distribution of the ZrO_2 nanoparticles at the intermetallic layer

in restricting the growth of thicker IMC layer. This is based on the EDX and XRD analyses. It was observed that other IMCs are produced in the ZrO_2 added SB solder alloy. These IMCs assists in inhibiting thicker Cu_6Sn_5 and Cu_3Sn IMC layer formation. This was reported earlier in section 4.4. The Zr from the ZrO_2 reacts with Sn and Cu to produce IMC's such as $ZrSn_2$ and ZrCu that restricts the vast diffusion of Cu and Sn. This happens because of the consumption of Cu and Sn to produce these IMC and limiting its availability. This was not observed for the Mo added solder joint, as there was less formation of IMCs. Moreover, the Mo nanoparticles did not appear as discrete particles at the IMC layer but reacted with Sn to produce the $MoSn_2$. This IMC alone is incapable in resisting the shear load, thus breaks at a lower shear stress. Also, based on EDX analyses, the discrete Mo nanoparticles were only detected on the top side of the IMC layers. This meant that there were no Mo nanoparticles acting as a blocking source for shearing at the IMC layer.

As observed, the 3 % ZrO_2 and 3 % Mo added solder joint provided highest shear stress and load in this research. In Chapter 1 and Chapter 2, it was mentioned there are no optimal percentage of additions that provides the trend to indicate the highest shear stress for a nanoparticle's additions. It is known that as the content of nanoparticles increases, the shear stress increases and followed by a drop after. In this study, the increase of the shear stress was optimal at 3 % of additions and is predicted to drop with a higher percentage of additions than the 3 %. To provide a comparison, in the study conducted by (Wu, et al., 2019) , the shear force of Al_2O_3 nanoparticles added in Sn0.3Ag0.7Cu was highest at 0.06 % and then dropped with 0.5 %. Similarly,

adding Al_2O_3 in the Sn9Zn produced the highest shear stress for the 1 % (38 MPa) additions compared to the 0.5 % (34 MPa) additions (Xing, et al., 2017). Separately, 0.1 % Mn additions had the highest shear stress of 58.75 MPa with the lowest value of 55.61 MPa recorded for the 0.15 % additions. These data prove that there are no optimal weight percentage of nanoparticles additions to produce the highest shear stress until it is put to test. Comparing the data from those studies, SB + 3 % ZrO_2 solder joint in this research had higher shear stress. Plus, comparison with data provided in the literature review (section 2.6.5.2) showed this addition had higher shear stress compared to other studies. This clarifies that the contribution of these nanoparticles to the shear stress and load is eminent with a higher weight percentage of nanoparticles.

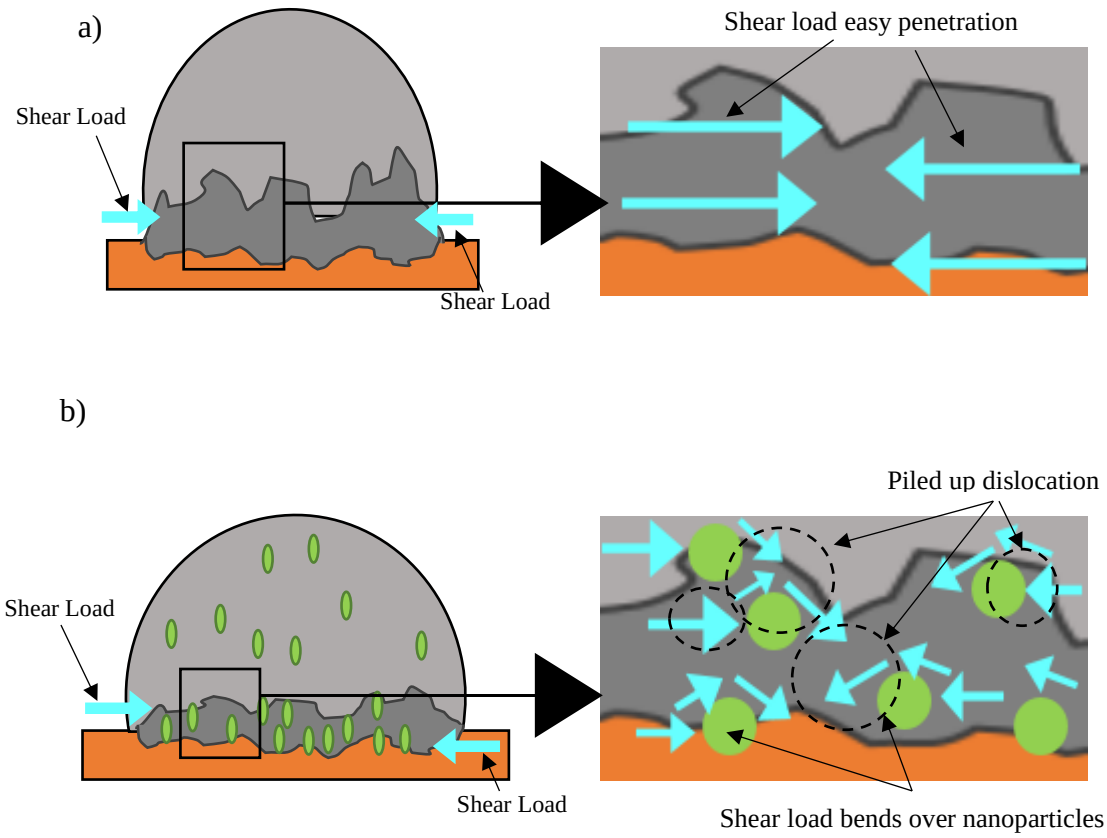

Figure 4. 26: Shear load at interface between a) SB/Cu and b) SB + 3 % ZrO_2/Cu.

4.5.3 Summary on the Mechanical Properties of SnBi, SnBi (with Mo Nanoparticles) and SnBi (with ZrO_2 Nanoparticles) Solder Joints

The highest hardness value was recorded for the 1 % ZrO_2 additions and 3 % Mo additions with the ZrO_2 additions producing the better result. Hardness properties are solely determined by the solder alloy's microstructure property and comparing with the shear strength, the latter property is more crucial. Electronic component's interconnections with the PCB board relies on the bonding of the solder joint and the solder joint's bonding is dependent on the shear strength. The solder joint of an electronic component should efficiently withstand shear and drop impact during the service time. Therefore, prioritising the shear strength is more important than the hardness. Comparing both of the nanoparticle's addition, the 3 % ZrO_2 added solder joints in all three weight percentages had higher average maximum shear stress and load. This concludes that the ZrO_2 added solder joint produced higher shear strength.

4.6 Analyses of Spreading Properties of SnBi, SnBi (with Mo Nanoparticles) and SnBi (with ZrO_2 Nanoparticles) Solder Joints.

Contact angle, spreading area and spreading ratio were taken into consideration to evaluate the spreading properties of the solders on the Cu substrate. The results of the average contact angle, average spreading area and spreading ratio are shown in Figure 4.27. The SB/Cu solder joint produced an average contact angle of 66.38 °, average spreading area of 14.45 mm^2 and a spreading ratio of 66.2 %.

The lowest contact angle was noted for the 3 % Mo added solder alloy followed by the 2 % and 1 % Mo added solder alloy. As the weight percentages of Mo nanoparticle increases, the contact angle decreases. The highest contact angle was produced for the 1 Mo % additions measuring 62.35 ° and the lowest contact angle was measured for the 3 Mo % additions measuring 53.03 °. The spreading area and ratio meanwhile had an inverse trend to the contact angle. The largest spreading area of 18.2 mm^2 was recorded for the 3 Mo % additions and the smallest area of 16.38 mm^2 was recorded for the 1 Mo % additions. Spreading ratio was highest for the 3 Mo % and the lowest for the 1 Mo % additions.

The lowest contact angle for the ZrO_2 additions was noted for the 2 % ZrO_2 (45.27 °) added solder alloy followed by the 1 % ZrO_2 (48.39 °) and 3 % ZrO_2 (56.13 °) additions. A decrease in the contact angle for the 2 % ZrO_2 nanoparticles was observed, while at a higher weight percentage of 3 % ZrO_2 additions, the contact angle increased. The spreading area and ratio were higher for the 2 % additions of ZrO_2 but lower for the 3 % ZrO_2 additions. Spreading area measuring 22.9 mm^2, 22.9 mm^2 and 18.73 mm^2 were obtained for each of the 1 %, 2 % and 3 % of ZrO_2 additions. The spreading ratio of 77.9 %, 78.7 % and 76.2% was calculated for each percentage of ZrO_2 additions.

a)

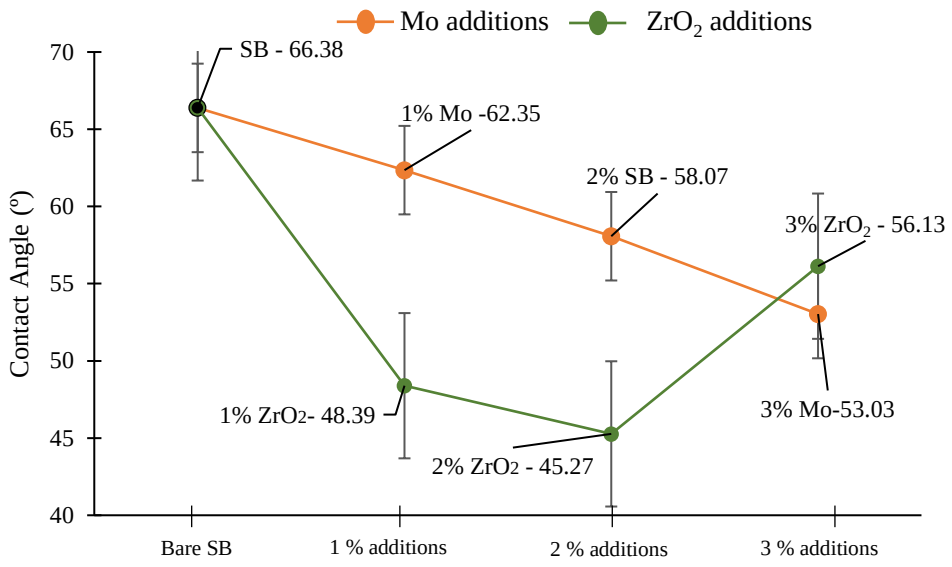
Mo additions
ZrO2 additions
Contact Angle (º)
70
65
60
55
50
45
40
SB - 66.38
1% Mo -62.35
2% SB - 58.07
3% ZrO2 - 56.13
3% Mo-53.03
1% ZrO2- 48.39
2% ZrO2 - 45.27
Bare SB
1 % additions
2 % additions
3 % additions

b)

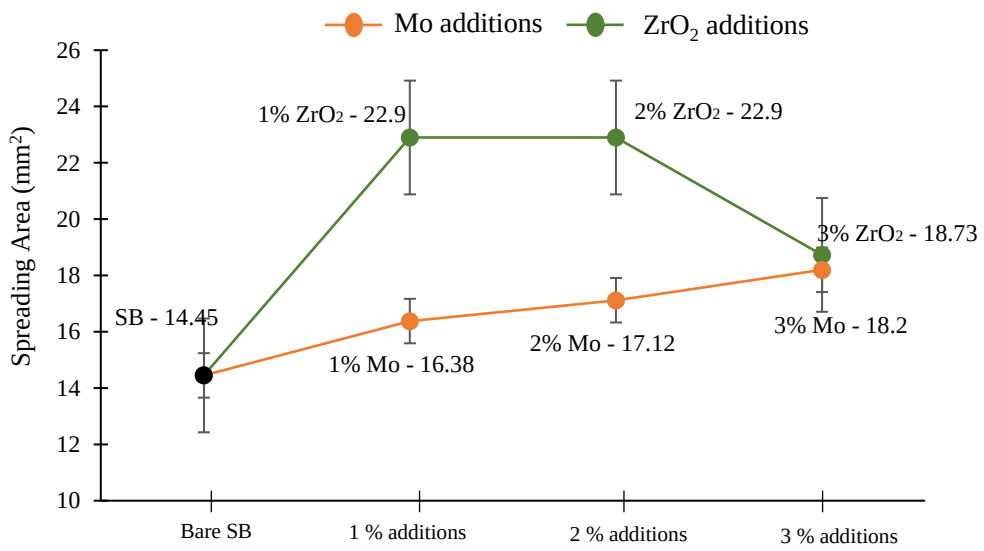
Mo additions
ZrO2 additions
Spreading Area (mm2)
26
24
22
20
18
16
14
12
10
1% ZrO2 - 22.9
2% ZrO2 - 22.9
3% ZrO2 - 18.73
SB - 14.45
1% Mo - 16.38
2% Mo - 17.12
3% Mo - 18.2
Bare SB
1 % additions
2 % additions
3 % additions

c)

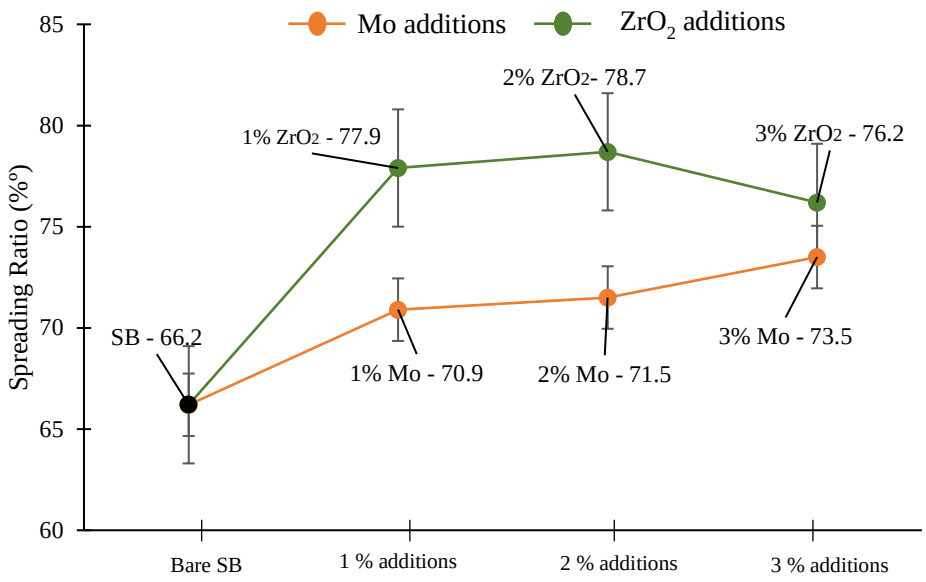

Figure 4. 27: Spreading properties of a) Average contact angle (°), b) Spreading area (mm^2) and c) Spreading ratio (%) of SB/Cu, SB + Mo/Cu b) SB/Cu, SB + ZrO_2/Cu nanoparticles solder alloy joints.

To produce better spreading ability, contact angles are recommended to be low accompanied by larger spreading area and ratio. The lowest contact angle was noted for the 2 % ZrO_2 nanoparticles added solder and the highest contact angle was noted for the pure SB solder alloy. The spreading area and ratio were higher for the 2 % ZrO_2 reinforced solder alloy, while the lowest was seen for the pure SB solder. The reinforcement of nanoparticles improved the spreading ability. The decrease in the contact angle occurred because of the reduction in the surface tension of the molten SB solder alloy. Proper segregation and mixture of the 2 % ZrO_2 and 3 % Mo nanoparticles in the solder alloy enables the nanoparticles to act as surface-active elements, therefore, reduces the surface tension of the molten solder alloy. (Jung, et al., 2018) explains a similar phenomenon with additions of TiO_2 and graphene nanoparticles in the Sn3.0Ag0.5Cu solder alloy. The larger contact angle and the lesser spreading

area happens due to the resistance of the fluidity by the nanoparticles. This situation occurred for the 1 % Mo and 3 % ZrO_2 additions as these nanoparticles were predicted to cling to the edge of the solder during melting process. The results from the EDX analyses on the IMC layer provides information to support this statement. The presences of Mo and ZrO_2 nanoparticles at the IMC layer were less for the 1 % Mo and 3 % ZrO_2 additions compared to the other weight percentages. This information is vital to inform that these nanoparticles did not exist in between the solder and substrate but existed at the edges of the solder alloy. Being surface-active elements, nanoparticles are most likely to present itself at high energy sites either at the interface or at the edges. Since these nanoparticles were not detected at the IMC layer as per the EDX analyses, it is concluded that these nanoparticles appeared at the edges of the solder alloy. Presence of the nanoparticles at the edge of the solder alloy restricts fluidity as mentioned. A different study presented this explanation too (Chellvarajoo & M.Z. Abdullah, 2018).

The smaller the particles size, the better the mixture of nanoparticles in the solder alloy, while larger sized particles will not mix properly in the molten solder alloy. This explains the production of lower contact angle for the smaller sized ZrO_2 nanoparticles additions. Some studies have also related the melting temperature as a factor that influences the spreading properties, but the melting temperature in this research did not change drastically to be the influencing factor (Ding, et al., 2018). Therefore, the spreading properties are influenced by the presences of the nanoparticles as discussed. Generally, the spreading

properties of both the Mo and ZrO_2 nanoparticles additions are favourable compared to the SB solder alloy.

CHAPTER 5

CONCLUSIONS

This study closes the research gap involving the study of nanoparticles additions to a low melting SB solder system. Plus, commonly, the studies related to the SB solder system only focuses on the element additions rather than nanoparticles additions. Based on the experimental results, some important properties related to the objectives for the conclusion can be drawn. The main components from each property will be explained in points to give a clear deduction from the research.

5.1 Thermal Properties

Proper distribution of the nanoparticles as noted for the 2 % Mo and 2 % ZrO_2 contributes to the lowest melting temperature of 139.73 °C and 140.89 °C respectively. Both temperatures were lower than the bare SB solder alloy's melting temperature (142.30 °C). Shorter pasty range due to local dissolution of the particles was also observed for these additions. Only the 1 % of additions for both nanoparticles had a higher melting temperature than the SB solder alloy and even that by a minimal range of 1-3 °C.

5.2 Microstructural Properties

The Mo and ZrO_2 nanoparticles were present in the lamellar β-Sn and Bi structure as discrete particles proven by the XRD and EDX analyses. The ZrO_2 nanoparticles added solder alloys had proper segregation of the particles with not much of agglomeration observed. The smallest average Bi area was found for the 2 % ZrO_2 additions (253981.67 μm^2) that was 41 % lower than the area for the bare SB solder. Meanwhile, Mo nanoparticles added solder had few agglomerations at higher weight content and did not perform well in refining the Bi area. Only certain area with narrower alternating lamellar structures was seen for the 3 % Mo additions. The smaller sized ZrO_2 nanoparticles produce better impact in refining the Bi area. The lower pasty range and higher undercooling helps the refinement process as well. In the 1 % Mo of additions, proper distribution of Mo nanoparticles refined the Bi area which was supported by the pasty range and undercooling.

5.3 Intermetallic Layer Properties

The IMC layers thicknesses for both nanoparticles added solder alloy showed a mixed trend. However, both the nanoparticles additions possessed thinner IMC layer than the SB/Cu joint. The IMC layer thickness for the 3 % Mo (0.8739 µm) and 3 % ZrO_2 (0.4804 µm) solder joints were thinner compared to the bare SB/Cu joint (1.26822) µm. The higher content of nanoparticles additions produced thinner IMC layer. The XRD analyses showed the presence of discrete ZrO_2 nanoparticles at the IMC layer. The Mo nanoparticles were not detected as discrete elements but reacted with Sn to produce $MoSn_2$. Presence

of nanoparticles of ZrO_2 as ceramic material contributed its effect at the joint as discrete particles and also reacted with Sn and Cu to form IMC's such as the $ZrSn_2$ and ZrCu. Inversely, Mo as the transition metal reacts with Sn and but failing to present as discrete particles.

5.4 Mechanical Properties

Influences of both the nanoparticles additions were evident for the hardness properties. The 1 % ZrO_2 nanoparticles additions produced the highest hardness value of 32.28 HV. The hardness value of 29.18 HV was calculated for the 3 % of Mo additions. The smaller sized ZrO_2 nanoparticles with proper segregation in the 1 % additions refines the microstructure of the Bi that further assisted in increasing the hardness value.

It was obvious that the 3 % Mo (137.721 MPa) and 3 % ZrO_2 (174.259 MPa) added solder joint had higher shear stress compared to the SB/Cu joint. The average maximum load was also higher in these percentage of additions. The lower percentage of additions had lower shear stress than the SB/Cu joint. The ZrO_2 additions possessed higher shear stress compared to the Mo additions. Presences of the discrete ZrO_2 nanoparticles together with the IMCs contributes to the increase in the shear stress value.

5.5 Spreading Properties

The ZrO_2 added SB solder alloy had better results compared to the Mo additions, specifically for the 2 % additions. The 2 % of ZrO_2 additions produced contact angle of 45.27 °, spreading area of 22.9 mm^2 and spreading ratio of 78.7 %. Smaller sized ZrO_2 nanoparticles distributed well at the interface and reduced the surface tension of the solder joint that eases the spreading. Then again, both nanoparticles additions had better effect on the spreading properties than the bare SB solder.

5.6 Key Conclusions/Contributions

There are few key conclusions that can be drawn from the research. One of them is relating to the melting temperature. The additions of both nanoparticles did not drastically increase and decrease the temperature because both nanoparticles did not alloy to the Sn and Bi in the SB solder. This is important to maintain a low temperature soldering and protect other device from high temperature exposure.

Another vital contribution is the enhancement of the shear stress of the SB solder alloy with the additions of the nanoparticles especially the ZrO_2 additions. The SnBi solder systems are known to possess low shear stress because of the brittleness of the Bi element. However, the introduction of these nanoparticles increased the shear stress of the SB solder joint and observed to produce competitive results with other mechanically established solder such as the SnAgCu solder alloy. This analysis closes the research gap between high

temperature and low temperature solder alloys, particularly concerning the nanoparticles additions.

Furthermore, the Bi size area was measured as the parameter of analysis for the microstructure properties. Usually, in solder alloy researches, the β-Sn and the interspacing between lamellar structures are taken as the parameter. Based on gathered literature studies and examinations, the Bi phases in acts as the influencing factor to the hardness properties for a typical SnBi system. So, measuring the Bi area will provide expressive relationship on the influence made by the nanoparticles to the microstructural and hardness properties. This is among the significant contribution from this study.

5.7 Future Works

This research work was based on the manual mixing method that relies on the physical properties of the nanoparticles to mix with the solder upon stirring. This limits the control to produce uniform segregation of nanoparticles in the solder alloy. Thus, as future works, the mixing of nanoparticles could be approached in an automated manner by dispersing the nanoparticles evenly throughout the solder.

Secondly, while the objectives of this project are to utilise a low melting temperature solder with Mo and ZrO_2 additions, limitation in the study of adding the same Mo and ZrO_2 additions in a high melting temperature solder such as SnAgCu with still appears. Therefore, for future contribution, the experiments can be approached with adding the same type of nanoparticles to the high

melting temperature solder alloys to give direct comparison from a same research between two types of solder alloys (high and low temperature).

Besides, the study has noted some drawbacks such as larger Bi area recorded for the 2 % Mo additions. To rectify this issue, further studies to improve such drawbacks can be approached directly. Through this way, the researchers can target to improve specific properties such as thermal, microstructural and mechanical of the low melting temperature solder, without jeopardising the other properties.

Adding to that, this research has opted to maintain the low melting temperature of the SB solder alloy upon adding Mo and ZrO_2. While this was successful, future research could be done to further lower the melting temperature of the SnBi solder system with the additions of different nanoparticles. By this, it will be useful to the electronic manufacturing industry as it can improve the microstructural and mechanical properties. Moreover, reinforcement of different types of nanoparticles into the SnBi solder system can provide results and literature that can be useful for further enhancement as a source of database.

LIST OF PUBLICATIONS

1. Effect of 3% molybdenum (Mo) nanoparticles on the melting, microstructure and hardness properties of as-reflowed low mass Sn-58Bi (SB) solder alloy. Journal of Advanced Research in Fluid Mechanics and Thermal Sciences 77, (1) 69-87, (2021).

2. Experimental study on the melting temperature, microstructural and improved mechanical properties of Sn58Bi/Cu solder alloy reinforced with 1%, 2% and 3% zirconia (ZrO_2) nanoparticle. Archives of Metallurgy and Materials, 66 (2), 407-418, 2021.

REFERENCES

A. Fawzy, M. Sobhy, S. A. Fayek & Nassr, E., 2013. Effect of ZnO nanoparticles addition on thermal, microstructure and tensile properties of Sn–3.5 Ag–0.5 Cu (SAC355) solder alloy.. *Journal of Materials Science Materials in Electronics,* 24(9).

A. Nabihah & M.S Nurulakmal, 2019. Effect of In Addition on Microstructure, Wettability and Strength of SnCu Solder. *Materials Today: Proceeding,* 17(3), pp. 803-809.

A. Porter, D., E. Easterling, K. & Y. Sherif, M., 2009. *Phase Transformations in Metals and Alloys.* Third ed. Florida: Taylor & Francis Group.

A.A El-Daly, A.E Hammad, A. Fawzy & D.A Nasrallh, 2013. Microstructure, mechanical properties, and deformation behavior of Sn–1.0Ag–0.5Cu solder after Ni and Sb additions. *Materials & Design,* Volume 43, pp. 40-49.

A.E Hammad & A.A. Ibrahiem, 2017. Enhancing the microstructure and tensile creep resistance of Sn-3.0Ag-0.5Cu solder alloy by reinforcing nano-sized ZnO particles. *Microelectronics Reliability,* Volume 75, pp. 187-194.

A.E.Hammad, 2018. Enhancing the ductility and mechanical behavior of Sn-1.0Ag-0.5Cu lead-free solder by adding trace amount of elements Ni and Sb. *Microelectronics Reliability,* Volume 87, pp. 133-141.

A.S.M.A. Haseeb & Leng, T. S., 2011. Effects of Co nanoparticle addition to Sn–3.8Ag–0.7Cu solder on interfacial structure after reflow and ageing.. *Intermetallics,* 19(5), pp. 707-712.

A.S.M.A. Haseeb, M.M. Arafat & Johan, M. R., 2012. Stability of molybdenum nanoparticles in Sn–3.8Ag–0.7Cu solder during multiple reflow and their influence on interfacial intermetallic compounds. *Materials Characterization,* Volume 64, pp. 27-35.

Abdelhadi, O., 2013. *Size effects in tin-based lead-free solder joints: Kinetics of bond formation and mechanical characteristics,* TUSCALOOSA: The University of Alabama.

Abtew, M. D. & Selvaduray, G., 2000. Lead-free Solders in Microelectronics.. *Materials Science and Engineering R Reports,* 27(5-6), pp. 95-141.

Affendy, M. G. & Mohamad, A. A., 2015. Effects of crosshead speeds on solder strength of Cu/Sn–9Zn/Cu lap joints. *Journal of King Saud University - Engineering Sciences,* 27(2), pp. 225-231.

Ahmed, M. et al., 2010. Influence of Ag micro-particle additions on the microstructure, hardness and tensile properties of Sn–9Zn binary eutectic solder alloy.. *Microelectronics Reliability,* 50(8), pp. 1134-1141.

Ali, B., Mohd Sabri, M. F., Jauhari, I. & Sukiman, N. L., 2016. Impact toughness, hardness and shear strength of Fe and Bi added Sn-1Ag-0.5Cu lead-free solders. *Microelectronics Reliability,* Volume 63, pp. 224-230.

Amagai, M., 1999. Characterization of chip scale packaging materials.. *Microelectronics Reliability,* pp. 1365-1377.

Amagai, M., 2008. A study of nanoparticles in Sn-Ag based lead free solders. *Microelectronics Reliability,* 48(1), pp. 1-6.

Amagai, M., 2008. A study of nanoparticles in Sn–Ag based lead free solders.. *Microelectronics Reliability,* pp. 1-16.

Amares, S. & Ervina , E., 2015. A Study of Temperature, Microstructure and Hardness Properties of Sn-3.8Ag-0.7Cu (SAC) Solder Alloy. *MATEC Web of Conferences,* Volume 27.

An, B. & Wu, . C.-m. L., 2007. *Evaluation of Wettability of Composite Solder Alloy Reinforced with Silver and Copper Particles.* Shanghai, IEEE.

Anderson, I. & Harringa, J. L., 2004. Elevated temperature aging of solder joints based on Sn-Ag-Cu: Effects on joint microstructure and shear strength. *Journal of Electronic Materials,* 33(12), p. 1485–1496.

Ani, F. C. et al., 2018. AC–xTiO2 nano-reinforced lead-free solder joint characterizations in ultra-fine package assembly. *Soldering & Surface Mount Technology,* 30(1), pp. 1-13.

Anon., 2014. *Asminternational.* [Online] Available at: www1.asminternational.org

Askeland, D. R. & Phule, P. P., 2006. *The science and engineering of materials..* s.l.:Tomson Canada.

B.S.S.Chandra Rao, J. Weng, L. Shen & K.Y. Zeng, 2010. Morphology and mechanical properties of intermetallic compounds in SnAgCu solder joints. *Microelectronic Engineering,* 87(11), pp. 2416-2422.

B.X.Vuong, et al., 2018. Role of cerium in microstructure and corrosion properties of Sn-1.0Ag solder alloys. *Materials Letters,* Volume 228, pp. 309-313.

Back, J.-H.et al., 2017. Interfacial reactions and mechanical strength of Sn-3.0Ag-0.5Cu/0.1㎛-Ni thin ENEPIG solder joint. *Journal of Welding and Joining,* 35(6), pp. 51-58.

Bai, X.-M. & Li, M., 2006. Calculation of solid-liquid interfacial free energy: A classical nucleation theory based approach. *The Journal of Chemical Physics,* 124(12).

Baker, H., 1999. *Introduction to Alloy Phase Diagrams.* s.l.:ASM International.

Bang, J. et al., 2018. *Intermetallic compound formation and mechanical property of SN-CU-XCR/CU lead-free solder joint.* Waimea, IEEE.

Bashir, M., A.S.M.A Haseeb, Saliqur Rahman, A. Z. M. & M. A. Fazal , 2016. Effect of Cobalt Doping on the Microstructure and Tensile Properties of Lead Free Solder Joint Subjected to Electromigration. *Materials Science.*

Billah, M. M., Shorowordi, K. M. & Sharif, A., 2014. Effect of micron size Ni particle addition in Sn–8Zn–3Bi lead-free solder alloy on the microstructure, thermal and mechanical properties.. *Journal of Alloys and Compounds,* Volume 585, pp. 32-39.

Billah, M., Shorowordi, K. M. & Sharif, A., 2014. Effect of micron size Ni particle addition in Sn–8Zn–3Bi lead-free solder on the microstructure, thermanl and mechanical properties.. *Journal of Alloys and Compounds,* pp. 32-39.

Boettinger, W., Kattner, U. & Moon, K.-W., 2006. *DTA and Heat Flux DSC Measurments of Alloys Melting and Freezing.* Washington: National Institute of Standards and Publication.

Bo-In Noh, Jung-Hyun Choi, Yoon, J.-W. & Jung, S.-B., 2011. Effects of cerium content on wettability, microstructure and mechanical properties of Sn–Ag–Ce solder alloys. *Journal of Alloys and Compounds,* 499(2), pp. 154-159.

C. Morando, O.Fornaro, O. Garbellini & H. Palacio, 2012. Microstructure evolution during the aging at elevated temperature of Sn-Ag-Cu solder alloys. *Procedia Materials Science,* Volume 1, pp. 80-86.

C.L. Chuang , L.C. Tsao, H.K. Lin & L.P. Feng, 2012. Effects of small amount of active Ti element additions on microstructure and property of Sn3.5Ag0.5Cu solder. *Materials Science & Engineering A,* Volume 558, p. 478–484.

C.M.T. Law, et al., 2006. Microstructure, solderability, and growth of intermetallic compounds of Sn-Ag-Cu-RE lead-free solder alloys. *Journal of Electronic Materials,* Volume 35, p. 89–93.

C.Y Lin, U.S Mohanty & J.H Chou, 2009. Synthesis and characterization of Sn–3.5Ag–XZn alloy nanoparticles by the chemical reduction method.. *Journal of Alloys and Compounds,* 472(1-2), pp. 281-285.

C.Y Lin, U.S Mohanty & J.H Chou, 2010. High temperature synthesis of Sn–3.5Ag–0.5Zn alloy nanoparticles by chemical reduction method. *Journal of Alloys and Compounds,* 501(2), pp. 204-210.

Callister, W. D. & Rethwisch, D. G., 2011. *Materials Science and Engineering.* s.l.:John Wiley and Sons.

Chang , H.-y., Chen, S.-w., Wong, D. S.-h. & Hsu, H.-F., 2003. Determination of reactive wetting properties of Sn, Sn–Cu, Sn–Ag, and Sn–Pb alloys using a wetting balance technique. *Journal of Materials Research,* 18(6).

Chang, S. et al., 2011. Effect of addition of TiO2 nanoparticles on the microstructure, microhardness and interfacial reactions of Sn3.5AgXCu solder.. *Materials & Design,* 32(10), pp. 4720-4727.

Chellvarajoo, S. & M.Z. Abdullah, 2016. Microstructure and mechanical properties of Pb-free Sn–3.0Ag–0.5Cu solder pastes added with NiO nanoparticles after reflow soldering process. *Materials & design,* Volume 90, pp. 499-507.

Chellvarajoo, S. & M.Z. Abdullah, 2018. Investigation on nano-reinforced solder paste after reflow soldering part 1: Effects of nano-reinforced solder paste on melting, hardness, spreading rate, and wetting quality. *Microelectronics Reliability,* Volume 84.

Chellvarajoo, S., M.Z. Abdullah & C.Y. Khor, 2015. Effects of diamond nanoparticles reinforcement into lead-free Sn–3.0Ag–0.5Cu solder pastes on

microstructure and mechanical properties after reflow soldering process. *Materials & Design,* Volume 82, pp. 206-215.

Chen, G. et al., 2016. Performance of Sn–3.0Ag–0.5Cu composite solder with TiC reinforcement: Physical properties, solderability and microstructural evolution under isothermal ageing. *Journal of Alloys and Compounds,* Volume 685.

Cheng, S., Huang, C.-M. & Pecht, M., 2017. A review of lead-free solders for electroncs application.. *Microelectronics Reliability,* Volume 75, pp. 77-95.

Chen, H., Wang, C., Li, M. & Tian, D., 2007. Influence of Thermal Cycling on the Microstructure and Shear strength of Sn3.5Ag0.75Cu and Sn63Pb37 solder joints on Au/Ni metallization.. *Materials Science and Technologies,* pp. 68-72.

Chen, S. et al., 2015. Sn–3.0Ag–0.5Cu Nanocomposite Solder Reinforced With Bi2Te3 Nanoparticles. *IEEE Transactions on Components, Packaging and Manufacturing Technology,* 5(8), pp. 1186 - 1196.

Chen, W., Xue, S., Wang, H. & Hu, Y., 2010. Effects of Ag on Properties of Sn-9Zn Lead-Free Solder. *Rare Metal Materials and Engineering,* 39(10), pp. 1702-1706.

Chen, X., Xue, F., Zhou, J. & Yao, Y., 2015. Effect of In on microstructure, thermodynamic characteristic and mechanical properties of Sn–Bi based lead-free solder. *Journal of Alloys and Compounds,* Volume 633, pp. 377-383.

Choudhury, S. F. & Ladani, L., 2016. Local shear stress-strain response of Sn-3.5Ag/Cu solder joint with high fraction of intermetallic compounds: Experimental analysis. *Journal of Alloys and Compounds,* Volume 680, pp. 665-676.

Chou, T.-T., Song, R.-W., Chen, W.-Y. & Duh, J.-G., 2019. Enhancement of the mechanical strength of Sn-3.0Ag-0.5Cu/Ni joints via doping minor Ni into solder alloy. *Materials Letters,* Volume 235, pp. 180-183.

Chriastelova, J. & Ozvold, M., 2008. Properties of solders with low melting point. *Journal of Alloys and Compounds,* 457(1-2), pp. 323-328.

Chu, K., Sohn, Y. & Moon, C., 2015. A comparative study of Cn/Sn/Cu and Ni/Sn/Ni solder joints for low temperature stable transient liquid phase bonding. *Scripta Materialia,* Volume 109, pp. 113-117.

D.C. Lin, et al., 2003. An investigation of nanoparticles addition on solidification kinetics and microstructure development of tin–lead solder.. *Materials Science and Engineering A,* 360(1-2), pp. 285-292.

D.C. Lin, T.S. Srivatsan, G-X. Wang & R. Kovacevic, 2007. Understanding the Influence of Copper Nanoparticles on Thermal Characteristics and Microstructural Development of a Tin-Silver Solder. *Journal of Materials Engineering and Performance,* Volume 16, p. 647–654.

Daniel , G., Unfried S., J., Tahiana, H. & J. Ramirez, A., 2010. Measuring Contact Angles on Sessile Drop Test Samples. *Welding Journal.*

Ding, M. et al., 2018. Effect of micro alumina particles additions on the interfacial behavior and mechanical properties of Sn-9Zn-1Al2O3 nanoparticles on low temperature wetting and soldering of 6061 aluminum alloys.. *Journal of Alloys and Compounds,* Volume 739, pp. 481-488.

Duan, L. et al., 2004. Microstructural evolution of Sn–9Zn–3Bi solder/Cu joint during long-term aging at 170 °C. *Journal of Alloys and Compounds,* 381(1-2), pp. 202-207.

E.A. Eid, A.N. Fouda & M. Duraia, E.-S., 2016. Effect of adding 0.5 wt% ZnO nanoparticles, temperature and strain rate on tensile properties of Sn–5.0 wt% Sb–0.5 wt% Cu (SSC505) lead free solder alloy. *Materials Science & Engineering A,* Volume 657, pp. 101-114.

E.H. Amalu, et al., 2011. A study of SnAgCu solder paste transfer efficiency and effects of optimal reflow profile on solder deposits. *Microelectronic Engineering,* 88(7), pp. 1610-1617.

E.Hare, 2013. *Intermetallics in solder joints..* SEM Lab Inc Snohomish, Washington.

E.N. Hodkin, M.G. Nicholas & D.M. Poole, 1970. The surface energies of solid molybdenum, niobium, tantalum and tungsten. *Journal of the Less Common Metals,* 20(2), pp. 93-103.

Efzan M.N, E. & Marini A, A., 2012. A Review of Solder Evolution in Electronic Application. *International Journal of Engineering and Applied Sciences,* 1(1), pp. 1-10.

Efzan Mhd Noor, E. & Singh, A., 2014. Review on the effect of alloying element and nanoparticle additions on the properties of Sn-Ag-Cu solder alloys. *Soldering & Surface Mount Technology,* 26(3), pp. 147-161.

Efzan, E. et al., 2010. Wettability and strength of In–Bi–Sn lead-free solder alloy on copper substrate. *Journal of Alloys and Compounds,* 507(1), pp. 290-296.

Efzan, E., Singh, A. & Chuen, Y. T., 2013. A review: Influence of nano particles reinforced on solder alloy.. *Soldering & Surface Mount Technology,* 25(4), pp. 229-241.

El-Daly, A. A. & Hammad, . A. E., 2010. Effects of small addition of Ag and/or Cu on the microstructure and properties of Sn–9Zn lead-free solders.. *Materials Science and Engineering,* 527(20), pp. 5212-5219.

El-Daly, A. A., Ibrahiem, A., Hammad, A. & Al-Ganainy, G., 2013. Enhancing mechanical response of hypoeutectic Sn–6.5Zn solder alloy using Ni and Sb additions. *Materials & Design,* Volume 52, pp. 966-973.

El-Daly, A., El-Taher, A. & Dalloul, T., 2014. Improved creep resistance and thermal behavior of Ni-doped Sn–3.0Ag–0.5Cu lead-free solder.. *Journal of Alloys and Compounds,* Volume 587, pp. 32-39.

El-Daly, A. et al., 2009. Thermal and mechanical properties of Sn–Zn–Bi lead-free solder alloys.. *Journal of Alloys and Compound,* 484(1-2), pp. 134-142.

Erer, A. M., Oguz, S. & Turen, Y., 2018. Influence of bismuth (Bi) addition on wetting characteristics of Sn-3Ag-0.5Cu solder alloy on Cu substrate. *Engineering Science and Technology, an International Journal,* 21(6), pp. 1159-1163.

Ervina Efzan, M. N., Amares , S. & Yap , T. C., 2013. A review: Influence of nano particles reinforced on solder alloy.. *Soldering and Surface Mount Technology,* pp. 229-241.

Ervina, E. & S.Y, T., 2013. Wettability of Molten Sn-Zn-Bi Solder on Cu Substrate. *Applied Mechanics and Materials,* Volume 315, pp. 675-680.

F.Khodabakhshi, R.Sayyadi & Javid, N. S., 2017. Lead free Sn-Ag-Cu solders reinforced by Ni-coated graphene nanosheets prepared by meechanical alloying. *Materials Science and Engineering: A,* Volume 702, pp. 371-385.

F.Q.Hu, Q.K. Zhang, J.J. Jiang & Z.L. Song, 2018. Influences of Ag addition to Sn-58Bi solder on SnBi/Cu interfacial reaction. *Materials Letters,* Volume 214, pp. 142-145.

F.X. Che, et al., 2010. The study of mechanical properties of Sn–Ag–Cu lead-free solders with different Ag contents and Ni doping under different strain rates and temperatures. *Journal of Alloys and Compounds,* 507(1), pp. 215-224.

F.Yang, et al., 2016. Properties and Microstructures of Sn-Bi-X Lead-Free Solders. *Advances in Materials Science and Engineering.*

Fathian, Z., Maleki, A. & Niroumand, B., 2017. Synthesis and characterization of ceramic nanoparticles reinforced lead-free solder.. *Ceramics International,* 43(6), pp. 5302-5310.

Fouzder, T. et al., 2011. Influence of SrTiO3 nano-particles on the microstructure and shear strength of Sn–Ag–Cu solder on Au/Ni metallized Cu pads. *Journal of Alloys and Compounds,* 509(5), pp. 1885-1892.

G.K. Sujan, A.S.M.A. Haseeb, Nishikawa, H. & M.A. Amalina, 2017. Interfacial reaction, ball shear strength and fracture surface analysis of lead-free solder joints prepared using cobalt nanoparticle doped flux. *Journal of Alloys and Compounds,* Volume 695, pp. 981-990.

G.Y. Li, X.D. Bi, Q.Chen & X.Q. Shi , 2011. Influence of Dopant on Growth of Intermetallic Layers in Sn-Ag-Cu Solder Joints. *Journal of Electronic Materials,* Volume 40, p. 165–175.

Gain, A. K. & Chan, Y., 2012. The influence of a small amount of Al and Ni nano-particles on the microstructure, kinetics and hardness of Sn-Ag-Cu solder on OSP-Cu pads.. *Intermetallics,* pp. 48-55.

Gain, A. K. & Y.C. Chan, 2012. he influence of a small amount of Al and Ni nano-particles on the microstructure, kinetics and hardness of Sn–Ag–Cu solder on OSP-Cu pads. *Intermetallics,* Volume 29, pp. 48-55.

Gain, A. K., Y.C. Chan & K.C. Yung, W., 2011. Effect of additions of ZrO2 nano-particles on the microstructure and shear strength of Sn–Ag–Cu solder on Au/Ni metallized Cu pads.. *Microelectronics Reliability,* 51(12), pp. 2306-2313.

Gain, A. K. & Zhang, L., 2019. Effects of Ni nanoparticles addition on the microstructure, electrical and mechanical properties of Sn-Ag-Cu alloy. *Materialia,* 5(2019), p. 100234.

Gancarz, T., 2016. Physical, Thermal, Mechanical Properties, and Microstructural Characterization of Sn-9Zn-XGa Alloys. *Metallurgical and Materials Transactions A,* Volume 47, p. 326–333.

Gao, L. et al., 2013. *Improvement of microstructure and mechanical properties of Sn-58Bi alloy with La2O3.* Dailan, IEEE.

Gao, L. et al., 2010. Effect of alloying elements on properties and microstructures of SnAgCu solders. *Microelectronic Engineering,* 87(11), pp. 2025-2034.

Gao, Y. et al., 2009. Nanoparticles of SnAgCu lead-free solder alloy with an equivalent melting temperature of SnPb solder alloy.. *Journal of Alloys and Compounds,* pp. 777-781.

Ghosh, M., Kar, A., Das, S. K. & Ray, A. K., 2009. Aging Characteristics of Sn-Ag Eutectic Solder Alloy with the Addition of Cu, In, and Mn. *Metallurgical and Materials Transactions A,* Volume 40, p. 2369–2376.

Gilleo, K., 1994. *The first 7000 years of soldering.,* s.l.: s.n.

Giuranno, D., Delsante, S., Borzone, G. & Novakovic, R., 2016. Effects of Sb addition on the properties of Sn-Ag-Cu/(Cu, Ni) solder systems. *Journal of Alloys and Compounds,* Volume 689, pp. 918-930.

Gong, J., Liu, C., P. Conway, P. & V. Silberschmidt, V., 2009. Formation of Sn dendrites and SnAg eutectics in a SnAgCu solder. *Scripta Materialia,* 61(7), pp. 682-685.

Gong, J., Liu, C., P. Conway, P. & V. Silberschmidt, V., 2009. Initial formation of CuSn intermetallic compounds between molten SnAgCu solder and Cu substrate. *Scripta Materialia,* 60(5), pp. 333-335.

Guo, W.-T., Liang, C.-L. & Lin, K.-L., 2019. he effects of Cu alloying on the microstructure and mechanical properties of Zn-25Sn-xCu (x= 0–1.0 wt%) high temperature Pb-free solders. *Materials Science and Engineering: A,* Volume 750, pp. 117-124.

Gu, Y. et al., 2015. Effect of nano-Fe2O3 additions on wettability and interfacial intermetallic growth of low-Ag content Sn–Ag–Cu solders on Cu substrates. *Journal of Alloys and Compounds,* Volume 627, pp. 39-47.

H. Lee, J. et al., 2013. The effects of solder deformation on the wetting characteristics and interfacial reaction of Sn–3.5Ag solders on Cu substrates in fluxless soldering. *Journal of Materials Science: Materials in Electronics,* Volume 24, p. 3255–3261.

H. Tsukamoto, T. Nishimura, S. Suenaga & Nogita, K., 2010. Shear and tensile impact strength of lead-free solder ball grid arrays placed on Ni (P)/Au surface-finished substrates. *Materials Science and Engineering B,* 171((1-3_).

H.F. Zou, Q.K. Zhang & Z.F. Zhang, 2012. Interfacial microstructure and mechanical properties of SnBi/Cu joints by alloying Cu substrate.. *Materials Science and Engineering: A,* Volume 532, pp. 167-177.

Halbo , L. & Ohlckers, P., 1995. *Electronic component, packaging and production.,* Oslo: University of Oslo.

Haseeb, A., Arafat, M. & Johan, M. R., 2012. Stability of molybdenum nanoparticles in Sn–3.8Ag–0.7Cu solder during multiple reflow and their influence on interfacial intermetallic compounds.. *Materials Characterization,* pp. 27-35.

Haseeb, A., Arafat, M. M., Tay, S. L. & Leong, Y. M., 2017. Effects of metallic nanoparticles on interfacial intermetallic Compounds in tin-based solders for microelectronic packaging.. *Journal of Electronic Materials,* 46(10), p. 5503–5518.

Haseeb, A. & Leng, T. S., 2011. Effects of Co nanoparticle addition to Sn–3.8Ag–0.7Cu solder on interfacial structure after reflow and ageing.. *Intermetallics,* p. 707–712.

Haseeb, Y.M.Leong & M.M.Arafat, 2014. In-situ alloying of Sn–3.5Ag solder during reflow through Zn nanoparticle addition and its effects on interfacial intermetallic layers. *Intermetallics,* Volume 54, pp. 86-94.

Hongtao, M. & Suhling, J. C., 2009. A review of mechanical properties of lead-free solders for electronic packaging. *Journal of Materials Science,* 44(5), pp. 1141-1158.

Hsiao, L.-Y. & Duh, J.-G., 2005. Synthesis and Characterization of Lead-Free Solders with Sn-3.5Ag-xCu (x = 0.2 , 0.5, 1.0) Alloy Nanoparticles by the Chemical Reduction Method. *Journal of The Electrochemical Society,* 152(9), pp. 105-109.

Hsu, H.-L.et al., 2019. Impurity evaporation and void formation in Sn/Cu solder joints. *Materials Chemistry and Physics,* Volume 225, pp. 153-158.

Huang, H.-z., Lu, D., Shuai, G.-w. & Wei, X.-q., 2016. Effects of Phosphorus Addition on the Corrosion Resistance of Sn–0.7Cu Lead-Free Solder Alloy. *Transactions of the Indian Institute of Metals,* 69(8).

Huizhen, H., Gewang, S., Xiuqin, W. & Chuanqiang, Y., 2017. Effects of sulfur addition on the wettability and corrosion resistance of Sn-0.7Cu lead-free solder. *Microelectronics Reliability,* Volume 74, pp. 15-21.

Hu, J., Hu, A., Li, M. & Mao , D., 2010. Depressing effect of 0.1 wt.% Cr addition into Sn–9Zn solder alloy on the intermetallic growth with Cu substrate during isothermal aging.. *Materials Characterization,* 61(3), pp. 355-361.

Humpston, G. & Jacobson, D. M., 2004. *Principles of Soldering.* s.l.:ASM International.

Hu, X., Li, K. & Min, Z., 2013. Microstructure evolution and mechanical properties of Sn0.7Cu0.7Bi lead-free solders produced by directional solidification. *Journal of Alloys and Compounds,* Volume 566, pp. 239-245.

Hu, X. et al., 2014. Effect of TiO2 nanoparticle addition on electroless Ni–P under bump metallization for lead-free solder interconnection. *Materials Science and Engineering: A,* Volume 600, pp. 67-75.

Hu, X. et al., 2017. Shear strength and fracture behavior of reflowed Sn3.0Ag0.5Cu/Cu solder joints under various strain rates. *Journal of Alloys and Compounds,* Volume 690, pp. 720-729.

Hu, Y., Ma, L. & Guo, F., 2016. *Influence of nano-particles on creep behaviors of Cu/Sn-0.3Ag-0.7Cu-xPOSS/Cu composite solder joints.* Wuhan, IEEE.

Ichitsubo, T. et al., 2005. Control of compound forming reaction at the interface between SnZn solder and Cu substrate. *Journal of Alloys and Compounds,* 392(1-2), pp. 200-205.

J. C. Boareto, et al., 2010. *Introduction of nanosized Al2O3 in Sn-Ag3.5 solders by mechanical alloying.* Berlin, IEEE.

J. Sundelin, J., T. Nurmi, S., K. Lepisto, T. & O. Ristolainen, E., 2006. Mechanical and microstructural properties of SnAgCu solder joints. *Materials Science and Engineering: A,* 420(1-2), pp. 55-62.

J. W. Morris, J., Goldstein, J. F. & Z. Mei, 1993. Microstructure and mechanical properties of Sn-In and Sn-Bi solders. *The Journal of The Minerals,* 45(7), pp. 25-27.

J.Keller, D.Baither, U.Wilke & G.Schmitz, 2011. Mechanical properties of Pb-free SnAg solder joint. *Acta Materialia,* 59(7), pp. 2731-2741.

J.Shen & Y.C Chan, 2009. Research advances in nano-composite solders. *Microelectronics Reliability,* 49(3), pp. 223-234.

Jeon, A.-J., Kim, S.-J., Lee, S.-H. & Kang, C.-Y., 2013. Effect of Indium Content on the Melting Point, Dross, and Oxidation Characteristics of Sn-2Ag-3Bi-xIn Solders. *Journal of Electronic Packaging,* 135(2), p. 210061–210065.

Jeon, S.-j.et al., 2012. Evaluation of drop reliability of Sn–37Pb solder/Cu joints using a high speed lap-shear test. *Microelectronic Engineering,* Volume 91, pp. 147-153.

Jing, Y., Sheng, G., Huang, Z. & Zhao, G., 2013. Effects of 0.1 wt% Ni addition and rapid solidification process on Sn–9Zn solder. *Journal of Materials Science: Materials in Electronics,* Volume 24, p. 4868–4872.

Jung, D.-H., Sharma, A. & Jung, J.-P., 2018. Influence of dual ceramic nanomaterials on the solderability and interfacial reactions between lead-free Sn-Ag-Cu and a Cu conductor. *Journal of Alloys and Compounds,* Volume 743, pp. 300-313.

K. Mehrabi, et al., 2016. Effect of alumina nanoparticles on the microstructure and mechanical durability of meltspun lead-free solders based on tin alloys. *Journal of Alloys and Compounds,* Volume 688, pp. 143-155.

K.Kannachai & Kongchayasukawat, R., 2018. Property alterations of Sn-0.6Cu-0.05Ni-Ge lead-free solder by Ag, Bi, In and Sb addition. *Transactions of Nonferrous Metals Society of China,* 28(6), pp. 1166-1175.

K.N. Prabhu, Deshapande, P. & Satyanarayan, 2012. Effect of cooling rate during solidification of Sn–9Zn lead-free solder alloy on its microstructure, tensile strength and ductile–brittle transition temperature. *Materials Science and Engineering: A,* Volume 533, pp. 64-70.

K.S. Kim, K.W. Ryu, C.H. Yu & J.M. Kim, 2005. The formation and growth of intermetallic compounds and shear strength at Sn–Zn solder/Au–Ni–Cu interfaces. *Microelectronics Reliability,* 45(3-4), pp. 647-655.

Kanlayasiri, K. & Meesathien, N., 2018. Effects of zinc oxide nanoparticles on properties of SAC0307 lead-free solder paste.. *Advances in Materials Science and Engineering,* pp. 1-10.

Kanlayasiri, K., Mongkolwongrojn, M. & Ariga, T., 2009. Influence of indium addition on characteristics of Sn–0.3Ag–0.7Cu solder alloy.. *Journal of Alloys and Compounds,* 485(1-2), pp. 225-230.

Kanlayasiri, K. & Sukpimai, K., 2016. Effects of indium on the intermetallic layer between low-Ag SAC0307-xIn lead-free solders and Cu substrate. *Journal of Alloys and Compounds,* Volume 668, pp. 169-175.

Kar, A. et al., 2008. Evolution of mechanical and electrical properties of tin–lead and lead freesolder to copper joint interface.. *Materials Letters,* pp. 151-154.

Kar, A., Ghosh, M., Ray, A. K. & Ghosh, R. N., 2007. Effect of copper addition on the microstructure and mechanical properties of lead free solder alloy. *Materials Science and Engineering: A,* 459(1–2), pp. 69-74.

Kattner, U. R., 2002. Phase diagrams for lead-free solder alloys.. *JOM,* pp. 45-51.

Khrapak, S. A., 2020. Lindemann melting criterion in two dimensions. *Physical Review Resarch ,* Volume 2.

Kikuchi, S. et al., 2001. Strength of bonding interface in lead-free Sn alloy solders.. *Materials Science and Engineering,* pp. 475-479.

Kim, D.-G.et al., 2008. Effect of reflow numbers on the interfacial reaction and shear strength of flip chip solder joints. *Journal of Alloys and Compounds,* 458(1-2), pp. 253-260.

Kindesjo, U., 2001. *Phasing out lead in solders,* s.l.: s.n.

Koo, J. et al., 2014. New Sn–0.7Cu-based solder alloys with minor alloying additions of Pd, Cr and Ca. *Journal of Alloys and Compounds,* Volume 608, pp. 126-132.

Koppes , J. P. et al., 2012. Utilizing the thermodynamic nanoparticle size effects for low temperature Pb-free solder.. *Materials Science and Engineering,* pp. 197-204.

Koscielski, M., Bukat, K., Jakubowska, M. & Mlozniak, A., 2010. *Application of silver nanoparticles to improve wettability of SnAgCu solder paste.* Warsaw, IEEE.

Kumar, K. M., V. Kripesh & Tay, A. A., 2008. Single-wall carbon nanotube (SWCNT) functionalized Sn–Ag–Cu lead-free composite solders.. *Journal of Alloys and Compounds,* 450(1-2), pp. 229-237.

L Wang, D.Q Yu, J Zhao & M.L Huang, 2002. Improvement of wettability and tensile property in Sn–Ag–RE lead-free solder alloy. *Materials Letters,* 56(6), pp. 1039-1042.

L. C. Tsao, et al., 2010. Effects of nano-Al2O3 additions on microstructure development and hardness of Sn3.5Ag0.5Cu solder. *Materials and Design,* 31(10), pp. 4831-4835.

L. Silva, B., G.C. Xavier, M., Garcia, A. & E. Spinelli, J., 2017. Cu and Ag additions affecting the solidification microstructure and tensile properties of Sn-Bi lead-free solder alloys. *Materials Science and Engineering: A,* Volume 705, pp. 325-334.

L.C Tsao, 2011. Suppressing effect of 0.5 wt.% nano-TiO2 addition into Sn–3.5Ag–0.5Cu solder alloy on the intermetallic growth with Cu substrate during isothermal aging. *Journal of Alloys and Compounds,* 509(33), pp. 8441-8448.

L.C Tsao, et al., 2013. Effects of nano-Al2O3 particles on microstructure and mechanical properties of Sn3.5Ag0.5Cu composite solder ball grid array joints on Sn/Cu pads. *Materials and Design,* Volume 50, p. 774–781.

L.C. Tsao, C.H. Huang, C.H. Chung & R.S. Chen, 2012. Influence of TiO2 nanoparticles addition on the microstructural and mechanical properties of Sn0.7Cu nano-composite solder.. *Materials Science and Engineering: A,* Volume 545, pp. 194-200.

L.C. Tsao & S.Y. Chang, 2010. Effects of Nano-TiO2 additions on thermal analysis, microstructure and tensile properties of Sn3.5Ag0.25Cu solder. *Materials & Design,* 31(2), pp. 990-993.

L.S.Silva, J.S.Souza & R.A.G.Silva , 2019. Effects of Ag addition on phase transitions, microstructures and solder/copper interfaces of Sn99.1-xCu0.9Agx alloys. *Journal of Thermal Analysis and Calorimetry,* Volume 136, p. 2205–2210.

Lai, Y., Hu, X., Jiang, X. & Li, Y., 2018. Effect of Ni Addition to Sn0.7Cu Solder Alloy on Thermal Behavior, Microstructure, and Mechanical Properties. *Journal of Materials Engineering and Performance,* 27(12).

Laurila, T., Vuorinen, V. & Kivilahti, J., 2005. Interfacial reactions between lead-free solders and common base materials.. *Materials Science and Engineering,* pp. 1-60.

Lee , L. M. & Mohamad, A. A., 2013. Interfacial Reaction of Sn-Ag-Cu Lead-Free Solder Alloy on Cu: A Review. *Advances in Materials Science and Engineering,* Volume 2013.

Lee, C.-J., Min, K. D., Park, H. J. & Jung, S.-B., 2020. Mechanical properties of Sn-58 wt%Bi solder containing Ag-decorated MWCNT with thermal aging tests. *Journal of Alloys and Compounds,* Volume 820.

Lee, H.-T. & Chen, M.-H., 2002. Influence of intermetallic compounds on the adhesive strength of solder joints. *Materials Science and Engineering: A,* 333(1-2), pp. 24-34.

Lee, J.-S.et al., 2008. Effects of Co addition in eutectic Sn–3.5Ag solder on shear strength and microstructural development. *Microelectronic Engineering,* 85(7), pp. 1577-1583.

Lee, J. & Jeong, H., 2014. Fatigue life prediction of solder joints with consideration of frequency, temperature and cracking energy density.. *International Journal of Fatigue,* pp. 264-270.

Lee, N.-C., 2002. *Reflow solderong processes and troubleshootiong SMT, BGA, CSP and Flip Chip Tehnologies.* s.l.:Newnes.

Lee, Y.-H. & Lee, H.-T., 2007. Shear strength and interfacial microstructure of Sn–Ag–xNi/Cu single shear lap solder joints. *Materials Science and Engineering: A,* 444(1-2), pp. 75-83.

Leong, Y. M. & A.S.M.A. Haseeb, 2012. *Soldering and interfacial characteristics of Sn-3.5Ag solder containing zinc nanoparticles.* Ipoh, IEEE.

Li, M. & Kuribayashi, K., 2006. Free solidification of undercooled eutectics.. *Materials Transactions,* pp. 2889-2897.

Lin, H.-J. & Chuang, T.-H., 2010. Effects of Ce and Zn additions on the microstructure and mechanical properties of Sn–3Ag–0.5Cu solder joints. *Journal of Alloys and Compounds,* 500(2), pp. 167-174.

Lin, J.-C., Liang, C.-L. & Lin, K.-L., 2019. Joint effects of Ti and Cu additions on microstructure and mechanical properties of Zn-25Sn-xCu-yTi high-temperature Pb-free solders. *Materials Science and Engineering: A,* Volume 765, p. 138323.

Lin, Y.-J., Zhou, M.-B., Ma, X. & Zhang, X.-P., 2016. *Influence of the solder volume and reflow process on solderability of the aluminum solder paste and reliability of Sn-0.3Ag-0.7Cu/6061Al solder joints in packages of LED lighting components and structures.* Wuhan, IEEE, pp. 1028-1032.

Liu , Y. et al., 2016. Microstructure and mechanical properties of as-reflowed Sn58Bi composite solder pastes. *Journal of Materials Processing Technology,* Volume 238, pp. 290-296.

Liu, J.-C.et al., 2015. Thermal property, wettability and interfacial characterization of novel Sn–Zn–Bi–In alloys as low-temperature lead-free solders. *Materials & Design,* Volume 84, pp. 331-339.

Liu, P., Gu, X., Fu, H. & Liu, Y., 2016. *The effects of Cu nanoparticles addition in Sn-3.0Ag-0.5Cu solder paste on the microstructure and shear strength of the solder joints.* Wuhan, s.n.

Liu, P., Yao, P. & Liu, J., 2009. Effect of multiple reflows on interfacial reaction and shear strength of SnAgCu and SnPb solder joints with different PCB finishes. *Journal of Alloys and Compounds,* 470(1-2), pp. 188-194.

Liu, Y. et al., 2017. Shear strength of LED solder joints using SAC-nano Cu solder pastes. *Journal of Semiconductors,* 38(9).

Li, Y. & Y.C Chan, 2015. Effect of silver (Ag) nanoparticle size on the microstructure and mechanical properties of Sn58Bi–Ag composite solders. *Journal of Alloys and Compounds,* Volume 645, pp. 566-576.

Luo, T., Chen, Z., Hu, A. & Li, M., 2012. Study on melt properties, microstructure, tensile properties of low Ag content Sn–Ag–Zn Lead-free solders. *Materials Science and Engineering: A,* Volume 556, pp. 885-890.

Luo, T., Hu, A., Li, M. & Mao, D., 2009. *Studies on microstructure and mechanical properties of Sn-Zn-Bi-Cr lead-free solder*. Beijing, IEEE.

Lu, T. et al., 2019. Microstructure, mechanical properties, and interfacial reaction with Cu substrate of Zr-modified SAC305 solder alloy. *Journal of Alloys and Compounds,* Volume 781, pp. 633-643.

Lu, Y. et al., 2018. Effect of Cu element addition on the interfacial behavior and mechanical properties of Sn9Zn-1Al2O3 soldering 6061 aluminum alloys: First-principle calculations and experimental research. *Journal of Alloys and Compounds,* Volume 765, pp. 128-139.

M. Abdelhadi, O. & Ladani, L., 2012. IMC growth of Sn-3.5Ag/Cu system: Combined chemical reaction and diffusion mechanisms. *Journal of Alloys and Compounds,* Volume 537, pp. 87-99.

M. Sahan, et al., 2019. Determination of Metal Content of Waste Mobile Phones and Estimation of Their Recovery Potential in Turkey. *International journal of environmental research and public health,* 16(5).

M. Shim, 2008. *Phase Transformations. In Introduction to Engineering Materials,* s.l.: s.n.

M.Li & Kuribayashi, K., 2006. Free Solidification of Undercooled Eutectics. *Materials Transactions,* 47(12), pp. 2889-2897.

M.M. Arafat, A.S.M.A. Haseeb & Johan, M. R., 2011. Interfacial reaction and dissolution behavior of Cu substrate in molten Sn-3.8Ag-0.7Cu in the presence of Mo nanoparticles. *Soldering & Surface Mount Technology,* 23(3), p. 140 – 149.

M.R. Harrison, J.H. Vincent & H.A.H. Steen, 2001. Lead-free reflow soldering for electronics assembly. *Soldering & Surface Mount Technology,* 13(3), pp. 21-38.

Ma, D.-l. & Wu, P., 2015. Effects of Zn addition on mechanical properties of eutectic Sn–58Bi solder during liquid-state aging. *Transactions of Nonferrous Metals Society of China,* 25(4), pp. 1225-1233.

Maeshima, T., Ikehata, H., Terui, K. & Sakamoto, Y., 2016. Effect of Ni to the Cu substrate on the interfacial reaction with Sn-Cu solder. *Materials & Design,* Volume 103, pp. 106-113.

Mahdavifard, M. H. et al., 2015. The effect of iron and bismuth addition on the microstructural, mechanical, and thermal properties of Sn–1Ag–0.5 Cu solder alloy. *Microelectronics Reliability,* 55(9-10), pp. 1886-1890.

Ma, H. T. & Suhling J., J., 2009. A review of mechanical properties of lead-free solders for electronic packaging. *Materials Science,* pp. 1141-1158.

Manko, H. H., 2001. *Solders and Soldering.* s.l.:McGraw Hill 4th Edition.

Ma, X., Wang, F., Qian, Y. & Yoshida, F., 2003. Development of Cu–Sn intermetallic compound at Pb-free solder/Cu joint interfaceMaterials Letters. *Materials Letters,* 27(22-23), pp. 3361-3365.

Mayappan, R. & Ahmad, Z. A., 2010. Effect of Bi addition on the activation energy for the growth of Cu5Zn8 intermetallic in the Sn-Zn lead-free solder. *Intermetallics,* 18(4), pp. 730-735.

Mayappan, R. et al., 2006. Effect of sample perimeter and temperature on Sn–Zn based lead-free solders. *Materials Letters,* 60(19), pp. 2383-2389.

Mayappan, R. et al., 2007. The effect of crosshead speed on the joint strength between Sn-Zn-Bi lead-free solders and Cu substrate. *Journal of Alloys and Compounds,* 436(1-2), pp. 112-117.

Mayappan, R. & Jasli, N. A., 2018. Silver effect on the intermetallic growth in the Sn-8Zn-3Bi lead-free solder. *Materials Today:Proceeding,* 5(9), pp. 17553-17560.

Ma, Y. et al., 2017. Reinforcement of graphene nanosheets on the microstructure and properties of Sn58Bi lead-free solder. *Materials & Design,* Volume 113, pp. 264-272.

Md Hasnine , 2018. Effects of In and Sb addition on the thermal and wetting behavior of Sn-3.5Ag solder. *Soldering & Surface Mount Technology,* 30(4), pp. 233-240.

Mei, Z., Holder, H. A. & Plas, H. A. V., 1996. Low-Temperature Solders. *Hewlett-Packard Journal,* Issue 10.

Miao, H.-W. & Duh, J.-G., 2001. Microstructure evolution in Sn–Bi and Sn–Bi–Cu solder joints under thermal aging. *Materials Chemistry and Physics,* 71(3), pp. 255-271.

Mohammed, G. & El-Gamal, S., 2018. Influence of SiC nanoparticles addition on the microstructure, thermal and tensile properties of Sn–Zn–Ag solder alloy. *Materials Research Express,* 5(8).

Murad, N., Aisha, S. R. & Mahadzir Ishak@Muhammad, 2017. Effects of Cooling Rates on Microstructure, Wettability and Strength of Sn3.8Ag0.7Cu Solder Alloy. *Procedia Engineering,* Volume 184, pp. 266-273.

N Mookam, Tunthawiroon, P. & Kanlayasiri, K., 2018. Effects of copper content in Sn-based solder on the intermetallic phase formation and growth during soldering. *IOP Conf. Series: Materials Science and Engineering,* Volume 361.

N.A. Saleh, M.I.I. Ramli & M.A.A Mohd Salleh, 2017. Effect of Zinc Additions on Sn-0.7Cu-0.05Ni Lead-Free Solder Alloy. *IOP Conference Series: Materials Science and Engineering,* Volume 238.

N.K. Liyana, M.A. Fazal, A.S.M.A. Haseeb & Rubaiee , S., 2019. Effect of Zn incorporation on the electrochemical corrosion properties of SAC105 solder alloys. *Journal of Materials Science: Materials in Electronics,* Volume 30, p. 7415–7422.

Nasir, N. M. et al., 2014. Effect of TiO2 Reinforcement on Microstructure and Microhardness of Low-Silver SAC107 Lead-Free Solder Composite Solder. *Material Science Forum,* Volume 803, pp. 273-277.

Nasir, S. S. M. et al., 2019. Effect of TiO2 nanoparticles on the horizontal hardness properties of Sn-3.0Ag-0.5Cu-1.0TiO2 composite solder. *Ceramics International,* 45(15), pp. 18563-18571.

Okamoto, H., 2010. *Phase Diagrams for Binary Alloys.* Second ed. Ohio: ASM International.

P. Lobry, L. Błaż , M. Sugamata & A. Kula, 2011. Effect of rapid solidification on structure and mechanical properties of Al-6Mn-3Mg alloy. *Archive Materials Science and Engineering,* 49(2), pp. 97-102.

P.L. Tu, Y.C. Chan & J.K.L. Lai, 1997. Effect of intermetallic compounds on the thermal fatigue of surface mount solder joints. *IEE,* 20(1), pp. 87 - 93.

Park, B.-G., Myung, W.-R., Lee, C.-J. & Jung, S.-B., 2020. Mechanical, electrical, and thermal reliability of Sn-58wt.%Bi solder joints with Ag-decorated MWCNT for LED package component during aging treatment. *Composites Part B: Engineering,* Volume 182.

Peng, F. et al., 2019. Microstructure of Sn-20In-2.8Ag solder and mechanical properties of joint with Cu. *Soldering & Surface Mount Technology,* 31(1), pp. 1-5.

Q.B.Tao, et al., 2016. Effect of Ni and Sb additions and testing conditions on the mechanical properties and microstructures of lead-free solder joints. *Materials Science and Engineering: A,* Volume 669, pp. 403-416.

Q.S. Zhu, et al., 2005. *Effect of Zn addition on microstructure of Sn-Bi joint.* Beijing, IEEE.

Q.V Bui & S.B Jung, 2013. Characterization of low speed shear test reliability of Sn–1.0Ag–XCe/ENEPIG solder joint. *Journal of Alloys and Compounds,* Volume 560, pp. 54-61.

R. Askeland, D., P. Fulay, . P. & J. Wright, W., 2011. *The Science and Engineering of Materials..* 6 ed. s.l.:Cengage Learning.

R. Kattner, U., 2002. Phase diagrams for lead-free solder alloys. *The Journal of The Minerals,* 54(12), pp. 45-51.

R. Khanna, R. Cayumil, P.S. Mukherjee & V. Sahajwalla, 2014. A Novel Recycling Approach for Transforming Waste Printed Circuit Boards into a Material Resource. *Procedia Environmental Sciences,* Volume 21, pp. 42-54.

R. Kotadia, H., D.Howes, P. & H.Mannan, S., 2014. A review: On the development of low melting temperature Pb-free solders.. *Microelectronics Reliability,* 54(6-7), pp. 1253-1273.

R.Garcia, L., R.Osório, W., C.Peixoto, L. & Garcia, A., 2010. Mechanical properties of Sn–Zn lead-free solder alloys based on the microstructure array. *Materials Characterization,* 61(2), pp. 212-220.

R.M Shalaby, 2010. Effect of rapid solidification on mechanical properties of a lead free Sn–3.5Ag solder.. *Journal of Alloys and Compounds,* 505(1), pp. 113-117.

Ramli, M. et al., 2016. Effect of TiO2 additions on Sn-0.7Cu-0.05Ni lead-free composite solder. *Microelectronics Reliability,* Volume 65, pp. 255-264.

Ren, G. & N. Collins, M., 2017. The effects of antimony additions on microstructures, thermal and mechanical properties of Sn-8Zn-3Bi alloys. *Materials & Design,* Volume 119, pp. 133-140.

Ren, G. & N.Collins, M., 2019. On the mechanism of Sn tunnelling induced intermetallic formation between Sn-8Zn-3Bi solder alloys and Cu substrates. *Journal of Alloys and Compounds,* Volume 791, pp. 559-566.

Roubaud, P. et al., 2001. *Impact of Intermetallic Growth on the Mechanical Strength.* s.l., APEX.

Rui, M. et al., 2012. *TiO2 nanoparticles functionalized Sn/3.0Ag/0.5Cu lead-free solder.* Guilin, IEEE.

S. Delsante, R. Novakovic & G. Borzone, 2018. Synthesis, characterization and thermal stability of SnAg and SnAgCu. *Journal of Alloys and Compounds,* Volume 747, pp. 385-393.

S. M. L. Nai, J. Wei & M. Gupta, 2006. Lead-free solder reinforced with multiwalled carbon nanotubes. *Journal of Electronic Materials,* 35(7), p. 1518–1522.

S.Amares, Ervina Efzan, M. N. & T.C Yap, 2014. Characterizations of Physical Properties of Sn-Bi Solder Alloy. *Advanced Materials Research,* Volume 845, pp. 261-265.

S.Chellvarajoo, Abdullah, M. & Samsudin, Z., 2015. Effects of Fe2NiO4 nanoparticles addition into lead free Sn–3.0Ag–0.5Cu solder pastes on microstructure and mechanical properties after reflow soldering process. *Materials & Design,* Volume 67, pp. 197-208.

S.H.Kim & Yu, J., 2013. Fe addition to Sn-3.5Ag solder for the suppression of Kirkendall void formation. *Scripta Materialia,* 69(3), pp. 254-257.

S.L. Tay, et al., 2013. Influence of Ni nanoparticle on the morphology and growth of interfacial intermetallic compounds between Sn–3.8Ag–0.7Cu lead-free solder and copper substrate. *Intermetallics,* Volume 33, pp. 8-15.

S.Wiese & Wolter, K.-J., 2004. Microstructure and creep behaviour of eutectic SnAg and SnAgCu solders. *Microelectronics Reliability,* 44(12), pp. 1923-1931.

Salimin, M., 2008. *Properties of low temperature Indium-based ternary lead free solders system,* s.l.: s.n.

Salleh, M. et al., 2012. Mechanical properties of Sn–0.7Cu/Si3N4 lead-free composite solder.. *Materials Science and Engineering: A,* Volume 556, pp. 633-637.

Salleh, M. M., McDonald, S. D. & Nogita, K., 2017. Effects of Ni and TiO2 additions in as-reflowed and annealed Sn0.7Cu solders on Cu substrates. *Journal of Materials Processing Technology,* Volume 242, pp. 235-245.

Satyanarayan & K.N Prabhu, 2011. Wetting behaviour and interfacial microstructure of Sn–Ag–Zn solder alloys on nickel coated aluminium substrates. *Materials Science and Technology,* 27(7), pp. 1157-1162.

Seelig, K., 1995. *A study of lead free solder alloys,* Cranston: AIM Inc.

Shang, S. et al., 2019. Enhancement of hardness of bulk solder by doping Cu nanoparticles at the interface of Sn/Cu solder joint. *Microelectronic Engineering,* Volume 208, pp. 47-53.

Sharma, A. et al., 2015. Electromigration of composite Sn-Ag-Cu solder bumps.. *Electronic Materials Letters,* 11(6).

Shen & Chan, 2009. Effects of ZrO2 nanoparticles on the mechanical properties of Sn–Zn solder joints on Au/Ni/Cu pads. *Journal of Alloys and Compounds,* 477(1-2), pp. 552-559.

Shen, J. & Chan, Y., 2009. Research advances in nano-composite solders.. *Microelectronics Reliability,* pp. 223-234.

Shen, J. et al., 2014. Effects of minor Cu and Zn additions on the thermal, microstructure and tensile properties of Sn–Bi-based solder alloys. *Journal of Alloys and Compounds,* Volume 614, pp. 63-70.

Shen, L., Foo, A. Q., Wang, S. & Chen, Z., 2017. Enhancing creep resistance of SnBi solder alloy with non-reactive nano fillers: A study using nanoindentation.. *Journal of Alloys and Compounds,* Volume 729, pp. 498-506.

Shen, L., Septiwerdani, P. & Chen, Z., 2012. Elastic modulus, hardness and creep performance of SnBi alloys using nanoindentation. *Materials Science and Engineering: A,* Volume 558, pp. 253-258.

Shim, M., 2008. Phase Transformations. In: *Introduction to Engineering Materials.* s.l.:s.n., pp. 1-38.

Shin, Y.-S., Lee, S., Yoo, S. & Lee, C.-W., 2009. *Mechanical and microstrcutural properties of SIC-mixed Sn-Bi composite solder bumps by electroplaying.* Rimini, IEEE.

Silva, B. L., da Silva, V. C. E., Garcia, A. & Spinelli, J. E., 2017. Effects of Solidification Thermal Parameters on Microstructure and Mechanical Properties of Sn-Bi Solder Alloys. *Journal of Electronic Materials volume,* Volume 46, p. 1754–1769.

Silva, B. L., Garcia, A. & Spinelli, J. E., 2014. The roles of dendritic spacings and Ag3Sn intermetallics on hardness of the SAC307 solder alloy. *Microelectronics Reliability,* 54(12), pp. 2929-2934.

Singh, A. & Durairaj, R., 2018. Effect on the wettability, hardness and shear strength properties of 3%-nano Titanium Oxide (TiO 2) added Sn-3.8Ag-0.7Cu (SAC)/Copper (Cu) solder joint. *MATEC Web of Conferences,* Volume 237.

Singh, A., Durairaj, R., Efzan, E. & Niakan, A., 2017. Influence of Nano-3%Al2O3 on the Properties of Low Temperature Sn-58Bi (SB) Lead-free Solder Alloy. *IOP Conference Series: Materials Science and Engineering,* Volume 2015.

Singh, A. & Mohd Noor, E. E., 2015. A Study of Temperature, Microstructure and Hardness Properties of Sn-3.8Ag-0.7Cu (SAC) Solder Alloy. *MATEC Web of Conferences,* Volume 27.

Spinelli, J. E., Silva, B. L. & Garcia, A., 2014. Microstructure, phases morphologies and hardness of a Bi–Ag eutectic alloy for high temperature soldering applications. *Materials & Design,* Volume 58, pp. 482-490.

Suganuma , K., 2001. Advances in Lead-Free Electronics Soldering. *Current Opinion in Solid State & Materials Science,* Volume 5, pp. 55-64.

Suganuma, K., 2004. *Lead-free soldering in electronics.* s.l.:Marcel Dekekr .

Sunderraj, D. A. J., D Ananthapadmanaban & Geethan, K. A. V., 2018. Preparation, hardness studies and characterization of 88 Sn-7.5Zn-2.5Al-2In and 88 Sn-7 Zn-2Al-2.5 In lead free soldering alloys. *IOP Conference Series: Materials Science and Engineering,* Volume 402.

Sun, L. & Zhang, L., 2015. Properties and Microstructures of Sn-Ag-Cu-X Lead-Free SolderJoints in Electronic Packaging. *Advances in Materials Science and Engineering,* Volume 2, pp. 1-16.

Suraski, D. & Karl , S., 2001. The Current Status of Lead-Free Solder Alloys. *Transaction on Electronic Packaging Manufacturing,* 24(4).

T. H. Cheng, L. C. Tsao, F. S. Wang & W. Y. Kuo, 2011. *Effect of Al2O3 addition in Sn-Ag-Cu solder balls on the microstructure and shearing strength of BGA packages with immersion Sn surface finish.* s.l., IEEE.

T. Laurila, et al., 2011. Effect of Constant and Cyclic Current Stressing on the Evolution of Intermetallic Compound Layers. *Journal of Electronic Materials volume,* Volume 40, p. 1517–1526.

T. Laurila, V. Vuorinen & J.K. Kivilahti, 2005. Interfacial reactions between lead-free solders and common base materials. *Materials Science and Engineering: R: Reports,* 49(1-2), pp. 1-60.

T.L. Yang, et al., 2015. Low temperature bonding for high temperature applications by using SnBi solders.. *Journal of Alloys and Compounds,* Volume 647, pp. 681-685.

T.T.Dele-Afolabi, et al., 2015. Investigating the effect of isothermal aging on the morphology and shear strength of Sn-5Sb solder reinforced with carbon nanotubes. *Journal of Alloys and Compounds,* Volume 649, pp. 368-374.

T.Y Kang, et al., 2011. Effect of Bismuth on Intermetallic Compound Growth in Lead Free Solder/Cu Microelectronic Interconnect. *Journal of Materials Science & Technology,* 27(8), pp. 741-745.

Takamatsu, Y., Esaka, H. & Shinozuka , K., 2012. Liquid-Phase Separation in the Interdendritic Region After Growth of Primary β-Sn in Undercooled Sn-2.8Ag-0.3Cu Melt. *Journal of Electronic Materials,* Volume 41, p. 2035–2044.

Tan, A. T., Tan, W. A. & Yusof, F., 2015. Influence of nanoparticle addition on the formation and growth of intermetallic compounds (IMCs) in Cu/Sn–Ag–

Cu/Cu solder joint during different thermal conditions. *Science and Technology of Advanced Materials,* 16(3).

Tegehall, P.-E., 2006. *Review of the Impact of Intermetallic Layers on the Brittleness of Tin-Lead and Lead-Free Solder Joints,* Mölndal: IVF Industrial Research and Development Corporation.

Tsao, L. et al., 2010. Effects of nano-Al2O3 additions on microstructure development and hardness of Sn3.5Ag0.5Cu solder.. *Materials & Design,* pp. 4831-4835.

Tu, X., Yi, D., Wu, J. & Wang, B., 2017. Influence of Ce addition on Sn-3.0Ag-0.5Cu solder joints: Thermal behavior, microstructure and mechanical properties. *Journal of Alloys and Compounds,* Volume 698, pp. 317-328.

W.M. Chen, S.K. Kang & C.R. Kao, 2012. Effects of Ti addition to Sn–Ag and Sn–Cu solders. *Journal of Alloys and Compounds,* Volume 520, pp. 244-249.

Wang, C.-h. & Shen, H.-t., 2010. Effects of Ni addition on the interfacial reactions between Sn–Cu solders and Ni substrate. *Intermetallics,* 18(4), pp. 616-622.

Wang, F., Huang, Y. & Du, C., 2016. Mechanical properties of SnBi-SnAgCu composition mixed solder joints using bending test. *Materials Science and Engineering: A,* Volume 668, pp. 224-233.

Wang, H., Zhang, K. & Zhang, M., 2019. Fabrication and properties of Ni-modified graphene nanosheets reinforced Sn-Ag-Cu composite solder. *Journal of Alloys and Compounds,* Volume 781, pp. 761-772.

Wang, X. et al., 2009. Strengthening mechanism of SiC-particulate reinforced Sn–3.7Ag–0.9Zn lead-free solder. *Materials Science.*

Wang, Y. et al., 2017. Synthesis of SnAgCu nanoparticles with low melting point by the chemical reduction method. *Microelectronics Reliability,* Volume 78, pp. 17-24.

Wang, Y., Wang, G., Song, K. & Zhang, K., 2017. Effect of Ni addition on the wettability and microstructure of Sn2.5Ag0.7Cu0.1RE solder alloy. *Materials & Design,* Volume 119, pp. 219-224.

Wan, Y. et al., 2018. Shear strength and fracture surface analysis of Sn58Bi/Cu solder joints under a wide range of strain rates. *Microelectronics Reliability,* Volume 86, pp. 27-37.

Wattanakornphaiboon, A., Canyook, R. & Fakpan, K., 2018. Effect of SnO2 reinforcement on creep property of Sn–Ag–Cu solders. *Materials Today: Proceedings,* Volume 5, p. 9213–9219.

Wen, Y. et al., 2017. Reliability enhancement of Sn-1.0Ag-0.5Cu nano-composite solders by adding multiple sizes of TiO2 nanoparticles. *Journal of Alloys and Compounds,* Volume 696, pp. 799-807.

Whalley, D., 2004. A simplified reflow soldering process model. *Journal of Materials Processing Technology 150,* pp. 134-144.

Whalley, D. C., 2004. A simplified reflow soldering process model.. *Journal of Materials Processing Technology,* 150(1-2), pp. 134-144.

Winter, M., 2012. [Online] Available at: http://www.webelements.com/

Wu, C., Yu, D., Law , C. & Wang, L., 2004. Properties of lead-free solder alloys with rare earth element addition.. *Materials Science and Engineering,* pp. 1-44.

Wu, J. et al., 2016. Recent progress of Sn–Ag–Cu lead-free solders bearing alloy elements and nanoparticles in electronic packaging. *Journal of Materials Science: Materials in Electronics,* Volume 27, p. 12729–12763.

Wu, J., Xue, S., Wang, J. & Mingfang Wu, 2019. Coupling effects of rare-earth Pr and Al2O3 nanoparticles on the microstructure and properties of Sn-0.3Ag-0.7Cu low-Ag solder. *Journal of Alloys and Compounds,* Volume 784, pp. 471-487.

Xiao-yan, Z., Mai-qun, Z., Xiao-qing, C. & Ming-xin, T., 2007. Effect of cerium on microstructure and mechanical properties of Sn-Ag-Cu system lead-free solder alloys. *Transactions of Nonferrous Metals Society of China,* 17(4), pp. 805-810.

Xing, F., Qiu, X.-M. & Li, Y.-D., 2015. Effects of Sn element on microstructure and properties of Zn–Cu–Bi–Sn high-temperature solder. *Transactions of Nonferrous Metals Society of China,* 25(3).

Xing, W.-q.et al., 2017. Effect of nano Al2O3 additions on the interfacial behavior and mechanical properties of eutectic Sn-9Zn solder on low temperature wetting and soldering of 6061 aluminum alloys.. *Journal of Alloys and Compounds,* Volume 695, pp. 574-582.

Xu, S., Chan, Y., Zhang, K. & Yung, K., 2014. Interfacial intermetallic growth and mechanical properties of carbon nanotubes reinforced Sn3.5Ag0.5Cu solder joint under current stressing.. *Journal of Alloy and Compound,* Volume 595, pp. 92-102.

Y. Miyazawa & T.Ariga, 1999. *Microstructural change and hardness of lead free solder alloys.* Tokyo, IEEE.

Y. Tang, G.Y. Li & Y.C. Pan, 2014. Effects of TiO2 nanoparticles addition on microstructure, microhardness and tensile properties of Sn–3.0Ag–0.5Cu–xTiO2 composite solder. *Materials & Design,* Volume 55, pp. 574-582.

Y. Tang, et al., 2019. Formation and growth of interfacial intermetallics in Sn-0.3Ag-0.7Cu-xCeO2/Cu solder joints during the reflow process. *Journal of Alloys and Compounds,* Volume 778, pp. 741-755.

Y.D. Han, et al., 2019. Study of mechanical properties of Ag nanoparticle-modified graphene/Sn-Ag-Cu solders by nanoindentation. *Materials Science and Engineering: A,* Volume 761.

Y.M Youssef, R.J Dashwood & P.D Lee, 2005. Effect of clustering on particles pushing and solidification behaviour in TiB2 reinforced aluminium PMMCs.. *Journal of Composite Materials,* 36(6), pp. 747-763.

Y.Tang, et al., 2017. Effects of Mn nanoparticles on tensile properties of low-Ag Sn-0.3Ag-0.7Cu-xMn solder alloys and joints.. *Journal of Alloys and Compounds,* Volume 719, pp. 365-375.

Yahaya, M. Z. et al., 2016. Hardness profiles of Sn-3.0Ag-0.5Cu-TiO2 composite solder by nanoindentation. *Materials Science and Engineering: A,* Volume 669, pp. 178-186.

Yang, L. et al., 2015. Improved microstructure and mechanical properties forSn58Bi solder alloy by addition of Ni-coated carbon nanotubes. *Materials Science and Engineering: A,* Volume 642, pp. 7-15.

Yang, L. et al., 2018. Microstructure and reliability of Mo nanoparticle reinforced Sn–58Bi-based lead-free solder joints. *Materials Science and Technology,* 34(8).

Yang, L. et al., 2019. Microstructure, IMCs layer and reliability of Sn-58Bi solder joint reinforced by Mo nanoparticles during thermal cycling. *Materials Characterization,* Volume 148, pp. 280-291.

Yang, Y. et al., 2013. Interdiffusion at the interface between Sn-based solders and Cu substrate. *Microelectronics Reliability,* 53(2), pp. 327-333.

Yee, S. C., Chu Wong, K. M. & Issabayeva, G., 2019. *A Study on the Shear Strength and Failure Modes of Sn-3.0Ag-0.5Cu Solder Joint Containing Pt.* Sarawak, IOP.

Yeo, H. K. & Han, K. H., 2009. Wetting and spreading of molten SnPb solder on a Cu–10%Nb micro-composite. *Journal of Alloys and Compounds,* 477(1-2), pp. 278-282.

Yoon, J.-W., Lee, C.-B. & Jung, S.-B., 2002. Interfacial reactions between Sn-58 mass% Bi eutectic solder and (Cu, electroless Ni-P/Cu) substrate. *Materials Transactions,* 43(8), pp. 1821-1826.

Yoon, J.-W.et al., 2009. Wettability and interfacial reactions of Sn–Ag–Cu/Cu and Sn–Ag–Ni/Cu solder joints. *Journal of Alloys and Compounds* , pp. 142-147.

Yu-peng, Z. et al., 2010. Study on Properties of Low-silver Lead-free Solder Alloys with Alloy Element Doping. *Journal of Materials Engineering,* Volume 10.

Z. Moser, W. Gasior & J. Pstrus , 2001. Surface tension measurements of the Bi-Sn and Sn-Bi-Ag liquid alloys. *Journal of Electronic Materials,* Volume 30, p. 1104–1111.

Z.H. Li, Y. Tang, Q.W. Guo & G.Y. Li, 2019. Effects of CeO2 nanoparticles addition on shear properties of low-silver Sn–0.3Ag–0.7Cu-xCeO2 solder alloys. *Journal of Alloys and Compounds,* Volume 789, pp. 150-162.

Z.L. Li, et al., 2016. Size effect on IMC growth in micro-scale Sn-3.0Ag-0.5Cu-0.1TiO2 solder joints in reflow process. *Journal of Alloys and Compounds,* Volume 685, pp. 983-991.

Z.Zhao, et al., 2016. Effect of nano-Al2O3 reinforcement on the microstructure and reliability of Sn–3.0Ag–0.5Cu solder joints. *Microelectronics Reliability,* Volume 60, pp. 126-134.

Zeng, G., McDonald, S. & Nogita, K., 2012. Development of high-temperature solders: Review. *Microelectronics Reliability,* 52(7), pp. 1306-1322.

Zeng, G., McDonald, S. & Nogita, K., 2012. Development of high-temperature solders: Review. *Microelectronics Reliability,* 52(7), pp. 1306-1322.

Zhang, C. et al., 2014. Effect of Sb content on properties of Sn-Bi solders. *Transactions of Nonferrous Metals Society of China,* 24(1), pp. 184-191.

Zhang, H. et al., 2014. *Effect of Fe content on the interfacial reliability of SnAgCu/Fe-Ni solder joint.* s.l., s.n.

Zhang, L. & Gao, L.-l., 2015. Interfacial compounds growth of SnAgCu(nano La2O3)/Cu solder joints based on experiments and FEM. *Journal of Alloys and Compounds,* Volume 635, pp. 55-60.

Zhang, L. et al., 2012. Development of SnAg-based lead free solders in electronics packaging. *Microelectronics Reliability,* 52(3), pp. 559-578.

Zhang, L. & K.N Tu, 2014. Structure and properties of lead-free solders bearing micro and nano particles. *Materials Science and Engineering: R: Reports,* Volume 82, pp. 1-32.

Zhang, L. et al., 2008. *Manufacture, microstructure and microhardness analysis of Sn-Bi lead-free solder reinforced with Sn-Ag-Cu nano-particles.* Shanghai, IEEE.

Zhang, L. & Tu, K., 2014. Structure and properties of lead-free solders bearing micro and nano particles.. *Materials Science and Engineering,* pp. 1-32.

Zhang, L. et al., 2010. Creep behavior of SnAgCu solders with rare earth Ce doping. *Transactions of Nonferrous Metals Society of China,* 20(3), pp. 412-417.

Zhang, P. et al., 2019. Effect of Nanoparticles Addition on the Microstructure and Properties of Lead-Free Solders: A Review. *Applied Sciences,* 9(10), pp. 1-20.

Zhang, Y., 2010. Tin and Tin alloys dor lead-free soldering.. In: *Modern Electroplating, Fifth Edition.* s.l.:John Wiley and Sons.

Zhao, X. et al., 2016. Effect of γ-Fe2O3 nanoparticles size on the properties of Sn-1.0Ag–0.5Cu nano-composite solders and joints. *Journal of Alloys and Compounds,* Volume 662, pp. 272-282.

Zhou, J., Sun, Y. & Xue, F., 2005. Properties of low melting point Sn–Zn–Bi solders. *Journal of Alloys and Compounds,* 397(1-2), pp. 260-264.

Zhou, S. et al., 2018. Improvement in the mechanical properties of eutectic Sn58Bi alloy by 0.5 and 1 wt% Zn addition before and after thermal aging. *Journal of Alloys and Compounds,* Volume 765, pp. 1243-1252.

Zhu, W., Zhang, W., Zhou, W. & Wu, P., 2019. Improved microstructure and mechanical properties for SnBi solder alloy by addition of Cr powders. *Journal of Alloys and Compounds,* Volume 789, pp. 805-813.

Zhu, Z. et al., 2018. Effect of the size of carbon nanotubes (CNT) on the microstructure and mechanical strength of CNTs-dope composite Sn0.3Ag0.7Cu-CNTs solder. *Materials Science and Engineering A,* Volume 727.

Zou, C., Gao, Y., Yang, B. & Zhai, Q., 2010. Melting and solidification properties of the nanoparticles of Sn3.0Ag0.5Cu lead-free solder alloy. *Materials Characterization,* 61(4), pp. 474-480.

APPENDIX A

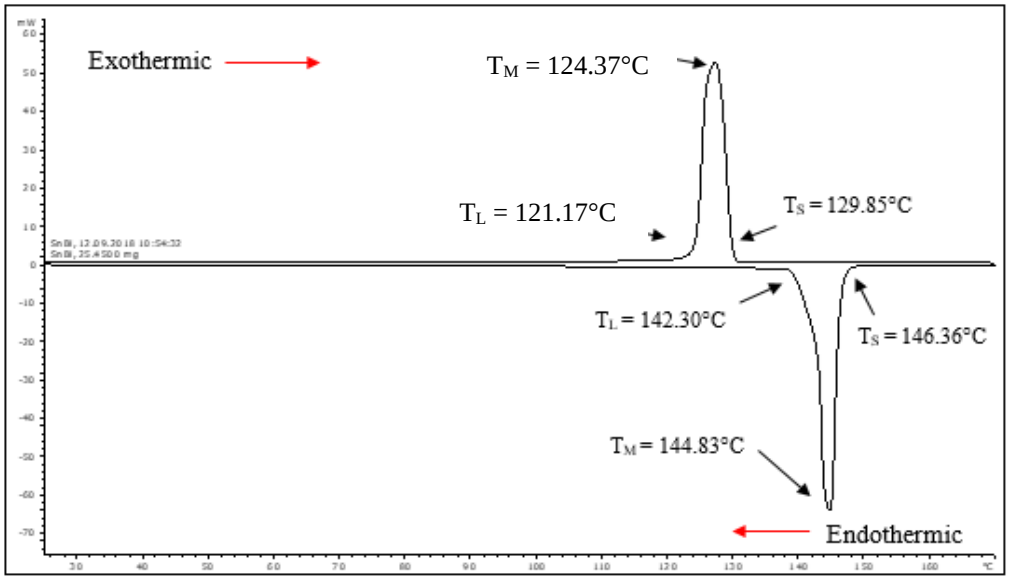

Figure A 1: DSC peak of SB solder alloy.

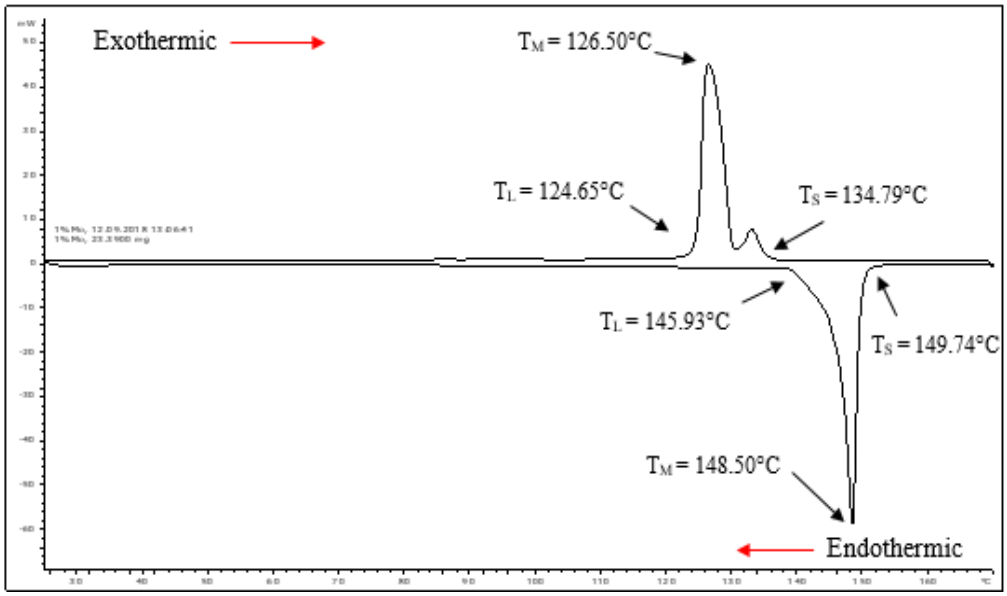

Figure A 2: DSC peak of SB + 1% Mo solder alloy.

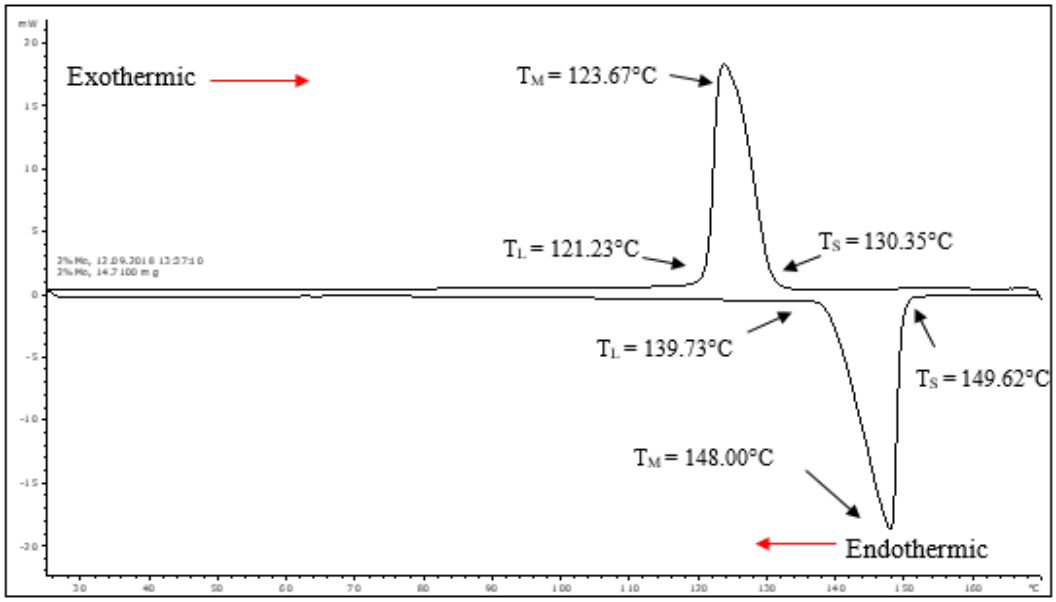

Figure A 3: DSC peak of SB + 2% Mo solder alloy.

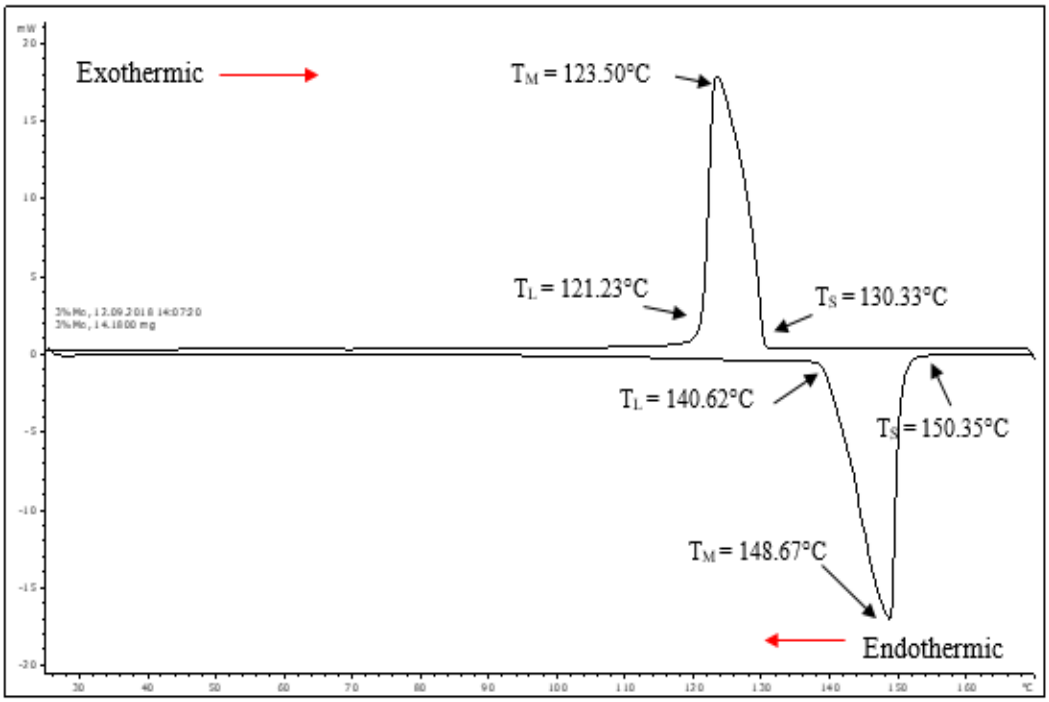

Figure A 4: DSC peak of SB + 3% Mo solder alloy.

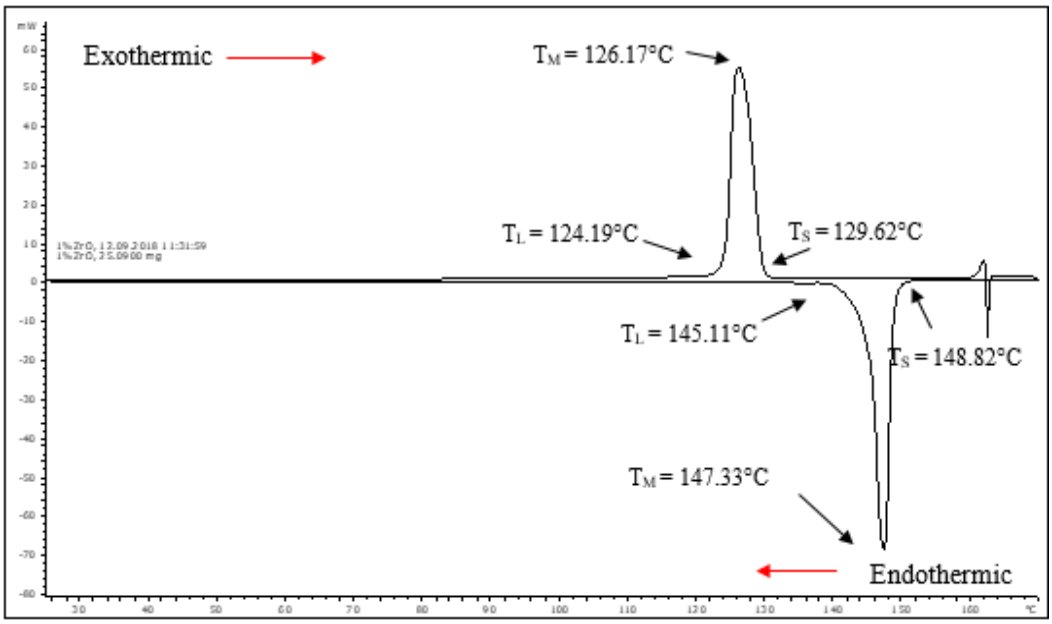

Figure A 5: DSC peak of SB + 1% ZrO_2 solder alloy.

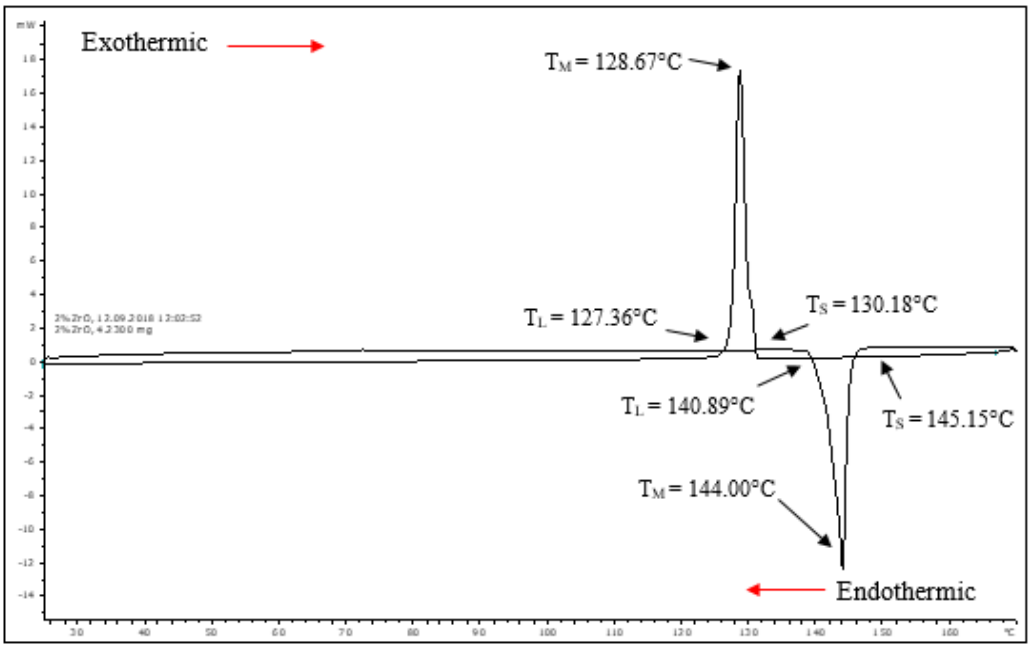

Figure A 6: DSC peak of SB + 2% ZrO_2 solder alloy.

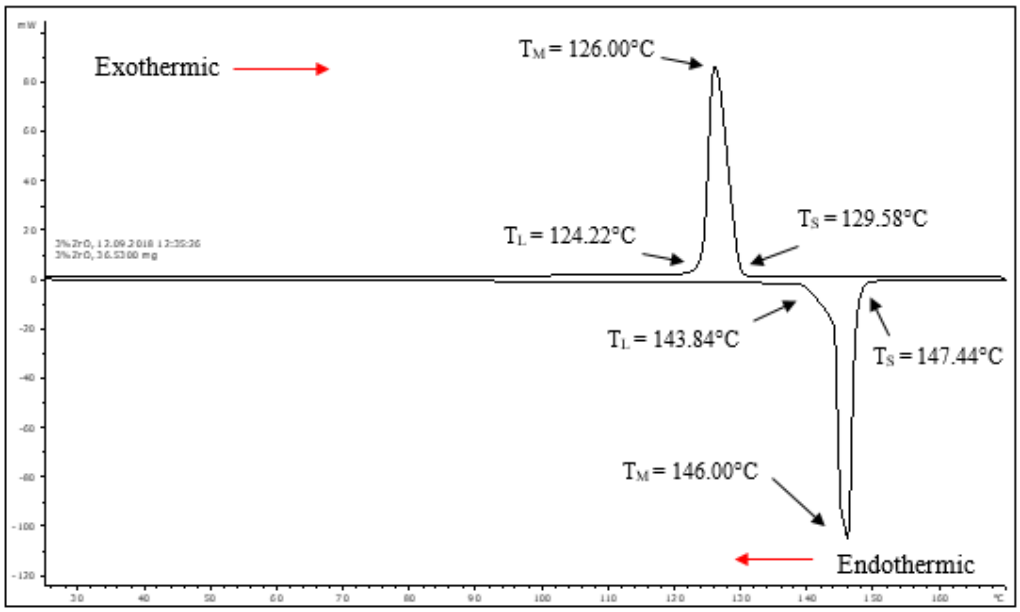

Figure A 7: DSC peak of SB + 3% ZrO_2 solder alloy.

APPENDIX B

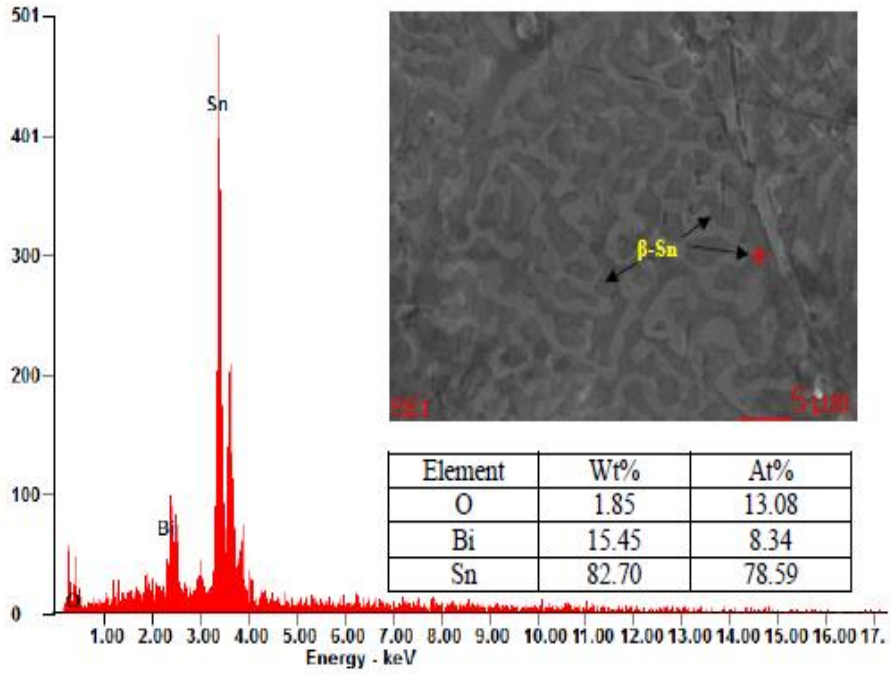

Element	Wt%	At%
O	1.85	13.08
Bi	15.45	8.34
Sn	82.70	78.59

Figure B 1: SEM and EDX of SB solder.

a)

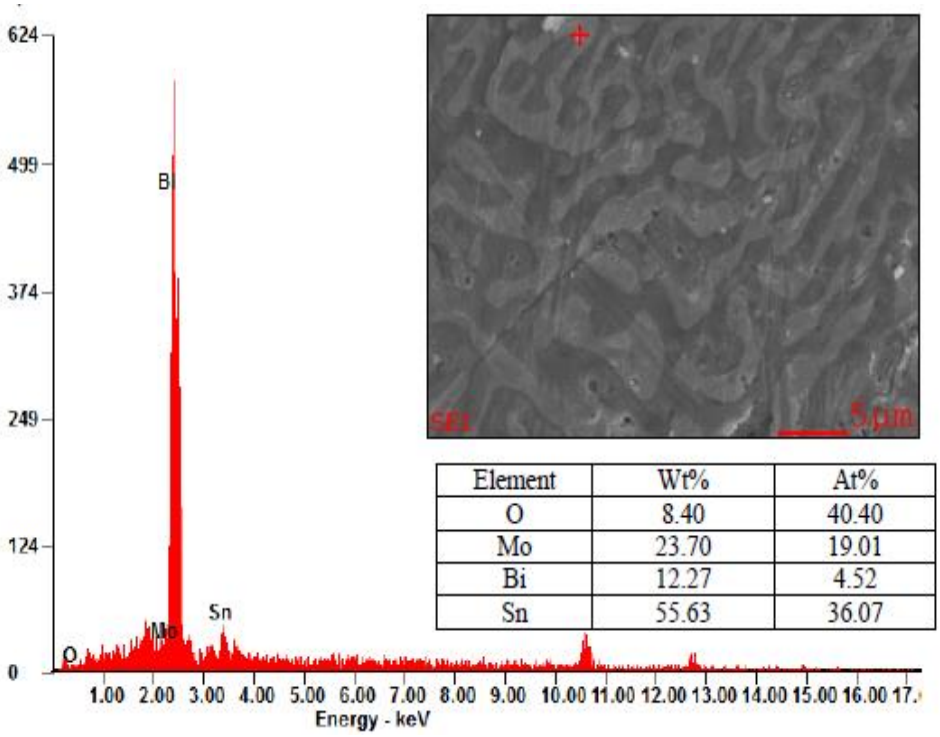

Element	Wt%	At%
O	8.40	40.40
Mo	23.70	19.01
Bi	12.27	4.52
Sn	55.63	36.07

b)

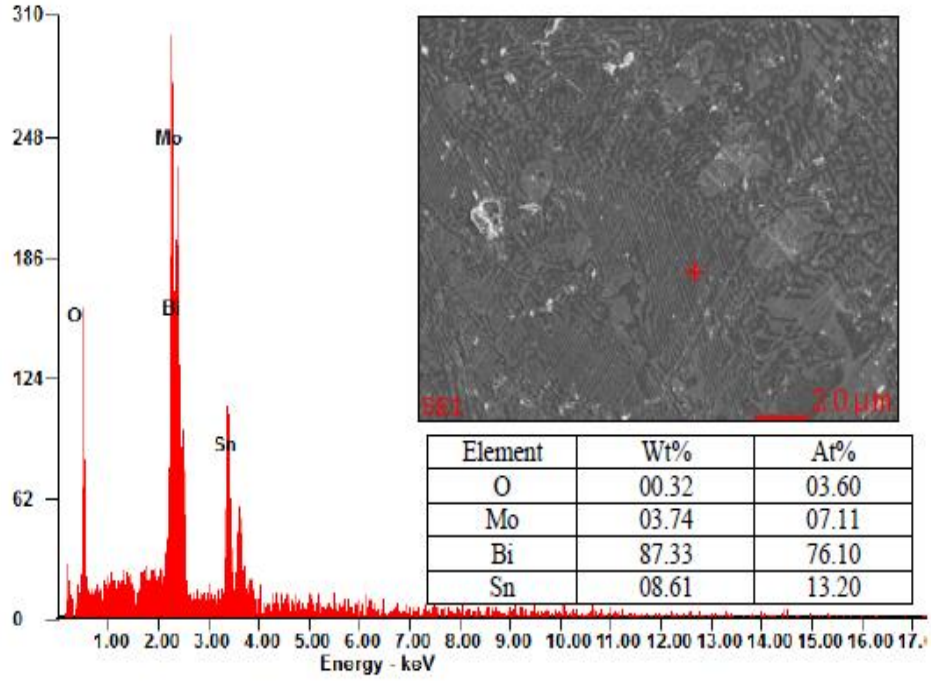

Element	Wt%	At%
O	00.32	03.60
Mo	03.74	07.11
Bi	87.33	76.10
Sn	08.61	13.20

Figure B 2 a) and b): SEM and EDX SB + 1 % Mo solder.

a)

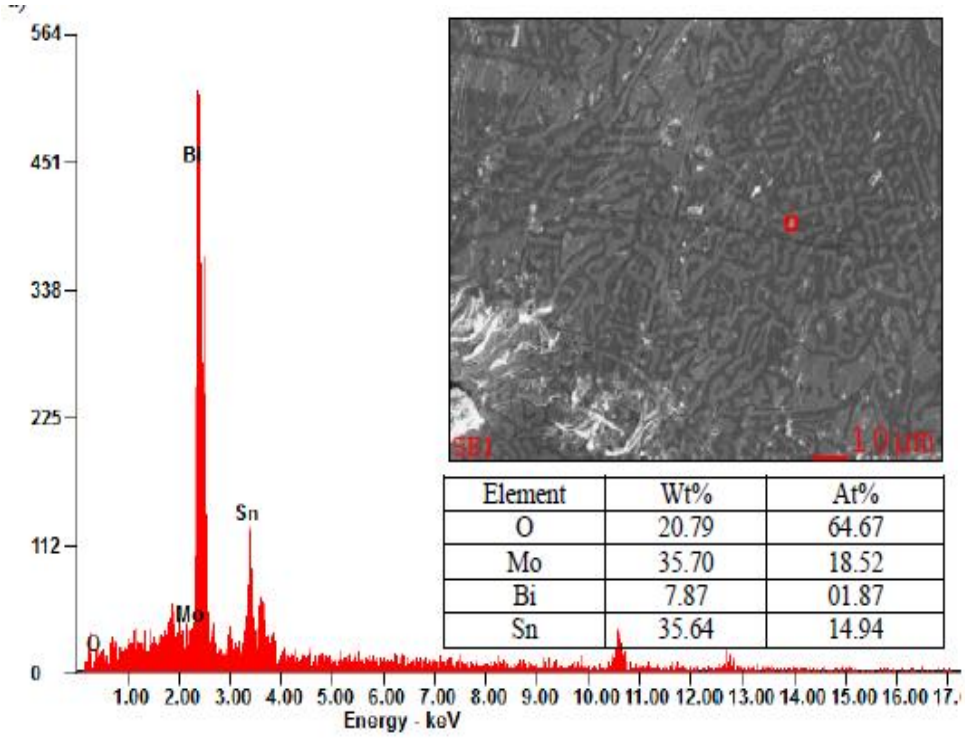

Element	Wt%	At%
O	20.79	64.67
Mo	35.70	18.52
Bi	7.87	01.87
Sn	35.64	14.94

b)

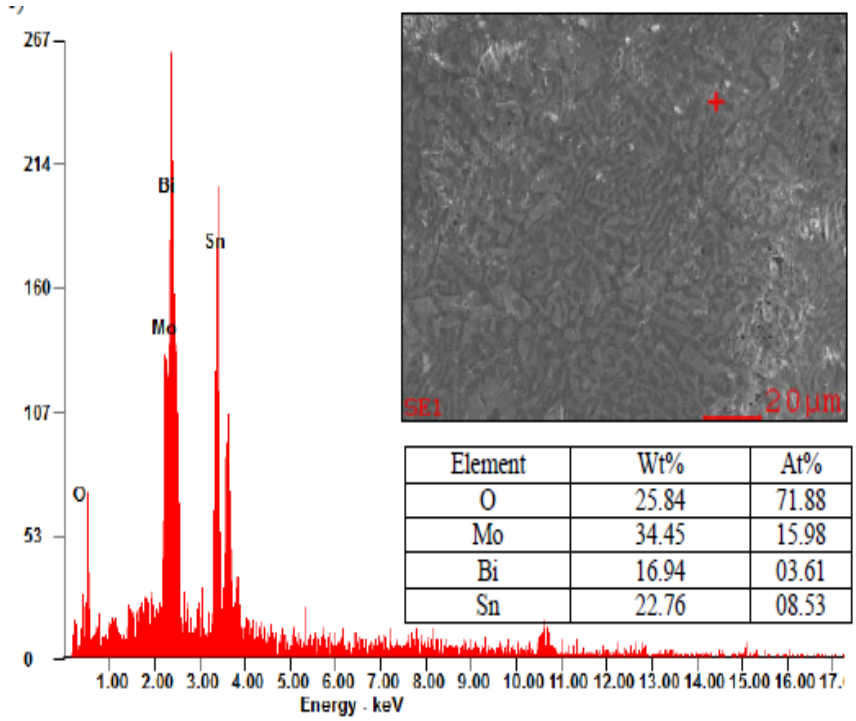

Element	Wt%	At%
O	25.84	71.88
Mo	34.45	15.98
Bi	16.94	03.61
Sn	22.76	08.53

Figure B 3 a) and b): SEM and EDX SB + 2 % Mo solder.

a)

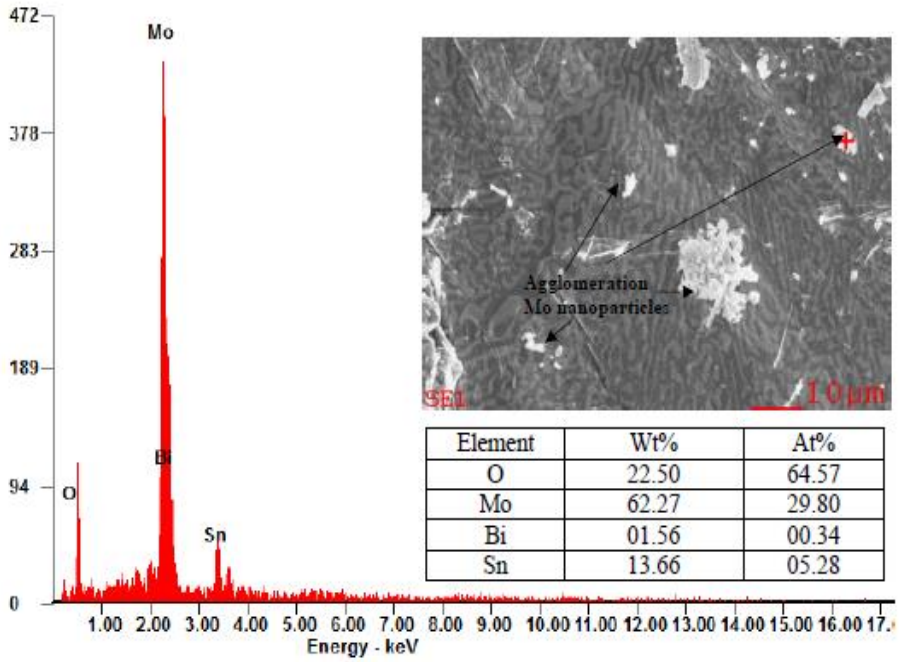

Element	Wt%	At%
O	22.50	64.57
Mo	62.27	29.80
Bi	01.56	00.34
Sn	13.66	05.28

b)

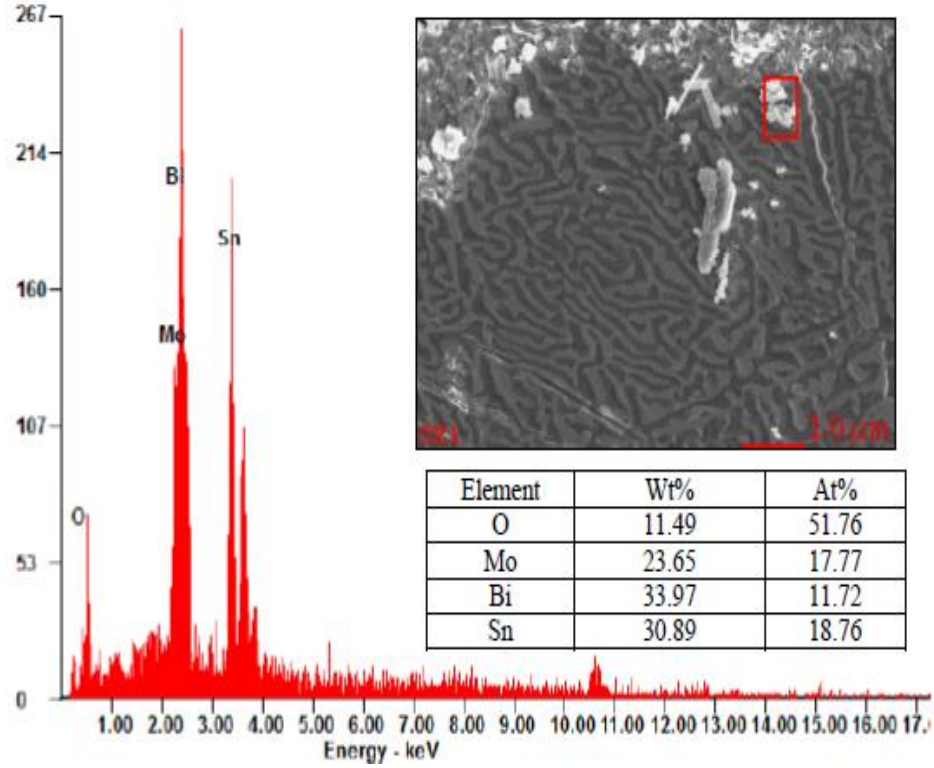

Element	Wt%	At%
O	11.49	51.76
Mo	23.65	17.77
Bi	33.97	11.72
Sn	30.89	18.76

Figure B 4 a) and b): SEM and EDX of SB + 3 % Mo solder.

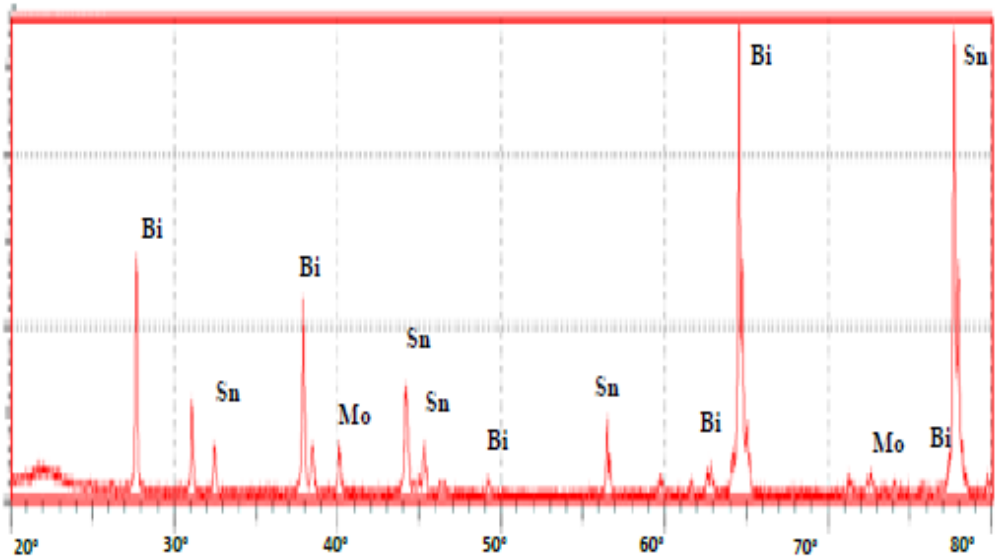

Figure B 5: XRD of SB + 2 % Mo solder.

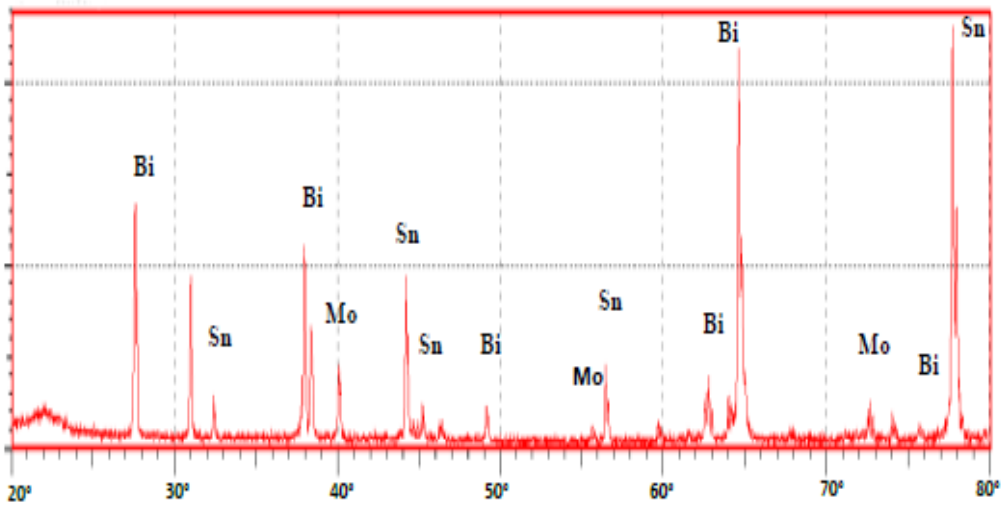

Figure B 6: XRD of SB + 3 % Mo solder.

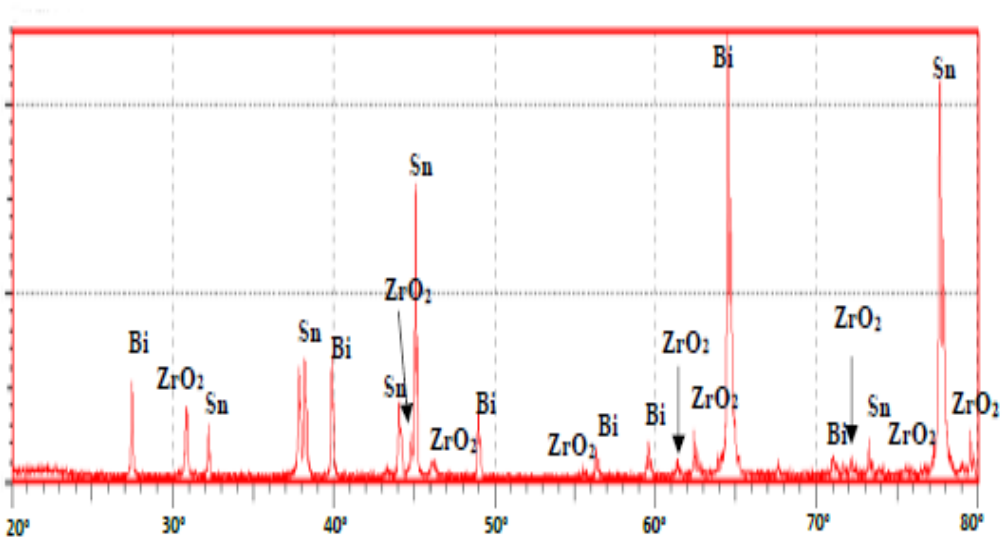

Figure B 7: XRD of SB + 2 % ZrO_2 solder.

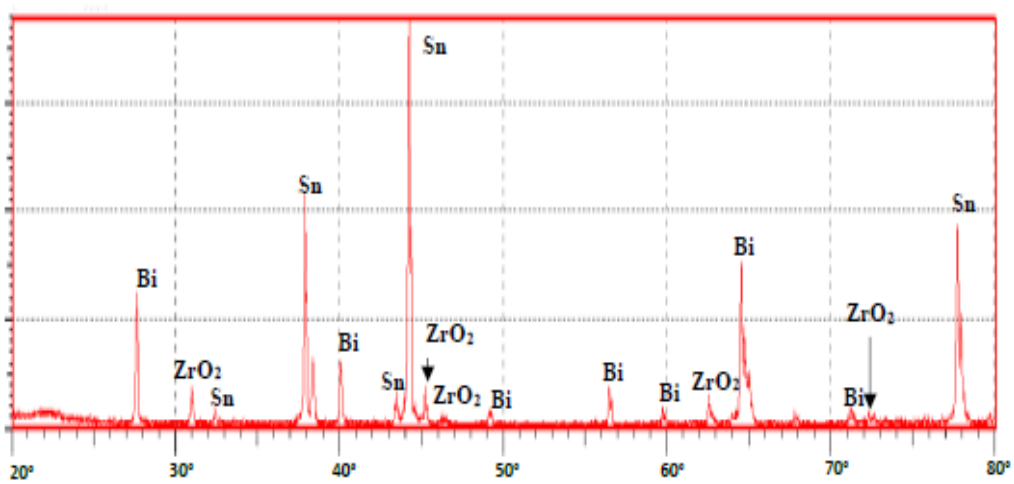

Figure B 8: XRD of SB + 3 % ZrO_2 solder.

a) b)

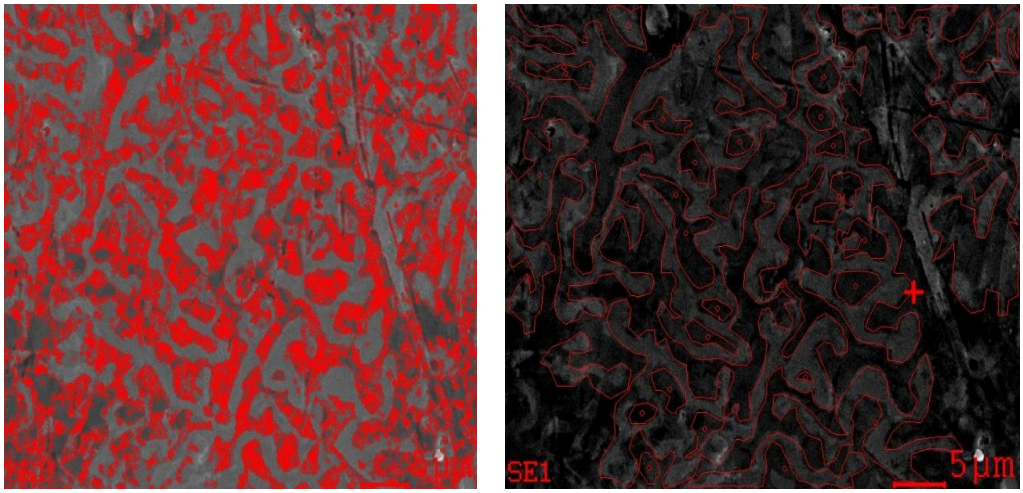

Average Bi Area = 291897µm^2 Average Bi Area = 571218.5µm^2

Total average area = 431557.8 µm^2

Figure B 9: Bi area in SB solder.

a) b)

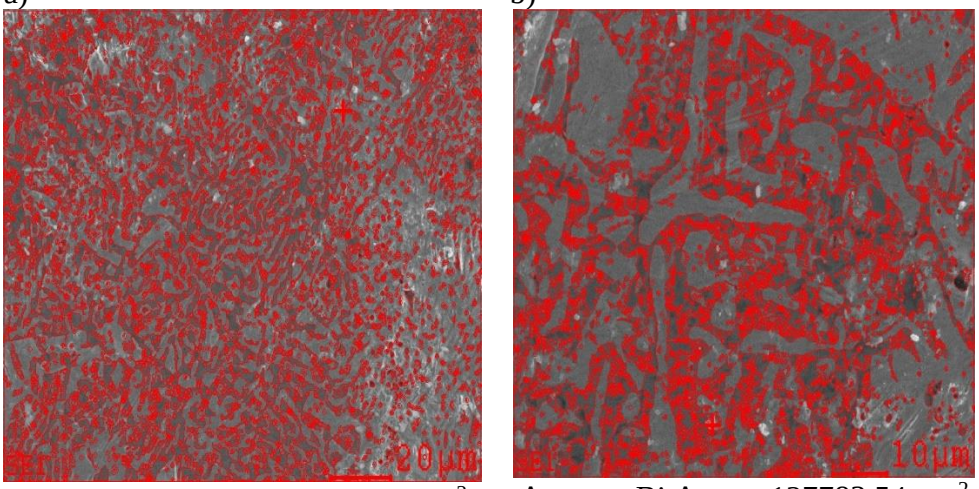

Average Bi Area = 258897.63 µm^2 Average Bi Area = 127783.54 µm^2

Total average area = 193340.59 µm^2

Figure B 10: Bi area in SB + 1 % Mo solder.

a) b)

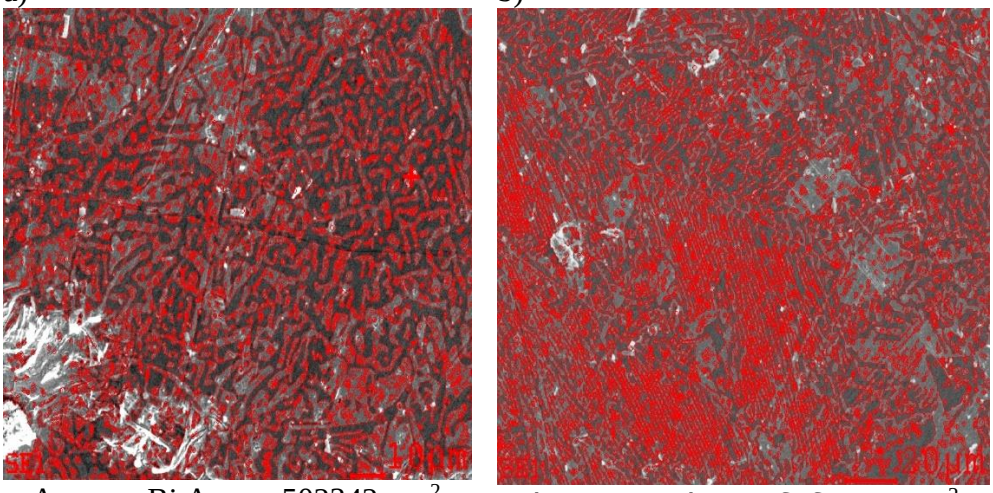

Average Bi Area = 502342 μm^2 Average Bi Area = 626452.5 μm^2

Total average area = 564397.3 μm^2

Figure B 11: Bi area in SB + 2 % Mo solder.

a) b)

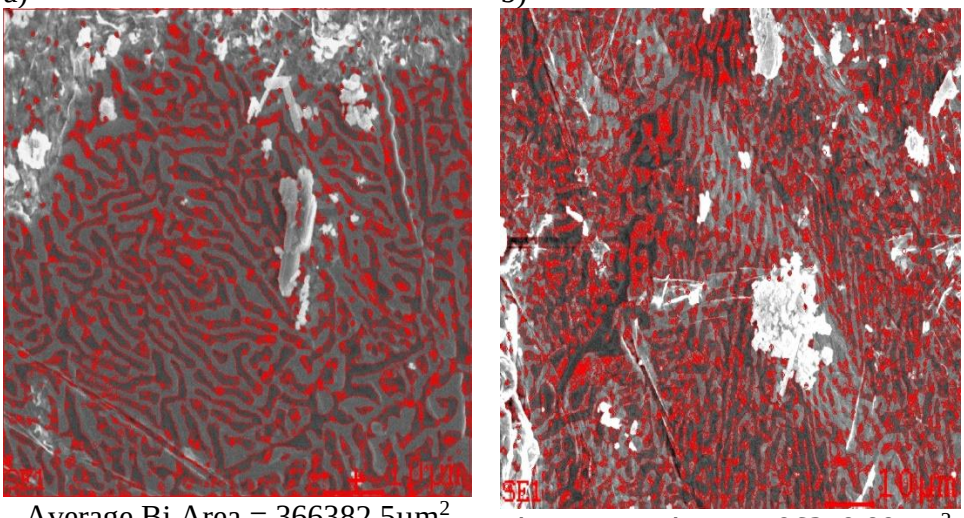

Average Bi Area = 366382.5μm^2 Average Bi Area = 296319.89μm^2

Total average area = 331351.19μm^2

Figure B 12: Bi area in SB + 3 % Mo solder.

a) b)

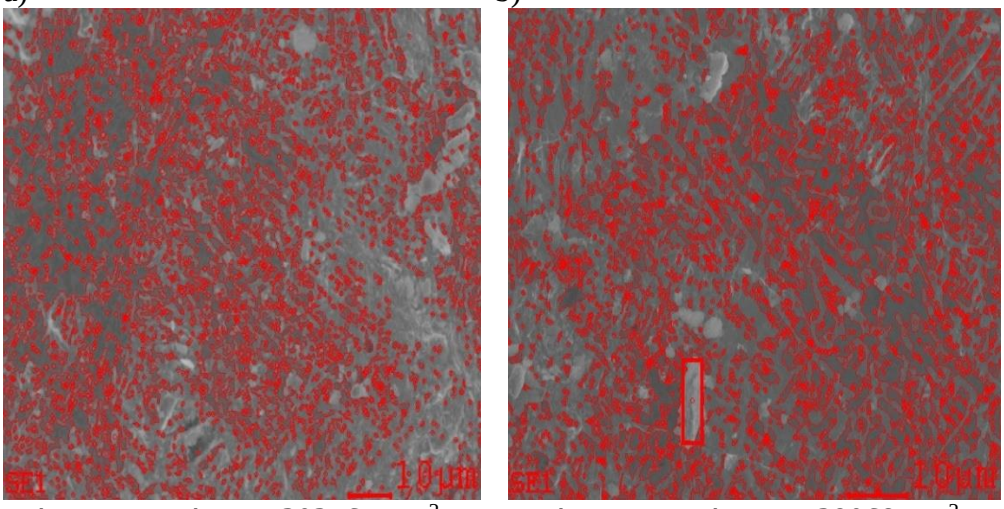

Average Bi Area = 303265 µm^2 Average Bi Area = 239068 µm^2

Total average area = 271166.5 µm^2

Figure B 13: Bi area in SB + 1 % ZrO_2 solder.

a) b)

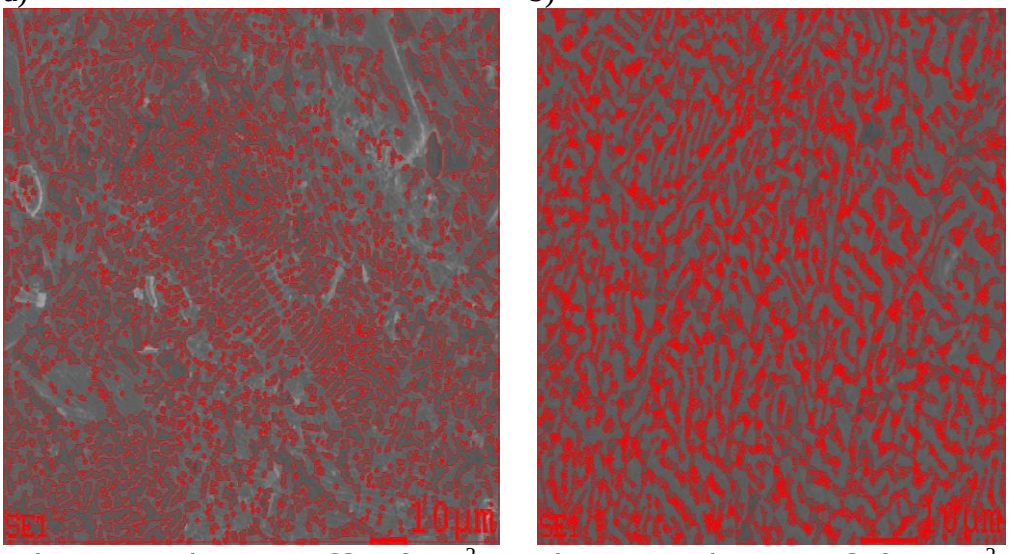

Average Bi Area = 255634.18 µm^2 Average Bi Area = 252329.17 µm^2

Total average area = 253981.67 µm^2

Figure B 14: Bi area in SB + 2 % ZrO_2 solder.

a) b)

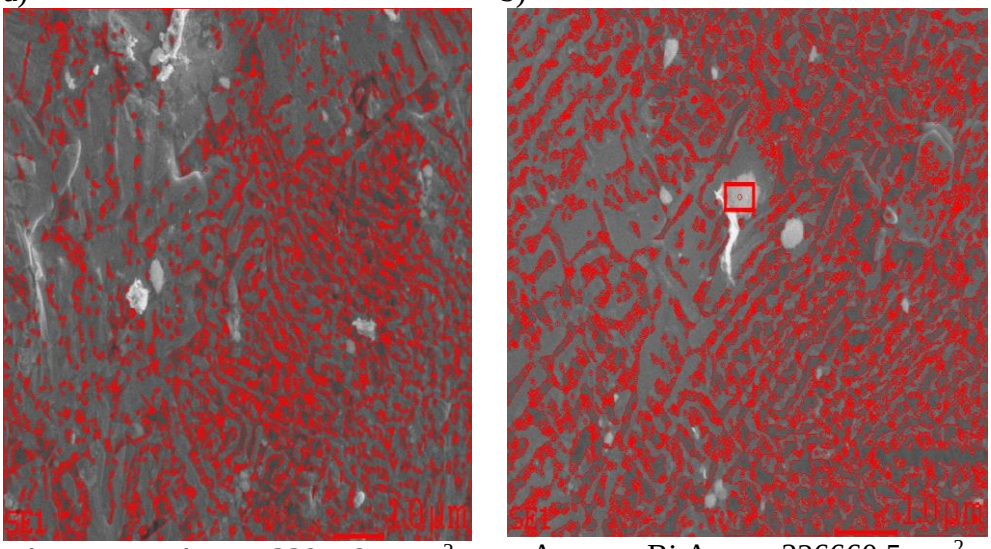

Average Bi Area = 339528.1 μm^2 Average Bi Area = 326660.5 μm^2

Total average area = 333094.3 μm^2

Figure B 15: Bi area in SB + 3 % ZrO_2 solder.

APPENDIX C

a)

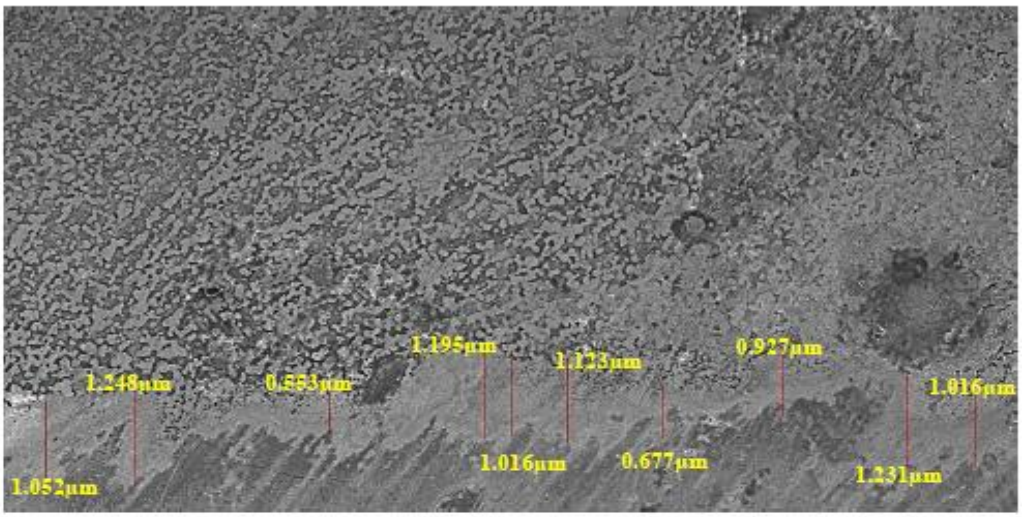

b)

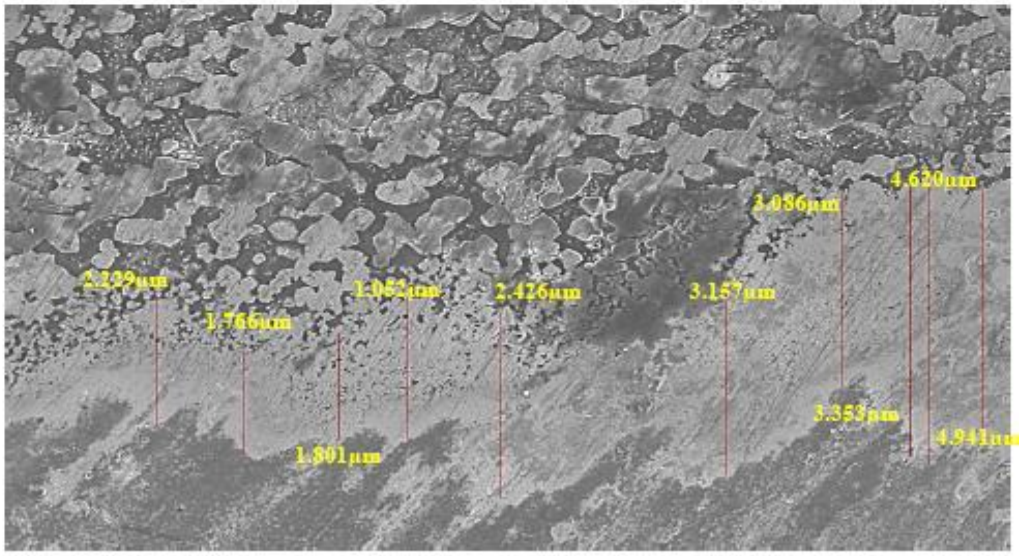

c)

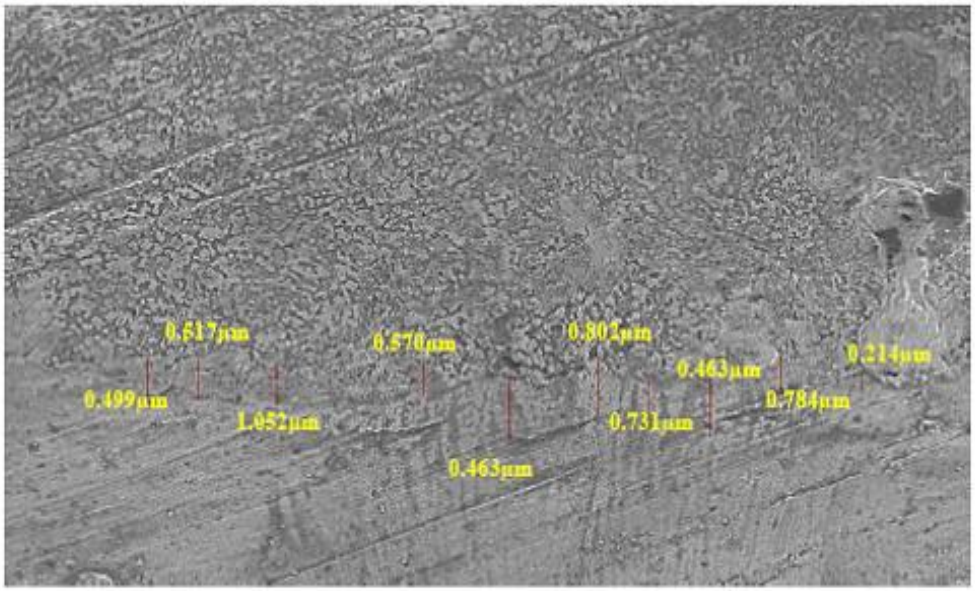

d)

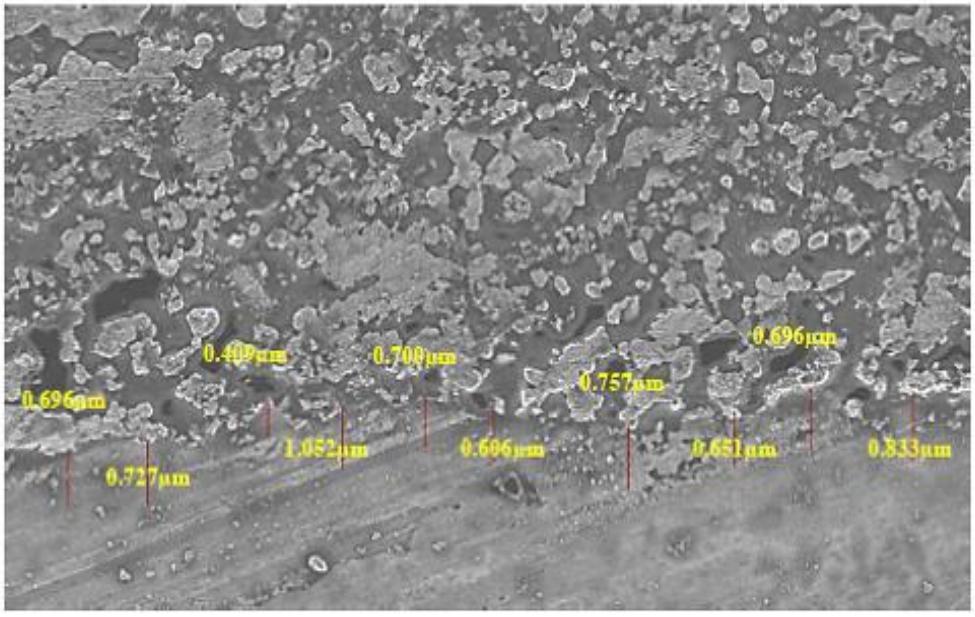

Figure C 1: IMC thickness of SB/Cu solder joint.

a)

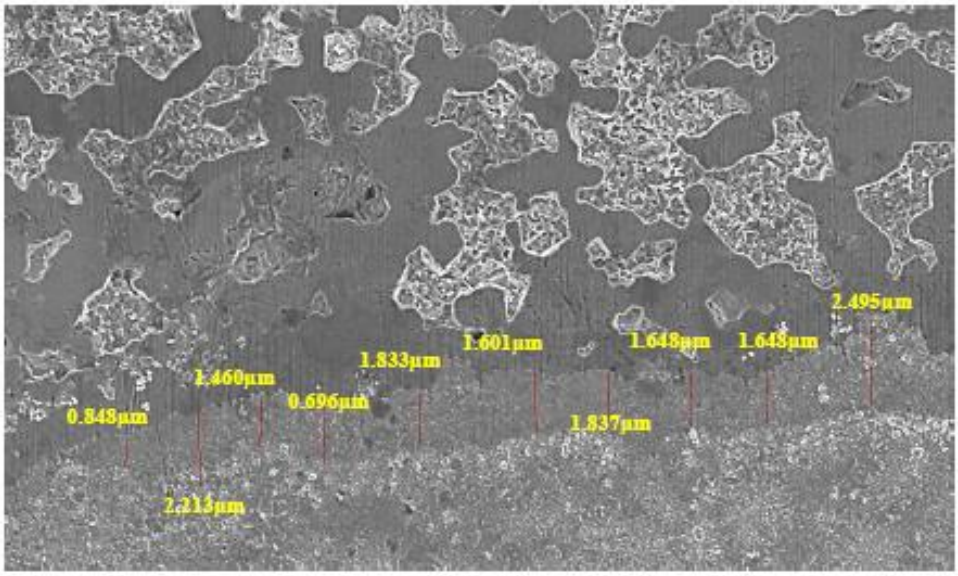
2.495µm
1.601µm
1.648µm
1.648µm
1.833µm
1.460µm
0.696µm
0.848µm
1.837µm
2.213µm

b)

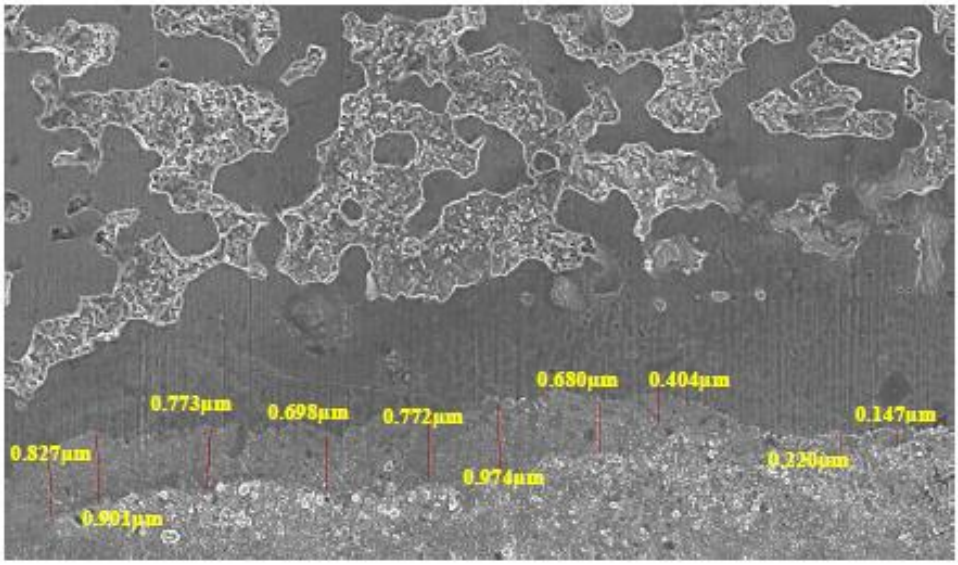
0.680µm
0.404µm
0.773µm
0.698µm
0.772µm
0.147µm
0.827µm
0.974µm
0.220µm
0.901µm

c)

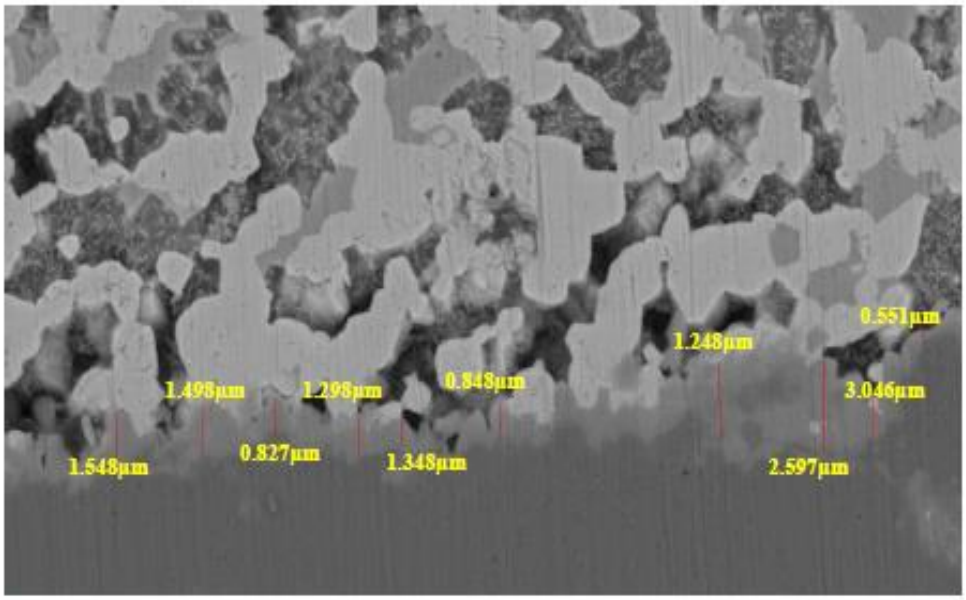

d)

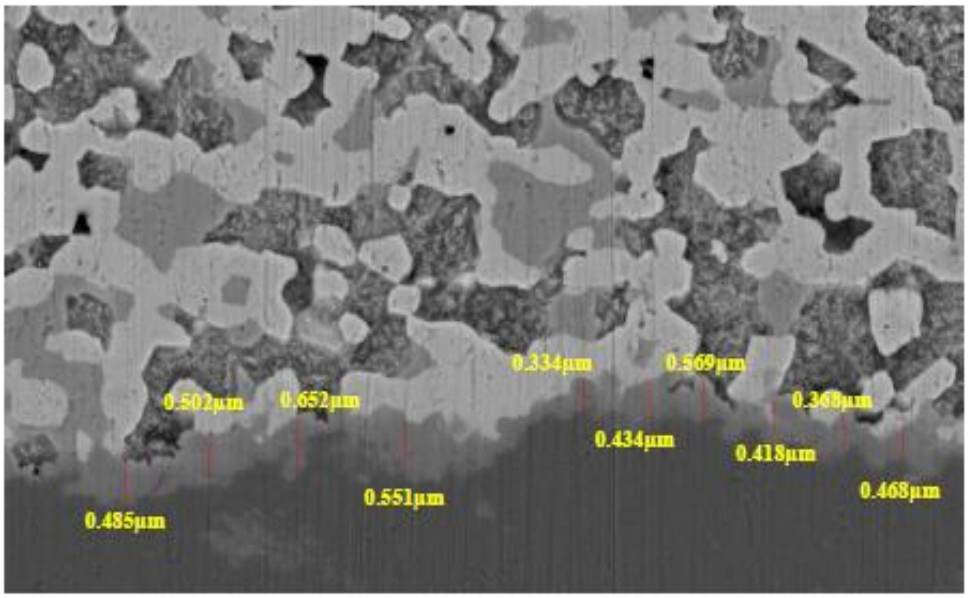

Figure C 2: IMC thickness of SB + 1 % Mo/Cu solder joint.

a)

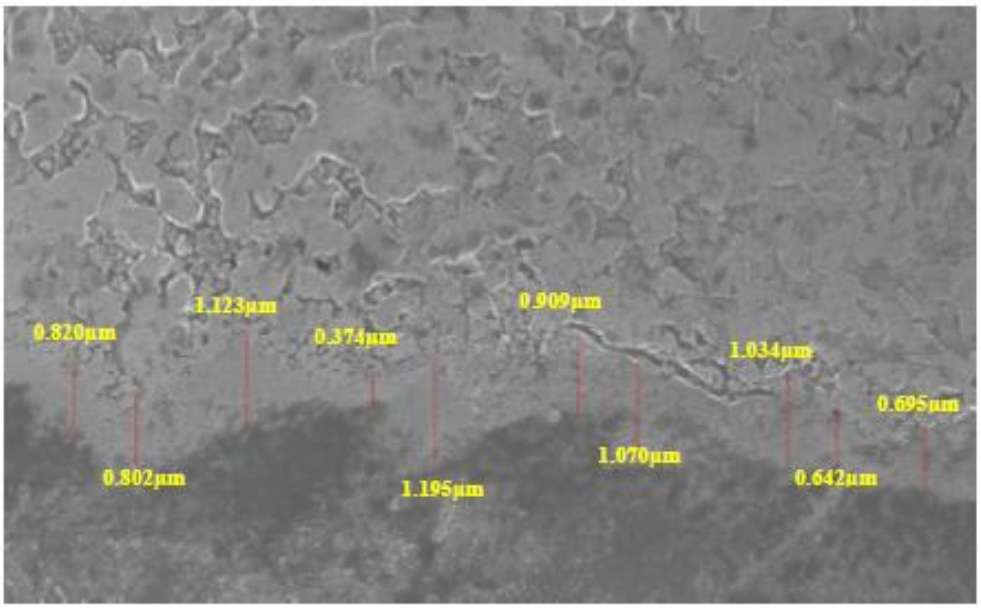
0.820µm
1.123µm
0.374µm
0.909µm
1.034µm
0.695µm
0.802µm
1.195µm
1.070µm
0.642µm

b)

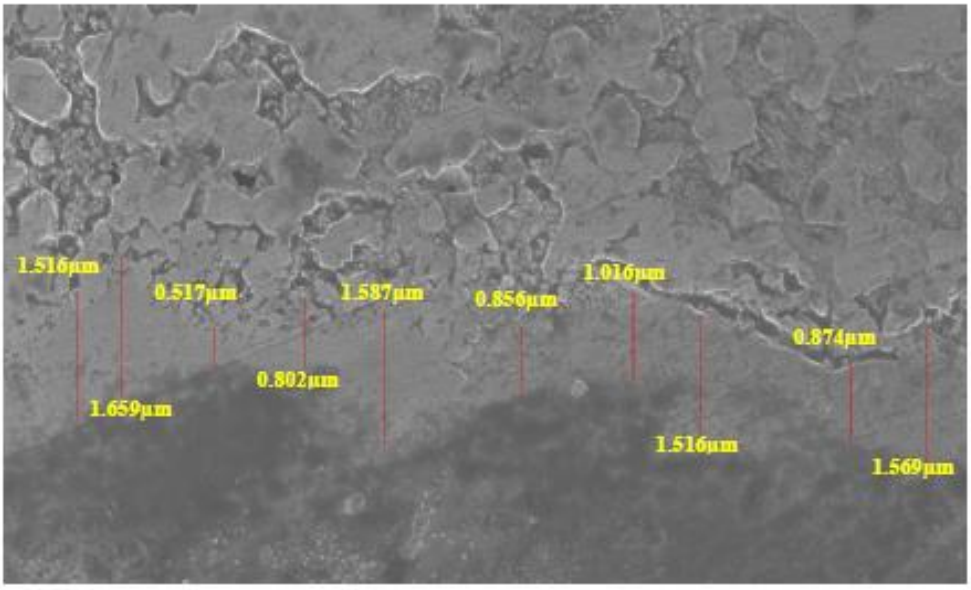
1.516µm
0.517µm
1.587µm
0.856µm
1.016µm
0.874µm
0.802µm
1.659µm
1.516µm
1.569µm

c)

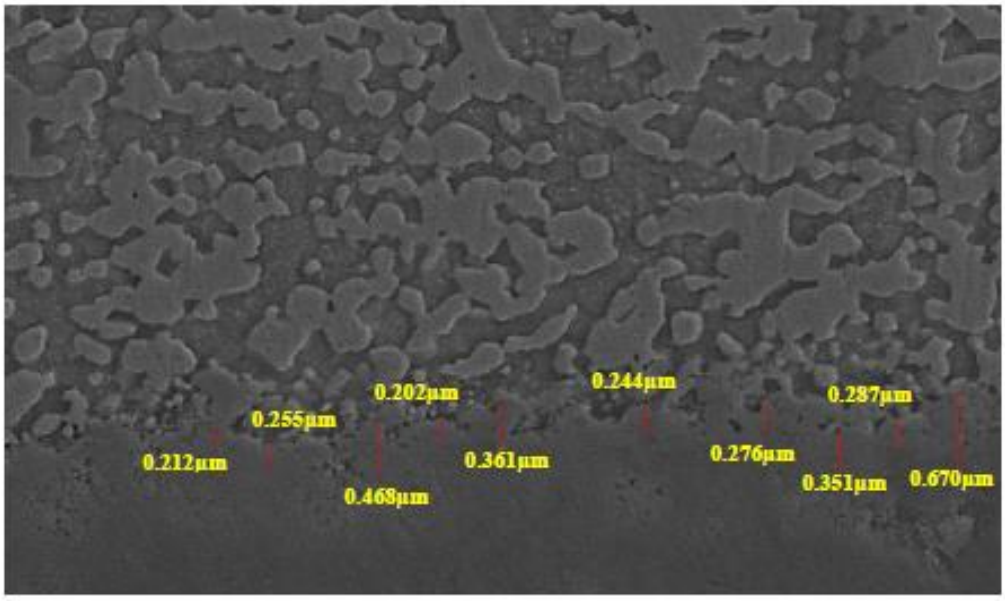

d)

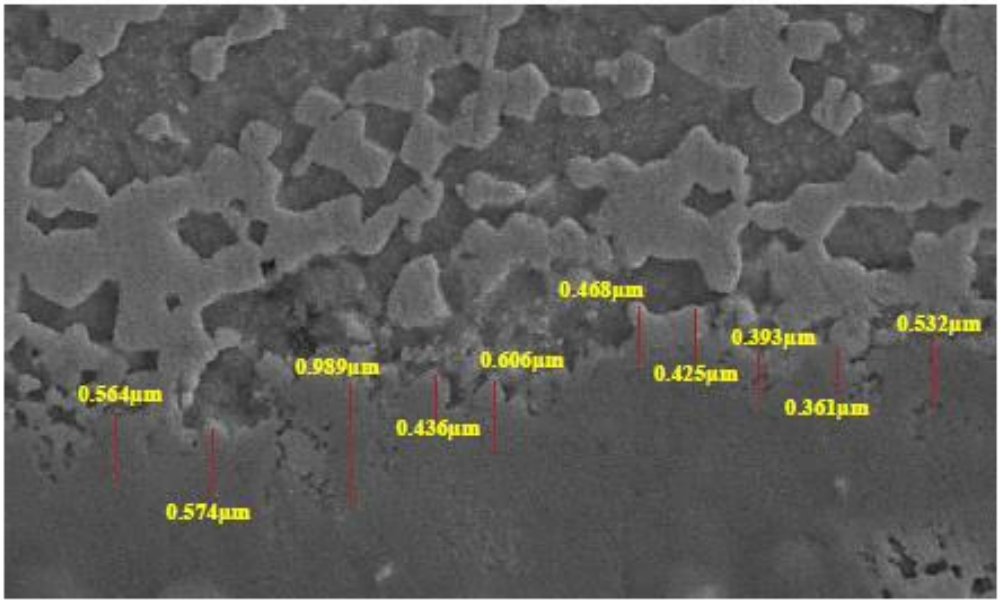

Figure C 3: IMC thickness of SB + 2 % Mo/Cu solder joint.

a)

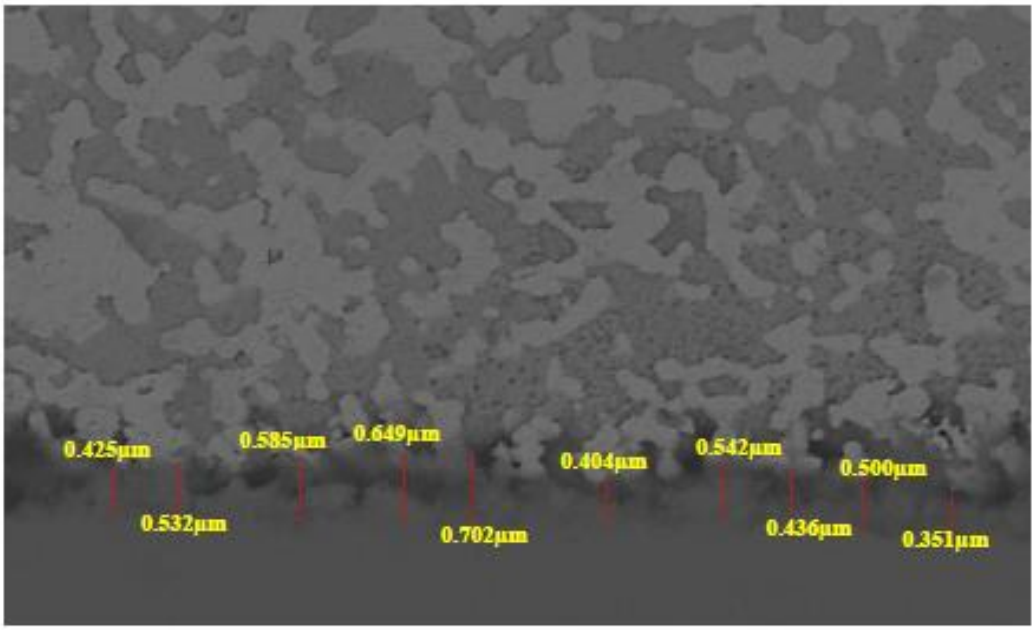
0.425µm
0.585µm
0.649µm
0.404µm
0.542µm
0.500µm
0.532µm
0.702µm
0.436µm
0.351µm

b)

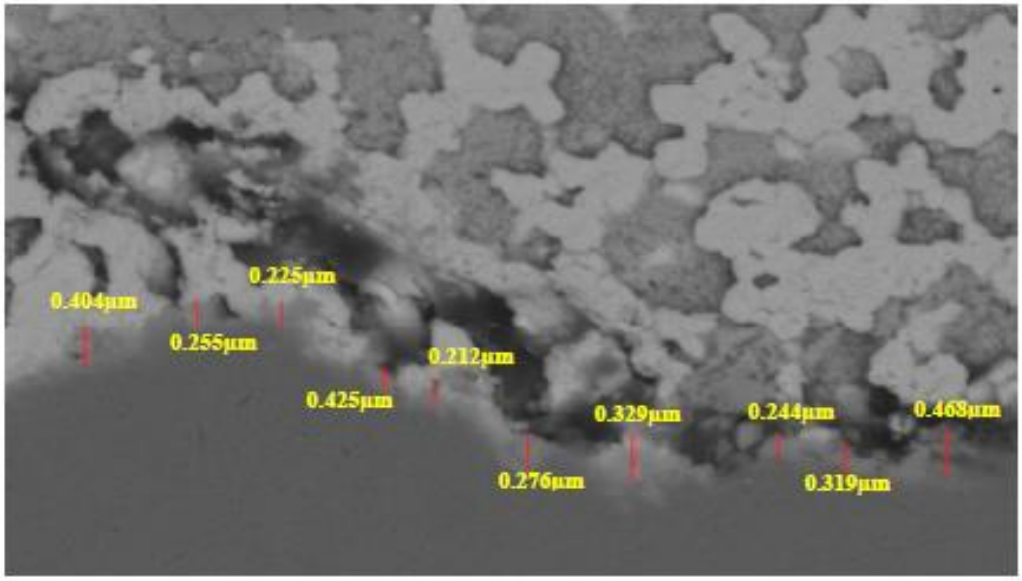
0.225µm
0.404µm
0.255µm
0.212µm
0.425µm
0.329µm
0.244µm
0.468µm
0.276µm
0.319µm

c)

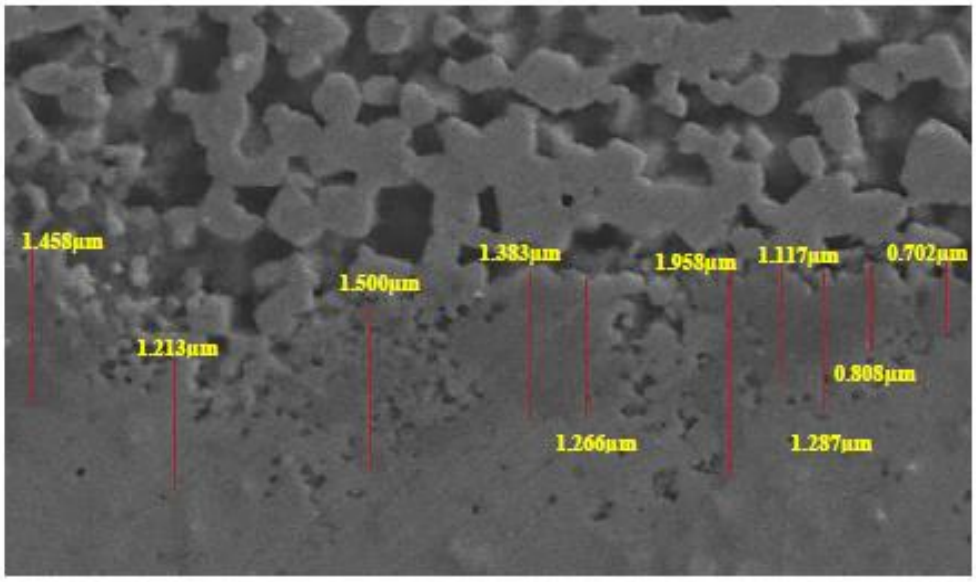

d)

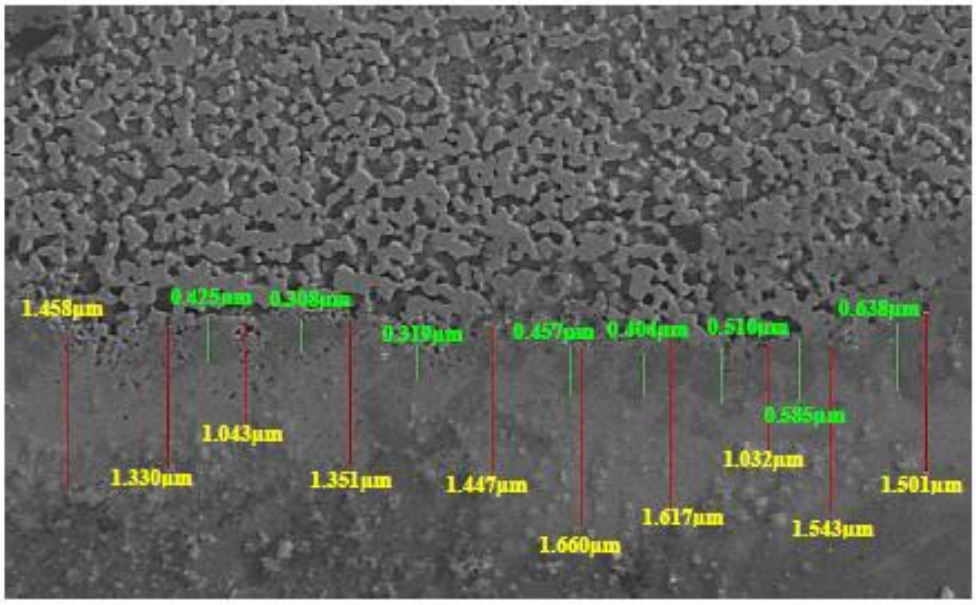

Figure C 4: IMC thickness of SB + 3 % Mo/Cu solder joint.

a)

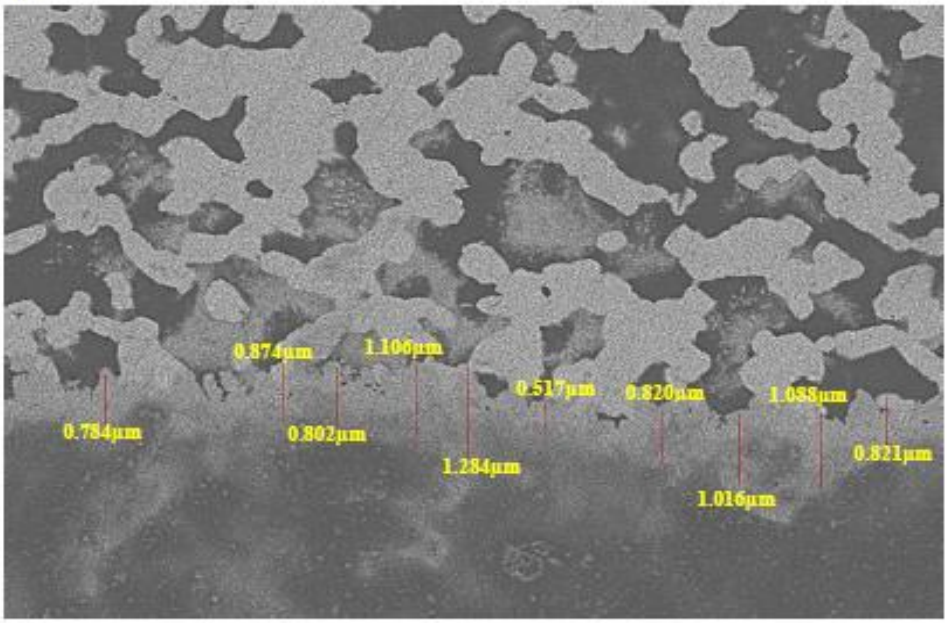
0.874µm
1.106µm
0.517µm
0.820µm
1.088µm
0.784µm
0.802µm
1.284µm
0.821µm
1.016µm

b)

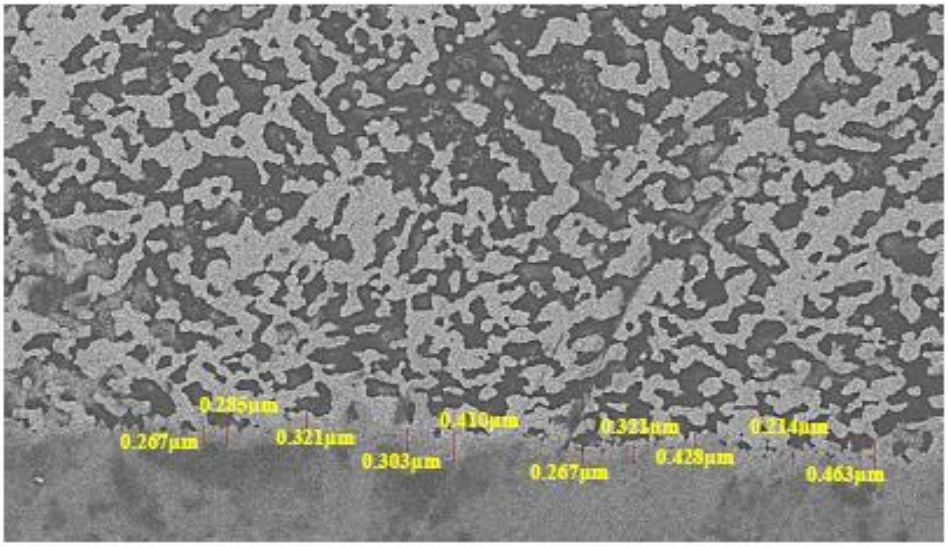
0.285µm
0.410µm
0.321µm
0.214µm
0.267µm
0.321µm
0.303µm
0.428µm
0.267µm
0.463µm

c)

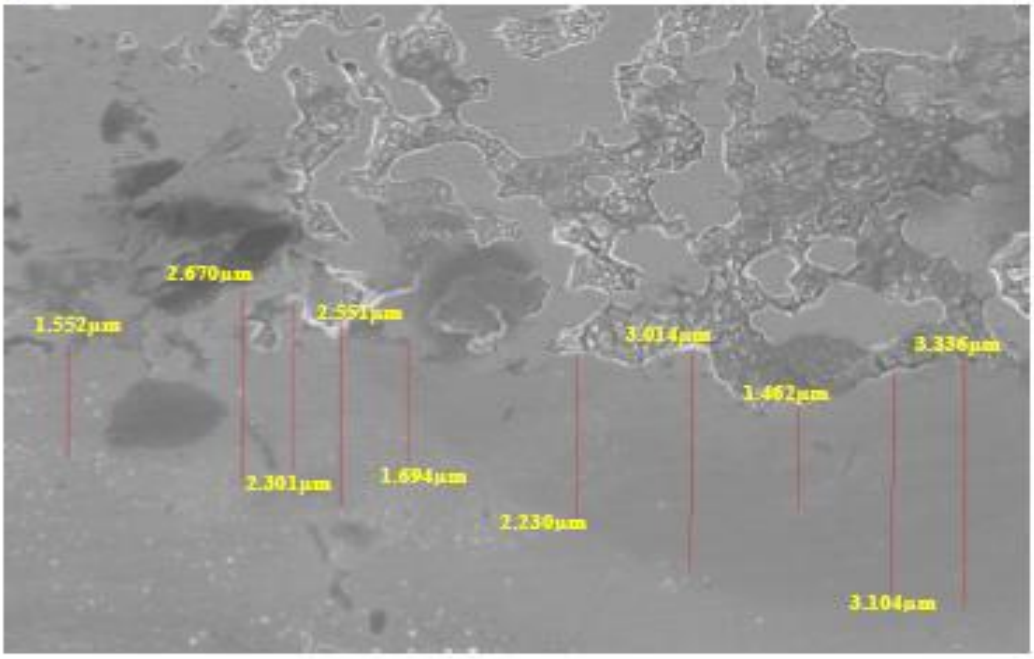

d)

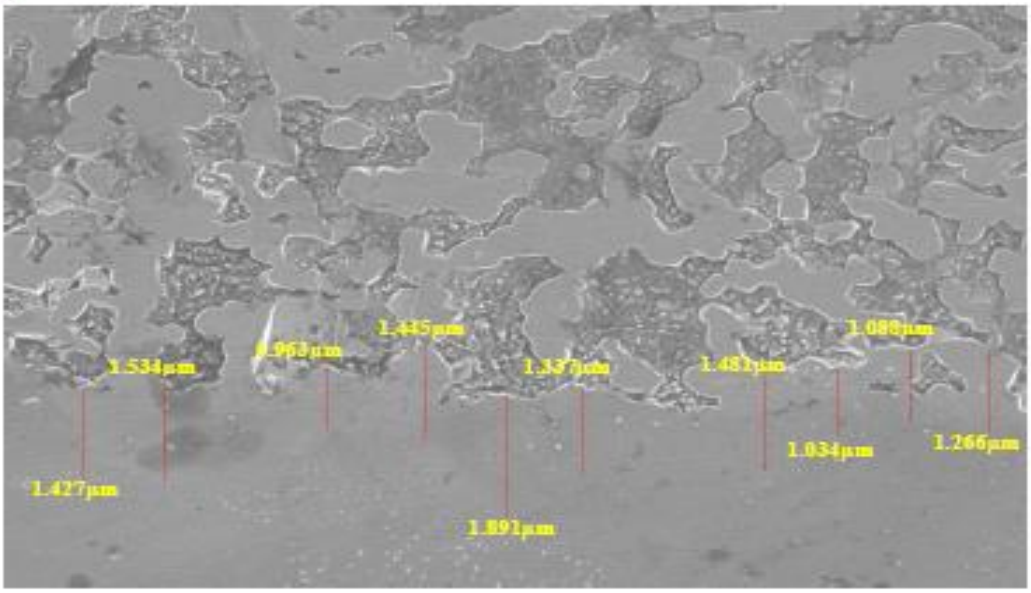

Figure C 5: IMC thickness of SB + 1% ZrO_2/Cu solder joint.

a)

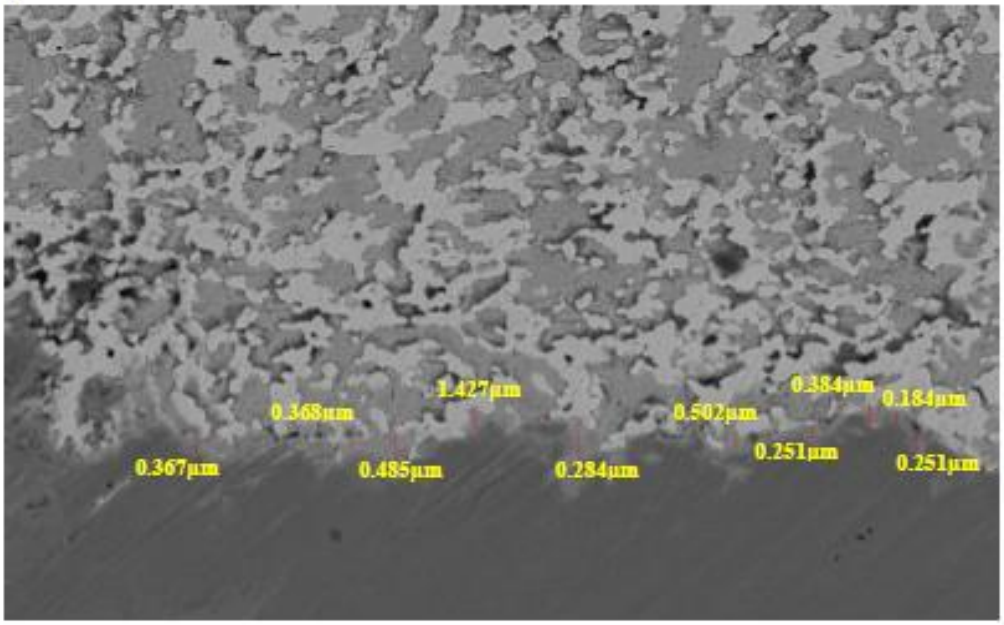
0.368µm
1.427µm
0.384µm
0.184µm
0.502µm
0.367µm
0.485µm
0.284µm
0.251µm
0.251µm

b)

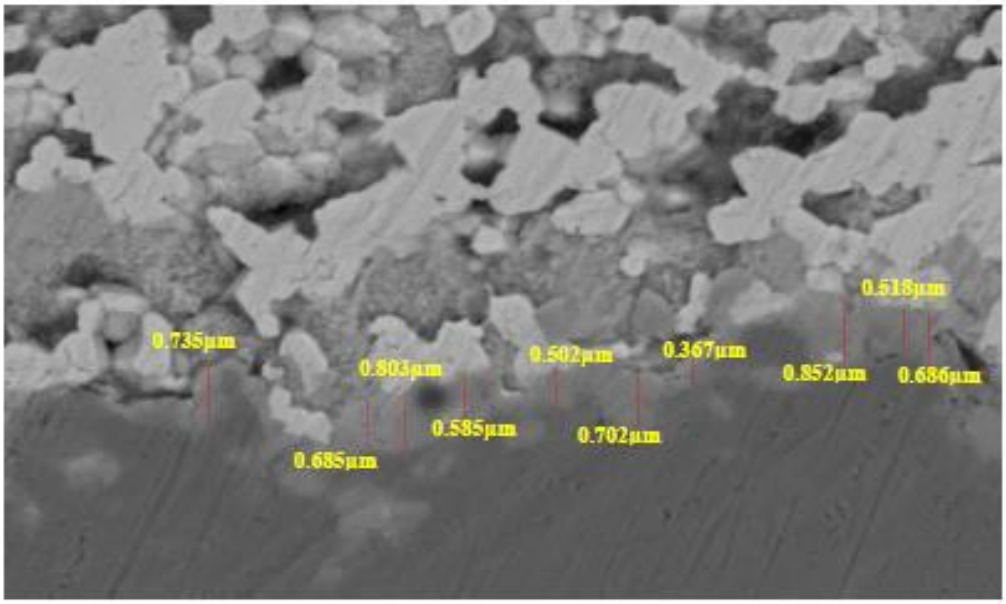
0.518µm
0.735µm
0.803µm
0.502µm
0.367µm
0.852µm
0.686µm
0.585µm
0.702µm
0.685µm

c)

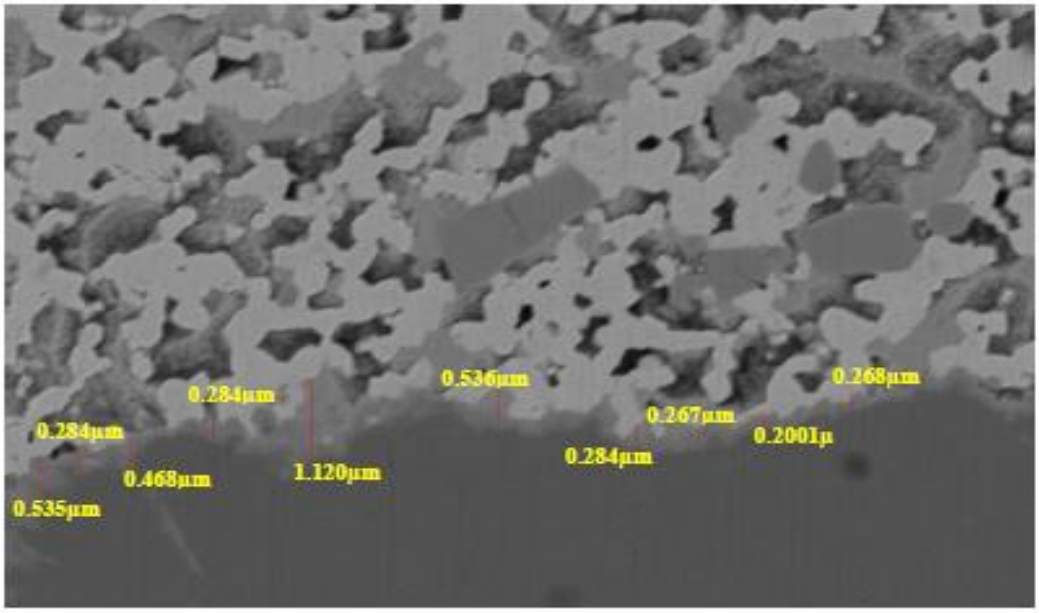

d)

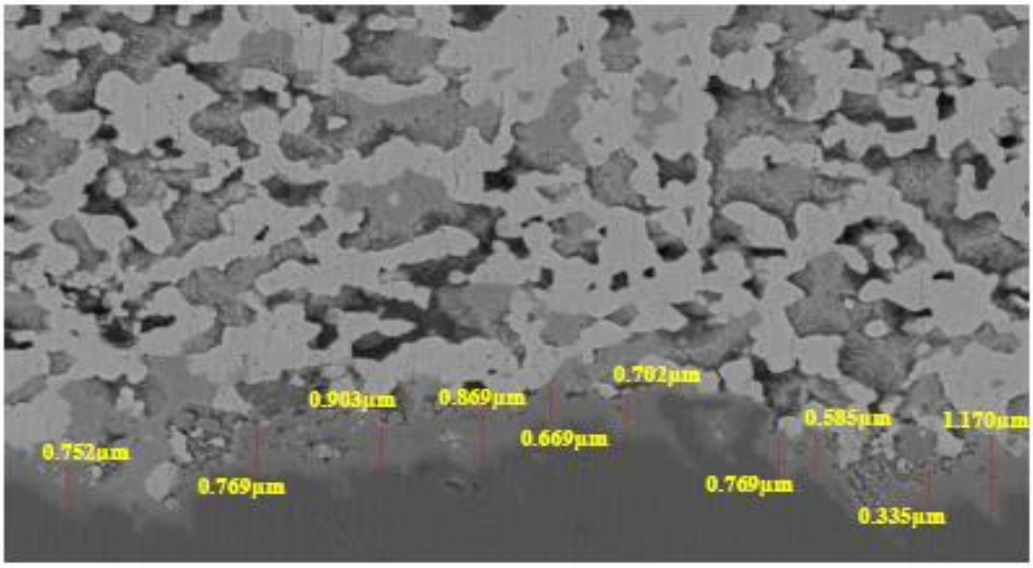

Figure C 6: IMC thickness of SB + 2 % ZrO_2/Cu solder joint.

a)

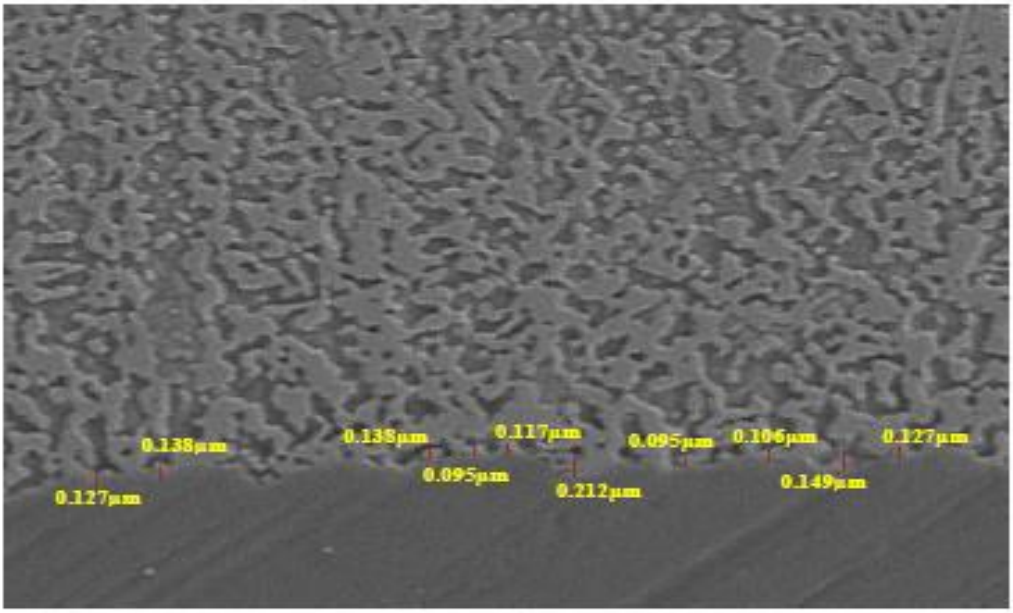
0.138µm
0.138µm
0.117µm
0.095µm
0.106µm
0.127µm
0.095µm
0.212µm
0.149µm
0.127µm

b)

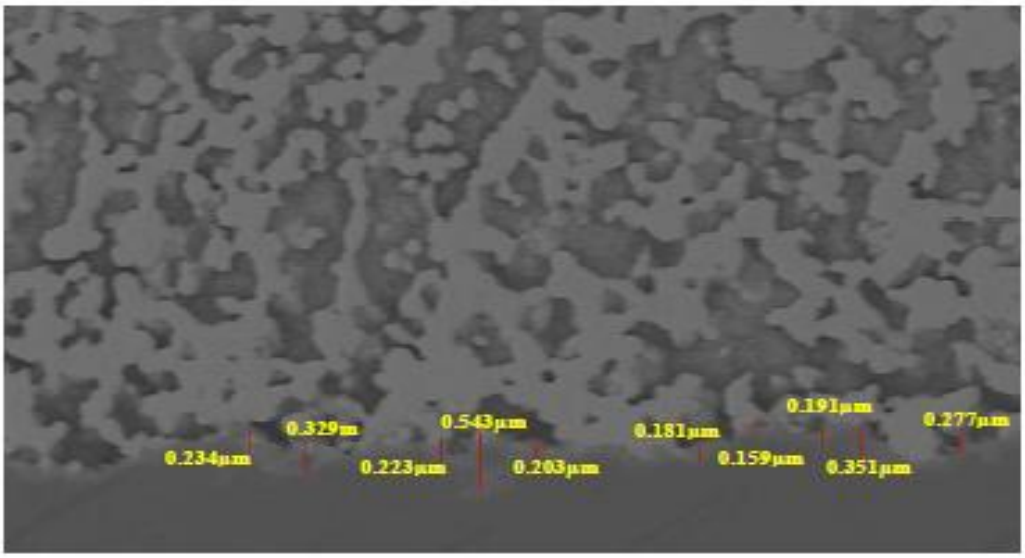
0.191µm
0.329m
0.543µm
0.181µm
0.277µm
0.234µm
0.223µm
0.203µm
0.159µm
0.351µm

c)

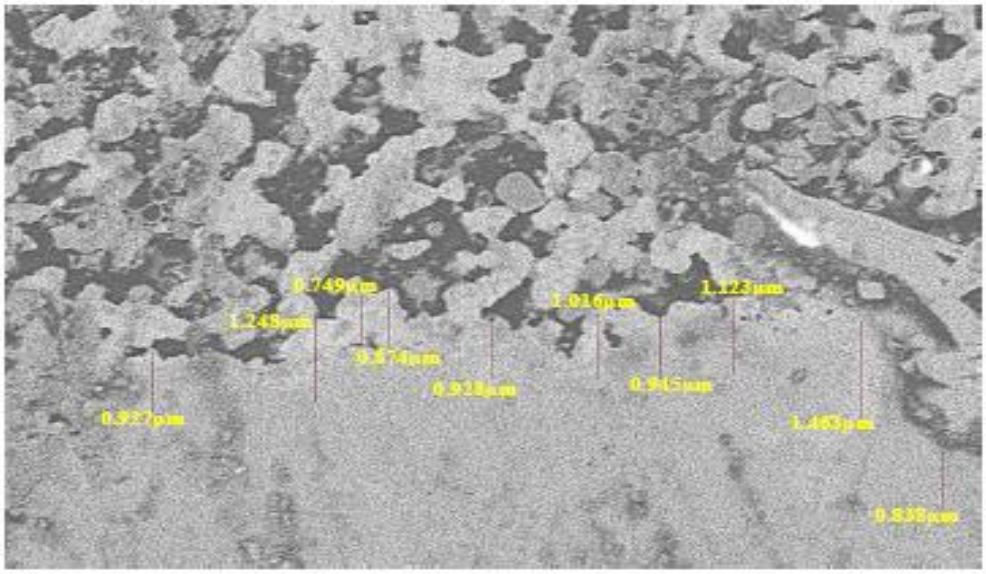

d)

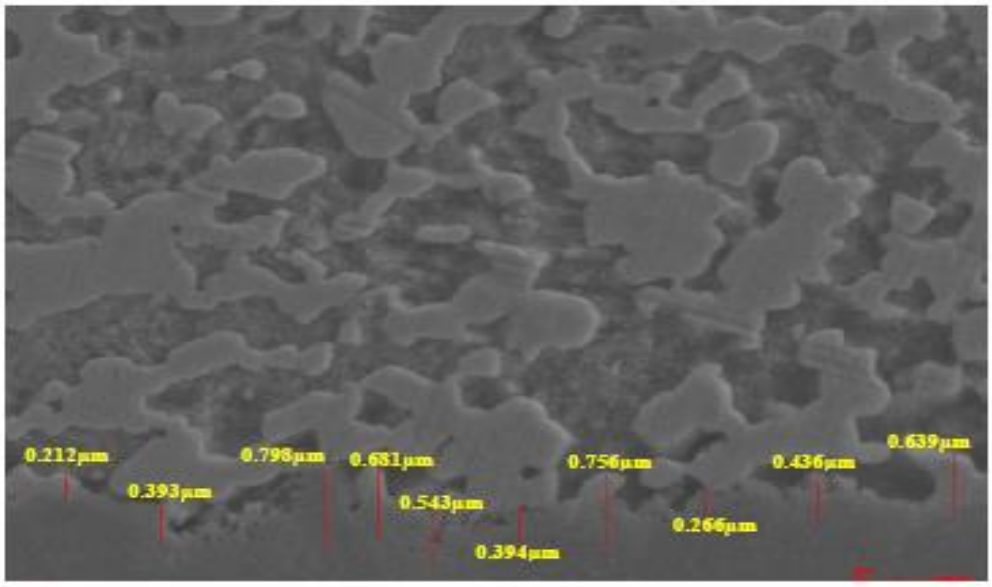

Figure C 7: IMC thickness of SB + 3 % ZrO_2/Cu solder joint.

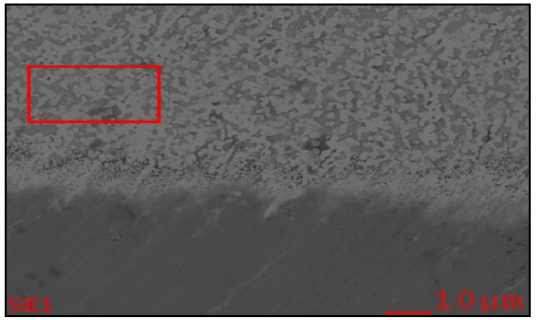

Element	Wt. %	At. %
Cu	02.02	05.98
Bi	89.25	80.21
Sn	08.73	13.81

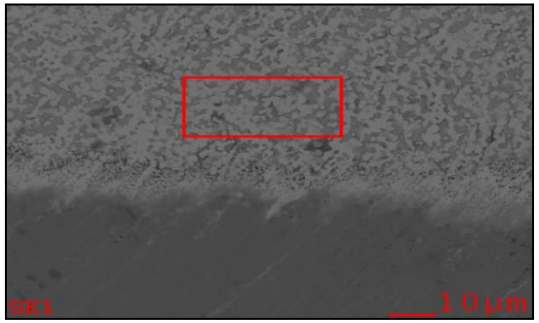

Element	Wt. %	At. %
Cu	08.39	20.83
Bi	74.22	56.04
Sn	17.40	23.13

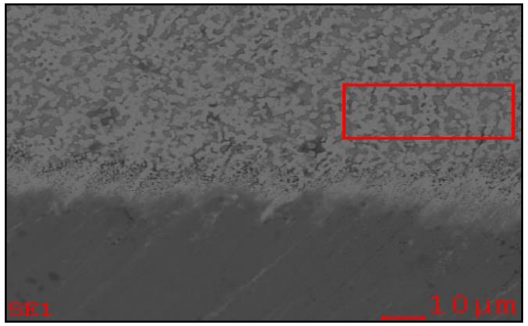

Element	Wt. %	At.%
Cu	02.80	08.18
Bi	89.18	79.26
Sn	08.03	12.56

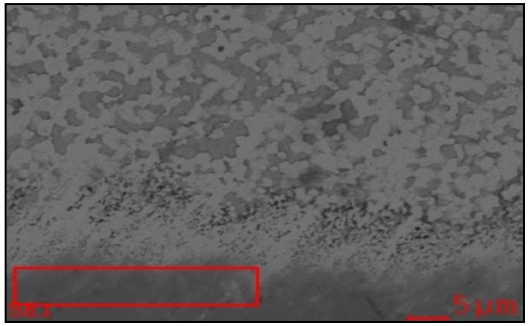

Element	Wt. %	At. %
Cu	63.00	77.70
Bi	07.45	02.79
Sn	29.54	19.51

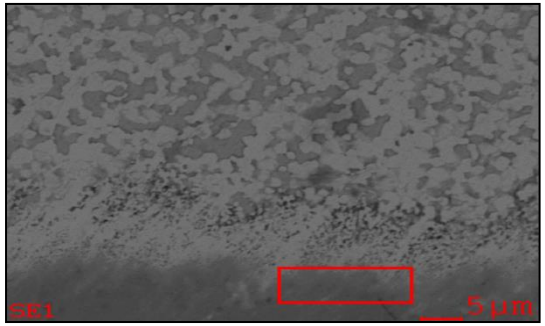

Element	Wt. %	At. %
Cu	44.25	64.21
Bi	22.41	09.89
Sn	33.34	25.90

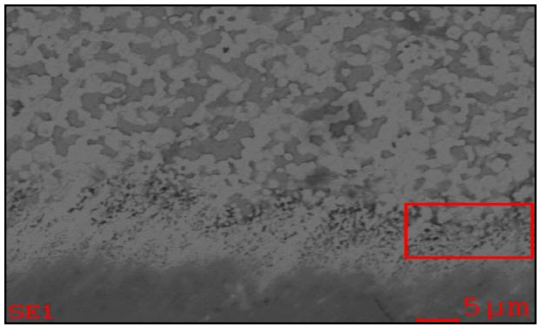

Element	Wt. %	At. %
Cu	02.02	05.98
Bi	89.25	80.21
Sn	08.73	13.81

Figure C 8: SEM/EDX of IMC layer of SB/Cu solder joint.

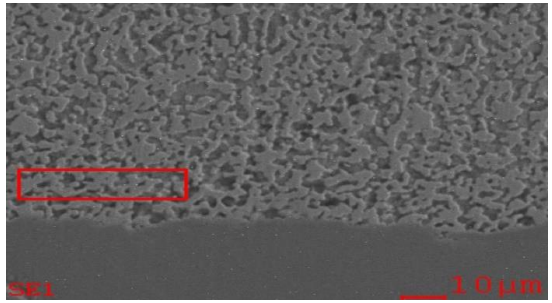

Element	Wt. %	At. %
Mo	02.80	04.98
Bi	79.50	64.84
Sn	13.88	19.94
Cu	03.82	10.25

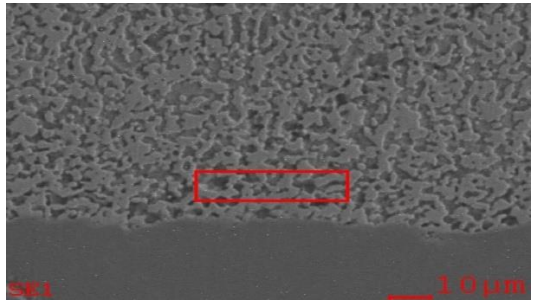

Element	Wt. %	At. %
Mo	03.01	05.41
Bi	82.25	67.76
Sn	10.39	15.06
Cu	04.35	11.77

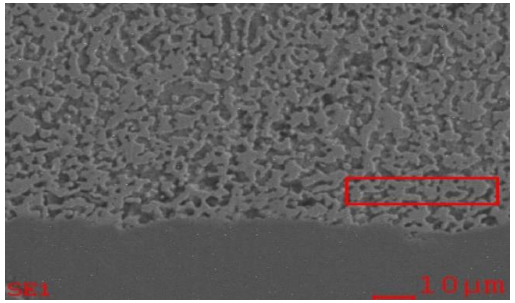

Element	Wt. %	At. %
Mo	02.96	05.26
Bi	75.16	61.33
Sn	20.31	29.17
Cu	01.58	04.24

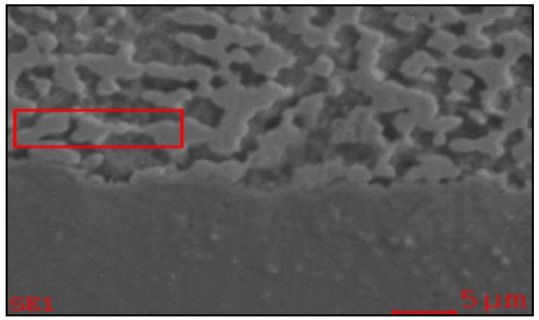

Element	Wt. %	At. %
Mo	02.22	03.79
Bi	73.46	57.65
Sn	20.19	27.90
Cu	04.13	10.66

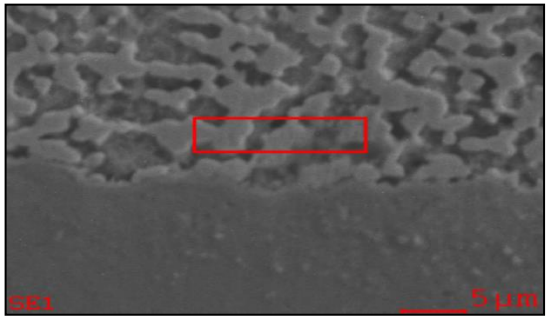

Element	Wt. %	At. %
Mo	02.35	03.74
Bi	71.87	52.51
Sn	16.28	20.94
Cu	09.50	22.82

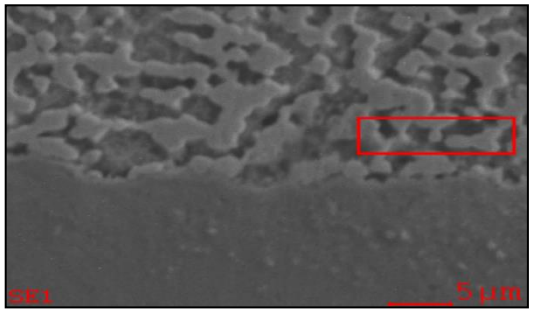

Element	Wt. %	At. %
Mo	02.37	04.25
Bi	80.66	66.33
Sn	13.12	18.99
Cu	03.85	10.42

Figure C 9: SEM/EDX of SB + 1 % Mo/Cu solder joint.

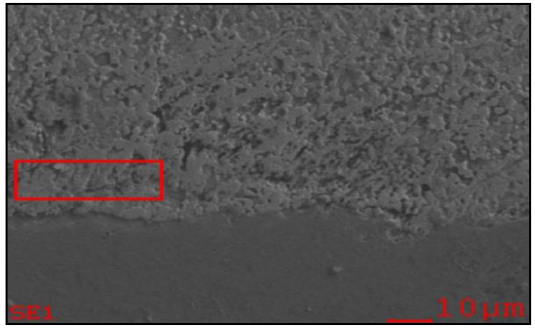

Element	Wt. %	At. %
Mo	02.01	03.31
Bi	66.13	50.02
Sn	28.18	37.53
Cu	03.68	09.14

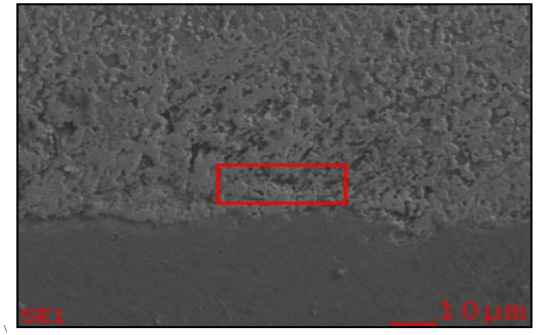

Element	Wt. %	At. %
Mo	02.30	03.69
Bi	61.54	45.21
Sn	32.29	41.77
Cu	03.86	09.33

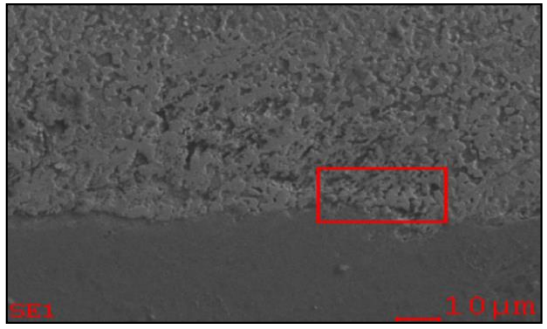

Element	Wt. %	At. %
Mo	02.30	03.69
Bi	61.54	45.21
Sn	32.29	41.77
Cu	03.86	09.33

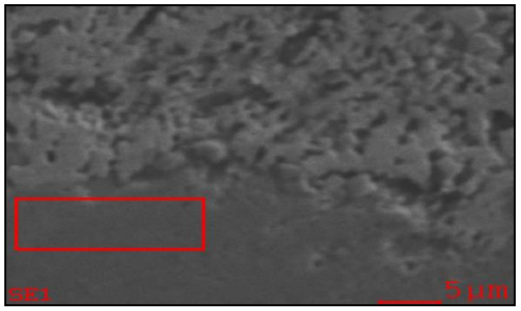

Element	Wt. %	At. %
Mo	04.16	07.84
Bi	84.58	73.24
Sn	09.94	15.16
Cu	01.32	03.76

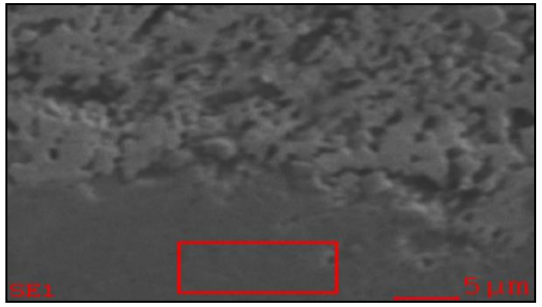

Element	Wt. %	At. %
Mo	05.44	05.44
Bi	69.20	69.20
Sn	22.93	22.93
Cu	02.43	02.43

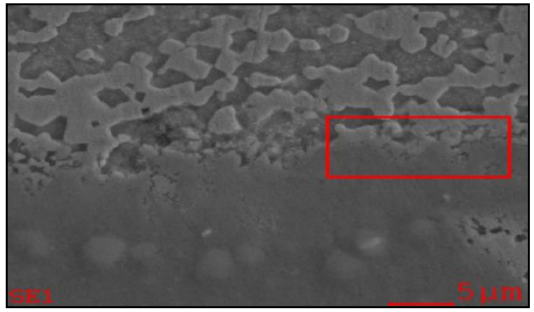

Element	Wt. %	At. %
Mo	02.59	04.37
Bi	71.05	55.17
Sn	22.65	30.97
Cu	03.72	09.49

Figure C 10: SEM/EDX of SB + 2 % Mo/Cu solder joint.

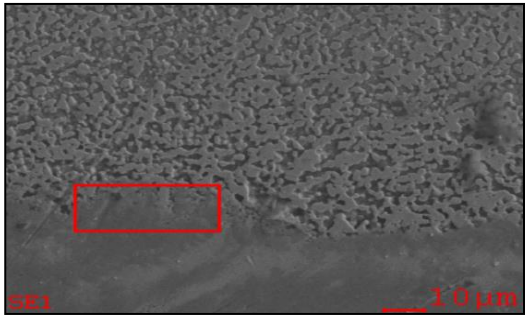

Element	Wt. %	At. %
Mo	02.69	03.48
Bi	44.88	26.66
Sn	35.88	37.52
Cu	16.56	32.34

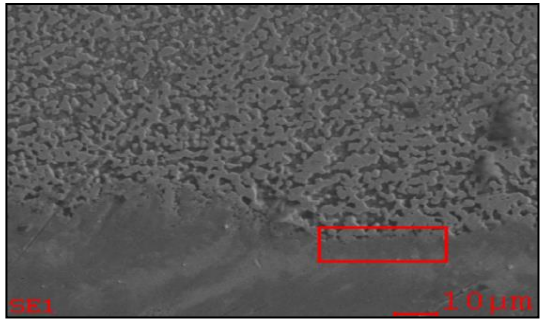

Element	Wt. %	At. %
Mo	02.85	02.81
Bi	21.02	09.53
Sn	37.37	29.84
Cu	38.77	57.82

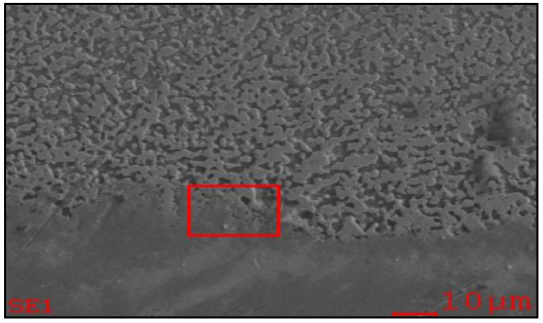

Element	Wt. %	At. %
Mo	04.18	05.36
Bi	44.22	26.01
Sn	34.71	35.96
Cu	16.89	32.68

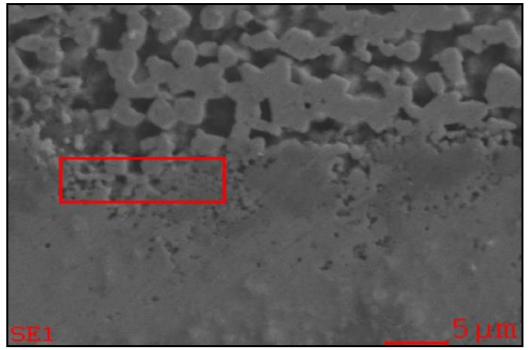

Element	Wt. %	At. %
Mo	03.83	05.14
Bi	52.66	32.44
Sn	27.33	29.65
Cu	16.17	32.77

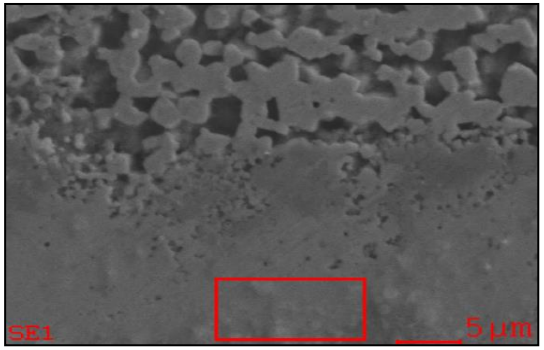

Element	Wt. %	At. %
Mo	01.66	02.48
Bi	71.97	49.23
Sn	10.54	12.69
Cu	15.82	35.60

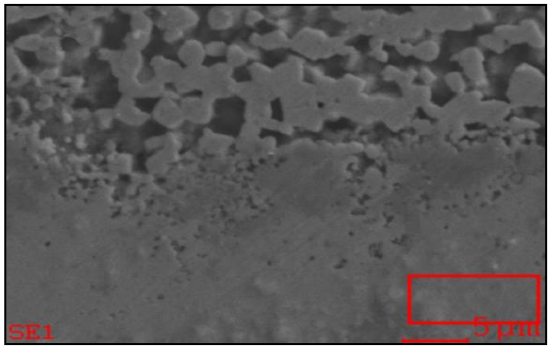

Element	Wt. %	At. %
Mo	01.75	02.53
Bi	68.90	45.82
Sn	12.36	14.47
Cu	16.99	37.17

Figure C 11: SEM/EDX of SB + 3 % Mo/Cu solder joint.

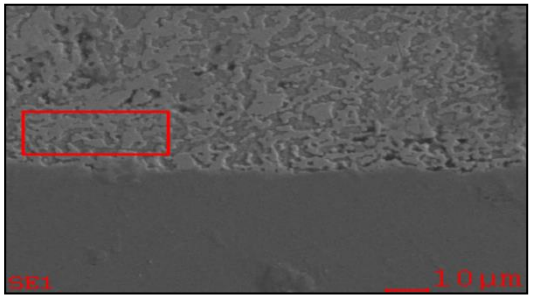

Element	Wt. %	At. %
Zr	03.01	05.21
Bi	65.85	49.70
Sn	27.93	37.12
Cu	03.21	07.97

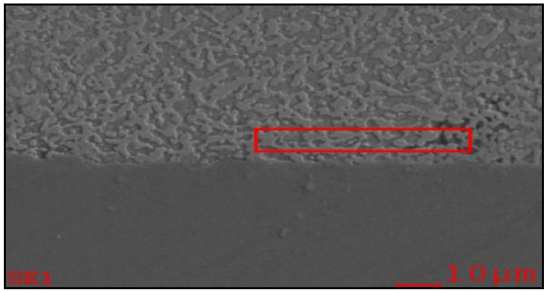

Element	Wt. %	At. %
Zr	03.04	05.00
Bi	59.43	42.68
Sn	33.10	41.86
Cu	04.43	10.47

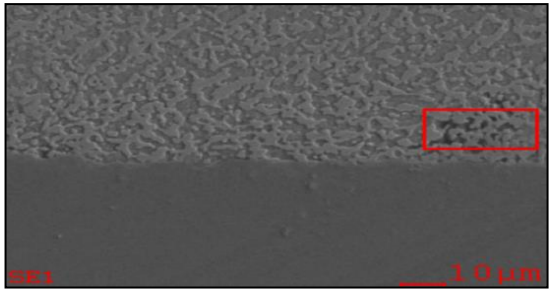

Element	Wt. %	At. %
Zr	03.18	05.53
Bi	67.35	51.12
Sn	26.03	34.78
Cu	03.44	08.58

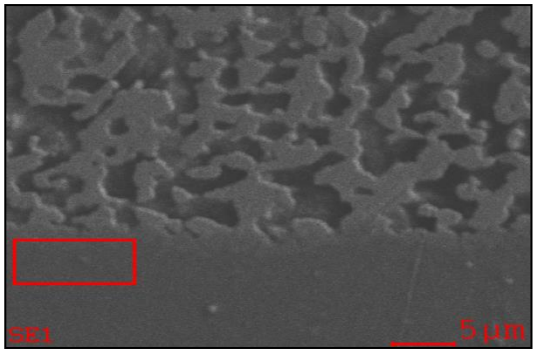

Element	Wt. %	At. %
Zr	04.43	07.11
Bi	57.42	40.20
Sn	32.86	40.50
Cu	05.30	12.19

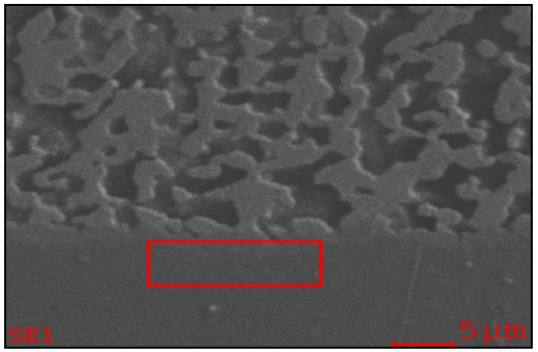

Element	Wt. %	At. %
Zr	04.38	08.08
Bi	77.75	62.67
Sn	14.72	20.88
Cu	03.15	08.36

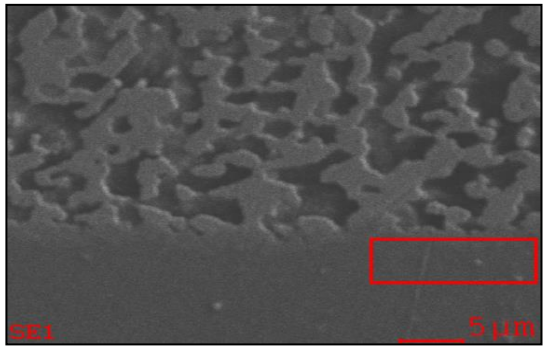

Element	Wt. %	At. %
Zr	03.90	07.44
Bi	84.38	70.34
Sn	07.80	11.44
Cu	03.93	10.78

Figure C 12: SEM/EDX of SB + 1 % ZrO_2/Cu solder joint.

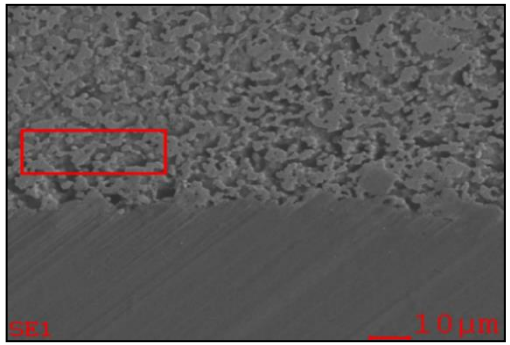

Element	Wt. %	At. %
Zr	03.01	05.21
Bi	65.85	49.70
Sn	27.93	37.12
Cu	03.21	07.97

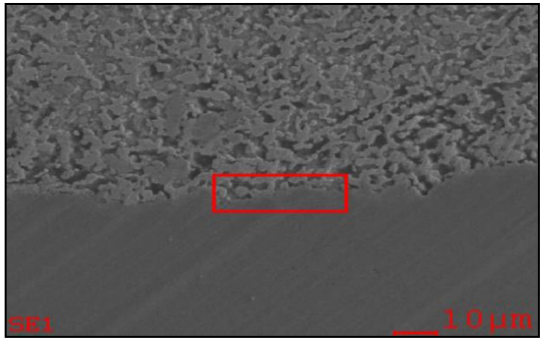

Element	Wt. %	At. %
Zr	03.18	04.26
Bi	52.90	30.89
Sn	21.85	22.47
Cu	22.07	42.39

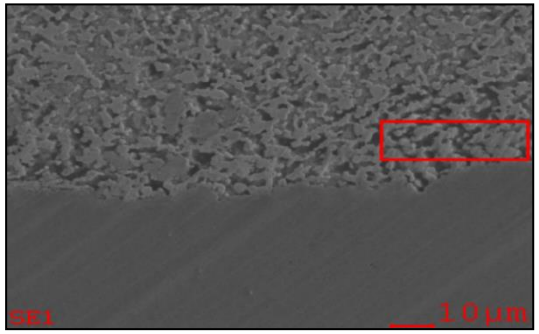

Element	Wt. %	At. %
Zr	02.41	04.79
Bi	85.26	74.00
Sn	10.55	16.12
Cu	01.79	05.10

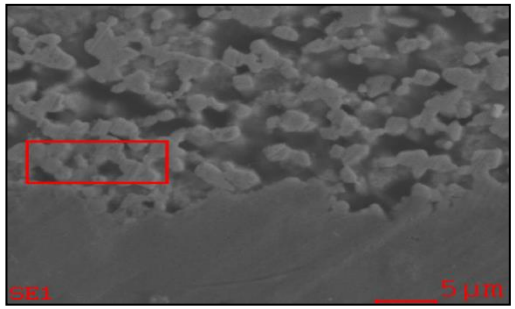

Element	Wt. %	At. %
Zr	00.42	00.78
Bi	74.84	59.88
Sn	21.06	29.67
Cu	03.68	09.67

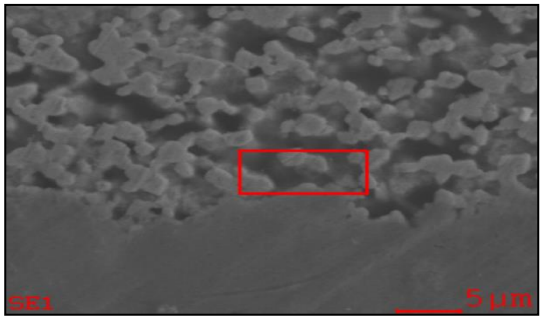

Element	Wt. %	At. %
Zr	00.72	01.43
Bi	83.63	72.25
Sn	13.75	20.91
Cu	01.90	05.41

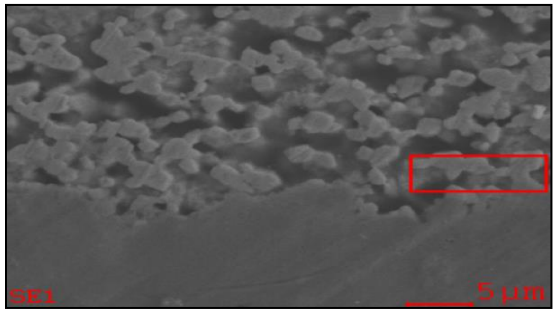

Element	Wt. %	At. %
Zr	01.77	03.23
Bi	73.34	58.31
Sn	21.90	30.66
Cu	02.98	07.80

Figure C 13: SEM/EDX of SB + 2 % ZrO_2/Cu solder joint.

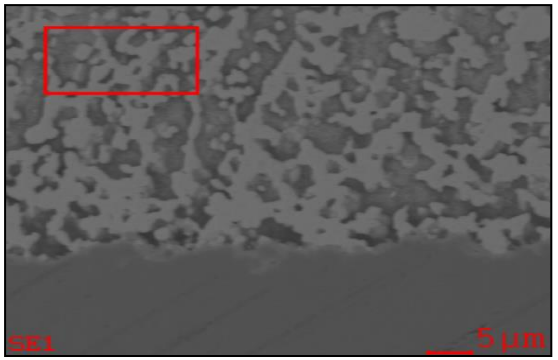

Element	Wt. %	At. %
Zr	02.95	17.2
Bi	65.28	43.07
Sn	28.95	33.62
Cu	02.81	06.11

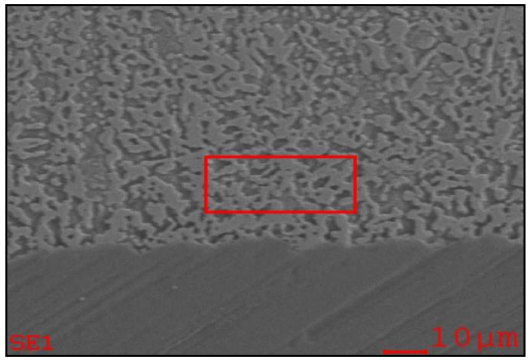

Element	Wt. %	At. %
Zr	00.64	01.17
Bi	71.36	56.77
Sn	25.67	35.95
Cu	02.33	06.10

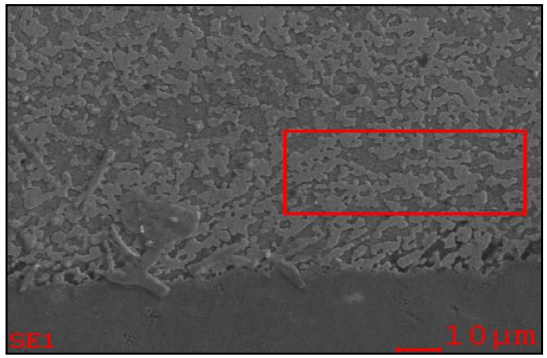

Element	Wt. %	At. %
Zr	00.68	01.12
Bi	52.73	37.89
Sn	44.72	56.58
Cu	01.87	04.41

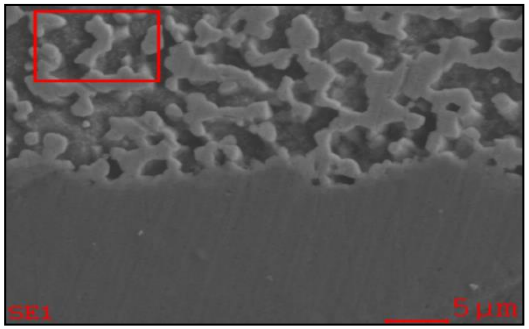

Element	Wt. %	At. %
Zr	00.30	00.53
Bi	63.91	49.28
Sn	34.43	46.74
Cu	01.36	03.44

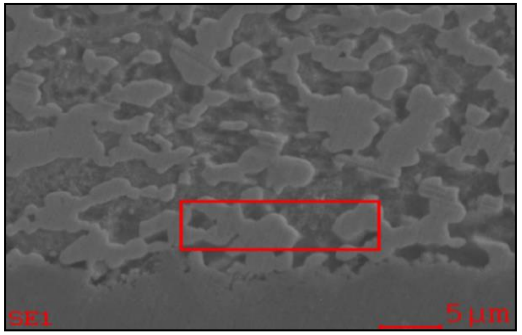

Element	Wt. %	At. %
Zr	00.47	00.83
Bi	68.37	53.14
Sn	28.32	38.76
Cu	02.84	07.27

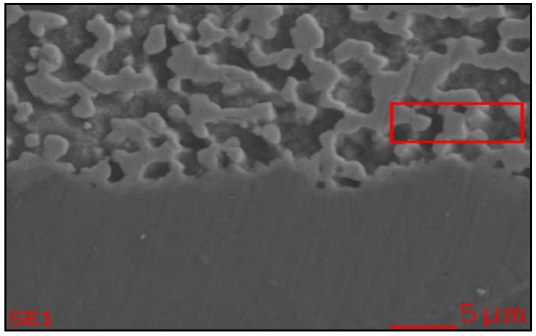

Element	Wt. %	At. %
Zr	00.25	00.48
Bi	84.38	72.24
Sn	12.24	18.45
Cu	03.14	08.83

Figure C 14: SEM/EDX of SB + 3 % ZrO_2/Cu solder joint.

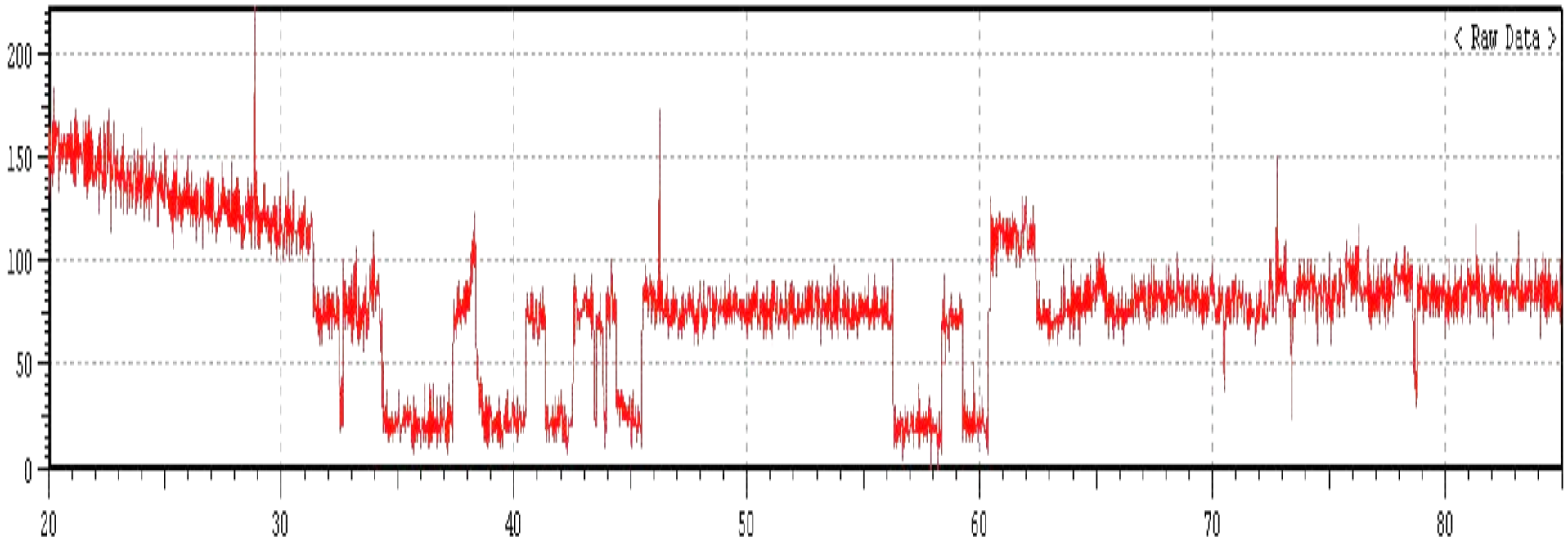

Figure C 15: XRD raw data of diffraction angle 2Θ of SB/Cu solder joint.

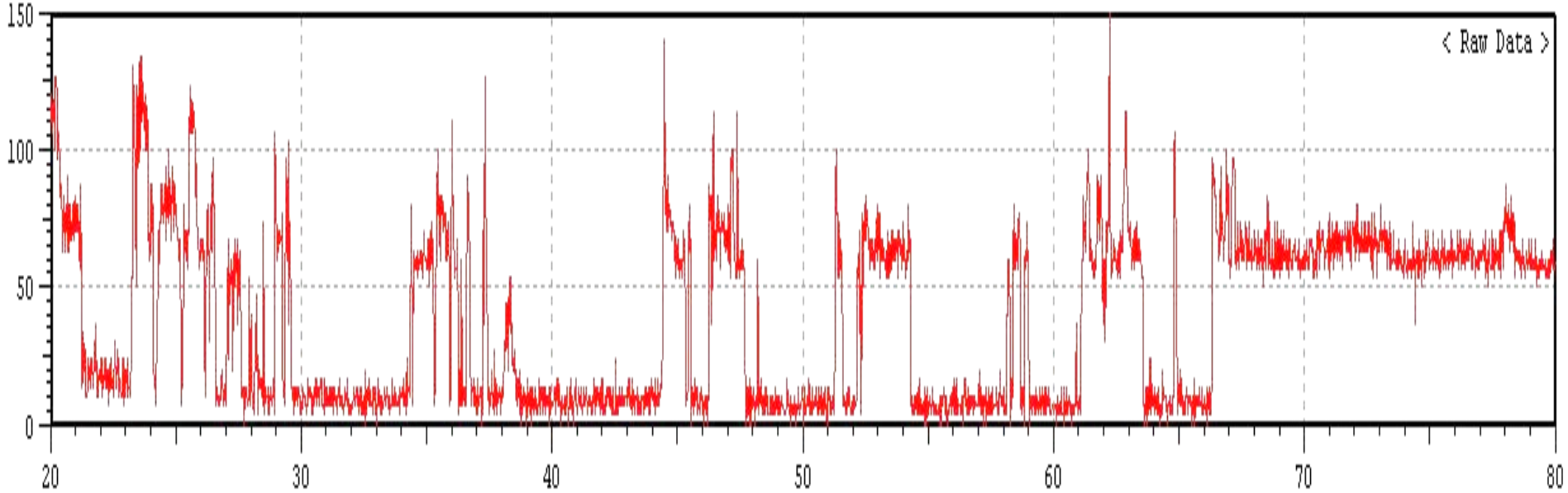

Figure C 16: XRD raw data of diffraction angle 2Θ of SB + 1 % Mo/Cu solder joint.

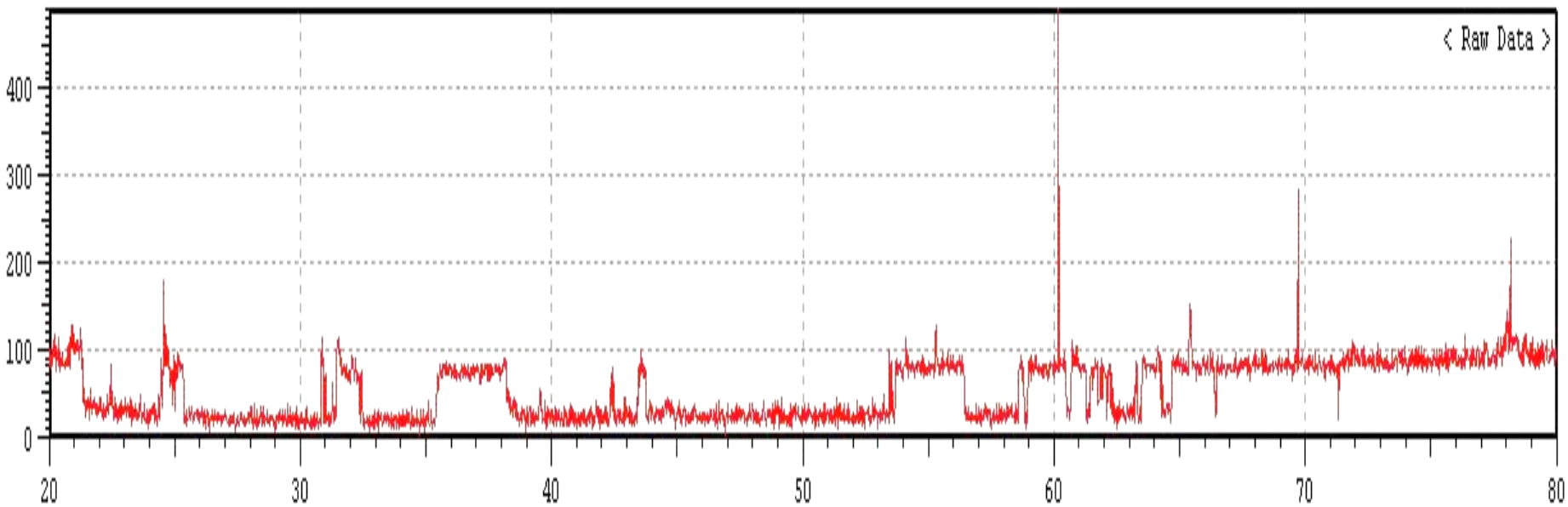

Figure C 17: XRD raw data of diffraction angle 2Θ of SB + 2 % Mo/Cu solder joint.

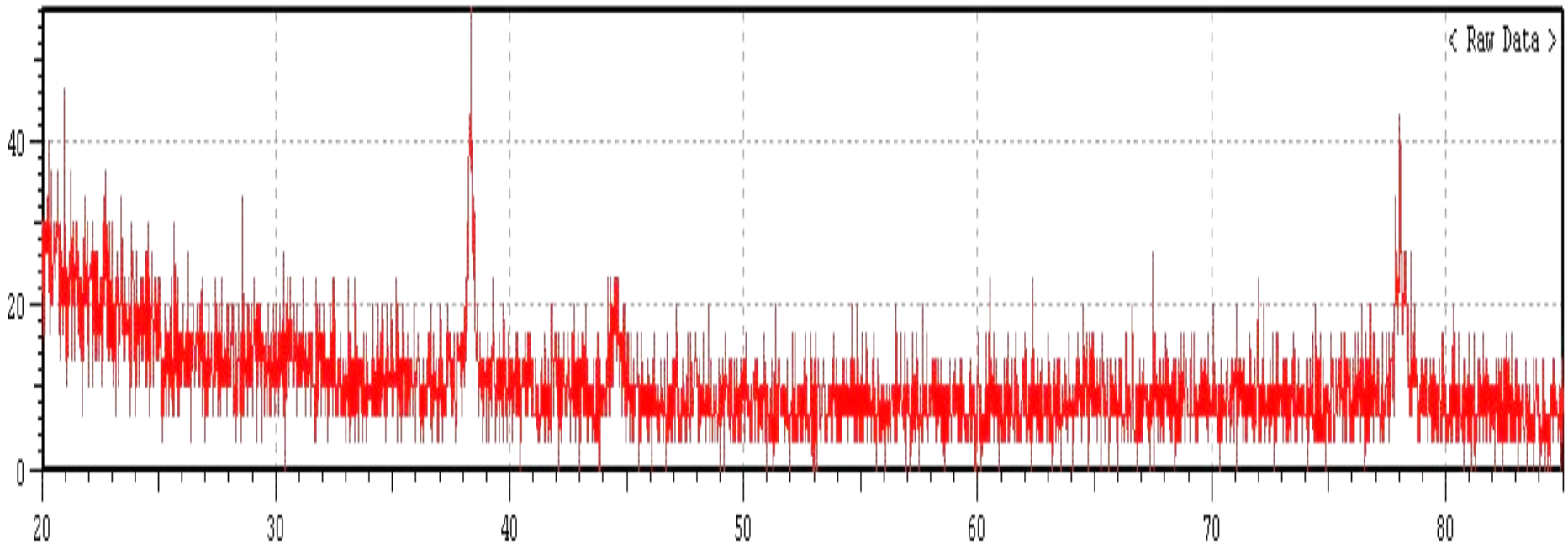

Figure C 18: XRD raw data of diffraction angle 2Θ of SB + 3 % Mo/Cu solder joint.

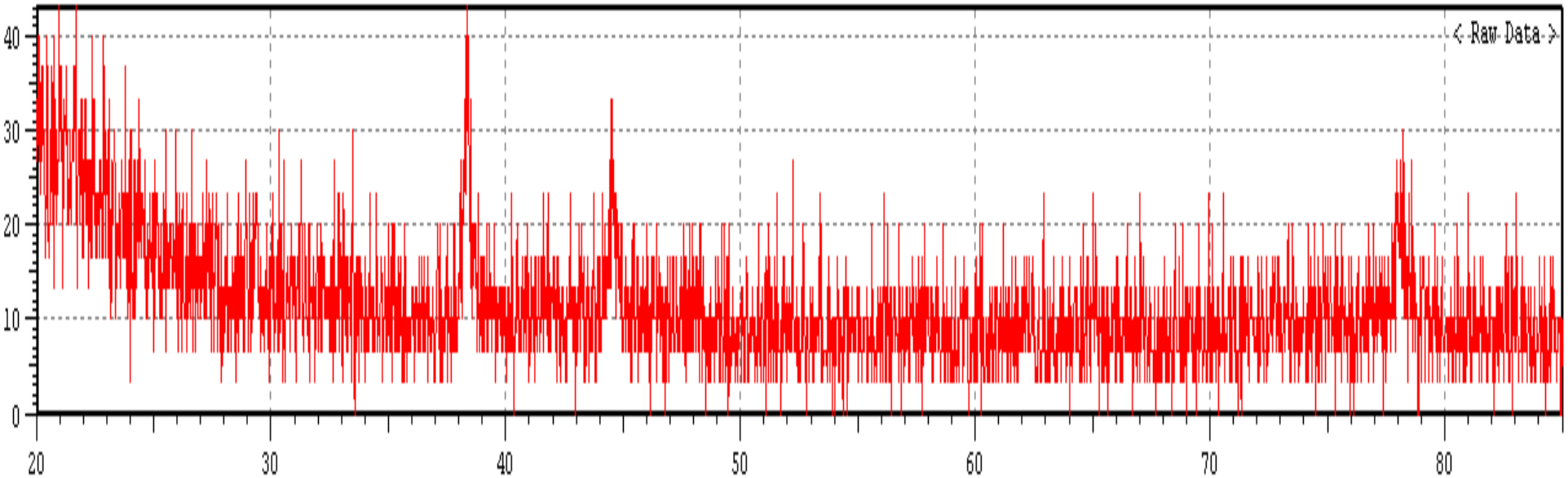

Figure C 19: XRD raw data of diffraction angle 2Θ of SB + 1 % ZrO_2/Cu solder joint.

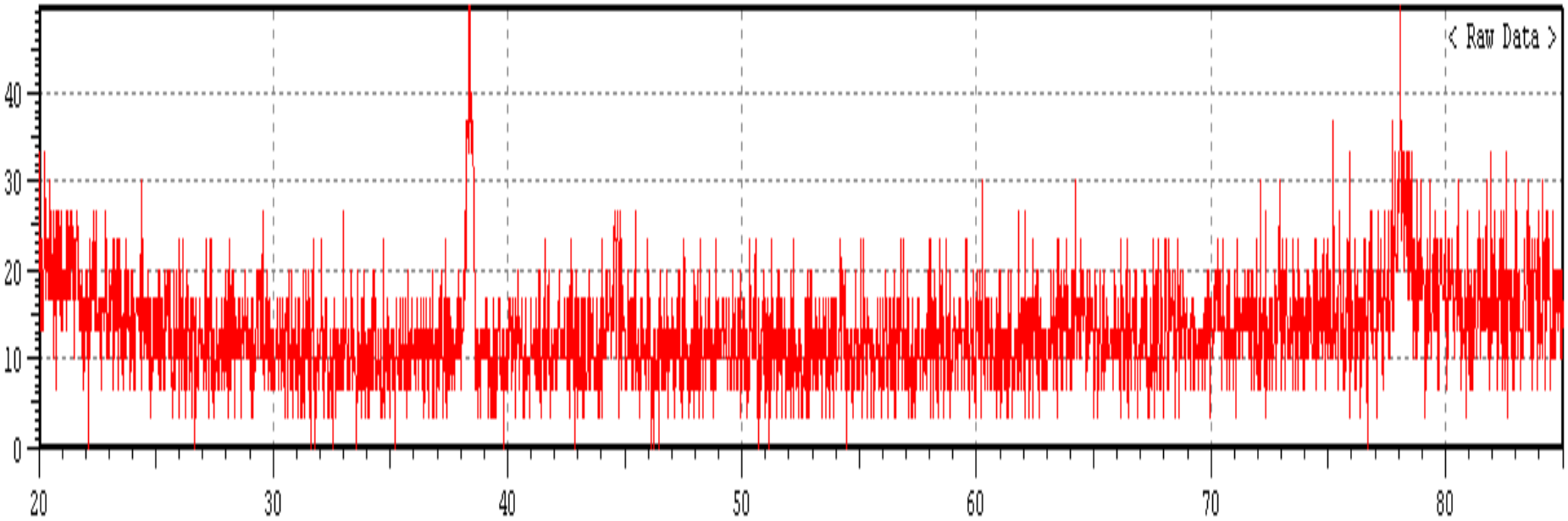

Figure C 20: XRD raw data of diffraction angle 2Θ of SB + 2 % ZrO_2/Cu solder joint.

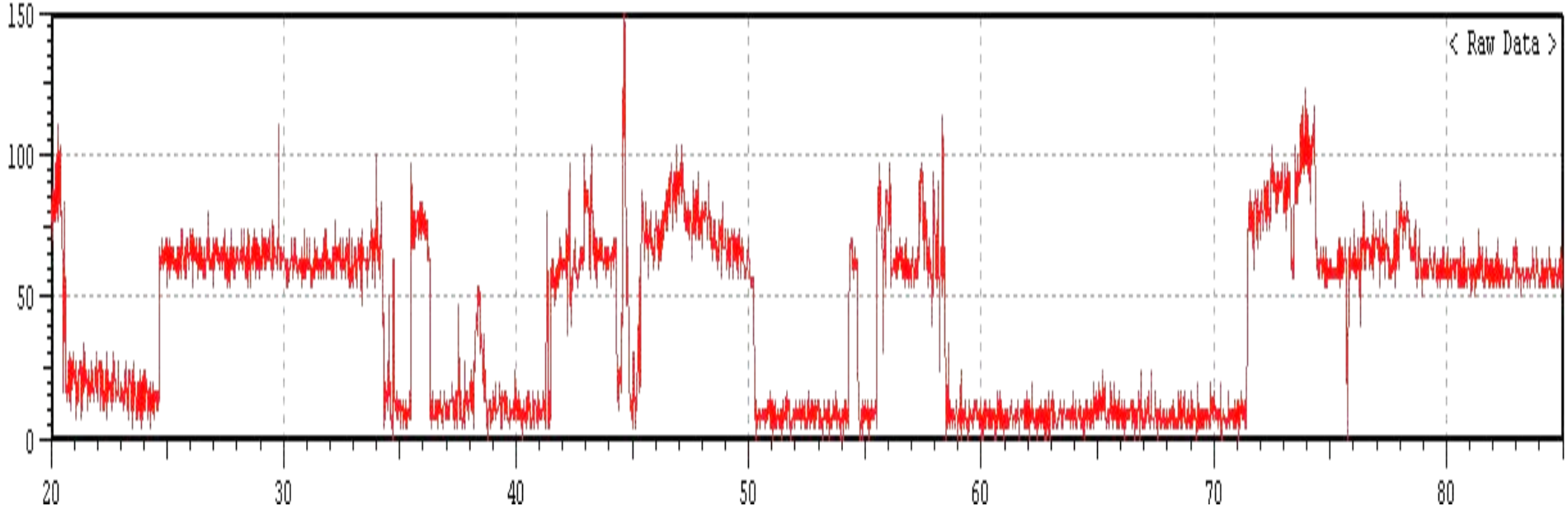

Figure C 21: XRD raw data of diffraction angle 2Θ of SB + 3 % ZrO_2/Cu solder joint.

Table C 1: Angle 2Θ of the phases and elements in XRD peaks for SB/Cu solder joint.

Element (2θ)					
Bi	**Sn**	**Cu**	**CuSn**	**Cu_6Sn_5**	**Cu_3Sn**
33.50	44.90	43.30	43.47	22.53	37.77
48.13	55.33	50.43	50.08	26.06	41.79
59.81	62.54	74.13	73.20	26.30	43.47
70.30	63.78			27.64	57.56
	64.58			30.09	67.86
	72.42			31.59	76.81
	79.47			32.58	
				33.42	
				35.14	
				36.22	
				36.97	
				38.13	
				38.88	
				39.39	
				40.30	

Table C 1 continued: Angle 2Θ of the phases and elements in XRD peaks for SB/Cu solder joint.

Bi	**Sn**	**Cu**	**CuSn**	**Cu_6Sn_5**	**Cu_3Sn**
				41.21	
				42.97	
				43.27	
				44.78	
				45.69	
				47.20	
				53.38	
				56.69	
				58.55	
				60.01	
				62.64	
				63.43	
				67.93	
				69.14	
				69.51	
				70.84	
				74.38	
				76.61	
				78.77	
				79.00	

Table C 2: Angle 2Θ of the phases and elements in XRD peaks for SB + 1 % Mo/Cu solder joint.

Element (2θ)							
Bi	**Sn**	**Cu**	**CuSn**	**Cu_6Sn_5**	**Cu_3Sn**	**$Cu_{10}Sn_3$**	**$MoSn_2$**
28.50	34.25	43.30	43.47	30.13	37.77	22.61	31.51
28.80	36.01	50.43	50.08	35.18	41.79	24.23	33.20
29.18	49.24	74.13	73.20	42.97	43.47	26.83	35.03
31.04	54.55			43.28	57.56	28.13	36.90
32.80	62.54			53.37	67.86	33.41	37.85

Table C 2: continued: Angle 2Θ of the phases and elements in XRD peaks for SB + 1 % Mo/Cu solder joint.

Bi	**Sn**	**Cu**	**CuSn**	**Cu_6Sn_5**	**Cu_3Sn**	**$Cu_{10}Sn_3$**	**$MoSn_2$**
39.46	65.91			56.70	76.81	36.34	42.56
41.27	72.10			60.03		37.11	48.88
44.46	76.52			62.64		37.44	57.49
45.57				70.84		39.26	58.58
47.97				74.39		42.36	59.77
52.88				76.64		42.74	61.01
55.77				78.75		44.21	62.35
60.46				78.98		44.83	65.20
62.87						46.18	68.31
63.59						48.46	69.97
67.14						48.87	
68.14						49.90	
68.71						51.19	
72.48						51.66	
73.86						51.94	
78.46						53.35	
						55.37	
						57.40	
						61.89	
						63.30	
						63.78	
						64.08	
						64.53	
						64.78	
						65.34	
						68.94	
						72.03	
						72.29	
						72.55	
						74.06	
						74.54	
						77.40	
						78.23	
						79.31	

Table C 3: Angle 2Θ of the phases and elements in XRD peaks for SB + 2 % Mo/Cu solder joint.

Element (2θ)					
Bi	**Sn**	**Cu**	**Cu_6Sn_5**	**$Cu_{10}Sn_3$**	**$MoSn_2$**
22.47	33.32	43.30	30.13	22.61	31.51
23.79	34.87	50.43	35.18	24.23	33.20
27.17	47.68	74.13	42.97	26.83	35.03
37.95	52.52		43.28	28.13	36.90
39.62	60.42		53.37	33.41	37.85
44.55	63.54		56.70	36.34	42.56
45.52	69.76		60.03	37.11	48.88
45.87			62.64	37.44	57.49
46.01			70.84	39.26	58.58
46.73			74.39	42.36	59.77
48.69			76.64	42.74	61.01
55.64			78.75	44.21	62.35
59.33			78.98	44.83	65.20
61.12				46.18	68.31
62.18				48.46	69.97
62.89				48.87	
64.50				49.90	
67.45				51.19	
70.77				51.66	
71.53				51.94	
71.87				53.35	
73.71				55.37	
75.32				57.40	
76.40				61.89	
				63.30	
				63.78	
				64.08	
				64.53	
				64.78	
				65.34	
				68.94	

Table C3 continued: Angle 2Θ of the phases and elements in XRD peaks for SB + 2 % Mo/Cu solder joint.

Bi	**Sn**	**Cu**	**Cu_6Sn_5**	**$Cu_{10}Sn_3$**
			72.03	
			72.29	
			72.55	
			74.06	
			74.54	
			77.40	
			78.23	
			79.31	

Table C 4: Angle 2Θ of the phases and elements in XRD peaks for SB + 3 % Mo/Cu solder joint.

Element (2θ)						
Bi	**Sn**	**Cu**	**CuSn**	**Cu_6Sn_5**	**$Cu_{10}Sn_3$**	**$MoSn_2$**
33.50	23.70	43.30	43.47	22.53	22.61	31.51
48.13	39.24	50.43	50.08	26.06	24.23	33.20
59.81	46.38	74.13	73.20	26.30	26.83	35.03
70.03	56.71			27.64	28.13	36.90
80.03	62.31			30.09	33.41	37.85
	71.09			31.58	36.34	42.56
	76.16			32.38	37.11	48.88
	84.38			33.42	37.44	57.49
				35.14	39.26	58.58
				36.22	42.36	59.77
				36.97	42.74	61.01
				38.13	44.21	62.35
				38.88	44.83	65.20
				39.38	46.18	68.31
				40.30	48.46	69.97
				41.21	48.87	
				42.97	49.90	
				43.27	51.19	
				44.78	51.66	

Table C 4 continued: Angle 2Θ of the phases and elements in XRD peaks for SB + 3 % Mo/Cu solder joint.

Bi	**Sn**	**Cu**	**CuSn**	**Cu_6Sn_5**	**$Cu_{10}Sn_3$**	**$MoSn_2$**
				45.69	51.94	
				47.20	53.35	
				48.24	55.37	
				53.38	57.40	
				56.69	61.89	
				58.55	63.30	
				60.01	63.70	
				62.64	64.08	
				63.43	64.53	
				67.93	64.78	
				69.14	65.34	
				69.51	68.94	
				70.84	72.03	
				74.38	72.29	
				76.61	72.55	
				78.77	74.06	
				79.00	74.54	
					77.40	
					78.23	
					79.31	

Table C 5: Angle 2Θ of the phases and elements in XRD peaks for SB + 1 % ZrO_2/Cu solder joint.

Element (2θ)												
BiO_2	**Sn**	**Cu**	**CuSn**	**Cu_6Sn_5**	**Cu_3Sn**	**$Cu_{10}Sn_3$**	**SnO**	**SnZr**	**Zr_5Sn_3**	**ZrCu**	**$ZrSn_2$**	**ZrO_2**
28.21	44.90	43.30	43.47	30.13	37.77	22.61	23.97	45.14	25.96	27.74	25.80	29.72
32.69	55.33	50.43	50.08	35.18	41.79	24.23	24.85	52.88	30.72	27.92	33.54	34.63
46.92	62.54	74.13	73.20	42.97	43.47	26.83	28.59	61.12	32.14	35.16	36.19	49.61
55.65	63.78			43.28	57.56	28.13	31.25	64.10	33.13	35.48	36.65	59.22
58.33	64.58			53.37	67.86	33.41	32.17	65.60	35.76	36.33	42.40	61.66
68.52	72.42			56.70	76.81	36.34	35.89	68.31	36.60	36.77	57.17	73.07
75.64	73.20			60.03	80.68	37.11	40.04	72.48	37.46	39.19	60.90	80.43
77.98	79.47			62.64	83.22	37.44	45.45	75.52	39.51	41.56	64.18	
87.12				70.84	84.11	39.26	48.16	77.03	44.32	42.97	65.19	
				74.39		42.36	49.01	78.15	45.38	43.72	66.23	
				76.64		42.74	51.50			45.12	67.31	
				78.75		44.21	54.55			47.38	75.37	
						44.83	55.22			56.10	76.08	
						46.18	57.17			57.28	76.81	
						48.46	60.03			57.72	78.31	
						48.87	65.24			71.78	79.08	
						49.90	67.14			74.96	84.11	
						51.19	70.06					
						51.66	76.01					
						51.94	76.88					

Table C 5 continued: Angle 2Θ of the phases and elements in XRD peaks for SB + 1 % ZrO_2/Cu solder joint.

Bi_2O_3	Sn	Cu	CuSn	Cu_6Sn_5	Cu_3Sn	$Cu_{10}Sn_3$	Cu_8Zr_3	SnO	SnZr	Zr_5Sn_3	$ZrSn_2$	ZrO_2
					53.35	78.85						
					55.37	81.26						
					57.40	84.93						
					61.89							
					63.30							
					63.70							
					64.08							
					64.53							
					64.78							
					65.34							
					68.94							
					72.03							
					72.29							
					72.55							
					74.06							
					74.54							
					77.40							
					78.23							
					79.31							
					80.11							
					80.68							
					81.26							

Table C 6: Angle 2Θ of the phases and elements in XRD peaks for SB + 2 % ZrO_2/Cu solder joint.

Element (2θ)													
Bi_2O_3	**Sn**	**Cu**	**CuSn**	**Cu_6Sn_5**	**Sn_3O_4**	**Cu_3Sn**	**$Cu_{10}Sn_3$**	**Cu_8Zr_3**	**SnO**	**SnZr**	**Zr_5Sn_3**	**$ZrSn_2$**	**ZrO_2**
22.74	44.90	43.30	43.47	30.13	21.77	37.77	22.61	26.16	23.97	26.03	26.03	25.80	29.72
27.95	55.33	50.43	50.08	35.18	27.00	41.79	24.23	26.55	24.85	28.40	30.88	33.54	34.63
32.39	62.54	74.13	73.20	42.97	30.63	43.47	26.83	28.20	28.59	30.92	32.24	36.19	49.61
46.45	63.78			43.28	31.62	57.56	28.13	29.12	31.25	33.67	33.27	36.65	59.22
55.08	64.58			53.37	32.02	67.86	33.41	30.48	32.17	34.74	35.91	42.40	61.66
57.56	72.42			56.70	31.62	76.81	36.34	35.97	35.89	36.34	36.73	57.17	73.07
67.79	73.20			60.03	32.02	80.68	37.11	36.49	40.04	36.82	37.72	60.90	80.43
74.85	79.47			62.64	32.20	83.22	37.44	37.09	45.45	38.27	39.64	64.18	
77.15				70.84	32.89	84.11	39.26	39.43	48.16	40.51	44.48	65.19	
				74.39	33.86		42.36	40.33	49.01	42.68	45.59	66.23	
				76.64			42.74	40.85	51.50	44.10		67.31	
				78.75			44.21	41.36	54.55	45.14		75.37	
							44.83	41.90	55.22	52.88		76.08	
							46.18	42.47	57.17	61.12		76.81	
							48.46	44.00	60.03	64.10		78.31	
							48.87	44.41	65.24	65.60		79.08	
							49.90	48.41	67.14	68.31		84.11	
							51.19	49.14	70.06	72.48			
							51.66	49.67	76.01	75.52			
							51.94	51.25	76.88	77.03			

Table C 6 continued: Angle 2Θ of the phases and elements in XRD peaks for SB + 2 % ZrO_2/Cu solder joint.

Bi_2O_3	Sn	Cu	CuSn	Cu_6Sn_5	Sn_3O_4	Cu_3Sn	$Cu_{10}Sn_3$	Cu_8Zr_3	SnO	SnZr	Zr_5Sn_3	$ZrSn_2$	ZrO_2
							53.35	78.85	78.15				
							55.37	81.26					
							57.40	84.93					
							61.89						
							63.30						
							63.70						
							64.08						
							64.53						
							64.78						
							65.34						
							68.94						
							72.03						
							72.29						
							72.55						
							74.06						
							74.54						
							77.40						
							78.23						
							79.31						
							80.11						
							80.68						
							81.26						

Table C 7: Angle 2Θ of the phases and elements in XRD peaks for SB + 3 % ZrO_2/Cu solder joint.

Element (2θ)													
BiZr	**Bi**	**Sn**	**Cu**	**CuSn**	**Cu_6Sn_5**	**Cu_3Sn**	**$Cu_{10}Sn_3$**	**SnO_2**	**Zr_3O_1**	**SnZr**	**ZrCu**	**$ZrSn_2$**	**ZrO_2**
20.60	33.50	34.25	43.30	43.47	30.13	37.77	22.61	31.45	24.99	45.14	26.91	25.80	18.24
24.36	48.13	36.01	50.43	50.08	35.18	41.79	24.23	36.40	31.76	52.88	34.84	33.54	24.99
24.90	59.81	49.24	74.13	73.20	42.97	43.47	26.83	40.78	34.48	61.12	35.71	36.19	31.76
29.97	70.03	54.55			43.28	57.56	28.13	52.46	36.27	64.10	36.22	36.65	34.48
30.84	80.03	62.54			53.37	67.86	33.41	62.59	40.84	65.60	36.85	42.40	36.27
33.15		65.91			56.70	76.81	36.34	65.55	47.57	68.31	38.24	57.17	40.84
33.95		72.10			60.03	80.68	37.11	77.85	52.65	72.48	38.42	60.90	47.57
34.54		76.52			62.64	83.22	37.44		56.59	75.52	40.97	64.18	52.65
35.13					70.84	84.11	39.26		62.96	77.03	42.19	65.19	56.59
33.95					74.39		42.36		67.97	78.15	42.76	66.23	62.96
34.54					76.64		42.74		69.06		43.78	67.31	67.97
35.13					78.75		44.21				45.67	75.37	69.06
35.52					78.98		44.83				55.48	76.08	
36.25							46.18				55.62	76.81	
37.74							48.46				58.07	78.31	
38.30							48.87				71.97	79.08	
39.00							49.90				75.66	84.11	
40.03							51.19						
41.93							51.66						
42.58							51.94						

Table C 7 continued: Angle 2Θ of the phases and elements in XRD peaks for SB + 3 % ZrO_2/Cu solder joint.

BiZr	**Bi**	**Sn**	**Cu**	**CuSn**	**Cu_6Sn_5**	**Cu_3Sn**	**$Cu_{10}Sn_3$**	**SnO_2**	**Zr_3O_1**	**SnZr**	**ZrCu**	**$ZrSn_2$**	**ZrO_2**
45.45							53.35						
46.21							55.37						
46.83							57.40						
47.61							61.89						
49.94							63.30						
51.11							63.70						
51.24							64.08						
51.67							64.53						
52.10							64.78						
53.74							65.34						
56.60							68.94						
57.26							72.03						
58.56							72.29						
60.11							72.55						
60.76							74.06						
61.61							74.54						
62.01							77.40						
							78.23						
							79.31						
							80.11						
							80.68						
							81.26						

APPENDIX D

Table D 1: Vickers microhardness of SB solder alloy.

Indentation Number	Diameter of Indentation (µm)	Vickers microhardness Number (HV)
1	D_1 :81.60 D_2 :81.60	27.84
2	D_1 :80.30 D_2 :83.65	27.59
3	D_1 :81.50 D_2 :73.35	29.39
4	D_1:78.60 D_2 :80.60	29.26
5	D_1 :78.10 D_2 :79.60	29.82
	Average	**28.78**

Table D 2: Vickers microhardness of SB + 1 % Mo solder alloy.

Indentation Number	Diameter of Indentation (µm)	Vickers microhardness Number (HV)
1	D_1 :82.55 D_2 :84.85	26.46
2	D_1 :84.10 D_2 :83.47	26.41
3	D_1 :83.60 D_2 :83.28	26.63
4	D_1:81.85 D_2 :78.85	28.72
5	D_1 :86.10 D_2 :81.75	26.32
	Average	**26.92**

Table D 3: Vickers microhardness of SB + 2 % Mo solder alloy.

Indentation Number	Diameter of Indentation (µm)	Vickers microhardness Number (HV)
1	D_1 :83.55 D_2 :81.85	27.11
2	D_1 :78.10 D_2 :80.60	29.45
3	D_1 :82.47 D_2 :79.60	28.23
4	D_1:75.43 D_2 :79.85	30.76
5	D_1 :81.60 D_2 :78.25	29.02
	Average	**28.91**

Table D 4: Vickers microhardness of SB + 3 % Mo solder alloy.

Indentation Number	Diameter of Indentation (µm)	Vickers microhardness Number (HV)
1	D_1 :77.10 D_2 :80.85	29.73
2	D_1 :85.60 D_2 :77.10	28.02
3	D_1 :80.10 D_2 :77.60	29.82
4	D_1:78.35 D_2 :79.60	29.73
5	D_1 :79.97 D_2 :81.10	28.58
	Average	**29.18**

Table D 5: Vickers microhardness of SB + 1 % ZrO_2 solder alloy.

Indentation Number	Diameter of Indentation (µm)	Vickers microhardness Number (HV)
1	D_1 :72.85 D_2 :74.85	33.99
2	D_1 :75.60 D_2 :76.10	32.23
3	D_1 :79.60 D_2 :79.50	29.30
4	D_1:74.32 D_2 :73.35	34.05
5	D_1 :77.10 D_2 :75.35	31.91
	Average	**32.28**

Table D 6: Vickers microhardness of SB + 2 % ZrO_2 solder alloy.

Indentation Number	Diameter of Indentation (µm)	Vickers microhardness Number (HV)
1	D_1 :82.10 D_2 :81.85	27.59
2	D_1 :81.60 D_2 :79.10	28.72
3	D_1 :85.10 D_2 :74.60	29.08
4	D_1:82.10 D_2 :79.12	28.53
5	D_1 :80.35 D_2 :81.35	28.36
	Average	**28.46**

Table D 7: Vickers microhardness of SB + 3 % ZrO_2 solder alloy.

Indentation Number	Diameter of Indentation (µm)	Vickers microhardness Number (HV)
1	D_1 :79.85 D_2 :83.95	27.64
2	D_1 :81.10 D_2 :85.28	26.79
3	D_1 :83.60 D_2 :86.85	25.53
4	D_1:82.10 D_2 :76.85	29.35
5	D_1 :80.10 D_2 :80.35	28.81
	Average	**27.62**

Table D 8: Maximum load and shear stress of SB/Cu solder joint.

Sample	Maximum Load (kN)	Maximum Shear Stress (MPa)
1	0.7383	156.760
2	0.2484	49.690
3	0.4605	92.104
4	0.5206	104.132
5	0.6047	120.649
Average	**0.5145**	**104.667**

Table D 9: Maximum load and shear stress of SB + 1 % Mo/Cu solder joint.

Sample	Maximum Load (kN)	Maximum Shear Stress (MPa)
1	0.4729	94.584
2	0.4922	98.442
3	0.2173	43.469
4	0.5346	106.923
5	0.3490	69.920
Average	**0.4132**	**82.668**

Table D 10: Maximum load and shear stress of SB + 2 % Mo/Cu solder joint.

Sample	Maximum Load (kN)	Maximum Shear Stress (MPa)
1	0.2387	47.751
2	0.2206	44.127
3	0.3917	78.346
4	0.4256	85.123
5	0.2851	57.034
Average	**0.3123**	**62.476**

Table D 11: Maximum load and shear stress of SB + 3 % Mo/Cu solder joint.

Sample	Maximum Load (kN)	Maximum Shear Stress (MPa)
1	0.5094	101.894
2	0.5666	113.319
3	0.9672	193.440
4	0.6989	139.782
5	0.7008	140.174
Average	**0.6885**	**137.721**

Table D 12: Maximum load and shear stress of SB + 1 % ZrO_2/Cu solder joint.

Sample	Maximum Load (kN)	Maximum Shear Stress (MPa)
1	0.4423	88.470
2	0.3298	65.970
3	0.5417	108.342
4	0.3161	63.232
5	0.5603	112.074
Average	**0.438**	**87.617**

Table D 13: Maximum load and shear stress of SB + 2 % ZrO_2/Cu solder joint.

Sample	Maximum Load (kN)	Maximum Shear Stress (MPa)
1	0.2936	58.725
2	0.3823	76.473
3	0.5598	111.969
4	0.4338	86.761
5	0.7620	152.400
Average	**0.4863**	**97.265**

Table D 14: Maximum load and shear stress of SB + 3 % ZrO_2/Cu solder joint.

Samples	Maximum Load (kN)	Maximum Shear Stress (MPa)
1	0.8432	168.655
2	0.8979	179.598
3	0.7142	142.840
4	1.1192	223.855
5	0.7817	156.347
Average	**0.8712**	**174.259**

APPENDIX E

Table E 1: Contact angle for SB solder alloy.

	Contact Angle (°)					Average Contact Angle (°)	Spread Area (mm^2)	Spread Ratio (%)
Sample 1	48.21	69.10	72.64	71.70	65.42	48.21	13.23	63.9
Sample 2	82.79	70.68	63.43	70.10	71.76	82.79	14.68	69.6
Sample 3	68.27	56.76	72.24	58.96	64.06	68.27	15.16	66.4
Sample 4	59.40	65.90	68.88	63.32	64.38	59.4	13.91	67.6
Sample 5	60.98	72.47	68.09	63.51	66.27	60.98	15.28	63.6
	Total Average					**66.38**	**14.45**	**66.2**

Table E 2: Contact angle for 1 % Mo + SB solder alloy.

	Contact Angle (°)					Average Contact Angle (°)	Spread Area (mm^2)	Spread Ratio (%)
Sample 1	63.92	57.45	62.71	74.38	64.62	64.62	15.86	74.5
Sample 2	76.37	69.02	76.64	70.20	73.06	73.06	13.43	65.9
Sample 3	61.03	62.43	68.04	62.40	63.48	63.48	14.68	68.5
Sample 4	56.12	53.66	57.81	49.93	54.38	54.38	19.72	73.6
Sample 5	53.75	63.13	58.37	49.64	56.23	56.23	18.17	72.1
	Total Average					**62.35**	**16.38**	**70.9**

Table E 3: Contact angle for 2 % Mo + SB solder alloy.

	Contact Angle (°)					Average Contact Angle (°)	Spread Area (mm^2)	Spread Ratio (%)
Sample 1	34.59	37.45	42.87	44.65	39.90	34.59	24.110	80.1
Sample 2	62.07	55.00	68.6	67.38	63.26	62.07	16.275	69.2
Sample 3	64.62	70.24	63.7	72.02	67.65	64.62	14.390	65.1
Sample 4	48.64	47.95	64.46	54.97	54.01	48.64	13.639	73.1
Sample 5	57.10	64.35	76.92	63.65	65.51	57.10	17.170	70.1
Total Average						**58.07**	**17.12**	**71.5**

Table E 4: Contact angle for 3 % Mo + SB solder alloy.

	Contact Angle (°)					Average Contact Angle (°)	Spread Area (mm^2)	Spread Ratio (%)
Sample 1	46.57	58.46	53.09	57.31	53.86	46.57	17.59	74.2
Sample 2	52.92	78.69	69.94	62.15	65.93	52.92	14.08	66.1
Sample 3	47.79	73.98	50.38	55.42	56.90	47.79	13.46	68.0
Sample 4	56.31	78.38	50.47	53.93	59.78	56.31	14.75	72.7
Sample 5	25.54	39.47	24.09	25.65	28.69	25.54	31.08	86.6
Total Average						**53.03**	**18.20**	**73.5**

Table E 5: Contact angle for 1 % ZrO_2 + SB solder alloy.

	Contact Angle (°)					Average Contact Angle (°)	Spread Area (mm^2)	Spread Ratio (%)
Sample 1	52.86	57.90	63.90	52.00	56.67	52.86	17.09	72.1
Sample 2	67.68	62.46	71.81	56.84	64.70	67.68	15.85	71.7
Sample 3	39.14	26.56	41.26	24.29	32.82	39.14	30.25	84.1
Sample 4	31.54	30.01	21.23	20.43	25.81	31.54	33.75	85.0
Sample 5	59.63	61.15	64.25	62.72	61.94	59.63	17.52	76.6
Total Average						**48.39**	**22.90**	**77.9**

Table E 6: Contact angle for 2 % ZrO_2 + SB solder alloy.

	Contact Angle (°)					Average Contact Angle (°)	Spread Area (mm^2)	Spread Ratio (%)
Sample 1	27.52	30.83	26.80	47.38	33.14	27.52	30.85	86.9
Sample 2	61.73	59.67	60.72	57.37	59.88	61.73	21.88	79.6
Sample 3	60.01	68.50	49.67	69.45	61.91	60.01	15.00	71.7
Sample 4	43.72	49.53	39.44	50.42	45.78	43.72	32.18	86.3
Sample 5	27.66	27.20	24.82	22.78	25.62	27.66	14.48	68.9
Total Average						**45.27**	**22.90**	**78.7**

Table E 7: Contact angle for 3 % ZrO_2 + SB solder alloy.

	Contact Angle (°)					Average Contact Angle (°)	Spread Area (mm^2)	Spread Ratio (%)
Sample 1	43.36	58.47	54.67	49.80	51.58	43.36	18.47	78.6
Sample 2	69.56	79.88	68.14	65.66	70.82	69.56	14.65	69.4
Sample 3	44.41	62.24	43.21	59.80	52.42	44.41	17.21	73.6
Sample 4	71.56	70.20	62.74	69.92	68.61	71.56	14.73	72.6
Sample 5	48.60	44.31	30.63	25.29	37.21	48.60	28.58	86.8
	Total Average					**56.13**	**18.73**	**76.2**